DEVELOPMENT OF HIGH ENERGY LASER TARGET MATERIALS : SYNTHESIS OF LOW DENSITY POROUS POLYMERS, AND CHARACTERISATION USING TIME DOMAIN NUCLEAR MAGNETIC RESONANCE

Christopher Stephen Andrew Musgrave

A Thesis Submitted for the Degree of PhD
at the
University of St Andrews

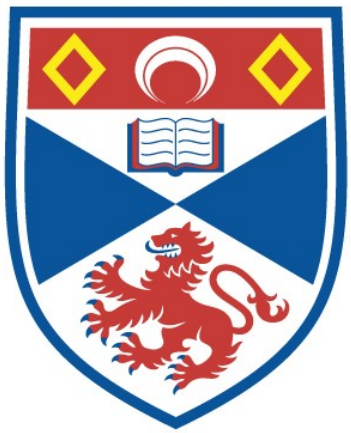

2014

Development of High Energy Laser Target Materials; Synthesis of Low Density Porous Polymers, and Characterisation using Time Domain Nuclear Magnetic Resonance

Christopher Stephen Andrew Musgrave

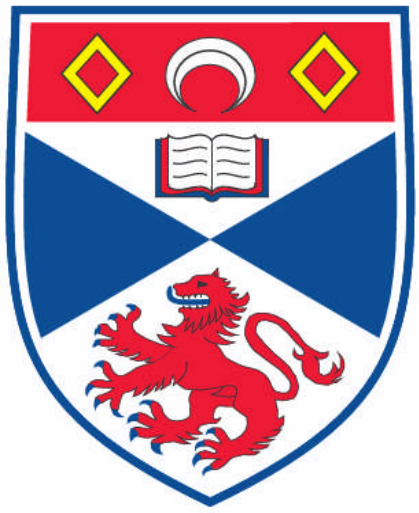

This Thesis is submitted in partial fulfilment for the degree of PhD at the University of St Andrews

December 2014

Declaration

1. Candidate's declarations:

I, Christopher Stephen Andrew Musgrave, hereby certify that this thesis, which is approximately 38,500 words in length, has been written by me, and that it is the record of work carried out by me, or principally by myself in collaboration with others as acknowledged, and that it has not been submitted in any previous application for a higher degree.

I was admitted as a research student in August, 2010 and as a candidate for the degree of PhD in August, 2011; the higher study for which this is a record was carried out in the University of St Andrews between 2010 and 2014.

Date …… Signature of candidate ……

2. Supervisor's declaration:

I hereby certify that the candidate has fulfilled the conditions of the Resolution and Regulations appropriate for the degree of PhD in the University of St Andrews and that the candidate is qualified to submit this thesis in application for that degree.

Date …… Signature of supervisor ……

In submitting this thesis to the University of St Andrews I understand that I am giving permission for it to be made available for use in accordance with the regulations of the University Library for the time being in force, subject to any copyright vested in the work not being affected thereby. I also understand that the title and the abstract will be published, and that a copy of the work may be made and supplied to any bona fide library or research worker, that my thesis will be electronically accessible for personal or research use unless exempt by award of an embargo as requested below, and that the library has the right to migrate my thesis into new electronic forms as required to ensure continued access to the thesis. I have obtained any third-party copyright permissions that may be required in order to allow such access and migration, or have requested the appropriate embargo below.

The following is an agreed request by candidate and supervisor regarding the publication of this thesis:

b) Embargo on all of print and electronic copy for a period of 3 years on the following ground(s):

1. Commercial sensitivity as this research was funded by the Atomic Weapons Establishment (AWE) and
2. Publication of thesis would preclude future publication.

Research sponsered by the AWE Outreach fund is primarily to support the UK's nuclear deterrent program. As such, an embargo is applied to protect any potential Ministry of Defence Intellectual Property. To compensate the candidate future publication is encouraged on material that does not fit into this criterion.

Abstract

This work details the synthesis of low density porous polymers, and characterisation with an emphasis on Time Domain Nuclear Magnetic Resonance (TD-NMR). High energy laser physics utilises low density porous polymers to study astrophysical phenomena at high pressures and temperatures in the form of plasma. Low Z, low density Polymerised High Internal Phase Emulsions (PolyHIPE) and aerogels form a large part of these capabilities, however increasingly stringent laser target parameters are now required to develop new capabilities. For low density porous polymers, this demands greater control over properties such as pore size, density, composition ($C_nH_{>n}$) and homogeneity through novel synthesis and characterisation.

Microstructure inhomogeneity of styrene-co-divinyl benzene (S-co-DVB) polyHIPEs in conjunction with novel t-butyl styrene and para divinyl benzene polyHIPEs were investigated using ^{1}H spin-lattice (T_1) and spin-lock ($T_{1\rho}$) NMR relaxation experiments using TD-NMR. The strong relationship between ^{1}H spin-lattice relaxation times and Dynmaic Mechanical Analysis (DMA) data, and application of relaxation experiments at varied temperatures reveal that structural inhomogeneity is based on poor emulsion stability and clustering of DVB polymer affecting bulk molecular motion.

Divinyl benzene (DVB) aerogels and a range of innovative $C_nH_{>n}$ aerogels such as poly-5-vinyl-2-norbornene were synthesised using free-radical, cationic or ring opening metathesis polymerisation techniques. A one-step synthesis of homogeneous density gradient DVB aerogels was developed for the first time, which is fundamental to be able to study plasma shock fronts. Characterisation using X-ray tomography revealed the homogeneous density gradient. Successful carbonisation of dichloroparaxylene (DCPX) aerogels has similar properties to resorcinol-formaldehyde (RF) aerogels, but is produced in significantly less time and shrinkage, presents as a candidate for future laser experiments.

Correlation between NMR relaxation times to established techniques of DMA and mercury porosimetry was explored to determine the suitability of TD-NMR in characterisation of low density porous polymers.

Acknowledgments

Whilst this thesis bears only my name, there are many people I must thank for their contribution throughout my studies. For me this is a large achievement, but in other parts of my life there have been tragedies that have affected me along the way. I would like to give a heartfelt mention to my grannie, Margaret Davidson, whom I will always love, and Douglas Faith of AWE who passed away throughout the duration of this work. Both had a strong influence during a difficult period, and their passing gave me more determination.

This work would not be possible without the auspices of the AWE Outreach fund. Furthermore, AWE scientists greatly assisted in much of the characterisation, in particular Dr Nick Bazin, Dr Tony Swain, Dr Niaz Khan, Dr Thomas Wildsmith, Mr Sav Chima and Dr Simon Pitts.

A special thank you must go to my supervisor Dr Wigen Nazarov who provided many contributions and infinite pastoral care unreservedly. The most honourable of men!

I am indebted to Dr Natalia Borisenko, Ms Lidia Borisenko and Mr Andrey Orekhov at the Lebedev Physical Institute, Moscow for X-ray tomography characterisation.

I thank the staff of School of Chemistry and the University of St Andrews for numerous assistance and support.

To my friends, Roadhouse. It had been one massive journey together.

My family has always been a constant source of strength and unconditional support. My mum and dad, my brothers; Ally, Ned, Joe and Donald, the rest of the growing Musgrave clan, and of course Hugo.

Anche, Serena e famiglia Mariani, grazie mille, sono molto grato per il vostro sostegno.

Contents

Abbreviations, Acronyms and Symbols

$\hbar$- Plancks constant

γ- Gyromagnetic ratio (NMR) or strain (DMA)

μ- Magnetic dipole moment

τ- Correlation time (NMR), relaxation time (DMA)

I- Intrinsic angular momentum (spin)

T_1- Spin-lattice relaxation

$T_{1\rho}$- Relaxation under spin-lock/relaxation under RF

ω_0- Larmor frequency

2VN- 2-vinyl naphthalene

5V2N- 5-vinyl-2-norbornene

$\mathbf{B}$- External magnetic field vector

B_0- External magnetic field magnitude

C- Carbon

CP- Cross-polarization

CPD- Critical Point Drier

CMC- Critical Micelle Concentration

CSA- Chemical Shielding Anisotropy

CTAB- Cetyltrimethylammonium bromide

DCE- Dichloroethane

DCPD- Dicylcodipentadiene

DCPX- Dichloroparaxylene

DDBSS- Dodecylbenzensulfonic acid sodium salt

DMA- Dynamic Mechanical Analysis

DSC- Differential Scanning Calorimetry

DVB- Divinyl benzene 80. 80% DVB isomers, 20% ethyl styrene isomers

E - Energy (NMR) or Young's modulus (DMA)

EDX- Energy Dispersive X-ray microanalysis

EUV- Extreme Ultraviolet Light

FEG-SEM- Field Emission Gun Scanning Electron Microscopy

GPC- Gel Permeation Chromatography

^{1}**H**- Proton nucleus (NMR)

H- Hydrogen

HIPE- High Internal Phase Emulsion

HLB- Hydrophobic-Lipophilic Balance

ICF- Inertial Confinement Fusion

kHz- Kilohertz

Laser- Light Amplification by Stimulated Emission of Radiation

MAS- Magic Angle Spinning

MHz- MegaHertz

NMR- Nuclear Magnetic Resonance

Para-DVB- para-divinyl benzene 85%

PolyHIPE- Polymerized High Internal Phase Emulsion

PS- Polystyrene

PVDF- Polyvinylidenefluoride

RF- Radiofrequency (NMR), Resorcinol-Formaldehyde aerogel

ROMP- Ring Opening Metathesis Polymerisation

S- Styrene

S-co-DVB- Styrene-co-Divinyl benzene

SEM- Scanning Electron Microscopy

Span® 20- Sodium monolaurate

Span® 80- Sodium monooleate

SSNMR- Solid-state Nuclear Magnetic Resonance

t-BS- 4-tertiary butyl styrene

TD-NMR- Time Domain Nuclear Magnetic Resonance

Tg- Glass transition temperature

TGA- Thermogravametric Analysis

Publications

N. G. Borisenko, W. Nazarov, C. S. A. Musgrave, Yu. A. Merkuliev, A. S. Orekhov and L. A. Borisenko, *J. Radioanal. Nucl. Chem*., **299**, 2, 961-964, 2014.

K. L. Anderson, W. Nazarov, C. S. A. Musgrave, N. Bazin and D. Faith, *J. of Radioanal. Nucl. Chem*., **299**, 2, 969-975, 2014.

L. A. Borisenko, A. S. Orekhov, C. S. A. Musgrave, W. Nazarov, Yu. A. Merkuliev and N. G. Borisenko, manuscript ready for submission (September 2014).

C. S. A. Musgrave and W. Nazarov, manuscript ready for submission (September 2014).

1. Introduction

1.1 Background

Matter at extremely high pressures and temperatures forms plasma, and is the fourth state of matter comprising of ionised gases in the form of positive or negatively charged ions, electrons and neutrons. Plasma is common throughout the universe, for example stars are largely comprised of plasma, supernovae events produce plasma, and plasma shock fronts arise from solar wind interacting with the Earth's atmosphere. Therefore, the study of plasma can help increase our understanding of the Earth and universe but unlike other states of matter plasma is short-lived thus difficult to investigate. However, these astrophysical events can be replicated in the laboratory using high energy lasers.

A high energy laser produces highly amplified and coherent light that interacts with a specially designed material called a 'target' to produce plasma. A target is typically 1 mm^3 and can be composed of metals, composites and low density polymers depending on the laser experiment. In addition, targets are often complicated in design, usually fabricated from a number of separate components to form the final laser target. A major component of these targets are low density porous materials. Low density porous materials are also used to incorporate high atomic weight elements (high Z) to use as 'fingerprints' in X-ray diagnostics.[1] Lasers can interact with targets either directly or indirectly depending on the design of the experiment. In direct drive experiments, a high energy laser is focused directly on a specific region of the target. These experiments are designed to create a shock front or a shock wave to study different aspects of shock behaviour and instabilities of matter in the plasma state. Indirect drive experiments are designed to deliver a uniform energy to the target. An example of target for indirect drive experiments consists of a metal hohlraum (usually a cylindrical container made of gold) encapsulating low density polymer foam, which contains another target component.[2] The laser is focused inside the hohlraum to distribute the laser energy uniformly to the central target component.

Requirements for laser experiments are developed from modeling software, which is validated by experiments on a high energy laser. The laser destroys the target to produce plasma, thus production and characterisation of the target needs to be thorough in order to have a good degree of confidence in the experimental results. The cost of these experiments can be as high as £100,000 per shot, therefore each experiment must be planned and executed with due diligence. High energy lasers are large scale projects, which can justify such cost per shot. For example, it cost $8 billion to construct the National Ignition Facility (NIF) in the USA, the largest laser in the world, and which is approximately the size of 3 football pitches and 6 stories high.

There are many high energy lasers throughout the world each designed with different laser configurations in order to perform experiments on different aspects of plasma physics. Some lasers used currently are NIF at the Lawrence Livermore National Laboratory (USA), OMEGA laser at the University of Rochester (USA), Laser Megajoule (France) and ORION at the Atomic Weapons Establishment (AWE) (UK). NIF consists of 192 laser beams synchronised to interact with the target at precisely the same time, increasing the surface temperature and producing a shock wave that will drive energy through the target to generate homogeneous plasma. NIF was designed to achieve ignition, and these experiments will one day achieve ignition for nuclear fusion energy, when the energy released from the fuel is greater than the energy input.[2] Fusion is the same mechanism that powers the Sun, and achieving ignition will solve the energy crisis by providing clean, sustainable energy. ORION in the UK consists of 10 long pulse beams (longer time, lower energy) and 2 short pulse beams (shorter time, higher energy), which gives more experimental flexibility. The major focus of ORION is to support the UK nuclear deterrent program studying weapons physics. This thesis is funded by the AWE Outreach program with the aim of improving the capabilities in synthesis and characterisation of the low density polymer components used in these high energy laser experiments.

There are two main methods for generation and confinement of plasma, Inertial Confinement Fusion (ICF) and Magnetically Confined Fusion (MCF). The principle of ICF is to produce energy by imploding a target filled with deuterium and tritium fuel to produce helium and neutrons releasing energy. MCF uses strong magnetic fields to confine the plasma for energy generation called a Tokomak. At time of writing, a proto-type Tokomak reactor was under construction as part of the International Thermonuclear Experimental Reactor (ITER) project.[3] However, the major downside of Tokomak is that there is a significant risk of damage to the plasma chamber from disruptions arising from insufficient and inhomogeneous confinement of the plasma.

In addition to important contributions to high energy physics, low density foams doped with various metals have been used to generate extreme ultraviolet light (EUV) as a component of next generation nanolithography technology for new generation of electronic circuits.[4–7]

1.2 Low Density Porous Polymers in High Energy Laser Physics

Low density foams are used extensively in high energy laser physics. For example, they are used to shield other component of a target from the laser as laser energy propagating through foam can increase the homogeneity of the laser interacting with the target, or act as a scaffold for other target components in the case of ICF.[8] Foams can be used to produce plasma jets to simulate astrophysical conditions to study young stellar objects.[9–11] Foams comprised of low atomic weight elements (low Z) produce fewer X-rays than higher Z equivalents creating opaque plasmas, which is highly desirable for some experiments. Opacity in plasma is a measure of absorption and/or scattering of radiation.[2,7,12,13]

Most of the synthetic and characterisation techniques used here (and in development of laser targets) could easily apply to other fields concerned with low density foams. Low density foams are being used in a number of growing bio-technology applications such as tissue engineering,[14–16] filtration[17,18] and ion/molecular recognition.[19]

Low density foams need to meet a number of stringent requirements to be considered for laser physics experiments;

1. Densities between 3 mg/cm^{-3} up to 100 mg/cm^{-3} depending on the experiment. Lower densities will generate less X-ray interference.
2. High degree of homogeneity for both pore distribution and foam density to ensure laser propagation is homogeneous.
3. Nanometer pore size up to a maximum of 1 μm. Large pore size becomes an issue in propagating laser.
4. For some targets, the foam must be strong enough for machining. Targets are small, with the foam components between 100 to 500 μm in size. An ultra-precision lathe can machine foams to these dimensions, however foams cannot fracture as this may remove many μm of material. The tolerance of dimensions is strict (± μm). Foams can be moulded to shape but as they derive from polymers, shrinkage can become an issue in certain systems.
5. Low Z composition is preferred due to generation of greater plasma opacity, however specific experiments can require high Z elements such as chlorine or copper.[20,1] Here, low Z elements of interest are
6. Density gradients are highly desirable for plasma shock front experiments. Fabricated targets containing air gaps and high density regions are not acceptable.

Two of the most common types of low density porous polymers that are used for laser physics experiments are aerogels and polymerised high internal phase emulsions (PolyHIPEs). Both are established materials,[21–32] but aerogels are perhaps more well-known than polyHIPEs. Aerogels, also known as 'frozen smoke', are used as a commercial insulating material[33–35] and have been a key component of NASAs Stardust program to collect solid particles undamaged from space.[36,37]

Targets utilising aerogels mostly use resorcinol-formaldehyde (RF) aerogel. RF has been considered for components in ICF,[38] or density gradient targets.[39] There are many desirable characteristics of RF such as nanometer pore size, and very low densities (20 mg/cm $^{-3}$) can be achieved. Despite containing oxygen, which is often acceptable for some experiments, can be eliminated through carbonisation to produce a carbon foam. Carbonised RF at low densities is strong enough for machining.[38]

PolyHIPEs are also used for laser experiments, and in contrast to aerogels there is a difference in pore size and elemental composition that distinguish polyHIPE and RF targets.[40] A PolyHIPE is formed on polymerisation of a high internal phase emulsion (HIPE), where a HIPE is an emulsion with greater than 74% internal phase. Typically this is a water-in-oil emulsion, with the oil phase consisting of polymerisable monomers. Removal of the internal phase leaves a dry, lightweight material with regular pore structure. PolyHIPE pore sizes are usually between 5-50 micrometers, but for laser targets pore size should ideally by 1 micrometer or below.

High energy laser physics experiments are becoming more complex and, consequently this increases the challenges for materials scientists to develop new low density materials. As a result, current materials commonly used no longer meet the criteria of new experiments. Alternatives to RF are desirable because of the lengthy synthesis process and high shrinkage, and current polyHIPEs often fail pore homogeneity tests. A problem for possible new target materials has been machining into regular, accurate dimensions since low density materials are often very fragile. PolyHIPE remains of interest as it is machinable at low densities.

In addition to the synthesis of new porous materials, there is a large dependency on characterisation. Accurate characterisation ensures more reliable experimental data and gives validity to theoretical modeling. This is particularly important for low density materials, which present many challenges for characterisation because of the lack of mass, and stringent tolerance limits for target specifications. Thus an

extensive range of techniques is used including SEM, mercury porosimetry, X-ray radiography, DSC, DMA, solid-state NMR and many more.

Each of the aforementioned techniques measures a specific property and they relate well to one another, providing a rigorous analysis of a target before it can be validated for use in a laser experiment. Conversely, one draw-back of such thorough analysis is the time taken to characterise every target in reasonable time, especially as the experimental conditions and target designs are getting increasingly challenging. There is now a greater demand for laser time and therefore efficient characterisation of targets is of great importance. The search for new methods to characterise laser materials is a continuous process and in this thesis a novel technique for low density material characterisation, Time Domain Nuclear Magnetic Resonance (TD-NMR) is presented. TD-NMR can provide a non-destructive analysis of a material by measuring nuclear spin relaxation, which could be a major contribution to the development and characterisation of laser targets.

1.3 Thesis Aims

The aim of this thesis was to develop new materials for a wide spectrum of high energy laser physics experiments and to improve characterisation capabilities of current low density laser target materials.

The interdisciplinary requirements to achieve these aims are reflected in the structure of this thesis. Chapters 2 and 3 detail the theoretical and experimental background required to do this work, highlighting the extensive effort that is mandatory to develop laser target materials. Chapter 4 investigates synthesis and physical properties of styrene-co-divinyl benzene (S-co-DVB), and derived polyHIPE systems including para-divinyl benzene (para-DVB) and tertiary butyl styrene (t-BS). Chapter 4 describes characterisation of polyHIPEs using TD-NMR, and relates ^{1}H nucleus T_1 and $T_{1\rho}$ relaxation times to other physical properties from other characterisation techniques, such as mercury porosimetry and dynamic mechanical analysis for validation. PolyHIPE microstructure inhomogeneity issues are discussed in chapter 4 and chapter 5, which employed NMR relaxation experiments at variable temperatures to analyse these issues in more detail and explore possible solutions. Styrene, t-BS, para-DVB and various copolymer of polyHIPEs were used in these experiments. Chapter 6 describes aerogel synthesis and characterisation and a new carbon-hydrogen aerogel systems. Synthesis of carbonised dichloroparaxylene (DCPX) aerogels, and homogeneous DVB density gradient aerogels are strong candidates for future laser targets. Each results chapter contains an appendix of supplementary information.

1.4 References

1 W. L. Perry, R. C. Dye, P. G. Apen, L. Foreman, and E. Peterson, *Applied Physics Letters*, 1995, **66**, 314.

2 M. Ragheb, *Inertial Confinement Fusion*, 2008.

3 *ITER: the world's largest Tokomak*, http://www.iter.org/mach.

4 M. Primout, D. Babonneau, L. Jacquet, B. Villette, F. Girard, D. Brebion, P. Stemmler, K. B. Fournier, R. Marrs, M. J. May, R. F. Heeter, R. J. Wallace, H. Nishimura, S. Fujioka, M. Tanabe, and H. Nagai, *High Energy Density Physics*, 2013, **9**, 750–760.

5 K. Nagai, *Encylopedia of Nanoscience and Nanotechnology*, American Scientific Publishers, 2011, 75–83.

6 M. Komura, K. Kamata, T. Iyoda, and K. Nagai, *Fusion Science and Technology*, 2013, **63**, 257–264.

7 T. Okuno, S. Fujioka, H. Nishimura, Y. Tao, K. Nagai, Q. Gu, N. Ueda, T. Ando, K. Nishihara, T. Norimatsu, N. Miyanaga, Y. Izawa, K. Mima, A. Sunahara, H. Furukawa, and A. Sasaki, *Applied Physics Letters*, 2006, **88**, 161501.

8 J. Biener, C. Dawedeit, S. H. Kim, T. Braun, M. A. Worsley, A. A. Chernov, C. C. Walton, T. M. Willey, S. O. Kucheyev, S. J. Shin, Y. M. Wang, M. M. Biener, J. R. I. Lee, B. J. Kozioziemski, T. van Buuren, K. J. J. Wu, J. H. Satcher, and A. V. Hamza, *Nuclear Fusion*, 2012, **52**, 062001.

9 C. D. Gregory, B. Loupias, J. Waugh, S. Dono, S. Bouquet, E. Falize, Y. Kuramitsu, C. Michaut, W. Nazarov, S. A. Pikuz, Y. Sakawa, N. C. Woolsey, and M. Koenig, *Physics of Plasmas*, 2010, **17**, 052708.

10 B. Loupias, C. D. Gregory, E. Falize, J. Waugh, D. Seiichi, S. Pikuz, Y. Kuramitsu, A. Ravasio, S. Bouquet, C. Michaut, P. Barroso, M. Rabec le Gloahec, W. Nazarov, H. Takabe, Y. Sakawa, N. Woolsey, and M. Koenig, *Astrophysics and Space Science*, 2009, **322**, 25–29.

11 C. D. Gregory, B. Loupias, J. Waugh, P. Barroso, S. Bouquet, E. Brambrink, S. Dono, E. Falize, J. Howe, Y. Kuramitsu, R. Kodama, M. Koenig, C. Michaut, S. Myers, W. Nazarov, M. M. Notley, A. Oya, S. Pikuz, M. Rabec le Gloahec, Y.

Sakawa, C. Spindloe, M. Streeter, L. a Wilson, and N. C. Woolsey, *Plasma Physics and Controlled Fusion*, 2008, **50**, 124039.

12 Y. Dong, J. Yang, L. Zhang, W. Shang, and T. Song, *Physics Letters A*, 2014, **378**, 813–816.

13 A. I. Gromov, N. G. Borisenko, S. Y. Gusikov, Y. A. Merkuliev, and A. V. Mitrofanov, *Laser and Particle Beams*, 1999, **17**, 661–670.

14 W. Busby, N. R. Cameron, and C. A. Jahoda, *Biomacromolecules*, 2001, **2**, 154–64.

15 E. M. Christenson, W. Soofi, J. L. Holm, N. R. Cameron, and A. G. Mikos, *Biomacromolecules*, 2007, **8**, 3806–14.

16 A. Barbetta, M. Dentini, E. M. Zannoni, and M. E. De Stefano, *Langmuir*, 2005, **21**, 12333–41.

17 F. Audouin, R. Larragy, M. Fox, B. O'Connor, and A. Heise, *Biomacromolecules*, 2012, **13**, 3787–94.

18 P. Krajnc, N. Leber, D. Stefanec, S. Kontrec, and A. Podgornik, *Journal of Chromatography A*, 2005, **1065**, 69–73.

19 C. Zhao, E. Danish, N. R. Cameron, and R. Kataky, *Journal of Materials Chemistry*, 2007, **17**, 2446.

20 N. Elliott, *Nuclear Instruments and Methods in Physics Research Section A: Accelerators, Spectrometers, Detectors and Associated Equipment*, 1995, **362**, 112–113.

21 J. M. Williams, *Langmuir*, 1988, **4**, 44–49.

22 N. R. Cameron and D. C. Sherrington, *Journal of Materials Chemistry*, 1997, **7**, 2209–2212.

23 N. R. Cameron, D. C. Sherrington, I. Ando, and H. Kurosu, *Journal of Materials Chemistry*, 1996, **6**, 719–726.

24 N. R. Cameron and D. C. Sherrington, *Journal of the Chemical Society, Faraday Transactions*, 1996, **92**, 1543.

25 D. Faith, C. J. Horsfield, and W. Nazarov, *Journal of Materials Science*, 2006, **41**, 3973–3977.

26 P. Hainey, I. M. Huxham, B. Rowatt, D. C. Sherrington, and L. Tetley, *Macromolecules*, 1991, **24**, 117–121.

27 S. S. Kistler, *Nature*, 1931, **127**, 741–741.

28 R. W. Pekala, US 4,873,218, 1989.

29 R. W. Pekala, C. T. Alviso, F. M. Kong, and S. S. Hulsey, in *Third International Symposium on Aerogels*, 1991, pp. 2–8.

30 R. W. Pekala and D. W. Schaefer, *Macromolecules*, 1993, **26**, 5487–5493.

31 L. W. Hrubesh, *Journal of Non-Crystalline Solids*, 1998, 225, 335–342.

32 J. K. Lee and G. L. Gould, *Journal of Sol-Gel Science and Technology*, 2007, **44**, 29–40.

33 *Thermablok Aerogel Ltd*, http://www.thermablok.co.uk.

34 *Spacetherm Aerogel Insulation*, http://www.proctorgroup.com/products/thermal–insul.

35 *Aspen Aerogels, Inc.*, http://www.aerogel.com.

36 S. M. Jones, *Journal of Sol-Gel Science and Technology*, 2006, **40**, 351–357.

37 S. M. Jones, *Gradient Composition Sol-Gel Materials*, Pasadena, 2000, vol. 3943.

38 B. Haendler, *Energy and Technology Review*, 1989.

39 Y. Zhong, B. Zhou, J. Gui, A. Du, Z. Zhang, and J. Shen, *Fusion Engineering and Design*, 2011, **86**, 238–243.

40 J. M. Williams, Jr, A. M. Nyitray, and M. H. Wilkerson, US 4,966,919, 1990.

2. Background theory

2.1 Molecular Weight

Most free radical polymerisation reactions are not controlled resulting in different chain lengths. Polymer chains can be described by their number average, $\overline{M}_n$, and the weight average, $\overline{M}_w$, molecular weight, respectively. $\overline{M}_w$ and $\overline{M}_n$ are different measures of molecular weight; $\overline{M}_n$ is a strict average of the weight divided by the number of chains present at length 'x', N_x, (equation 2.1), whereas $\overline{M}_w$ is presents an average based upon the weight of each chain, W_x in the fraction they are present (equation 2.2). This means that $\overline{M}_w$ can be a reflection of higher weight chains present. These values can be obtained from techniques such as gel permeation chromatography (GPC) by comparing to known standards. The division of $\overline{M}_w$ by $\overline{M}_n$ gives a value known as dispersity ($Đ_M$). $Đ_M$ is a measure of the polymer chain size homogeneity, so values close to 1 suggest the length of the polymer chains are roughly the same throughout the measured sample. FRP often has high $Đ_M$ (≈4 and above) as there is no control, whereas low values can be achieved using controlled polymerisation techniques, even in polyHIPEs.[2]

$$\overline{M}_n = \frac{\sum N_x M_x}{\sum N_x} \qquad (2.1)$$

$$\overline{M}_w = \frac{\sum W_x M_x}{\sum W_x} \qquad (2.2)$$

2.1.1 Molecular weight in Living polymerisation

Molecular weight in living polymerisation is a controllable factor due to the mechanism of the polymerisation; strictly speaking there is no termination reaction (hence it is called 'living') as polymerisation can begin once more monomer is added. In the absence of termination reactions, molecular weight is dependent on the ratio of living initiator to monomer present (equation 2.3), which results in the $Đ_M$ having values closer to 1 but no more than 1.5.

$$v = \frac{[M]_0 - [M]}{[I]_0} \qquad (2.3)$$

v is the kinetic chain chain length, which is the number of monomer units in each polymer chain initiated by each living initiator (I_0). Thus, $\overline{M}_n$ can be obtained and $Đ_M$ is then calculated in the same manner mention in the previous section once $\overline{M}_w$ is known.

2.2 Free radical polymerisation (FRP)

Free radical polymerisation (FRP) is the most common method of producing polymers. This is due to its versatility and tolerance of many functional groups.[1] One disadvantage of FRP is that it is an uncontrolled technique resulting in high values of the $Đ_M$ and despite this FRP remains the main method of producing polyHIPEs. However more controlled radical polymerisation techniques such as RAFT can control the polymerisation reaction, which based upon the amount of the RAFT initiator that is present in the reaction. RAFT can achieve narrower $Đ_M$ values (and different cell wall morphology related to RAFT reagents concentrations) compared to conventional radical polymerisation, which has been shown in polyHIPEs.[2]

2.2.1 Steps of free radical polymerisation

Polymerisation consists of three stages; initiation, propagation and termination. Initiation begins the polymerisation, propagation is the stage whereby the polymer grows, and termination end chain growth by combination or disproportionation mechanisms (scheme 2.1). These stages occur with all polymerisation techniques, however the specific mechanisms vary, particularly for living polymerizations, the polymerisation can be reactivated on addition of more monomer.

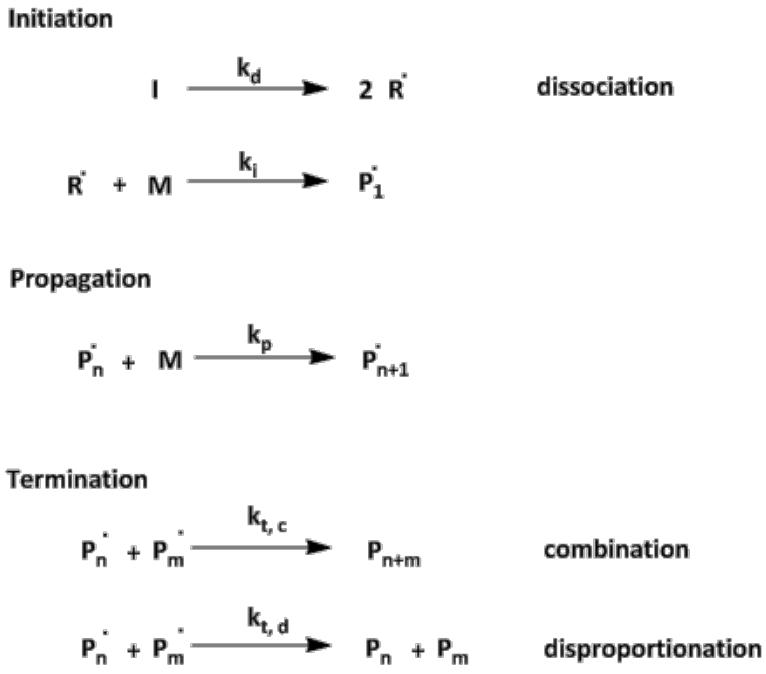

Scheme 2.1. General free-radical polymerisation scheme.

Initiation is the decomposition of an unstable molecule, called the initiator, into two radical species. The initiator combines with a monomer functional group to create a new covalent bond, leaving a replacement radical that can continue reacting with other monomer units growing the polymer chain. This begins the propagation step. The readiness of the initiator to decompose does not necessarily determine quick initiation as the initiator radical species can recombine, react with solvent or react with monomers. The efficiency factor, f, indicates the effective initiator radical concentration, and has the maximum possible value of 1, but is typically 0.3-0.8.[3]

Propagation is the step whereby the chain continually grows by repetitive addition of monomer units. With each addition of another monomer unit, a radical is left at the end of the chain for further addition of monomer units. During propagation, if multiple functional group monomers are present cross-linking reactions can occur. Factors such as stability of the radicals produced are important to propagation, for example styrene has 4 resonance structures allowing the radical to exist for a longer amount of time, thus the possibility of reaction with another radical is increased (figure 2.1).

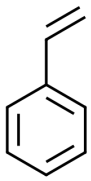

Styrene

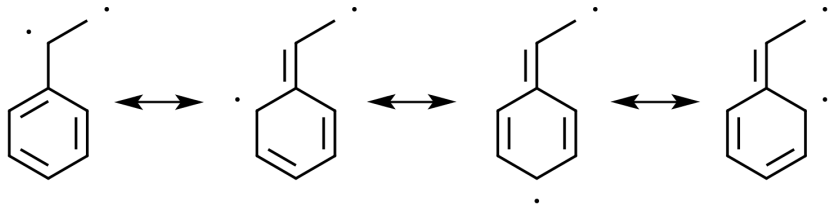

Figure 2.1. Resonance structures of styrene.

The final polymerisation step is termination whereby the reactive species is quenched, ceasing growth of the polymer chain by one of two mechanisms; combination, or disproportionation (scheme 2.1). Another termination mechanism is through chain-transfer, whereby the propagating chain combines with another species that is not a polymer chain such as solvent, initiator and other reactive species. This is a competitive process with the inactive molecule terminating the reactive species. Such chains transfer reactions will result in decreased average polymer chain length.[3–5]

2.3 Ionic polymerisation

Ionic polymerisation is a type of polymerisation that uses positively or negatively charged species to form polymers.[3] The polymerisation steps are the same as free-radical polymerisation, however there are mechanistic differences that distinguishes each type of polymerisation from one another.

Cationic polymerisation is a type of ionic polymerisation that utilizes an electrophilic initiator to form a positively charged reactive species for polymerisation. In addition, the same monomer can be polymerised by using multiple methods.[3,6] Conversely, anionic polymerisation utilizes a nucleophilic initiator to polymerise. This work utilises cationic polymerisation exclusively, and the polymerisation steps discussed in the following section.

2.3.1 Steps of Cationic Polymerisation

Cationic polymerisation initiators are typically Lewis acids, an electron pair acceptor, such as tin (IV) chloride and boron trifluoride.[3,6] The reactive species is a carbanion, and formed by a two-step process whereby the initiator first forms a π complex followed by an intramolecular rearrangement to form an ion pair with the monomer.[3] A co-catalyst is necessary for the initiation step in cationic polymerisation. This is a small molecule such as water, acetic acid or a phenol, used as proton donators to the monomer functional group.[3,6] Using stronger Lewis acids and more acidic co-catalysts initiation is faster, as the stronger proton donation encourages the formation of the catalyst-co-catalyst complex which proceeds to formation of the π complex.

The general polymerisation scheme shares similarities with FRP steps, however the difference is the initiation steps; demonstrating the co-catalyst activity to generate the ion pair with the monomer (scheme 2.2). There are two proposed terminations mechanisms, a unimolecular or bimolecular extinction. There is no clear agreement in literature on which happens, so both mechanisms have been included here.[3]

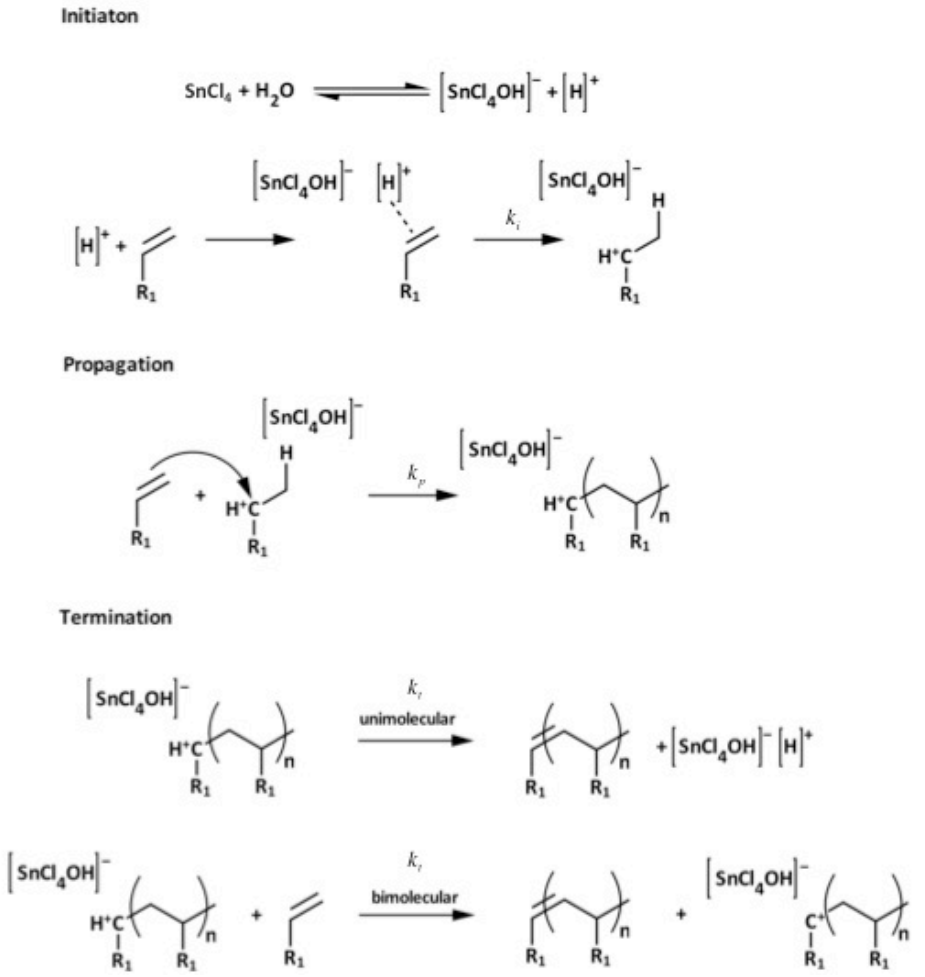

Scheme 2.2. The general scheme for cationic polymerisation using tin (IV) chloride and a vinyl group.

The acidic nature of the initiator provides an indication of the rate of propagation as a stronger the acid will more readily transfer its proton to the monomer, resulting in a faster rate.[3] The solvent polarity can also influence the reaction rate due to the distance the solvent creates between the ion pair. If the solvent is more polar it causes a bigger the gap between the ion pair, which results in the creation of space for another monomer to approach the reactive centre.[3] This increases the rate of polymerisation.

2.4 Olefin Metathesis Polymerisation

Olefin (alkene) metathesis uses metal catalysts to rearrange carbon-carbon double bonds. Thus, olefin metathesis polymerisation is the formation of polymers through the rearrangement of carbon-carbon double bonds.

Olefin metathesis provided polymer science with more controlled routes to polymers; enantioselective reactions and low $Đ_M$ values can be achieved.[7–9] This is explained by specific stereochemistry of the ligands on the catalyst, meaning monomers approaching the metal centre require a specific geometry.[7,10] Catalyst ligands are often large, with one de-coordinating with the metal centre whereby the monomer can now interact if the approach to the metal is correct. The catalysts used in this work are given in figure 2.2.

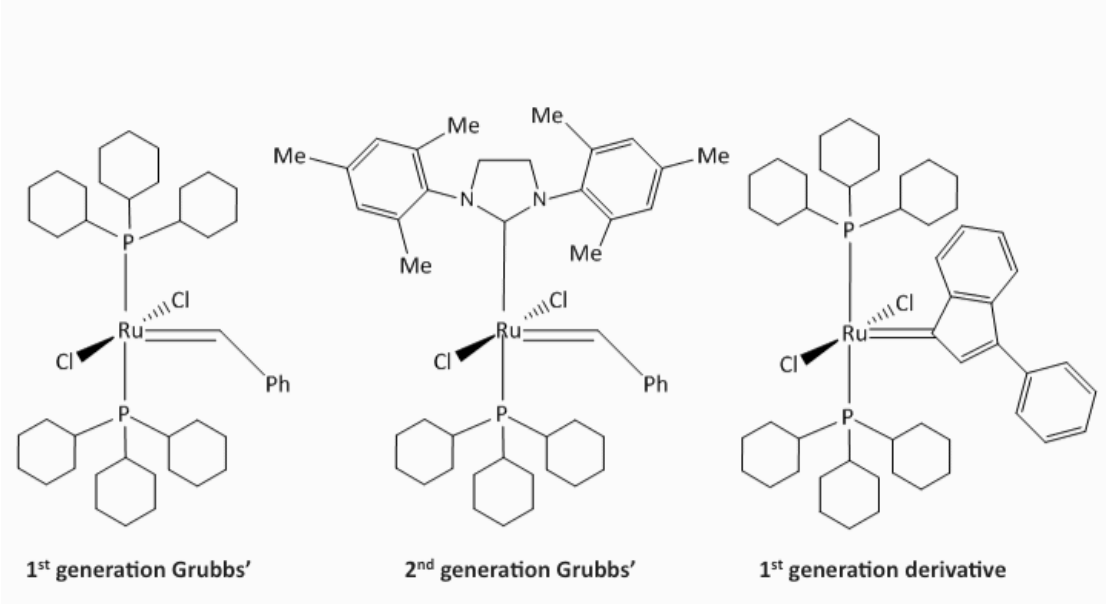

Figure 2.2. The Grubbs' type catalysts used in this work. The metal centre is surrounded by large ligands that influence polymerisation.

2.4.1 Ring Opening Metathesis Polymerisation (ROMP)

A class of metathesis reactions used for low density material synthesis is ROMP. Cyclic alkene monomers are opened by coordination to the metal catalyst, where metathesis occurs, before addition of another monomer unit in the same manner to form a propagating chain. The polymerisation matches the level of bond unsaturation as the monomer, and the reaction is driven by the release of ring strain, despite unfavorable entropy.[11] Typical ROMP monomers are norbornene and dicyclopentadiene (figure 2.3).

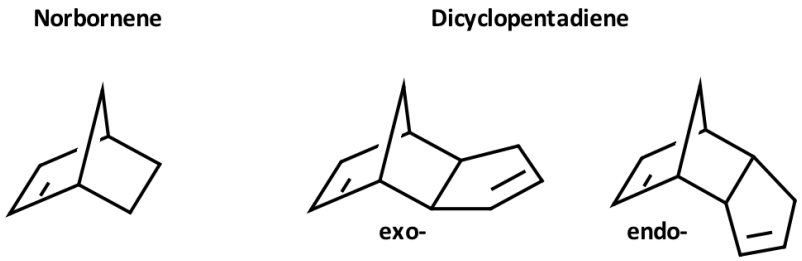

Figure 2.3. Structures of norbornene and DCPD monomers. The exo- isomer is more reactive than the endo- isomer.[12]

2.4.2 Steps of ROMP

Catalysis begins by loss of a phosphine ligand (for Grubbs' catalysts) to provide space for the incoming olefin to coordinate to the metal for metathesis. Furthermore, under the correct conditions there is no specific termination process.[13,14] This is known as living polymerisation, when rates of initiation and propagation are similar they give control of molecular weight.[13,15] When this occurs the polymer chain remains active after the consumption of the monomer resulting in polymerisation that will reactivate on addition of more monomer (scheme 2.3) - there is no specific termination reaction that occurs in normal FRP.

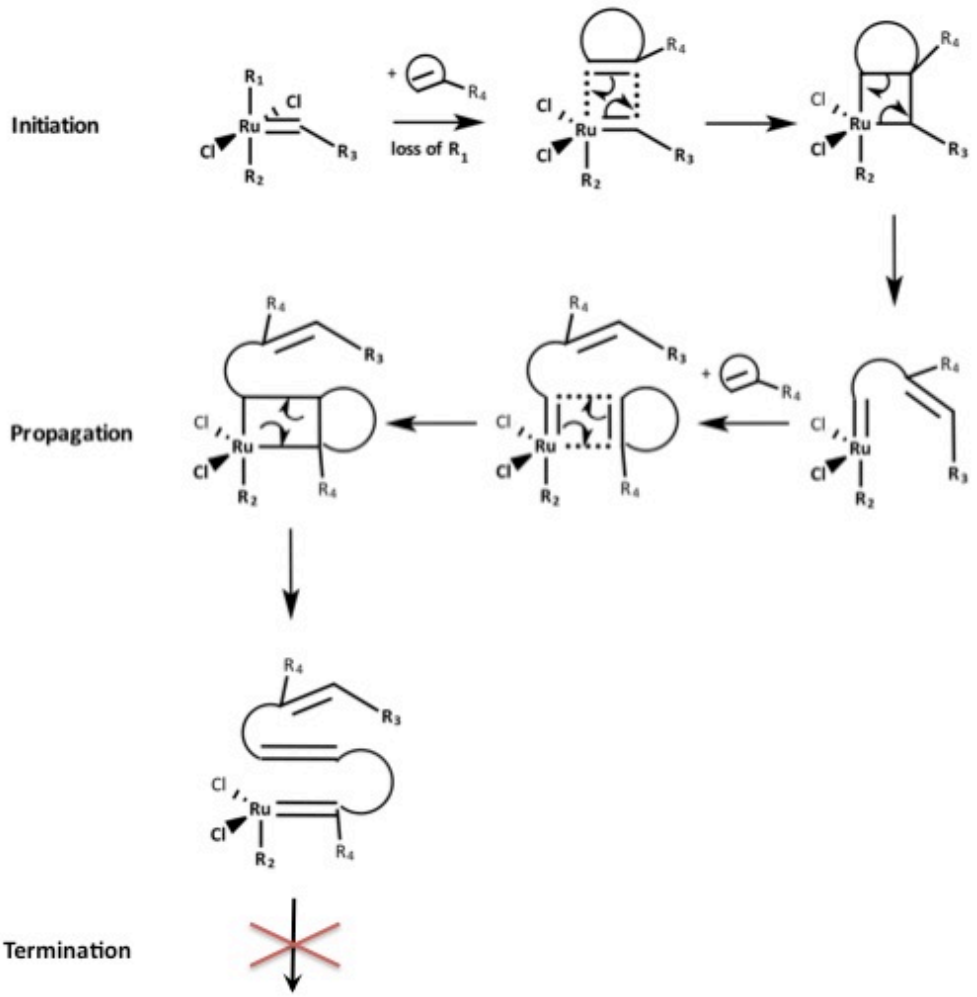

Scheme 2.3. 'Living' ROMP mechanistic scheme. The final species is the dormant reactive speies or 'living' polymer chain.

Grubbs type catalysts are perhaps the most well known ROMP catalysts (figure 2.2). The catalyst is based on ruthenium, as this metal gives the best reactivity to olefins.[16] This was most applicable to this work due to the requirement of using hydrocarbon monomers. With a large number of ligand possibilities, the effects on initiation and propagation steps have been well studied for these catalysts.[17] Initiation and propagation are inversely related to ligand size. Greater rates of initiation are followed by a decrease in propagation rates and visa versa.[17] For example, replacing chlorine with a larger halogen causes an increase in initiation but decrease in propagation.[17] For second-generation Grubbs' catalysts, a stronger donor ligand is used to enhance catalyst activity by facilitating loss of the phosphine ligand prior to olefin coordination.[18] However, initiation is slower by comparison to first-generation catalysts.[17]

Grubbs' type catalysts are stable to many functional groups and temperature, particularly in the solid-state.[17] However in a solvated state, both generations of catalysts are can be deactivated by nitrile and amine functional groups, and dissolved dioxygen.[19] In addition, methanol or chlorinated solvents are detrimental to catalyst function.[17]

2.5 Emulsions

An emulsion is defined as a stable suspension of droplets of an immiscible liquid droplets dispersed inside another liquid.[20,21] An emulsion comprises of a continuous (external) phase and dispersed (internal) phase and an emulsifying agent otherwise known as a surfactant. Two immiscible liquids are thermodynamically unstable and will separate over time. The role of the surfactant is to reduce the interfacial tension enough that the two liquids become more thermodynamically stable to facilitate formation and stability of the emulsion, as well as forming a physical barrier between the liquids.[22] Surfactants also help in determining the emulsion type such as an oil-in-water (o/w) or water-in-oil (w/o) emulsion. Other factors that sub-categorise emulsions are based on different characteristics of the emulsion. One example is the size of the dispersed liquid droplets; macroemulsions contain droplets in the region of 1 to 100 μm diameter, miniemulsions droplets are sized between 50 nm to 1 μm, and microemulsions have 0.01 to 0.20 μm sized droplets.[23,22] Another factor is the type of surfactant or stabilising agent used. Pickering emulsions use small solid particles to stabilise droplets instead of a liquid/solvated surfactant.

To form an emulsion, two immiscible liquids and a surfactant(s) are required with mechanical agitation to disperse one phase into the other. Mechanical agitation is achieved using various apparatus, such as an overhead stirrer, or the less known double syringe technique (HIPEs). In the case of microemulsions, these are formed spontaneously due to thermodynamic stability of the very small droplets.[22] The syringe technique for HIPE formation is explained in detail in chapter 3. Each

method, except microemulsions, creates shear force that produces droplets of one of the liquids, dispersed in the other phase. The surfactant stabilises the dispersion and prevents it from returning to the constituent components by reducing surface tension and instability mechanisms (coalescence and Ostwald ripening).

Formation of an emulsion begins with micelle formation of one of the phases, this occurs when the critical micelle concentration (CMC) has been reached. A micelle is an aggregate of surfactant molecules, usually spherical in shape when the CMC has been reached. The CMC is the point when the concentration of the surfactant is high enough for surfactant micelles to form.[21] Once the CMC has been reached, there is a decrease in the repulsive forces (surface tension, interfacial tension) between the liquids that would cause an emulsion to break.[21,22] Surfactant concentration above the CMC has no significant effect on these forces, however in excess concentration the surfactant can cause destabilise the emulsion.[24]

2.5.1 High Internal Phase Emulsions (HIPEs) and Polymerised High Internal Phase Emulsions (PolyHIPEs)

In 1982 Unilever patented and trademarked a new class of emulsion-based materials from High Internal Phase Emulsions (HIPEs) called polyHIPEs.[25] HIPEs were adapted to use hydrophobic monomers, which could then be polymerised in the presence of an initiator to form a new structure that is highly porous with regular pore sizes, and lightweight. To be classed as a HIPE, the dispersed phase must occupy greater than 74% of the total volume of the system.[26,27] 74% represents the maximum volume fraction of close packing of spherical droplets can undergo before deformation occurs, which means the emulsion is highly stressed.

A compositional phase diagram displays changing water, oil and surfactant ratios of a HIPE; notably there is only a small region where these emulsions are stable.[28] Commonly HIPEs are water-in-oil (w/o) emulsions, however oil-in-water (o/w) emulsions and oil-water-oil (o/w/o) emulsions have been prepared.[29] In addition,

despite the narrow regions stability, polyHIPEs with internal phase volumes as high as 99% internal phase have been prepared.[27]

2.5.2 Structure of HIPEs and PolyHIPEs

PolyHIPEs have been shown to have high stability at extremely high levels of porosity despite having a minimum of 74% pore volume.[28] The HIPE droplets act as a template for the material and produce a regular pore structure, which is unique and different from other foam production techniques. Other compositional phase diagrams illustrate that small changes to emulsion components will affect the resulting polyHIPE microstructure, producing an open cell, closed cell or an unconnected polymeric material.[28,30]

The pore structure is templated by the internal phase droplets, which is then removed after polymerization of the continuous phase. In addition, the internal phase predominately contains a radical initiator, which starts the polymerization of the continuous phase into a solid polymer. There are many different approaches to polymerisation of the continuous phase such as using ultraviolet radiation[31] and redox chemistry.[32] The HIPE structure, and its conversion to a polyHIPE have a distinctive structures (figure 2.4).

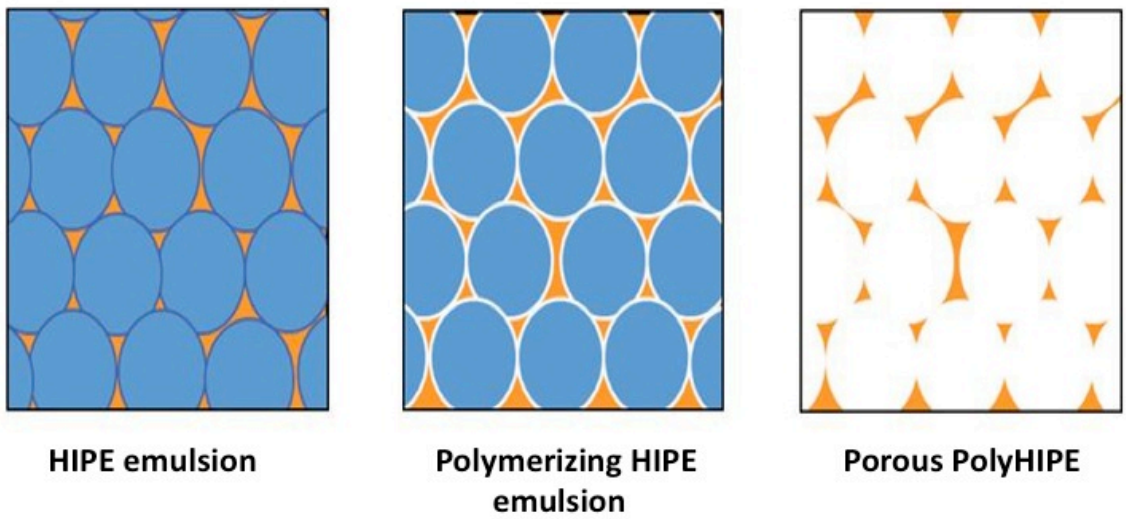

Figure 2.4. A representation of a HIPE and polyHIPE microstructure. The blue is the internal phase, and yellow the continuous phase.

HIPEs are above the maximum close packing percentage for spherical droplets, thus increasing internal phase will increasingly deform droplets (figure 2.5). The nature of the surfactant film is crucial in HIPE stability for conversion into a polyHIPE. Higher internal phases therefore put a great deal of stress on the surfactant film, which can be a concern if increased porosity polyHIPEs are a requirement.

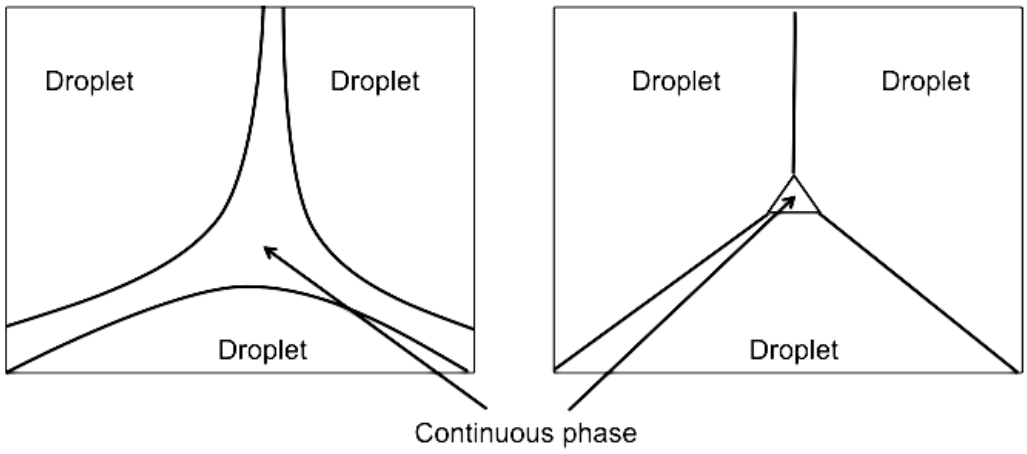

Figure 2.5. The effect on the continuous phase of a HIPE when increasing the content of the internal phase. The surfactant film will have difficulty resisting the increased pressure to prevent an increased rate of action of coarsening mechanisms.

2.6 Factors effecting HIPE Stability

2.6.1 Surfactants

The role of a surfactant is to facilitate emulsion formation and provide stability. It creates a film around each droplet acting as a stabilizer and a barrier between the two phases. A surfactant is composed of a hydrophilic (lipophobic) and hydrophobic (lipophilic) component, in other words a hydrocarbon chain with a polar group attached to it (figure 2.6). The degree of hydrophobicity/philicity is dependent on the size of the hydrocarbon chain and the polarity of the head. Therefore the surfactant has some degree of solubility in both liquids, which is important to emulsification as it reduces surface tension between liquids.[22] Surfactants are categorised into three classes; anionic, cationic and non-ionic. This refers to the polar nature hydrophilic head. The first general rule in determining if an emulsion is

o/w or w/o is the Bancroft rule: the liquid in which the surfactant is more soluble becomes the continuous phase.[22,21]

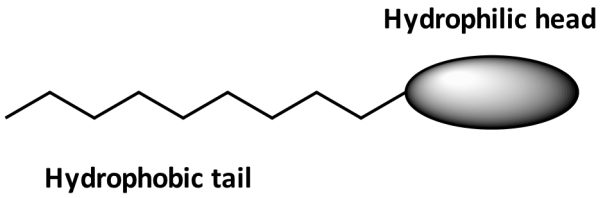

Figure 2.6. Schematic of the structure of a generic surfactant molecule.

Additionally, there is a scale by which all classes of surfactants can be measured by its hydrophile-lipophile balance (HLB) value.[33] This is particularly useful for anionic surfactants. The HLB value is a measure of how hydrophobic/hydrophilic a surfactant is, and can be used as a general guide when forming emulsions. The HLB ranges from 1 to 20; high values represent hydrophilic surfactants and low values represent lipophilic surfactants, thus favoring formation of w/o and o/w emulsions respectively. For w/o styrene-co-divinyl benzene (S-*co*-DVB) HIPEs the HLB value of the surfactants is ideally from 2 to 6.[25]

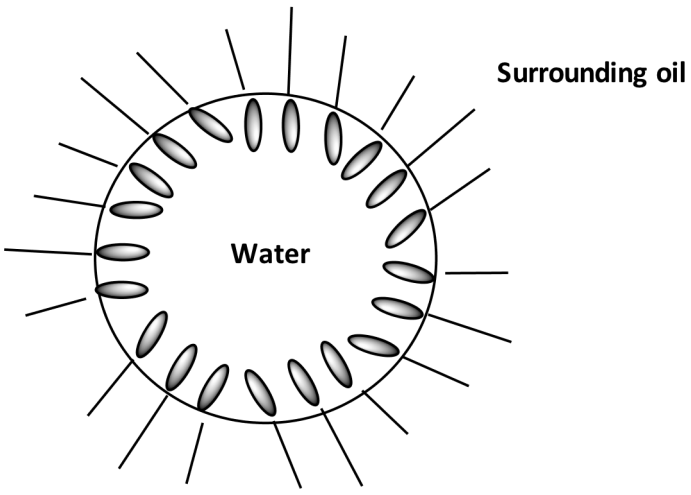

Figure 2.7. Schematic of the organisation of surfactant molecules around a water droplet.

A surfactant film forms around the phase in which it has greater solubility with to form droplets of that liquid (figure 2.7). The surfactant acts as a stabilising agent by preventing the emulsion from breaking, through mechanisms such as coalescence

and Ostwald ripening. The surfactant can be thought of as forming an elastic film around the droplets acting as a physical and chemical barrier to keep the emulsion stable.[22] Figure 2.9 displays the surfactants used in this work and their HLB values.

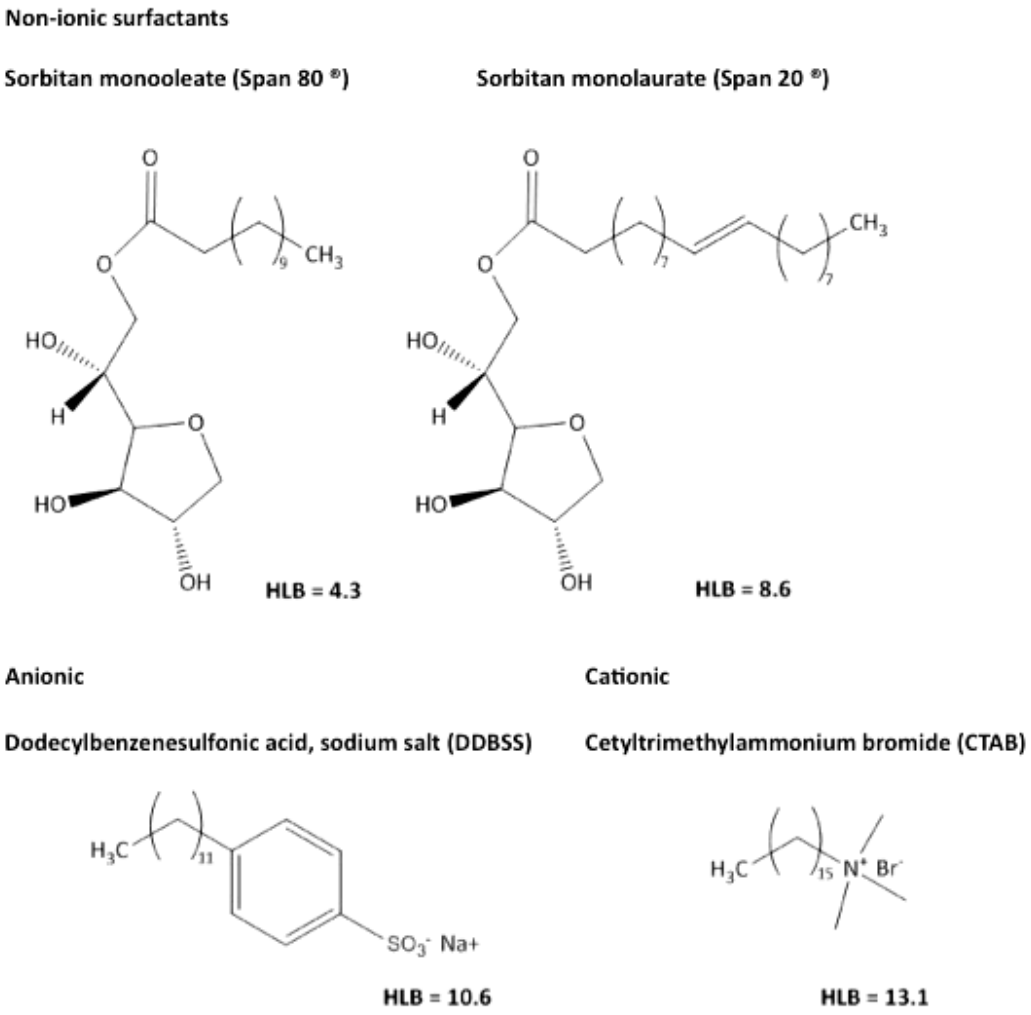

Figure 2.9. HLB values of anionic, cationic and non-ionic surfactants used in this work.

2.6.2 Ostwald Ripening and Coalescence

HIPEs are macroemulsions and thus thermodynamically unstable and will break over time, returning to a more stable state as separated liquids. Two instability mechanisms that lead to breaking of emulsions are called Ostwald ripening and coalescence. When liquids are emulsified, the phenomenon of Ostwald ripening occurs. It is defined as the growth of larger droplets at the expense of smaller droplets as larger droplets are more thermodynamically favorable than smaller droplets.[34,35] The mechanism of action is mediated by the mutual solubility of the two phases with each other, with one phase passing through the surfactant film to grow the larger droplet. The properties of the emulsion phases can influence the ripening rate; more hydrophobic substances have a reduced rate of ripening due to a reduction in solubilty.[34]

Coalescence is an emulsion coarsening mechanism that consists of the combination of smaller droplets to form larger droplets. It occurs with rupturing of surfactant films to create a larger droplet.[22] This large droplet is favourable to form as it has a smaller surface area and more thermodynamically stable than more numerous smaller droplets.

Factors such as temperature, surfactants and size distribution of droplets are inter-linked with the rates of Ostwald ripening and coalescence.[22] Reducing the rate of ripening and coalescence can be achieved using suitable surfactants.[22] In HIPEs, the elastic film will be under increased pressure given the large internal phase volumes thus rates are likely higher compared to other emulsion classes. Similarly, methods to retard Ostwald ripening involve dissolving a co-surfactant/stabiliser into the continuous phase; this can be a very hydrophobic molecule, which creates a concentration gradient with the continuous phase, preventing it from diffusing into an adjacent droplet.[34] Furthermore, it has been possible to greatly reduce Ostwald ripening and coalescence by freezing the emulsion due to the molecules having little thermal energy for motion.[36]

2.6.3 Droplet Size Distribution

The size distribution of droplets affects the rate of Ostwald ripening and coalescence in an emulsion.[22] An emulsion is more stable when the droplet distribution is narrow as the growth of larger droplets through Ostwald ripening and coalescence is reduced as these mechanisms look to create larger droplets due to favorable thermodynamics. A narrow size distribution can be obtained by suitable mixing of the emulsion, however once the emulsion is formed coarsening mechanisms begin to undo stability.

2.6.4 Temperature

Temperature affects every aspect of an emulsion; changes can occur in viscosity of the phases and surfactant film, solubility of the species present, and vapor pressures all of which affect emulsion stability.[22] With increasing temperature the viscosity of each phase will decrease causing the interfacial tension to decrease. This should increase emulsion stability as there are less repelling force between droplets. However, with this increase in temperature factors such as coalescence and Ostwald ripening can dominate due to the thermal energy increasing molecular motion. Specifically, increasing the temperature weakens the surfactant film around the droplets, which are less viscous, increasing coalescence as the surfactant film is more likely to burst in addition to increased droplet collisions.[22] Ostwald ripening increases as increased temperature causes increased solubility of the phases with each other, which mediates the mechanism of action.

Furthermore, increased temperature will increase the vapor pressure causing an increased flow between phases, thus reducing stability.[22] Finally, emulsion inversion or breaking can occur due to possible changing solubility of a surfactant as the temperature is varied.[22,22] For HIPEs to withstand additional stresses that temperature can place on the stability of the system, choice of surfactants become hugely important to produce a homogeneous pore structure.

2.7 Gels and Aerogels

Gels are defined as a single macromolecular structure that extends throughout the entire reaction vessel, containing solvent in the pores.[20] Thus an aerogel is gel with the solvent removed, leaving air to occupy the space that was once the solvent giving rise to the pore structure and low bulk density.

Gels are formed from by aggregation of polymer clusters through chemical bonds or physical interactions using sol-gel chemistry. This process is dependent on the experimental conditions, including solution concentration and pH.[20,37] The solvated monomer begins polymerisation due to solvated initiator and grows into polymer clusters which can aggregate together to form a polymer network.[20,37] One simple method of knowing the gel has formed is by holding the vessel upside-down; if the gel has formed it will stick to the vessel and stay in place. To obtain an aerogel, the gel must be dried but this carries a risk of damaging the structure through capillary action. Capillary action occurs with oven or vacuum drying techniques causing damage to the gel network by evaporating solvent, thus supercritical solvent drying is used to remove the solvent without damage (more detail in chapter 3 appendix 3.9). The porous material is first saturated with liquid carbon dioxide (CO_2) and left to exchange with the existing solvent from a previous process. Once the exchange is complete the supercritical fluid, commonly carbon dioxide, is exchanged and the material is heated until the CO_2 reaches its critical point. The supercritical fluid is then slowly vented to leave a dry, undamaged sample. The synthetic process can be thought of 4-stage process (figure 2.10).

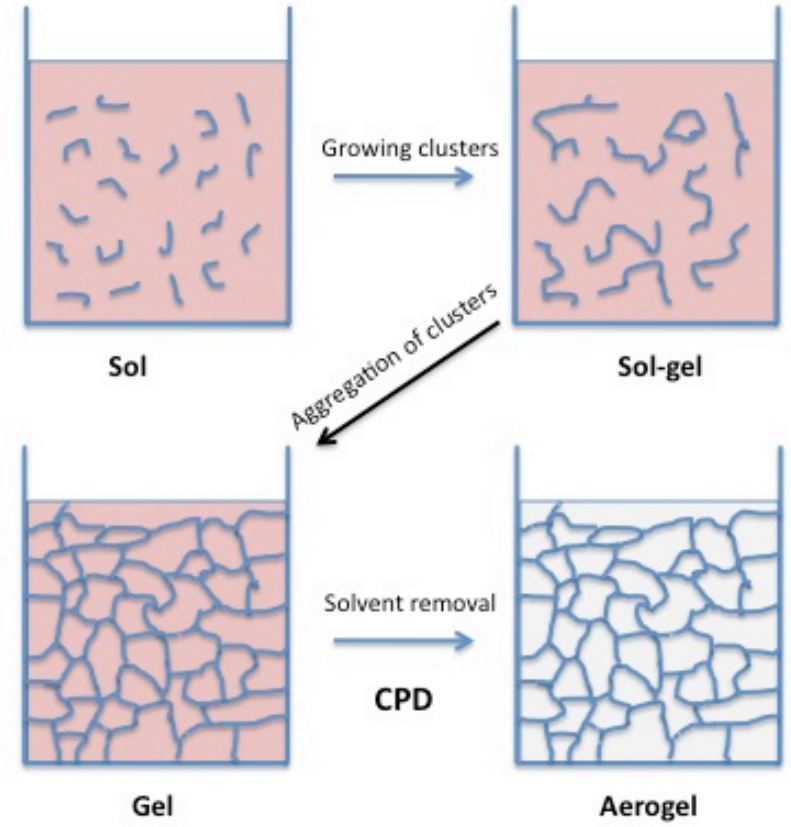

Figure 2.10. Representation of the process of forming an aerogel beginning from a sol, sol-gel and gel. The solvent (red) is removed at the final stage.

2.7.1 Factors affecting Gel Formation

Whilst the majority of published literature is concerned with specific aspects of sol-gel chemistry and gel formation, the research presented here could not hope to cover all aspects but discusses several factors that needed to be taken into account for the production of low density aerogels.

Two specific considerations for the synthesis of gels are the solvent chosen for the polymerisation and the concentration of the monomer solution.[20] These two are particularly linked for synthesis of low density systems because solvent can be responsible for shortening polymer chains through chain-transfer,[3] and low concentrations of monomer means that gel formation is slower and more difficult as there is less mass present to form the network.[20] Thus, low density solutions can be affected significantly if the wrong solvent is used, particularly with chain transfer from chlorinated solvents, as shortening of chains can prevent network formation.

Furthermore, factors that affect polymerisation also need to be considered here such as temperature and initiator concentration.

2.8 Nuclear Magnetic Resonance (NMR)

2.8.1 Principles of NMR

The intrinsic angular momentum, $\mathbf{I}$, of magnetic nuclei is known as spin. The magnitude of the angular momentum is quantized in units of $\hbar = h/2\pi$ and given by

$$|\mathbf{I}| = \hbar\left[I(I+1)\right]^{1/2}\hbar \qquad (2.4)$$

where I is the spin quantum number of a nucleus and is either a full or half-integer value e.g. ½, 1, ³⁄₂ etc. The numbers of unpaired protons and neutrons in the nucleus largely determines I.[38]

Spin angular momentum is a vector quantity and therefore both the direction and magnitude are quantized, leading to $2I+1$ projections onto a chosen axis, typically the *z* axis;

$$I_z = m_I\hbar \qquad (2.5)$$

m_I is the magnetic quantum number and has $2I+1$ orientations between $+I$ and $-I$ and $\hbar$ is Planck's constant. Thus, a spin $I = ½$ nucleus has two different orientations in the presence of a magnetic field (figure 2.13). Spin angular momentum can be represented by $\boldsymbol{I}$, which can be denoted by I_z to indicate the axis of projection.

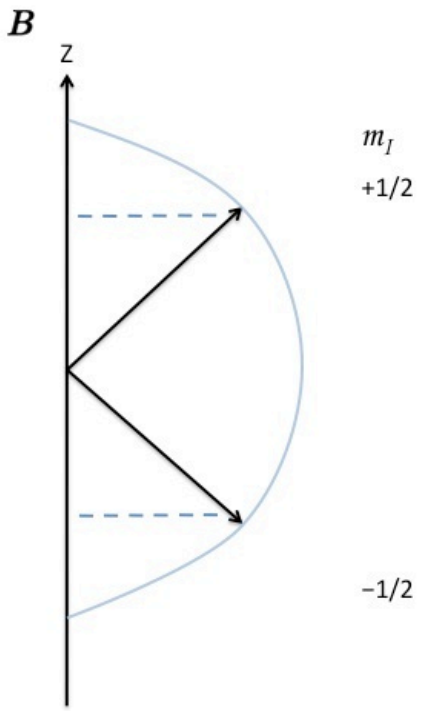

Figure 2.11. The two orientations for a spin $I = ½$ nucleus. Image adapted from P. J. Hore, in Nuclear Magnetic Resonance, Oxford University Press Inc., New York, U.S.A, 1995, ch.1 pp. 3.

Another vector quantity, the magnetic dipole moment ($\boldsymbol{\mu}$), is determined by

$$\boldsymbol{\mu} = \gamma \cdot \mathbf{I} \tag{2.6}$$

where γ is a constant of proportionality called the gyromagnetic ratio, and $\mathbf{I}$ is the spin angular momentum vector. The magnetic dipole moment is a vector quantity and can either be parallel or anti-parallel to the spin angular momentum depending on the sign of the gyromagnetic ratio.

The $(2I+1)$ orientations of the spin angular momentum are degenerate in energy in the absence of an applied magnetic field. Conversely, in the presence of a magnetic field ($\mathbf{B}$) the degeneracy is lifted and the energy of the system is given by

$$E = -\boldsymbol{\mu} \cdot \mathbf{B} \tag{2.7}$$

This removal of degeneracy is known as the Zeeman interaction (figure 2.12) and when a strong magnetic field is applied, the quantization of the *z* axis is no longer

arbitrary but along the direction of the applied magnetic field instead. The energy of a state is given by the following equation;

$$E_z = \mu_z \cdot B = -\gamma m_I \hbar B \qquad (2.8)$$

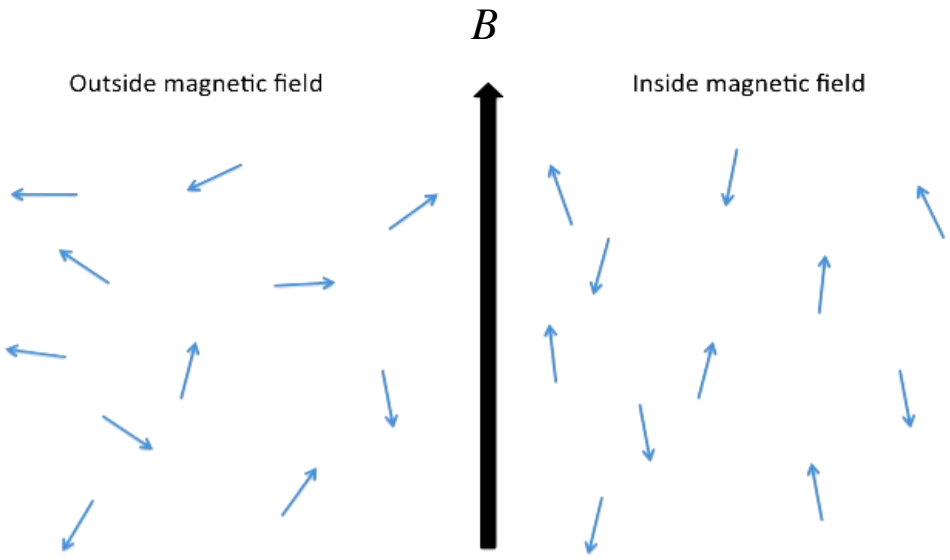

Figure 2.12. Depicts the alignment of randomly orientated spins in the presence of a strong magnetic field $\mathbf{B}_0$.

NMR has a selection rule, $\Delta m_I = \pm 1$, for observable transitions between energy levels and the frequency of a transition, known as the Larmor frequency, ω_0, is given by equation 2.8.

$$\omega_0 = 2\pi\upsilon_0 = \frac{\Delta E}{\hbar} = -\gamma B_0 \qquad (2.9)$$

The Larmor frequency, ω_0, is in units of rad s^{-1}, and frequencies of common NMR active nuclei are given in Table 2.1. The Larmor frequency is the resonance condition of a nucleus (1 spin system), each having a unique frequency, which varies at different field strengths.

Table 2.1. The natural abundance, the gyromagnetic ratio (γ) and the resonance frequencies (ω_0) of several common $I = ½$ nuclei at 9.4 T and 14.1 T fields (for Bruker).

Nucleus	Natural abundance (%)	γ (10^7 rad T^{-1} s^{-1})	ω_0 / MHz (9.4 T)	ω_0 / MHz (14.1 T)
^{1}H	99.99	26.75	400.0	600.13
^{13}C	1.11	6.73	100.6	150.90
^{19}F	100.00	25.18	376.5	464.69
^{31}P	100.00	10.84	162.1	242.94

2.8.2 Boltzmann Distribution and Bulk Magnetisation

At thermal equilibrium the NMR active nuclei in a material will occupy available energy levels according to the Boltzmann distribution ratio providing the difference in population of the spins in the lower (n_{lower}) or higher energy (n_{upper}) level in the case of a spin $I = ½$ nucleus,

$$\frac{n_{upper}}{n_{lower}} = e^{\frac{-\Delta E}{kT}} \qquad (2.10)$$

The gap in energy between these two energy levels is given by the term ΔE, as seen in equation 2.10, and is equal to $-\gamma\hbar B_0$. Therefore, the Boltzmann distribution is dependent on the individual nucleus and experimental conditions such as the strength of the static magnetic field and temperature. At higher external magnetic field strengths, sensitivity improves due to the energy gap between energy levels increasing. This is explained in more detail in the following passages.

However, while equation 2.10 defines the ratio between the occupancy of the energy level by the spins in a system, the population difference between the two energy levels is defined by

$$M_0 = n_{upper} - n_{lower} \qquad (2.11)$$

This sum has been called the bulk magnetisation ($\mathbf{M}_0$), which aligns itself with the

direction of the external magnetic field, B_0, along the predefined z-axis. It is the detectable magnetisation of a NMR experiment, and strictly speaking, is known as the net magnetisation, however bulk magnetisation is also used.

The population distribution has a dependence on the temperature of the sample seen in the Boltzmann distribution (equation 2.10) and a dependence on the magnetic field resulting in an increase in energy gap between the two energy levels of a spin $I = ½$ nucleus. The net magnetization ($\mathbf{M}_0$) is proportional to the excess magnetisation (M_0) created from the distribution of spins that can be calculated by use of Curie's law. Curie's law is given as

$$M_0 = \frac{N_v \hbar^2 \gamma^2}{4kT} B_0 \qquad (2.12)$$

where N_v is the total number of spins per unit volume, k is Boltzmann's constant, T is the absolute temperature, $\left(\frac{\hbar}{2\pi}\right)$ is the reduced Planck's constant and γ is the gyromagnetic ratio. Curie's law states that the magnetisation is proportional to magnetic field and inversely proportional to the temperature, when the external magnetic field is sufficiently small and/or temperature is sufficiently high.[39] Curie's law is simplified to

$$M_0 = C\frac{B_0}{T} \qquad (2.13)$$

where C is the Curie constant and is a reflection of the magnetic susceptibility of a material. Therefore the amount of magnetisation present will increase with a decrease of temperature and/or an increase in magnetic field hence these terms are included in the Boltzmann distribution.

When the resonance condition of a nucleus is fulfilled, the bulk magnetisation rotates about the static magnetic field axis; this is the Larmor precession. This is

derived from the torque a magnetic moment experiences in a magnetic field. Thus the motion of the bulk magnetisation is defined by

$$\dot{\mathbf{M}}_0 = \gamma|\mathbf{M} \cdot \mathbf{B}| \tag{2.14}$$

where $|\mathbf{M} \cdot \mathbf{B}|$ is the torque experienced by $\mathbf{M}_0$ and γ is the gyromagnetic ratio of a nucleus.[39] In a static magnetic field predefined to the z axis, the term above can be solved by

$$\mathbf{B} = B_0\mathbf{k} \tag{2.15}$$

where $\mathbf{k}$ is the unit vector in the z axis. The component form of the equations of motion for magnetisation in each axis are defined as

$$\begin{aligned} \dot{M}_x &= \gamma B_0 M_y \\ \dot{M}_y &= -\gamma B_0 M_x \\ \dot{M}_z &= 0 \end{aligned} \tag{2.16}$$

that can be solved by the following set of equations (2.17), whereby the starting condition of $M_y(0) = 0$ is assumed (no magnetisation in this axis at this time).

$$\begin{aligned} M_x(t) &= M_x(0)\cos(\gamma B_0 t) \\ M_y(t) &= -M_x(0)\sin(\gamma B_0 t) \\ M_z &= M_z(0) \end{aligned} \tag{2.17}$$

These equations describe the motion in the x-y plane, and the z component is constant. The magnetisation travels with an angular velocity $\omega_0 = \gamma B_0$ i.e. the Larmor frequency. These equations of motion are particularly important to understanding relaxation in NMR and will be returned to later in this chapter.

2.8.3 The Vector Model

To better understand an NMR experiment it is convenient to treat the system of spins within a sample according to classical mechanics rather than quantum mechanics. This can be achieved for spin $I = ½$ nuclei by application of the vector model approach to a system of spins.[40] The vector model provides a non-mathematical picture that can be used to understand NMR spectroscopy at a simpler level by introducing the idea of the 'rotating frame'. The 'laboratory frame' views the bulk magnetisation as precessing and aligned with the predefined z axis. The effect of an applied pulse, a linearly oscillating magnetic field, moves the bulk magnetisation down into the x-y plane. In addition, as soon as the magnetisation vector has moved from the z axis, the magnetisation also starts to precess around the axis it has been pushed down into. Remaining in the laboratory frame, visualizing these motions can be difficult. The rotating frame is thought of as rotating around the z-axis at the same frequency as the applied radiofrequency pulse, thereby the applied pulse is viewed as a temporary application of a static field. This simple pictorial view of the magnetisation makes understanding of simple NMR experiments much easier.

The strength and duration of the initial pulse determines the flip angle, β, from the z axis. Once the pulse has stopped, the offset magnetisation may precess around a residual magnetic field (ΔB_0) at specific angular frequency (Ω) if the ω_{RF} pulse does not match the Larmor frequency, ω_0. The angular frequency is given by the offset of these two frequency terms to give

$$\Omega = \omega_0 - \omega_{RF} \qquad (2.18)$$

and because only the external magnetic field is present, relaxation begins and the system returns to the equilibrium position along the z axis.

2.9 NMR Relaxation

Once magnetisation has been moved from an equilibrium state and into the x-y plane by a radiofrequency pulse, the process by which it returns to equilibrium is known as relaxation. There are three relaxation processes in NMR, spin-spin relaxation, spin-lattice relaxation, and relaxation under RF/spin-lattice relaxation in the rotating frame which have time constants T_2, T_1 and $T_{1\rho}$ respectively. Lattice is a term used to describe the surrounding environment of the spin.

T_1 is also known as longitudinal relaxation and T_2 is known as transverse relaxation, and these terms describe the relaxation times for magnetisation parallel to and perpendicular to the B_0 field, respectively. The Bloch equations combine these relaxation terms with the equations of precession for magnetisation (equation 2.16) to give

$$\begin{aligned} \dot{M}_x &= \gamma[\mathbf{M}\cdot\mathbf{B}]_x - \frac{M_x}{T_2} \\ \dot{M}_y &= \gamma[\mathbf{M}\cdot\mathbf{B}]_y - \frac{M_y}{T_2} \\ \dot{M}_z &= \gamma[\mathbf{M}\cdot\mathbf{B}]_z + \frac{\left(M_0 - M_z\right)}{T_1} \end{aligned} \qquad (2.19)$$

where the magnetisation in the x-y plane, M_z and M_y, relax to zero and the magnetisation in the z axis, M_z, relaxes back to equilibrium, M_0. When the solved equations of motion (equation 2.17) include these relaxation terms, the magnetisation components evolve as

$$\begin{aligned} M_x(t) &= M_x(0)\cos(\omega_0 t)e^{\left(\frac{-t}{T_2}\right)} \\ M_z(t) &= M_0 - \left[M_0 - M(0)\right]e^{\left(\frac{-t}{T_1}\right)} \end{aligned} \qquad (2.20)$$

In practice it is not possible to entirely measure the relaxation times due to the exponential behavior of relaxation so approximations are made. T_1 relaxation is measured by the time for 63% of its initial value to be obtained, and T_2 is measured by the time is takes for the magnetisation to reduce to 37% of its initial value. T_1 and T_2 relaxation have distinctive growth and decay respectively that is represented by figure 2.13 and figure 2.14 respectively.[39]

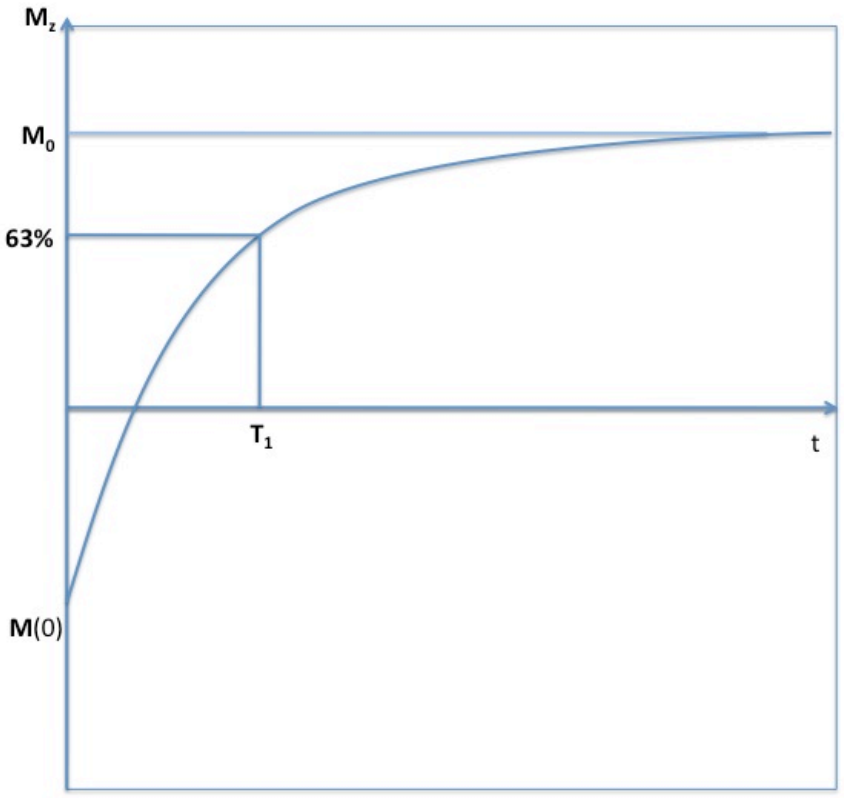

Figure 2.13. Longitudinal relaxation, T_1, is the time for magnetisation to reach 63% of the equilibrium value, $\mathbf{M}_0$.

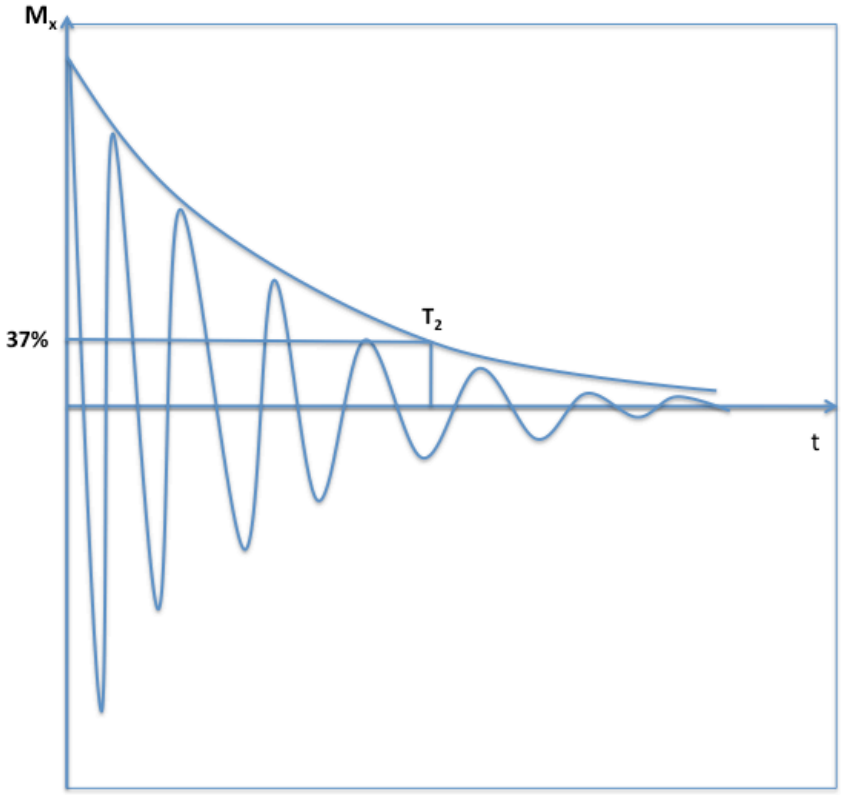

Figure 2.14. Transverse relaxation, T_2, is the time for magnetisation to dephase to 37% of the initial magnetisation value in the x-y plane.

Whilst figures 2.13 and 2.14 schematically demonstrate the relaxation modes in practice, and the Bloch equations describe the motion of the relaxing magnetisation and time parameters, the mechanism by which relaxation occurs is largely dipolar. Two spins, I and S, are separated by (r) and angle (θ) relative to each other and the magnetic field, and for a heteronuclear spin $I = ½$ system they have two gyromagnetic ratios (γ_I and γ_S respectively) to give the expression

$$\text{Dipolar splitting/Hz} = K_{IS}(3\cos^2\theta - 1)$$

$$2\pi K_{IS} = \left(\frac{\mu_0}{4\pi}\right)\frac{\hbar\gamma_I\gamma_2}{r_{IS}^3} \qquad (2.21)$$

where μ_0 is the permeability of a vacuum ($4\pi \cdot 10^{-7}$ H m^{-1}). The size of the dipolar coupling in solution is vastly smaller (zero as the motion is isotropic) than in solids because the angular dependence term $3\cos^2\theta - 1$ is averaged out to zero due to the rapid tumbling molecules experience whilst in solution, which does not occur in

solids. In spin-lattice relaxation, the dipolar coupled spins I and S relax by single spin flipping across adjacent energy levels (figure 2.15) caused by motion of the spins due to a fluctuation in the local magnetic field. As this process occurs, the energy of the spins is transferred to or from the motions of the molecule until the Boltzmann distribution of populations is restored.

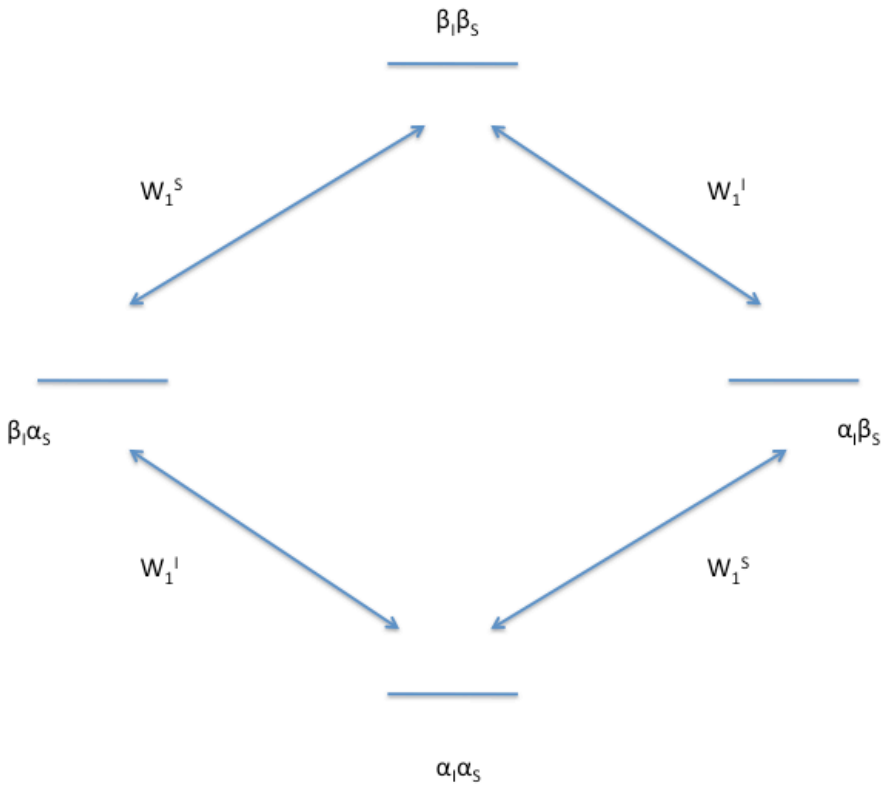

Figure 2.15. The energy levels for a pair of spin $I = ½$ nuclei I and S, showing the single spin flip transitions. Image adapted from P. J. Hore, in Nuclear Magnetic Resonance, Oxford University Press Inc., New York, U.S.A, 1995, ch.5 pp. 61.

Furthermore, the spin-lattice relaxation has a dependence on molecular motion.[38] The correlation time, τ_C, is defined as the time taken for random rotational diffusion in a molecule to move roughly 1 radian (60°).[38] Short correlation times and long correlation times correspond to faster and slower molecular motion, respectively. The correlation time is related to spectral density $J(\omega)$ by the expression

$$J(\omega) = \frac{2\tau_C}{1+\omega^2\tau_C^2} \qquad (2.22)$$

where ω is the angular frequency and the spectral density is described as being proportional to the probability of finding a component of random motion at a particular frequency.[38] The spectral density is proportional to the spin-lattice relaxation time as the spin flipping mechanism for relaxation is dependent on the local magnetic fields having an oscillating frequency at the Larmor frequency. When $J(\omega) = \frac{1}{\omega_0}$ the T_1 time is at a minimum and it increases either side of this, with faster or slower molecular motion to the left and right of the minimum respectively.

In addition to affecting the net magnetisation terms, the effect of temperature can increase or decrease molecular motion, which will affect relaxation. Different motions exist in polymers such as slow polymer chain rotation or fast hanging end group rotations that activate under certain conditions.[41,42] The two different motion regimes of a small molecular effect T_1 relaxation separately (figure 2.16).[43]

Transverse (T_2) relaxation also has a dipolar dependence on the orientation of spins, given by the term $3\cos^2\theta - 1$. Factors such as an increase in temperature, or reduced molecular size can result in greater molecular tumbling causing a greater averaging of this dipolar term, yet relaxation increases. Conversely, decreasing molecular motion decreases the T_2 relaxation time.

In addition to spin-lattice and spin-spin relaxation, there is another relaxation type called relaxation under RF, or spin-lattice relaxation in the rotating frame, with the time constant $T_{1\rho}$. In situations where the RF pulse is not switched off once magnetisation has been pushed into the x-y plane, $T_{1\rho}$ relaxation occurs. It can be thought that $T_{1\rho}$ takes characteristics of both T_1 and T_2 relaxation.[43] To measure $T_{1\rho}$ a pulse, known as a spin-lock, is applied to hold the bulk magnetisation for as long as possible in the x-y plane during which relaxation then occurs. $T_{1\rho}$ is characterised by the following expression;

$$M_y(t) = M_0 \exp\left(\frac{-\tau}{T_{1\rho}}\right) \qquad (2.23)$$

where τ is the time of the spin-lock. Thus, as the time of the spin-lock increases the amount of magnetisation present once the lock is switched off will decrease as more time has passed for relaxation to occur.

The behavior of all relaxation mechanisms with a varying correlation time is summarised in figure 2.16.

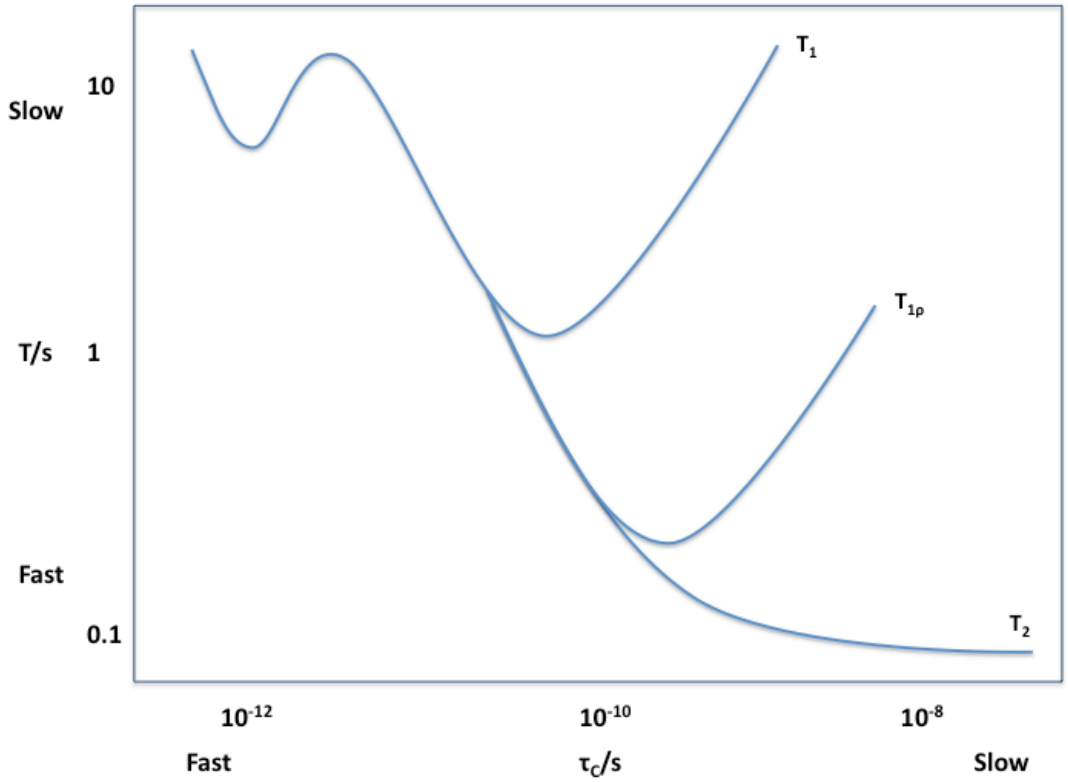

Figure 2.16. The dependence of T_1, $T_{1\rho}$ and T_2 on correlation time that corresponds to fast and slow molecular motion. Image adapted from R. K. Harris, in Nuclear Magnetic Resonance Spectroscopy; A Physiochemical View, Longman Scientific & Technical, Harlow, England, 1987, ch 3 pp. 87 and ch. 8 pp. 147.

2.10 Solid-state NMR Interactions

2.10.1 Dipolar Coupling

In addition to its importance to relaxation, dipolar coupling is one mechanism in solid-state NMR that broadens NMR spectra. It is a through space effect that arises because of the interaction between the magnetic dipole of a nucleus and other nuclear sites nearby. The size of the interaction is dependent upon the orientation and distance of the nuclear sites to each other, therefore anisotropic. The magnitude of this interaction between two spins I and S is given by;

$$\omega_D = \left(\frac{\omega_D^{PAS}}{2}\right) \cdot \left(3\cos^2\theta - 1\right) \qquad (2.24)$$

where θ is the angle between the spins and the magnetic field, and ω_D^{PAS} is the dipolar coupling constant in the principal axis system (PAS) given by;

$$\omega_D^{PAS} = \left(\frac{\mu_0}{4\pi}\right) \cdot \frac{\gamma_I \gamma_S \hbar}{r_{IS}^3} \qquad (2.25)$$

The internuclear distance between two spins I and S is given by r_{IS}^3. Therefore, the strength of the two magnetic dipole moments (proportional to γ_1 and γ_S), and the distance and angle of the internuclear axis of the two spins are the factors that affect the strength of the dipolar interaction. The effect splits a signal into a doublet (if $I = S = ½$), which is known as the Pake doublet in a powdered crystalline species. The magnitude of splitting is affected by the type of spin system; for a heteronuclear spin system, $I \neq S$, the maximum magnitude is $2\omega_D$ and in a homonuclear spin system, $I = S$, the magnitude is given by $3\omega_D$.

2.10.2 Chemical Shielding Anisotropy (CSA)

The electrons surrounding a nucleus have an effect on the magnetic field experienced by a nucleus. In addition, the nature of the surrounding nuclei will also affect a nucleus. This known as shielding and is essential in structure determination using NMR. The shielding of a nucleus is anisotropic; it depends on the orientation the nucleus to the magnetic field and the three-dimensional shielding tensor, which is given by σ. In the principal axis system, this tensor is diagonal and can be represented by an ellipsoid; it is the length of this ellipsoid that reflects the magnitude of the anisotropic nature of the shielding, or CSA.

The chemical shift, δ, can be described as having an isotropic part, δ_{iso}, and an anisotropic part, which has a magnitude, Δ_{CSA}, and asymmetry (or shape), η_{CS}, where η_{CS} is between 0 and 1. Equation 2.26 summarises below.

$$\delta = \delta_{iso} + \tfrac{1}{2}\Delta_{CSA}\left[\left(3\cos^2\theta - 1\right) + \eta_{CS}\left(\sin^2\phi - 1\right)\right] \qquad (2.26)$$

In the solution-state, molecules are constantly tumbling and because of the orientation dependent term $3\cos^2\theta - 1$ averaging to zero, this interaction has no effect and the chemical shift becomes simply the isotropic value. However, in the solid-state with a powdered crystalline sample this is not the case. Each single crystal has its own orientation with respect to B_0 and therefore each crystal has its own chemical shift. All these shifts are seen in the NMR spectrum producing a broad, yet characteristic 'powder-pattern' line shapes (figure 2.17).

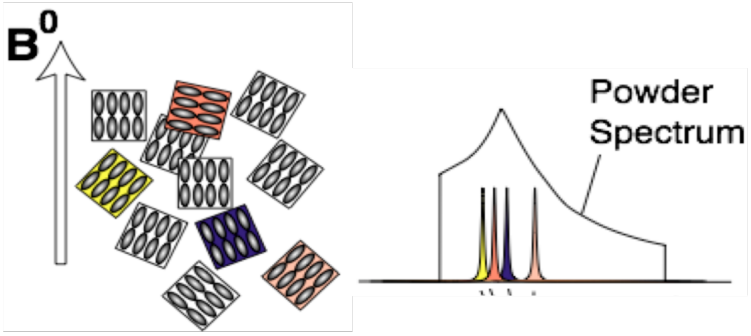

Figure 2.17. The unique orientations of a powdered sample all have a different chemical shift with respect to the magnetic field. The effect is a broadening of the spectrum as seen on the right-hand side. Image from M. H. Levitt, in Spin Dynamics, John Wiley and Sons, Chichester, England, 2008, 2nd edn, ch.9, pp. 205.

2.11 References

1 M. P. Stevens, in *Polymer Chemistry: An Introduction*, Oxford University Press, Inc., New York, 3rd edn., 1999.

2 K. L. Anderson, W. Nazarov, C. S. A. Musgrave, N. Bazin, and D. Faith, *Journal of Radioanalytical and Nuclear Chemistry*, 2013.

3 J. M. G. Cowie, *Polymers: Chemistry and Physics of Modern Materials*, Blackie and Sons, Limited, London, 2nd edn., 1991.

4 M. J. Bowden, in *Macromolecules: An introduction to polymer science*, eds. F. A. Bovey and F. H. Winslow, Academic Press, Inc., New York, 1st edn., 1979, p. 25.

5 R. J. Young, *Introduction to Polymers*, Chapman and Hall Ltd, New York, 1st edn., 1981.

6 P. C. Painter and M. M. Coleman, *Polymer Synthesis*, Technomic Publishing Company, Inc., Lancaster, 1st edn., 1994.

7 T. J. Seiders, D. W. Ward, and R. H. Grubbs, *Organic letters*, 2001, **3**, 3225–3228.

8 C. W. Bielawski and R. H. Grubbs, *Progress in Polymer Science*, 2007, **32**, 1–29.

9 S. E. Lehman, Jr and K. B. Wagener, in *Handbook of Metathesis volume 3*, ed. R. H. Grubbs, Wiley-Vch, 1st edn., 2003, pp. 283–353.

10 J. A. Tallarico, M. L. Randall, and M. L. Snapper, *Tetrahedron*, 1997, **53**, 16511–16520.

11 G. Black, D. Maher, and W. Risse, in *Handbook of Metathesis volume 3*, ed. R. H. Grubbs, Wiley-Vch, 1st edn., 2003, pp. 2–71.

12 J. D. Rule and J. S. Moore, *Macromolecules*, 2002, **35**, 7878–7882.

13 M. Szwarc, *Nature*, 1956, **178**, 1168–1169.

14 T. R. Darling, T. P. Davis, M. Fryd, A. a. Gridnev, D. M. Haddleton, S. D. Ittel, R. R. Matheson, G. Moad, and E. Rizzardo, *Journal of Polymer Science Part A: Polymer Chemistry*, 2000, **38**, 1709.

15 T. D. Tilley, R. H. Grubbs, and J. E. Bercaw, *Organometallics*, 1984, **3**, 274–278.

16 R. H. Grubbs, in *Handbook of Metathesis volume 1*, ed. R. H. Grubbs, Wiley-Vch, 1st edn., 2003, pp. 1–3.

17 M. S. Sanford and J. A. Love, in *Handbook of Metathesis volume 1*, ed. R. H. Grubbs, Wiley-Vch, 1st edn., 2003, pp. 112–131.

18 M. S. Sanford, J. A. Love, and R. H. Grubbs, *Journal of the American Chemical Society*, 2001, **123**, 6543–6554.

19 C. Slugovc, S. Demel, S. Riegler, J. Hobisch, and F. Stelzer, *Journal of Molecular Catalysis A: Chemical*, 2004, **213**, 107–113.

20 C. J. Brinker and G. W. Scherer, *Sol-Gel Science; The Physics and Chemistry of Sol-Gel Processing*, Academic Press, Inc., San Diego, 1st edn., 1990.

21 D. J. Shaw, *Introduction to Colloid and Surface Chemistry*, Butterworth-Heinemann Ltd, Oxford, 4th edn., 1991.

22 M. J. Rosen, *Surfactants and Interfacial Phenomena*, John Wliey & Sons, Inc., New York, 1st edn., 1978.

23 S. Slomkowski, J. V. Alemán, R. G. Gilbert, M. Hess, K. Horie, R. G. Jones, P. Kubisa, I. Meisel, W. Mormann, S. Penczek, and R. F. T. Stepto, *Pure and Applied Chemistry*, 2011, **83**, 2229–2259.

24 M. P. Aronson, *Colloids and Surfaces*, 1991, **58**, 195–202.

25 D. Barby and Z. Haq, Euro. Pat. Appl. 60138, 1982.

26 N. R. Cameron and D. C. Sherrington, *Journal of Materials Chemistry*, 1997, **7**, 2209–2212.

27 N. R. Cameron, *Polymer*, 2005, **46**, 1439–1449.

28 J. M. Williams and D. a. Wrobleski, *Langmuir*, 1988, **4**, 656–662.

29 H. Zhang and A. I. Cooper, *Chemistry of Materials*, 2002, **14**, 4017–4020.

30 J. M. Williams, *Langmuir*, 1991, **7**, 1370–1377.

31 D. Cummins, C. J. Duxbury, P. J. L. M. Quaedflieg, P. C. M. M. Magusin, C. E. Koning, and A. Heise, *Soft Matter*, 2009, **5**, 804.

32 S. D. Kimmins and N. R. Cameron, *Advanced Functional Materials*, 2011, **21**, 211–225.

33 W. C. Griffin, *Journal of Cosmetic Science*, 1949, **1**, 311–326.

34 C.-S. Chern, *Principles and Applications of EMULSION POLYMERIZATION*, John Wliey & Sons, Inc., Hoboken, 1st edn., 2008.

35 L. Ratke and P. W. Voorhees, *Growth and Coarsening: Ostwald Ripening in Material Processing*, Springer-Verlag, Berlin, 1st edn., 2002.

36 P. Walstra, in *Encylopedia of Emulsion Technology Volume 4*, ed. P. Becher, Marcel Dekker, Inc., New York, 1996, pp. 20–21.

37 R. W. Pekala, US 4,873,218, 1989.

38 P. J. Hore, *Nuclear Magnetic Resonance*, Oxford University Press, Inc., New York, 1995.

39 B. Cowan, *Nuclear Magnetic Resonance and Relaxation*, Cambridge University Press, United Kingdom, 1st edn., 1997.

40 P. J. Hore, J. A. Jones, and S. Wimperis, in *NMR: The Toolkit*, Oxford University Press, Inc., New York, 2003, pp. 1–5.

41 H. W. Spiess, *Colloid*, 1983, **261**, 193–209.

42 S. Matsuoka, *Relaxation Phenomena in Polymers*, Hanser, New York, 1992.

43 R. K. Harris, *Nuclear Magnetic Resonance; A Physiochemical View*, Longman Scientific & Technical, Harlow, 2nd edn., 1987.

3. Experimental Techniques and Theory

3.1 Synthesis of PolyHIPEs

In this thesis, all HIPEs (therefore polyHIPEs) were prepared using by the syringe method (figure 3.1), which was developed at Los Alamos National Laboratory, USA.[1] This method involves two gas tight syringes connected by a luer connector. Liquids are pumped by hand through the connection and the shear force from passing the liquids through the narrow orifice produces droplets of the liquids to induce emulsification. The method was primarily designed to reduce air bubble content that is likely to cause inhomogeneity in the final polyHIPE. The emulsions made at Los Alamos for laser targets were polymerised in the emulsification syringe to eliminate air bubbles completely. However, emulsions in this work were transferred to a glass vial or a plastic syringe before curing because these foams were made for research purpose and not experiments on lasers. Cooled monoliths were washed using various techniques such as Soxhlet or gentle mechanical agitation in solvents and then dried in air, or in some cases for polyHIPEs lower than 100 mg/cm $^{-3}$, by Critical Point Drying apparatus using liquid CO_2 as the supercritical fluid (as described in section 3.7).

One syringe was filled with deionised water containing the dissolved initiator and the other syringe contained monomers and surfactant. Care was taken to ensure the air was removed from the syringes before connection. Emulsions were prepared by continuously pumping the contents of the syringes back-and-forth through the luer connector into the other syringe until emulsification was completed. This was indicated by a sudden increase in viscosity and a homogeneous mixture was obtained. The number of plunges required to form an emulsion varied. This also varied by changing the polymer system and the range of plunges was as little as 6 to as many as 70 or more. Changing the composition of the emulsion gave rise to variations within the same system as variations in viscosity and/or hydrophobicity. It is conceivable that the force used per push was different each time therefore resulting in a different number of pushes to obtain emulsification.

The emulsion was then transferred to a glass vial or plastic syringe, sealed and polymerised at 60°C for 72 hours. Once cooled, the vial was broken or the syringe cut to remove the polyHIPE and the solid monoliths were washed by Soxhlet extraction with water, followed by methanol. For polyHIPEs below 50 mg cm^{-3}, gentle mechanical agitation was used instead of Soxhlet. PolyHIPEs were put into plastic baskets with holes to protect them from any damage yet allow penetration of the solvent and then placed into a vessel containing a magnetic stirrer and a solvent. After a period of 24-48 hours, the solvent was changed from water to methanol. PolyHIPEs contained in plastic syringes were easier to remove than glass vials because of reduced adhesion. They were washed in the same way as polyHIPEs from glass vials. Finally, the monoliths were dried in an oven at 40°C.

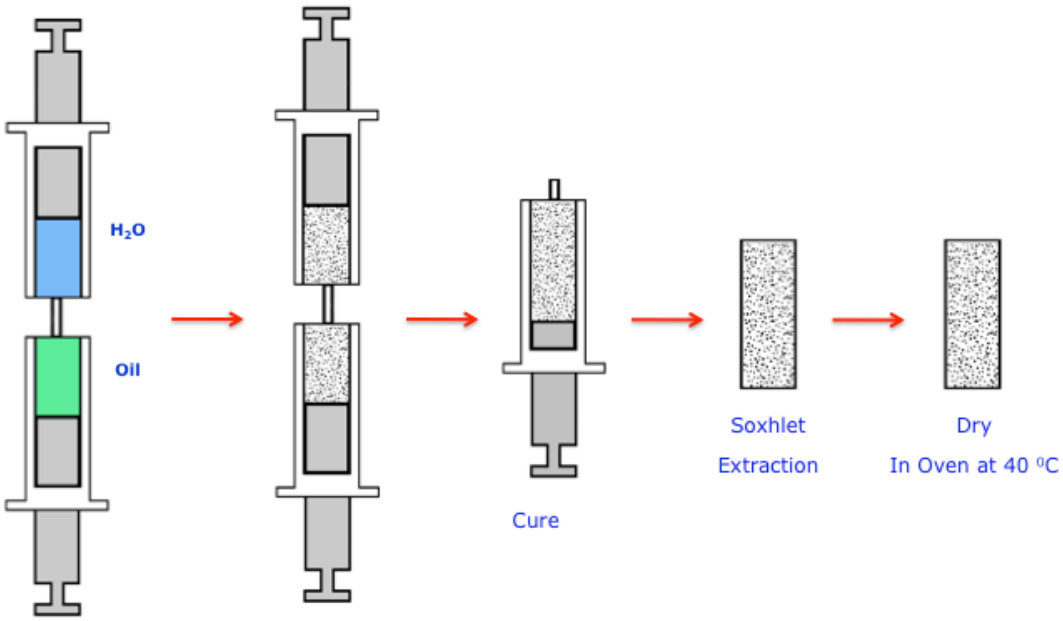

Figure 3.1. A schematic for the preparation of a HIPE into a polyHIPE using the syringe method.

3.1.1 Materials and Reagents

Reagents used were styrene, deuterated styrene (S-d_8), divinyl benzene 80 (DVB) (technical grade), para-divinyl benzene (85%, 10% meta-divinyl benzene), methanol, deionised water, deuterated water (D_2O), sorbitan monooleate (Span® 80), sorbitan monolaurate (Span® 20), azobisisobutyronitrile (AIBN), potassium persulfate, dodecylbenzensulfonic acid (DDBSS) sodium salt, cetyltrimethylammonium bromide (CTAB) and 2-vinyl naphthalene (2VN).

All chemicals were used as received except for the monomers, which had the inhibitor extracted before use.

3.1.2 Synthesis of varied molar ratio S-co-DVB polyHIPEs

Styrene and DVB (table 3.1) were combined with Span® 80 (0.28 g, 0.65 mmol) and mixed thoroughly, then transferred to a 10 mL gas tight syringe. Deionized water (8.8 mL, 0.49 mol) containing potassium persulfate (0.44g, 1.63 mmol) was transferred to another 10 mL gas tight syringe. The double syringe emulsification procedure was carried out as described in chapter 3. Generally, the resulting HIPEs were homogeneous and that increasing DVB volumes reduced emulsion viscosity. Once emulsified, HIPEs were transferred to a plastic syringe, sealed, and placed into a 60°C oven to polymerise for 72 hours. Then, polyHIPE monoliths were washed with water, then methanol and dried at 30°C.

Table 3.1. Volumes of monomers used to produce varied molar ratio S-co-DVB polyHIPEs.

Volume/moles of styrene (mL/mmol)	Volume/mols of DVB (mL/mmol)	DVB content (%)
1.143/6.25	0/0	0
0.996/8.654	0.109/7.692	10
0.885/7.678	0.219/1.538	20
0.774/6.731	0.328/2.308	30
0.664/5.769	0.438/3.077	40
0.553/4.808	0.547/3.845	50
0.442/3.846	0.656/4.615	60
0.332/2.884	0.766/5.385	70
0.221/1.922	0.875/6.154	80
0.111/9.615	0.985/6.923	90
0/0	1.09/7.692	100

3.1.3 Synthesis of t-BS-co-DVB polyHIPEs

T-butyl styrene and DVB (table 3.2) were combined with Span® 80 (0.28 g, 0.65 mmol) and mixed thoroughly, then transferred to a 10 mL gas tight syringe. Deionized water (8.8 mL, 0.49 mol) containing potassium persulfate (0.44g, 1.63 mmol) was transferred to another 10 mL gas tight syringe. The double syringe emulsification procedure was carried out as described in chapter 3. Generally, the resulting HIPEs were homogeneous and that increasing DVB volumes reduced emulsion viscosity. In addition, t-BS containing HIPEs were more stiff than S equivalents. Once emulsified, HIPEs were transferred to a plastic syringe, sealed, and placed into a 60°C oven to polymerise for 72 hours. Then, polyHIPE monoliths were washed with water, then methanol and dried at 30°C.

Table 3.2. Volumes of monomers used to produce varied molar ratio t-BS-co-DVB polyHIPEs.

Volume/moles of t-BS (mL/mmol)	Volume/mols of DVB (mL/mmol)
1.143/6.25	0/0
1.029/5.625	0.109/0.769
0.8/4.375	0.335/1.538
0.571/3.125	0.547/3.845
0.343/1.875	0.766/5.385

3.1.4 Synthesis of S-co-para-DVB polyHIPEs

Styrene and para-DVB (table 3.3) were combined with Span® 80 (0.28 g, 0.65 mmol) and mixed thoroughly, then transferred to a 10 mL gas tight syringe. Deionized water (8.8 mL, 0.49 mol) containing potassium persulfate (0.44g, 1.63 mmol) was transferred to another 10 mL gas tight syringe. The double syringe emulsification procedure was carried out as described in chapter 3. Generally, the resulting HIPEs were homogeneous and that increasing DVB volumes reduced emulsion viscosity. 100% para-DVB HIPEs were less viscous that the 100% DVB equivalent. Once emulsified, HIPEs were transferred to a plastic syringe, sealed, and placed into a 60°C oven to polymerise for 72 hours. Then, polyHIPE monoliths were washed with water, then methanol and dried at 30°C.

Table 3.3. Volumes of monomers used to produce varied molar ratio S-co-para-DVB polyHIPEs.

Volume/moles of styrene (mL/mmol)	Volume/mols of para-DVB (mL/mmol)
0.885/7.692	0.219/1.538
0.774/6.731	0.328/2.308
0.332/2.884	0.766/5.385
0/0	1.09/7.692

3.1.5 Synthesis of Mixed Surfactant PolyHIPEs

Mixed surfactant system polyHIPE were synthesised in the same manner as previous polyHIPEs. Table 3.4 contains the details on concentrations of surfactants used in the mixed surfactant polyHIPE investigations.

Table 3.4. Components and quantities of mixed surfactant systems used in polyHIPEs.

Surfactant system	Span® 80 (g/mmol)	Span® 20 (g/mmol)	CTAB (g/mmol)	DDBSS (g/mmol)
Span® 80/20	0.21/0.490	0.07/0.20	N/A	N/A
CTAB, DDBSS, Span 80	0.18/0.412	N/A	0.008/0.022	0.012/0.034
CTAB, DDBSS, Span 20	N/A	0.168/0.485	0.007/0.019	0.0102/0.029

3.1.6 Synthesis of Deuterated S-co-DVB PolyHIPEs

Styrene (0.882 mL, 7.692 mmol) and DVB (0.219 mL, 1.538 mmol) were combined with Span® 80 (0.28 g, 0.65 mmol) and mixed thoroughly, then transferred to a 10 mL gas tight syringe. Deuterated water (8.8 mL, 0.49 mol) containing potassium persulfate (0.44g, 1.63 mmol) was transferred to another 10 mL gas tight syringe. The resulting HIPE was homogeneous. Once emulsified, the HIPE was transferred to a plastic syringe, sealed, and placed into a 60°C oven to polymerise for 72 hours. Then, polyHIPE monoliths were washed with water, then methanol and dried at 30°C.

3.1.7 Synthesis of 2VN PolyHIPEs

2VN homopolymer polyHIPE was synthesised by combining 1g, 6.485 mmol, toluene (0.375 mL, 3.53 mmol) with Span® 80 (0.28 g, 0.65 mmol) and mixed thoroughly, then transferred to a 10 mL gas tight syringe. 2VN-co-DVB was synthesised by combining 2VN (0.9g, 5.837 mmol), toluene (0.375 mL, 3.53 mmol), and DVB (0.055 mL, 0.422 mmol) with Span® 80 (0.28 g, 0.65 mmol) and mixed thoroughly, then transferred to a 10 mL gas tight syringe. Deionised water (8.8 mL, 0.49 mol) containing potassium persulfate (0.44g, 1.63 mmol) was transferred to another 10 mL gas tight syringe. Generally, the resulting HIPEs were homogeneous but fragile with the emulsion partly breaking during polymerisation. Once emulsified, HIPEs were transferred to a plastic syringe, sealed, and placed into a 60°C oven to

polymerise for 72 hours. Then, polyHIPE monoliths were washed with water, then methanol and dried at 30°C.

3.2 Synthesis of Aerogels

By definition gels are polymer networks across the entire the vessel used for polymerisation and contain solvent between pores.[14] Aerogels are gels with the solvent removed by supercritical drying.

Gels were prepared using different reagents, which are detailed in the following sections, nevertheless general preparation of gels was to mix the monomer and solvent in a glass vial at a ratio to achieve 100 mg/cm^{-3} density. The initiator was added at a concentration shown in table 3.5 and homogenously mixed with the solvent and monomer to initiate polymerisation. Polymerisations using Grubbs type catalysts were performed at room temperature. The time taken for gels to form was 10 seconds to 40 minutes, but all were left overnight to ensure sufficient polymerisation had been achieved. The catalysts used are given in figure 3.2.

Table 3.5. Monomer and initiator types and concentrations that formed aerogels.

Monomer	**Initiator**	**Initiator concentraion (% of monomer (mols))**	**Solvents**
DVB	AIBN	10, 20	Toluene
	$SnCl_4$	10, 20, 45	DCE
DCPD	Grubbs type catalysts	0.05, 1.6	Toluene
Norbornene	Grubbs type catalysts	0.03, 1.1	Toluene
5V2N	$SnCl_4$	21, 42	DCE
DCPX	$SnCl_4$	38.1, 76.2	Toluene

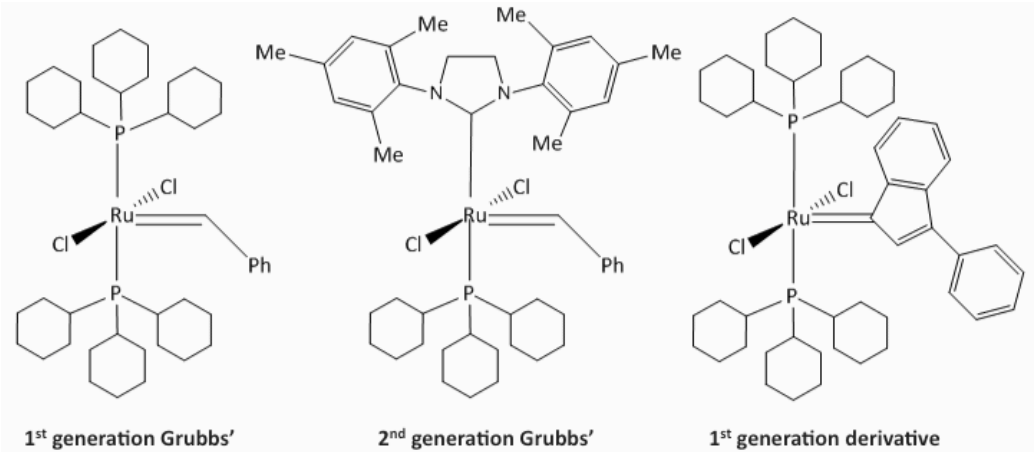

Figure 3.2. The Grubbs' type catalysts used for DCPD aerogel formation and their generation.

Once each system had gelled, gels were removed from the glass vial, exchanged with methanol, and then dried using a critical point drier (CPD) with carbon dioxide as the supercritical fluid.

In some cases, carbonisation of aerogels was performed to remove unwanted elements from the material. Higher Z elements cause more interference of X-ray scattering in the plasma state, thus it is desirable to remove these elements if possible. DCPX aerogels contained chlorine thus carbonisation was performed to eliminate, or reduce the amount contained in the aerogel.

3.2.1 Materials and reagents

Divinyl benzene 80 (DVB), methanol, benzene, toluene, 1,2-dichloroethane (DCE), azobisisobutyronitrile (AIBN), tin (IV) chloride, dicylcopentadiene (DCPD) (mixture of exo- and endo- isomers), norbornene (mixture of isomers), 5-vinyl-2-norbornene (5V2N) (mixture of isomers), 1,4-dichloro p-xylene (DCPX), chlorobenzene, bromobenzene, benzylidene-bis (tricyclohexylphosphine)-dichlororuthenium (Grubbs 1), bis(tricyclohexylphosphine)-3-phenyl-1H-inden-1-ylideneruthenium dichloride (LG Grubbs), (1,3-Bis(2,4,6-trimethylphenyl)-2-imidazolidinylidene) dichloro(phenylmethylene) (tricyclohexylphosphine) ruthenium (Grubbs 2).

All chemicals were used as received except for monomers which had the inhibitor extracted before use using a silica column.

3.2.2 Instrumentation and characterisation

Techniques used to characterise aerogels were SEM, elemental analysis, TD-NMR, SSNMR and X-ray tomography. All gels were dried using a Polaron® critical point drier (CPD) with carbon dioxide as the supercritical fluid, exchanged from methanol. Carbonisation of aerogels was performed using a tube furnace with temperature and ramp rate program. Aerogels were heated to 400°C, at 2°C per minute and kept at 400°C for one hour. The furnace was then switched off and cooled by convection. The carbonisation was carried out under an inert N_2 atmosphere.

Densities of aerogels were obtained by mass and volumetric measurements of cylindrical shaped samples. The weights of samples were measured using a five figure balance. Aerogel length and diameters (thus radius and volume) were obtained using a calibrated calipers guage with an electronic display.

Throughout this work, high concentrations of initiator have been used. High initiator concentration will produce shorter chain lengths, and increase polymerisation rates. However, for DVB and DCPX, as they are bifunctional monomers, high initiator concentrations were used as it was postulated that it could be another route to gel network formation. Shorter chains are compensated by being composed of bifunctional monomers thus have an increased cross-linking concentrated, may result in gel formation due to increased number of polymer clusters formed. Higher concentrations were attempted in ROMP (1.6% compared to 0.05%) but no gels were formed. All solvents had water removed by using molecular sieve beads with 3 Å pore diameter.

3.2.3 Synthesis of DVB Aerogel Initiated by AIBN

AIBN was dissolved in toluene before addition of DVB in a glass vial. DVB was added using a pipette and the solution was mixed thoroughly before placed into a 60°C oven to polymerise. Gels were carefully removed from the glass vial and placed into another vessel containing methanol to allow the solvents to exchange. After a period of 24-48 hours with regular changing of the methanol, gels were dried using a critical point drier using carbon dioxide as the supercritical fluid to give a dry aerogel. Aerogels were an off-white colour. It was observed that decreasing target density of gels resulted in more fragile gels, which meant removing from the glass often resulted in damage to the gel. Gels of all densities often stuck to the glass vial, which meant that on breaking of the glass the gel was damaged in the process but in some cases near perfect cylinders were obtained. Table 3.5 contains the experimental details for DVB aerogel formation.

Table 3.5. Volumes and masses used to form all DVB gels initiated by AIBN.

Target density (mg/cc)	Mass/mol of DVB (g/mmol)	Mass/mol of AIBN (g/mmol)	Volume of Toluene (mL)
100	0.50/3.84	0.1215/0.768	4.5
50	0.25/1.92	0.063/0.384	4.75
25	0.125/0.96	0.032/0.192	4.85

3.2.4 Synthesis of DCPD and Norbornene Aerogel Initiated by Grubbs type Catalysts

Gels of DCPD or norbornene were formed by mixing DCPD or norbornene in toluene in a glass vial, then addition of an aliquot of Grubbs type catalyst in toluene. Addition and mixing of the catalyst into the solution was fast due to the speed at which gels formed. Once all reagents were mixed together, the solution was left at room temperature (24±1°C) to gel. Gels formed in a matter of seconds, but left to cure overnight to ensure extensive polymerisation throughout the system. Gels were carefully removed from the glass vial and placed into another vessel containing

methanol to allow the solvents to exchange. After a period of 24-48 hours with regular changing of the methanol, gels were dried using a critical point drier using carbon dioxide as the supercritical fluid to give a dry aerogel. Aerogels were colored white. DCPD of higher density was robust and were not damaged on removal from the glass vial whereas lower density gels were very soft and easily damaged on breaking of the glass.

Table 3.6 contains the experimental details for DCPD, and table 3.7 contains the details for norbornene aerogel formation.

Table 3.6. Volumes and masses used to form all the DCPD gels initiated by Grubbs type catalysts.

Target density (mg/cc)	**Mass/mol of DCPD (g/mmol)**	**Grubbs type catalyst**	**Mass/mol of Grubbs type catalyst (g/mmol)**	**Volume of toluene (mL)**
100	0.50/3.84	Grubbs 1	$1.5x10^{-3}/1.82x10^{-3}$ 0.05/0.061	4.5
		Grubbs LG	$1.5x10^{-3}/1.63x10^{-3}$ 0.05/0.054	
		Grubbs 2	$1.5x10^{-3}/1.77x10^{-3}$ 0.05/0.059	
50	0.25/1.92	Grubbs 1	$7.5x10^{-4}/9.11x10^{-4}$	4.75

Table 3.7. Volumes and masses used to form all the norbornene gels initiated by Grubbs type catalysts.

Target density (mg/cc)	**Mass/mol of norbornene (g/mmol)**	**Mass/mol of Grubbs type catalyst (g/mmol)**	**Volume of toluene (mL)**
100	0.50/5.31	$1.5x10^{-3}/1.82x10^{-3}$ 0.05/0.061	5

3.2.5 Synthesis of 5V2N Aerogel Initiated by Tin (IV) Chloride

5V2N gels were prepared by mixing the monomer with dichloroethane (DCE) in a glass vial. A pipette was used to add the initiator. Transfer of the initiator to the vial was fast, and performed in a fume cupboard, as tin (IV) chloride produced white fumes on contact with air. This did not present a problem for polymerisation, as water was the co-catalyst for cationic polymerisation using tin (IV) chloride as neither the monomer or initiator was dried. The solution was left at room temperature to polymerise, which typically took overnight to gel. Gels were carefully removed from the glass vial and placed into another vessel containing methanol to allow the solvents to exchange. After a period of 24-48 hours with regular changing of the methanol, gels were dried using a critical point drier using carbon dioxide as the supercritical fluid to give a dry aerogel. Aerogels were a brown/yellow color.

Post cross-linking experiments of 5V2N were performed by adding a mixture of DCE and cross-linking monomer to the wet gel. Bifunctional monomers were used to ensure cross-linking between chains occurred. Gels were left overnight to ensure sufficient swelling of the gel by the solvent/monomer mixture and diffusion of the monomer into the gel network. Then, an aliquot of Grubbs catalyst in DCE was added to initiate cross-linking. Gels were left for a period of 24-48 hours to react at room temperature, after which they were cleaned in methanol and dried using a CPD using carbon dioxide as the supercritical fluid.

Table 3.8 contains the experimental details for 5V2N aerogel formation, and table 3.9 contains the experimental details for post cross-linking experiments of 5V2N aerogels.

Table 3.8. Volumes and masses used to form 5V2N gels initiated by tin (IV) chloride.

Target density (mg/cc)	Mass/mol of 5V2N (g/mmol)	Mass/mol of tin (IV) chloride (g/mmol)	Volume of DCE (mL)
100	0.50/4.16	0.226/0.86 0.445/1.71	4.5

Table 3.9. Volumes and masses used to post cross-link 5V2N gels.

Cross-linking monomer	Mass/mol of cross-linker (g/mmol)	Mass/mol of Grubbs type catalyst (g/mmol)
DCPD	0.05/0.384	$1.5x10^{-3}/1.82x10^{-3}$
1,3 cyclooctadiene	0.05/0.462	$1.5x10^{-3}/1.82x10^{-3}$

3.2.6 Synthesis of DCPX Aerogel Initiated by Tin (IV) Chloride

DCPX gels were prepared by dissolving the monomer in dry toluene contained in a glass vial. In a fume cupboard, tin (IV) chloride was added to the mixture using a pipette, then the entire solution mixed thoroughly before placed in an oven at 86°C. Gels formed within 48 hours, and were left an additional 72 hours to cure. The glass vials were carefully broken, and gels were so robust that often they were undamaged on removal. Gels were transferred to another vessel containing methanol to allow the solvents to exchange. After a period of 24-48 hours with regular changing of the methanol, gels were dried using a critical point drier using carbon dioxide as the supercritical fluid to give a dry aerogel. Aerogels were a deep red colour. Table 3.10 contains the experimental details for DCPX aerogel formation.

Table 3.10. Volumes and masses used to form DCPX gels initiated by tin (IV) chloride.

Target density (mg/cc)	Mass/mol of DCPX (g/mmol)	Mass/mol of tin (IV) chloride (g/mmol)	Volume of toluene (mL)
100	0.50/2.86	0.283/1.09 0.565/2.18	5

3.2.7 Synthesis of DVB Density Gradient Aerogel Initiated by Tin (IV) Chloride

In a fume cupboard, DCE and tin (IV) chloride were mixed together in a glass vial. DVB was added using a pipette and then a glass melting point tube was inserted vertically as fast as possible. The mixture was left at room temperature to polymerise. Gels formed within minutes and left at least 24 hours to cure, and then carefully removed from the glass vial and placed into another vessel containing methanol to allow the solvents to exchange. After a period of 24-48 hours with regular changing of the methanol, gels were dried using a critical point drier using carbon dioxide as the supercritical fluid to give a dry aerogel. Aerogels were an orange color in regions of high density, and white in regions of low density.

Table 3.11 contains the experimental details of DVB density gradient aerogel formation.

Table 3.11. Volumes and masses used to form DVB density gradient gels initiated by tin (IV) chloride.

Target density (mg/cc)	Mass/mol of DVB (g/mmol)	Mass/mol of tin (IV) chloride (g/mmol)	Volume of DCE (mL)
100	0.07/0.538	0.036/0.137	0.7

3.3 Low Field Solid-State NMR Experiments

Low field NMR experiments were performed using a 0.47 Tesla Bruker MQ20 NMR relaxometer operating at 19.85 MHz for ^{1}H nuclei. Powdered samples were contained in 10 mm NMR inactive silica tubes. The machine had a programmable temperature controller that allowed experiments to be performed in the range of –100°C to +200°C by using liquid nitrogen and nitrogen gas to achieve low or high temperatures respectively. Background checks were performed to ensure that there was no contribution to the NMR signals from the sample tubes. All experiments performed under static conditions, as the MQ20 does not have magic angle spinning (MAS) capabilities. Experiments performed were T_1 saturation recovery and $T_{1\rho}$ relaxation experiments of ^{1}H nuclei.

Two model studies on a semi-crystalline polymer, polyvinylidene fluoride (PVDF), and polystyrene GPC standards, were performed to validate the experimental set-up. The delivery of the apparatus was delayed by 6 months therefore it was necessary to use well-characterised polymers such as PVDF and polystyrene to achieve validation. PVDF is a well characterised polymer using many techniques including relaxation experiments using high-field SSNMR.[2–4] Both T_1 and $T_{1\rho}$ relaxation experiments were performed, and measured using a temperature range from –50°C and +180°C with 10°C steps. The system was left to reach an equilibrium state for at least 20 minutes after each successive heating before experiments were performed. It was postulated that the results of these initial experiments could be translated to low density polymers by applying a similar set of experimental parameters.

Appendix 3.12 contains the detailed analysis of the relaxation data of PVDF and polystyrene on the MQ20.

3.3.1 Spin-lattice (T_1) Saturation Recovery Pulse Sequence

Nuclear spins outside of a strong magnetic field are degenerate in energy and have a random direction with respect to a magnetic field. The T_1 saturation recovery experiment recreates this situation inside the magnet by applying many 'saturation' pulses to saturate the spins again. In addition, application of pulses means saturation recovery is often faster measure of T_1 compared to inversion recovery method, which waits a large amount of time to restore degeneracy. This experiment is a measure of the time taken for the spins to reestablish 63% of the net magnetisation ($\mathbf{M}_0$), the difference in population of energy levels. Performing a number of pulses sequentially puts the spins out of this energy equilibrium and then a time delay (tau) is introduced before finally measuring what magnetisation is then returned to the the x-y plane.

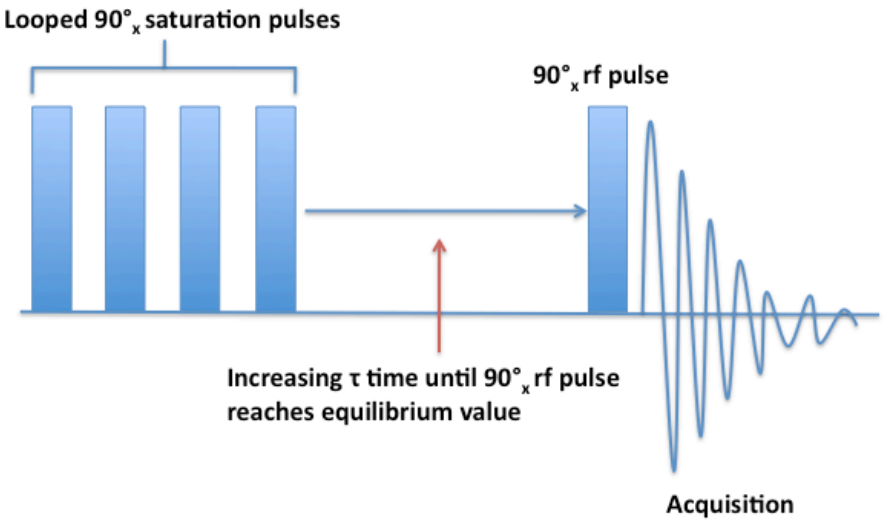

Figure 3.3. T_1 saturation recovery pulse sequence, 90° saturation pulses followed by a varied tau (τ) time and a 90° pulse.

T_1 relaxation experiment was performed using the pulse sequence shown in figure 3.3. The number of saturation pulses was 4 pulses per loop and two loops in total, giving 8 saturation pulses before acquisition. The varied tau (τ) time range was 0.1 ms to 10 s. The apparatus software calculated the increase of tau based upon the 40, 60 or 80 data points depending on the experiment. A recycle delay of 1 second was used after each data point acquired. Experiments performed used a 90° ^{1}H rf power

at 6 dB which was calculated to be 73.5 and 91.2 kHz for a duration of 3.40 and 2.74 microseconds (μs) respectively.

3.3.2 Relaxation under RF ($T_{1\rho}$) Pulse Sequence

$T_{1\rho}$ is known as T_1 in the rotating frame, or relaxation under RF. The experiment begins with a 90° pulse to flip the magnetization from the z axis into the x-y plane. A spin lock pulse is then applied along the y axis, which effectively locks magnetization in this axis i.e. polarizes the spins in the axis of the applied pulse. For the duration of the spin lock, spins that are poorly spin-locked dephase from the x-y axis, while spins that are more easily polarized continue to be locked in place. Once the spin lock time expires, the remaining signal from the magnetization that remains is then acquired. The experiment is repeated with increasing spin lock times until all the magnetisation has dephased, resulting in acquisition of no signal.

This experiment is relevant to semi-crystalline polymers as the relaxation times between the amorphous and crystalline phases differ due to different mobility as a result of molecular structure. A $T_{1\rho}$ experiment using high-field SSNMR of PVDF reveals these two domains.[2] This is also expected at low field strength for semi-crystalline polymers as seen in the initial trials performed on PVDF (Appendix 3.12); therefore efficient spin-lock and inefficient spin-lock components may exist in polyHIPEs or aerogels (not necessarily crystalline).

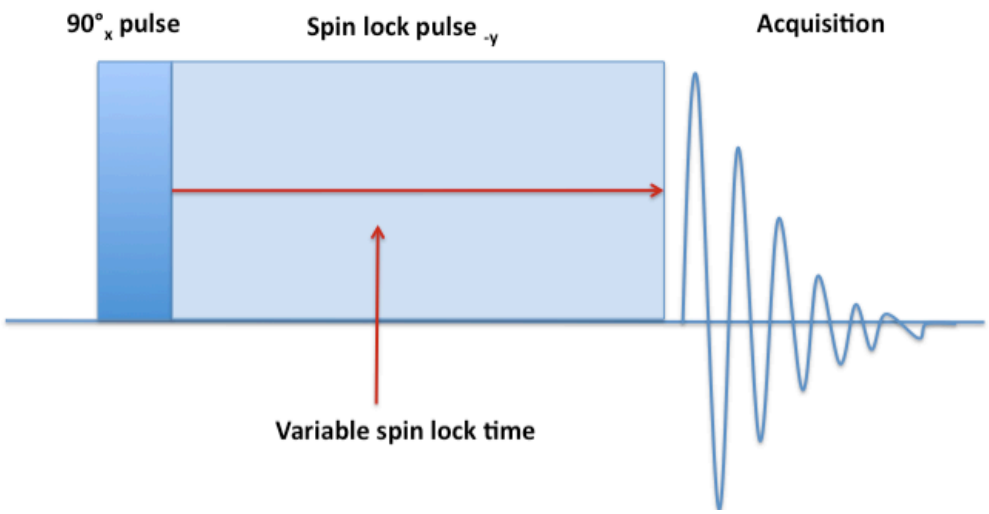

Figure 3.4. The $T_{1\rho}$ pulse sequence has an increasing tau to let more magnetization in the x-y plane relax back to equilibrium.

The $T_{1\rho}$ experiment was performed with the pulse sequence shown in figure 3.4. Experiments performed used a 90° ^{1}H rf power at 6 dB which was calculated to be 73.5 and 91.2 kHz for a duration of 3.40 and 2.74 microseconds (μs) respectively. The effective spin lock field is attenuated by the duration of the spin lock pulse which was incremented from 0.1 to 40 ms. The spin lock time increase between experiments was calculated by the apparatus software based upon the 60 data points and the time range for the experiment which was 0.1 ms to 40 ms. A recycle delay of 5 seconds was used after each acquired data point.

3.4 High Field Solid-State NMR Experiments

The NMR experiments were performed on two solid-state NMR spectrometers; one of which was a 400 MHz Bruker Avance III solid-state NMR spectrometer with a 9.4 T wide-bore magnet. Powdered samples were packed into zirconia rotors with Kel-F drive caps for use with a 4mm HFXY or 4mm double resonance MAS probes respectively. The other spectrometer used was a 400 MHz Varian VNMRS spectrometer operating with a 9.4 T wide-bore margent. Powdered samples were packed into 4.0 mm zicronia rotors with a Vespel™ drive cap for use with a Varian Chemagnetics T3 probe in double resonance mode. All spectra were obtained at ambient temperature and ^{13}C chemical shifts were externally referenced to adamantane using $^{13}CH_2$ resonance (38 ppm).

3.4.1 Cross-Polarization (CP) Parameters

CP experiments were performed to increase the signal of nuclei by a boost from another nuclei. Commonly this is a ^{1}H-^{13}C CP where the ^{1}H nuclei are used to boost the less abundant ^{13}C nuclei. This is performed by matching both sets of nuclear spins to allow transfer of magnetisation from ^{1}H to ^{13}C nuclei mediated by dipolar coupling. CP-MAS parameters used on the Bruker Avance III spectrometer are given in table 3.12 and CP-MAS parameters used on the Varian VNMRS spectrometer are given in table 3.13.

Table 3.12. The ^{1}H-^{1C}C CP-MAS parameters used for experiments performed on the Bruker Avance III spectrometer. A recycle delay of 5 seconds was used.

Material	Contact time (μs)	Power during contact (kHz)	Decoupling power (kHz)	Decoupling sequence	MAS Speed (kHz)
S-co-DVB (all molar ratios)	800	71.4	71.4	Spinal64	14
T-BS-co-DVB	1000	83.3	83.3	Tppm15	12.5
2VN	1000	71.4	71.4	Tppm15	12
5V2N	1500	83.3	83.3	Tppm15	12.5

Table 3.13. The ^{1}H-^{13}C CP-MAS parameters used for experiments performed on the Varian VNMRS spectrometer. A recycle delay of 3 seconds was used.

Material	Contact time (μs)	Power during contact (kHz)	Decoupling power (kHz)	Decoupling sequence	MAS Speed (kHz)
S-co-DVB X:X*	1000	83.3	83.3	Spinal64 (all exps)	10
Styrene	1000	83.3	83.3		12
DVB	1000	83.3	83.3		12
T-BS	1000	83.3	83.3		12

*where X:X is the varied molar ratio for S-co-DVB

A CP experiment is performed by firstly a $90°_x$ pulse on the proton channel to flip magnetization from the z axis into the –y axis. Then a second pulse is applied along the y axis with a field of $B_1(^1\mathrm{H})$ and spin locks the ^{1}H magnetization, whilst simultaneously another pulse is applied with another field B_1 to spin lock ^{13}C. For cross-polarization to occur, which is achieved by setting the amplitudes of the pulses, the Hartman-Hann matching condition must be fulfilled[5,6] (equation 3.1)

$$\gamma_{\mathrm{H}} B_1(^1\mathrm{H}) = \gamma_{\mathrm{C}} B_1(^{13}\mathrm{C}) \qquad (3.1)$$

and when performing CP under MAS conditions, the match now becomes

$$\gamma_{\mathrm{H}} B_1\left(^1\mathrm{H}\right) = \gamma_{\mathrm{C}} B_1\left(^{13}\mathrm{C}\right) \pm \omega_{MAS} \qquad (3.2)$$

Once matched, both sets of spins are spin-locked on the –y axis and transfer of magnetization from ^{1}H spins to ^{13}C spins occurs. This transfer occurs via the dipolar coupling and causes a redistribution of energy between the spins, but overall the energy remains constant. The contact pulse is applied for an optimum time during which the transfer occurs. This is switched off and decoupling of the ^{1}H spins begins while the ^{13}C signal is acquired. A representation of the general CP pulse sequence is given in figure 3.5.

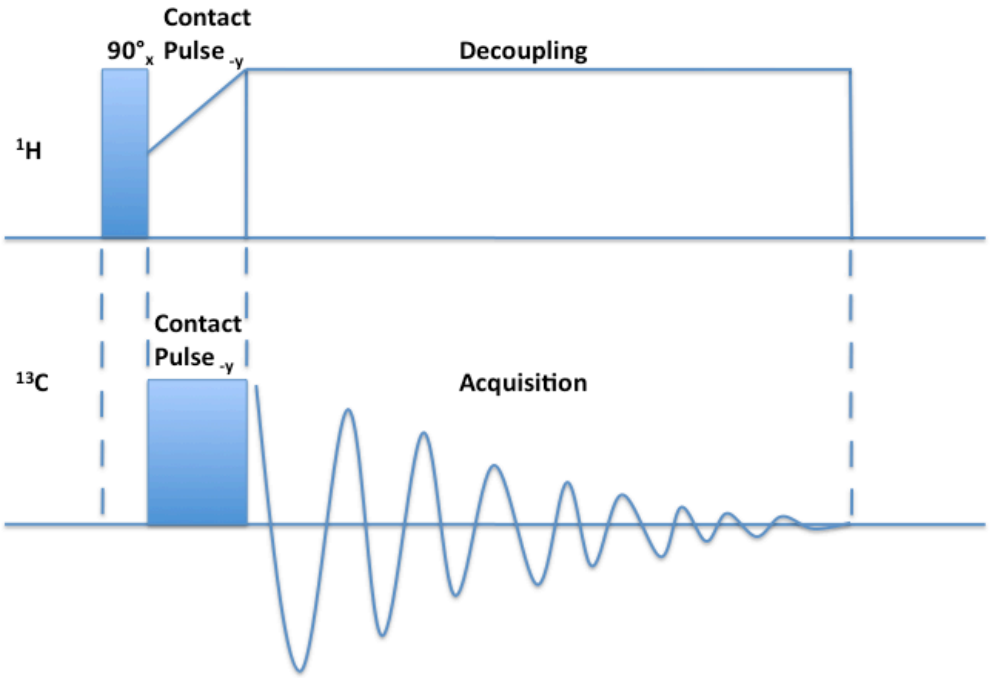

Figure 3.5. A representation of a ^{1}H-^{13}C cross-polarization pulse sequence.

3.4.2 Direct Polarisation Parameters

More specific structural investigations were performed using direct polarization experiments on a deuterated styrene-co-DVB polyHIPE. It was postulated that direct polymerisation of the ^{13}C nuclei in the cross-linking DVB whilst styrene contributions are eliminated would yield more information on the nature of the cross-linking in these materials. The parameters used are in table 3.14.

Table 3.14. The ^{13}C-^{1}H direct polarisation parameters used for experiment performed on the Varian VNMRS spectrometer. A recycle delay of 5 seconds was used.

Material	DEPTH filter used	Pulse power (kHz)	Decoupling power (kHz)	Decoupling sequence	MAS Speed (kHz)
S-d_8-DVB	no	83.3	83.3	Spinal64	15
	yes	83.3	83.3		Static

The DEPTH experiment is designed to eliminate unwanted contributions to a spectrum from, for example, the NMR probe or contaminations in the sample. This is achieved by using two 180 degree pulses together after the 90 degree direct polarization pulse. Spins that do not experience a true 90 or 180 pulse are lost, thus

only contributions from the sample remain. Figure 3.6 is a schematic of a general DEPTH pulse sequence.

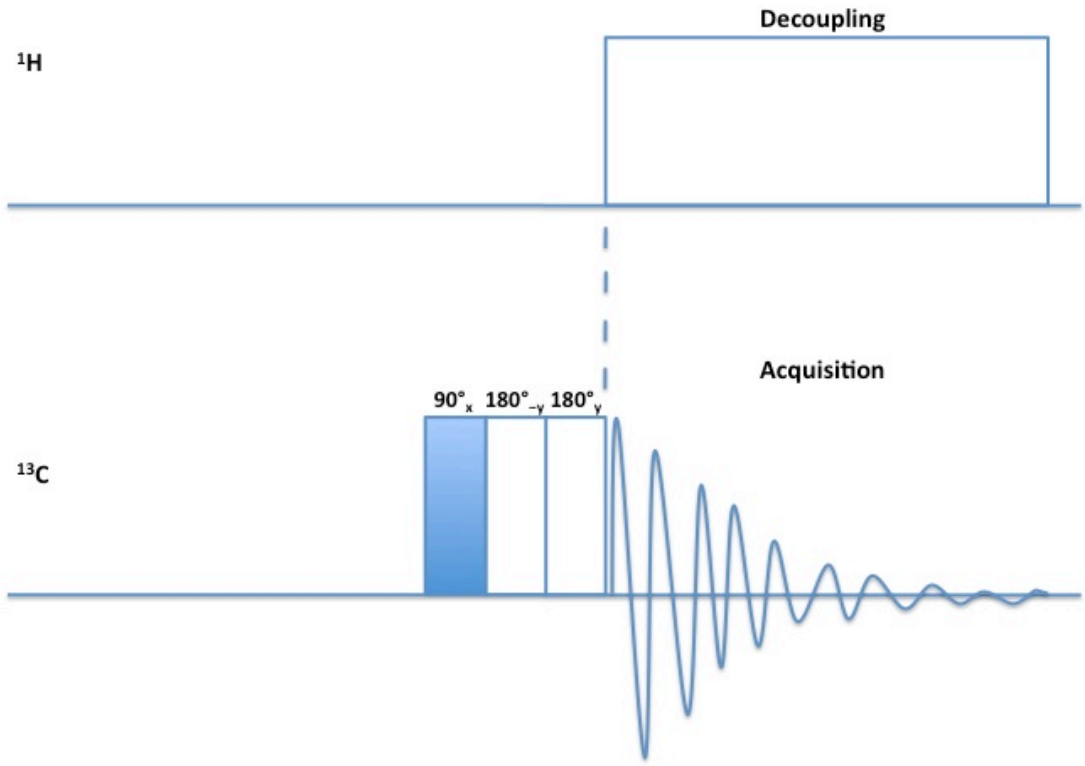

Figure 3.5. A representation of a ^{13}C DEPTH pulse sequence.

3.5 Dynamic Mechanical Analysis (DMA)

DMA is a characterisation technique that measures the responses of a material on application of an oscillatory force. It can be viewed as a measure of polymer chain relaxation.[7] In other words, the polymer chains restore themselves to an equilibrium state on response to the applied force. Properties such as yield point and (Young's) modulus can be determined by measuring the response to the applied force.

DMA data is obtained using sophisticated apparatus, and a complete description is beyond the scope of this work. Briefly, a motor produces a sinusoidal force and through a cantilever in contact with the material the stress is applied. A linear variable differential transformer (LVDT) detects the deformation response of the material. The rate of the applied stress, or frequency, over a period of time will generate data points; for example a frequency of 1 Hz will measure a material's response every second.[8]

The application of the oscillating force can be extremely varied; factors such as the material dimensions, direction of the application of the stress, and domains of measurements such as strain, time or temperature are all important varibles.[8] The applied force is called stress, σ, and the deformation response is called strain, γ. Thus DMA data is often presented as stress-strain curves (figure 3.6).[8] The modulus can be described as a measure of material stiffness, thus used a guide of a material's performance (application dependent).[8] The initial, linear portion of the stress-strain curve gives Young's modulus, and is obtained through a constant application of force rather than an oscillation (which calculates the elastic modulus, E'). Calculation of the elastic modulus is more complicated than Young's modulus, and the relationship it has between other moduli is given in figure 3.7. However, Young's modulus in this case is more simple, and given by

$$E = \frac{\sigma}{\gamma} \qquad (3.3)$$

The strain, γ, is obtained from measuring a change in a dimension (ΔY) against the original value of that dimension, Y (3.4). Often DMA experiments use

$$\gamma = \frac{\Delta Y}{Y} \tag{3.4}$$

which can use Hooke's Law to relate stress and strain

$$\sigma = k \cdot \gamma \tag{3.5}$$

where k is the spring constant (a measure of the elasticity of a spring) and σ is the stress. However, there are other types of modulus, and can be calculated from the strain response from the application of a sinusoidal stress; the elastic modulus, E', the imaginary loss modulus, E'', and the complex modulus, E^*.[8] This work does not measure the imaginary loss or complex moduli, but it is necessary to mention these for completion, as these terms are all related (figure 3.7).[8] Furthermore, some articles referenced throughout this work appear to use both elastic and Young's modulus interchangeably. Whilst they measure the same property (hence the interchanging is understandable), they are calculated differently.[8] The measure of material stiffness forms an important argument in this work, and to avoid confusion this has been mentioned now. Modulus is used as a general term in this work.

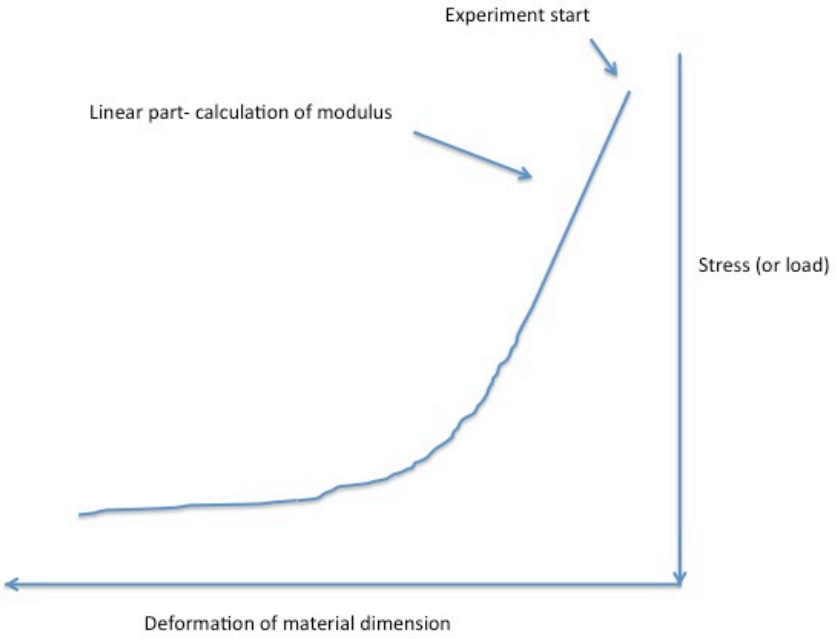

Figure 3.6. An example of a DMA/stress-strain curve (image adapted from experiments carried out in this work).

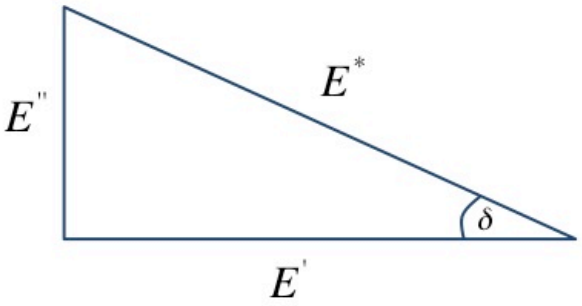

Figure 3.7. The relationship between E', E'' and E^*. Imaged adapted from K. P. Menard, in *Dynamic Mechanical Analysis; A Practical Introduction*, CRC Press, Bota Raton, U.S.A, 2008, 2 edn., ch.1, pp. 4.

Similar to many mechanical characterisation techniques, DMA is sensitive to structural changes in a material; such as a change in the level of cross-linking (affecting strength), bulk density, crystallinity of material, and molecular weight.[8] Furthermore, the addition of plasticizers will effect the modulus depending on the nature of the addivitve.[8] Thus DMA can be an extremely important tool in design, production and characterisation of functional materials.

3.5.1 Relationship between DMA and NMR relaxation times

DMA and NMR are two polymer characterisation techniques that can be related by relaxation times. In DMA, relaxation times (τ) refer to the molecular chain relaxation in response to an applied stress (equation 3.6). In NMR, relaxation times refer to the response of perturbed nuclear spins returning to an equilibrium state, which uses correlation time (τ_C) to define molecular motion (equation 3.7). Literature[9–12] describes the loss modulus, E'', and T_1 relaxation in detail. They both have frequency (ω) dependency and similar form of expression (derived), which can relate them;

$$E'' = \delta E'' \omega J(\omega \tau_C \varepsilon) \tag{3.6}$$

$$\frac{1}{T_1} = A\left[J\left(\omega \tau_C \varepsilon\right) + 4J\left(2\omega \tau_C \varepsilon\right)\right] \tag{3.7}$$

Thus it could be expected that correlations between DMA experiments and spin-lattice relaxation times exist despite the large difference in frequencies of the probed motion. The loss modulus describes the energy loss in a material due to internal molecular motions.[8] Spin-lattice relaxation loses energy from the radiofrequency pulse by spin flipping relaxation mechanism throughout the molecular structure (or lattice).[12] It was postulated that comparison of modulus and T_1 relaxation was one strategy used to improve existing issues in polyHIPE foams.

DMA experiments were performed using an Instron 5582, with a 10 kN maximum press load and 100 kN maximum plate load. Manufacturer software analysed the stress-strain plots to obtain Elastic modulus (Automatic Young's modulus). PolyHIPE cylinders with parallel surfaces were used in these experiments, and synthesised by addition of freshly prepared HIPE into a sealed steel mould to cure. Multiple cylinders (three or four) for each material were used to ensure reproducibility. The dimensions of each disc were 10 mm diameter and had 7 mm depth on average.

3.6 Mercury porosimetry

Mercury porosimetry is a characterisation technique that measures different physical properties of a material such as pore size diameter, pore area and porosity by using pressurized mercury to intrude into the porous structure. Liquid mercury has a high surface tension which does not penetrate material pores, and it has a high contact angle with surfaces which prevents the material from wetting, thus it will only enter the structure under pressure.[13] By using a non-wetting liquid and knowing the pressures used, these aforementioned properties can be calculated using the following equations.

Pore diameters, D, are calculated using the relationship

$$D = \frac{-4\gamma\cos\theta}{P} \tag{3.8}$$

where γ is the surface tension of mercury, θ is the contact angle and P is the applied pressure. The density of the bulk sample, ρ_{se}, is calculated by

$$\frac{W_s}{V_p - V_{Hg}} \tag{3.9}$$

where W_s is the weight of the sample, V_s is the volume of the empty penetrometer, and V_{Hg} is the volume of mercury. The skeletal density, ρ_{sa}, is calculated by

$$\frac{W_s}{V_{se} - V} \tag{3.10}$$

where W_s is the weight of the sample, V_{se} is the volume of the penetrometer minus the volume of mercury, and V is the total volume of mercury filling pores. Knowing both densities the porosity of the material can be obtained, which is important when characterising low density materials (equation 3.11).

$$\text{Percent porosity} = \left(1 - \frac{\rho_{se}}{\rho_{sa}}\right)100 \qquad (3.11)$$

The apparatus consists of a vessel for the sample called a penetrometer, pumps to create the vacuum and pressure for the mercury to intrude into the material. The penetrometer has a capillary 'stem' containing the mercury and is also used to monitor how much mercury has intruded into the sample. At low pressure, the mercury flows down the stem around the material and then higher pressures are used to induce intrusion to begin measurement. Pore diameters as small as 3 nm in size can be accessed by using pressures of 60,000 psi.[13] The applied pressure is constant and consistent to produce a pressure-volume intrusion curve plotting volume of mercury intruded and the pressure from which data can be obtained.

Analysis was performed using a Micromeritics Autopore IV 9500. Intrusion and extrusion contact angles were 140 degrees. Penetrometers had a 1.19 mL stem volume and a bulb volume of 5 mL. Pressures ranged from 0 to 60,000 psi.

3.7 Scanning Electron Microscopy (SEM)

SEM is a well-established surface analysis technique that uses a focused electron beam to image materials. It can achieve high magnifications (nm resolution for the Carl Ziess apparatus used in this work) without loss of image quality as well as X-ray analysis capabilities.[14] SEM can be valuable in polymer characterisation elucidating local surface information and microstructures.

SEM uses a cathode filament to produce high-energy primary electrons, the electron beam. Lenses focus the beam into a very small diameter, before interacting with the specimen. The beam diameter is affected by factors such as the aperture angle, cathode filament type, beam current, and the distance from the specimen.[14] Most of these factors need to be optimised in order to obtain focused images. To compensate for beam astigmatism caused by manufacturing processes a unit of coils called a stigmator to correct the electron beam in the X and Y directions.[14]

The electron beam interacts with the protons and electrons in a specimen. The interactions can be elastic where no energy is lost, or inelastic where energy is lost, depending on interaction of beam electrons with either the nucleus or electron cloud.[14] In an elastic interaction, electrons are called backscattered electrons (BSE). An inelastic interaction can cause electrons from the electron cloud to have sufficient energy to leave, called secondary electrons (SE). The detector can detect both types of electron scattering, however, the instrument must be tuned to whichever is of interest.[14] Difference between BSE and SE are two fold, the energy and the information they provide. SE give more depth information, whereas BSE gives more surface information. From the detected electron type, a surface image is then formed.

Imaging difficulties can arise from beam astigmatism but also from the specimen. Specimens are ideally electrical conductors, however non-conducting samples like synthetic polymers, can suffer from a build up of electrons on the surface of a specimen which can cause charging.[14] Charging can cause issues with scanning and

affect the image quality. Conducting specimens dissipate the charge of the electron beam whereas non-conducting samples cannot, but strategies such as sputter coating with a conducting metal such as gold or palladium can overcome charging. Sputter coating a sample may overcome charging, but there is a risk of altering the surface structure. This has been observed low density trimethylol propane triacrylate (TMPTA) foam.[15] It was observed that the result of the sputter coating increased the observed surface pore size by 1 order of magnitude.

However, using a different type of machine called an environmental SEM (ESEM or FESEM), with charge compensation attachment can resolve this problem. FESEM uses a low vacuum to reduce charging thus samples can be imaged without the need to coat.[14] A charge compensator blows ionized gas over the target area to negate the build up of charge.

Fractured polyHIPE monoliths were imaged using a Carl Ziess Ultra Plus Field Emission (FE)SEM or a Jeol JSM 5600 SEM. Most materials were uncoated to prevent increased wall thickness from metal deposition. However, this increased material charging, affecting image quality on occasion. This was overcome by application of low accelerating voltages between 2 and 5 kV and, when needed, a gas injection probe to blow nitrogen gas onto the sample to neutralise the charge. The Carl Ziess Ultra Field Plus FE-SEM had EDX capabilities.

3.7.1 Energy Dispersive X-ray (EDX) Microanalysis

The information from SEM images alone is often inadequate to fully characterise a low density porous polymer. Particularly, for example, it may be valuable to learn if there are various by-products from the polymer synthesis in the structure. EDX can provide this information as it detects characteristic X-ray radiation from an electron of an element. The X-rays are generated from inelastic interactions of the electron beam with the orbital electrons of the specimen.[14] The orbital electrons achieve an excited state, and the energy from the return to an equilibrium state can be

sufficiently high to release X-ray radiation. X-ray analysis was not used extensively in polyHIPE characterisation due to the low atomic weight of the polymer composition.

3.8 Critical Point Drier (CPD)

Conventional drying techniques such as drying in air or oven damages low density porous materials as capillary action and evaporation from the surface results in collapse of porous structure causing shrinkage. Shrinkage is a main contributor to the increase in density of porous materials. In this thesis, particularly fragile porous polyHIPEs and aerogels below 100 mg/cm $^{-3}$ were dried using CPD apparatus.

The solvent used for polymerisation is exchanged with another solvent that has a low critical point. The critical point of a solvent occurs at high temperature and pressure (Figure 3.8). Liquid CO_2 is heated inside a pressure vessel where CO_2 passes the liquid/gas phase boundary into the supercritical gas region. The supercritical fluid is slowly vented and as no surface tension is involved no shrinkage of the porous material occurs that would normally occur from capillary action.

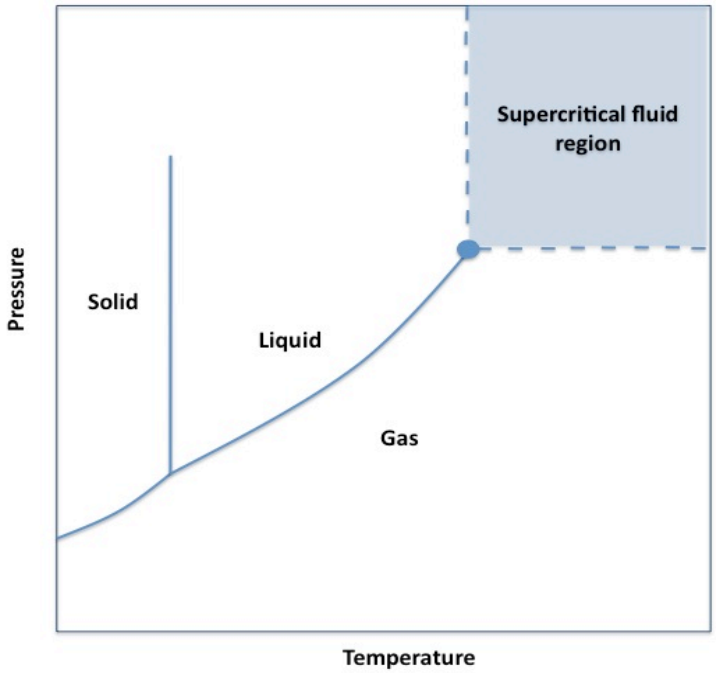

Figure 3.8. The pressure-temperature diagram of CO_2. Above 34°C (73 Atmospheres) CO_2 becomes a supercritical fluid. Image adapted from M. McHugh and V. Krukonis, in *Supercritical Fluid Extraction*, Butterworth-Heinemann, U.S.A, 1994, ch.1 pp. 11.

The supercritical fluid used with a Polaron® CPD was liquid CO_2. Porous materials were flushed with liquid CO_2 over a period of 24 hours to ensure full solvent exchange had occurred before being heating to 36°C, and held at this temperature for 30 to 60 minutes to ensure that the CO_2 was at the supercritical phase. Subsequently the supercritical CO_2 was vented over 24 hours to obtain dried foams with minimal shrinkage. It is standard practice to heat liquid CO_2 to 36°C, a few degrees above the critical point of CO_2, to ensure total conversion into a supercritical fluid throughout the entire material.

3.9 Differential Scanning Calorimetry (DSC)

DSC is a routine thermal analytical technique used to identify phase transitions of a material, by detecting the difference in heating between the material under investigation and the reference material.[17] Information or phase transitions is extremely important in polymer characterisation, particularly in designing new materials in order to optimise their properties for the application of interest.[18,19]

A DSC experiment consists of heating a reference sample, which has no phase transitions over a specified temperature range, and the material of interest in a constant, pre-programmed manner. The difference in heat is measured through attached thermocouples to the plates holding each sample. Additional thermocouples are used to measure the temperature of the furnace and heat-sensitive plate, with instrument software processing the data to produce a DSC trace (figure 3.9).

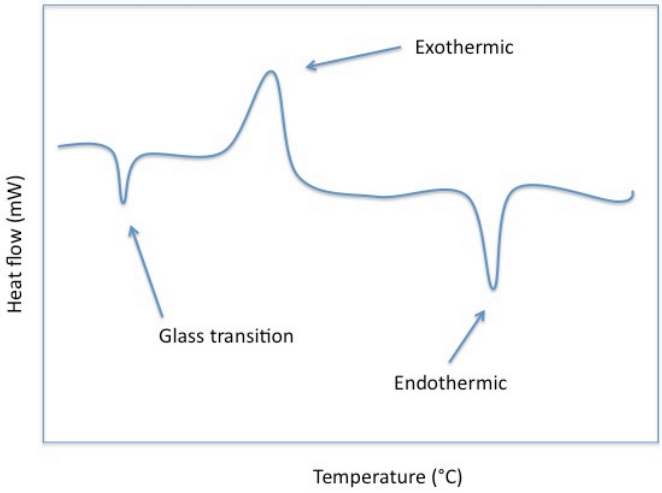

Figure 3.9. Schematic of a DSC plot. Image adapted from T. Hatekeyama and F. X. Quinn, in *Thermal Analysis; Fundamentals and Applications to Polymer Science*, John Wiley & Sons, Ltd, Chichester, 2000, ch. 1, pp. 6.

Phase transitions are either exothermic or endothermic and this change in temperature is detected by the heat sensitive plate.[17] Crystallisation transitions are endothermic whereas melts are exothermic, which are shown as troughs and peaks in the resulting plots. Issues can arise in data when the scanning rate is high resulting in significant differences in the temperature of the furnace and sample as they are both separately monitored by separate thermocouples.

Analysis was performed using a TA Instruments Q100 DSC. Temperature range used was 20°C to 250°C with a ramp rate of 10°C per minute.

3.10 Gel Permeation Chromatography (GPC)

GPC is an established and valuable polymer characterisation technique to measure the range of molecular weights of a polymer. The technique uses a column comprised of a pore-containing cross-linked resin to achieve separation of a solvated polymer. Molecular weights are calculated based upon the time they take to pass through the column and, in combination with light-scattering detectors, compared to a calibration curve of known molecular weights to obtain the molecular weights of the unknown material.[20,21] A range of known molecular weight samples are used for calibration, and the calibration is performed in a solvent in which the unknown polymer is soluble to ensure a consistent experiment is performed.

Briefly, a polydisperse material interacts with the cross-linked resin based upon the size of the polymeric chains. Small chains can penetrate the pores of the resin and so will take longer to pass through the column whereas larger chains that cannot access these pores and go through the column faster.[20,21] Thus separation of long and short chain molecules is achieved. A large number of samples are drawn off and the light-scattering detector measures the intensity of scattered light from each sample.[20] The results are then compared to the calibration curve for that time to obtain the molecular weight for each sample.

Analysis was performed by commercial analysis using a Micrometrics GPC machine, and the eluent was toluene.

3.11 Thermogravimetic Analysis (TGA)

Thermogravimetric analysis is a thermal analytical technique relevant to polymer characterisation. The technique monitors changes in the mass of a sample as a function of temperature or time.[17] TGA therefore can provide information on decomposition temperature and stability, making it complementary to information obtained by DSC (phase transitions do not change the overall mass) and other thermal analytical techniques.[17]

TGA uses a thermobalance to perform experiments. This refers to a number of components such as the furnace for heating, a microbalance to monitor weight and the temperature control unit containing instrument software. Samples are loaded onto a crucible (inside the furnance) and then heated via the temperature control unit. Experimental conditions such as heating rate and temperature rate are optimised. Software can record, then analyse the data.[17]

Experiments can be performed in different gas atmospheres, high pressure, and vacuum. The conditions applicable to this work are experiments performed in a gas atmosphere. Gases are categorised as non-interactive and interactive; non-interactive gases (helium, nitrogen etc) do not affect the sample, whereas interactive gases (oxygen in air) will change the sample in some way, such as combustion.[17] Using a non-interactive gas is ideal for standardising conditions before an interactive gas is used for further experiments.

Analysis was performed using a TA Instruments Q500 TGA. Temperatures used ranged from 0°C to 700°C with a ramp rate of 10°C per minute. Experiments were carried out under a nitrogen atmosphere.

3.12 Appendix

3.12.1 Model studies of poly(vinyldenefluoride) (PVDF) and polystyrene GPC standards TD-NMR Analysis

Model studies were performed using PVDF and polystyrene GPC standards to assess the capabilities of the newly arrived MQ20 TD-NMR apparatus. These experiments could also be of use to apply to low density polymers, which were a primary interest for this work.

3.12.1.1 Spin-lattice (T_1) Relaxation Analysis of PVDF

At 30% crystalline, PVDF is classified as a semi-crystalline polymer. At high magnetic field strengths it has been shown that probing T_1 and $T_{1\rho}$ relaxation can select specific regions in PVDF.[2,3] Specifically, this refers to the crystalline and amorphous phases, but also the end groups and reverse addition units have been selected by these experiments. In this case, the motional regimes are at MHz and kHz frequency for T_1, and $T_{1\rho}$ respectively. By measuring these parameters at varying temperatures, relaxation profiles can be obtained that reflect molecular motion. In addition, this approach may detect transitions such as the glass transition (Tg), which is further information to compare to other characterisation techniques. With comparison to data obtained at 300 MHz, analysis of PVDF would allow an assessment of the capabilities of the MQ20.

The magnetic field (B_0) and temperature (T) are two main parameters in the Curie law (equation 3.12) for calculation of net magnetization. Therefore a change in the B_0 field or temperature will result in a change in the net magnetisation. Application of a lower B_0 field may emphasise the temperature dependency of magnetisation, thus molecular motion, by comparison to varying temperatures at higher magnetic field strength.

$$M_0 = C\frac{B_0}{T} \qquad (3.12)$$

The T_1 relaxation profile of PVDF were recorded using the saturation recovery method between –50°C and +180°C (figure 3.10). The details on pulse lengths and tau (τ) times used are stated in section 3.2.1. The minimum in the graph is related to the correlation time (τ_C), which is about 30°C. At lower temperatures the motion is slow and as the temperature is increased, τ_C is passed and into the fast motion regime. The relaxation times was recorded at 60 different points ranging from 0.1 ms to 32 s, which was calculated by the instruments software, and analyzed using the equation 3.13 to give the spin-lattice relaxation time.

$$y = A_1 \cdot (1 - e^{(-x/t_1)}) + y_0 \qquad (3.13)$$

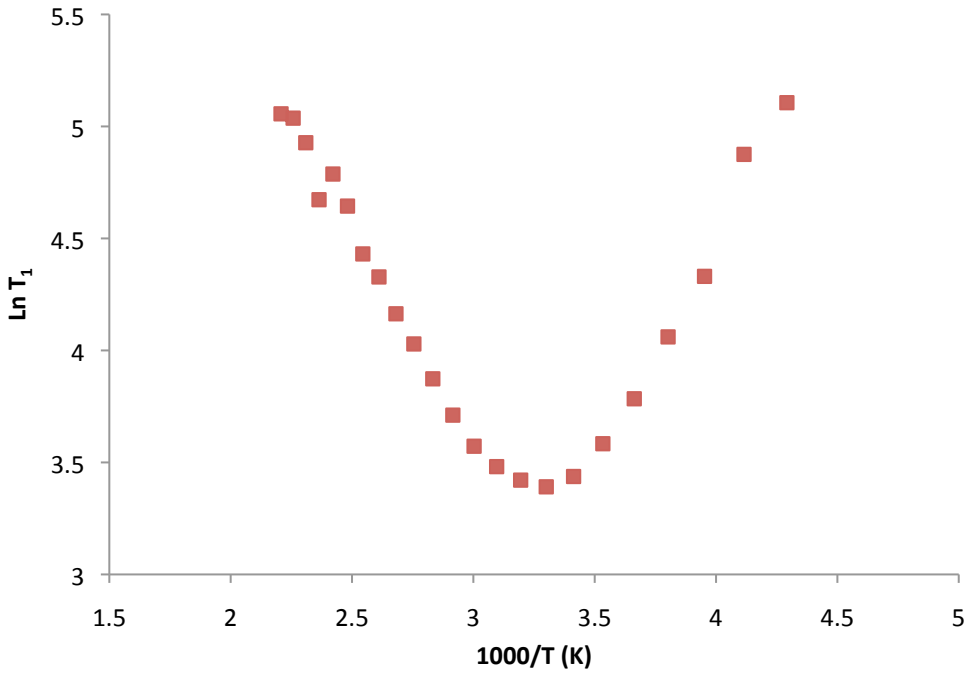

Figure 3.10. The T_1 relaxation profile of PVDF across –50°C to +180°C.

Although PVDF has two distinct domains, spin diffusion times of about 4 ms would be efficient on the timescale of the measurement, hence a bulk T_1 was reported.[4] Spin diffusion is the 'mixing' of spin states interacting with each other, which is mediated by dipolar coupling, resulting in an exchange of energy between each spin. This would complicate interpretation of multiple component fitted data as

justification of each component would become difficult. However, $T_{1\rho}$ relaxation times were fitted to two components in order to form a comparison to high-field data. The profile contains both the extreme narrowing limit past the T_1 minimum and the rigid motion beforehand, and application of this experiment to polystyrene may be informative.

3.11.1.2 Relaxation Under RF ($T_{1\rho}$) Analysis of PVDF

The values of $T_{1\rho}$ relaxation were obtained by analysis of the FID of each experiment using equation 3.14 or equation 3.15. For PVDF two components were chosen (equation 3.14), but all other data was fitted with one component (equation 3.15). Fitting two components to polystyrene and low density porous polymers was attempted, despite being entirely amorphous, but was not successful for a number of reasons. Specifically, there were two issues with the two component fit. Firstly, a two component fit produced large errors, often the magnitude as the measurements and so could not be considered reliable. Secondly, a two component fit of variable temperature relaxation plots revealed two exactly the same, albeit different time, functions suggesting that spin mixing occurred. If any crystalline behaviour existed a similar profile to PVDF (figure 3.10) was expected. Therefore a one component was used for polystyrene and low density porous polymers.

$$y = y_0 + A_1 e^{(-x/t_1)} + A_2 e^{(-x/t_2)} \quad (3.14)$$

$$y = y_0 + A e^{(-x/t)} \quad (3.15)$$

The $T_{1\rho}$ relaxation profile at variable temperature (figure 3.11) demonstrated the difference in the relaxation for the crystalline and the amorphous regions, which agrees with known $T_{1\rho}$ data.[2–4] The relaxation profile contains two large features; curves with minima that correspond to about –40°C and +110°C, which correspond to Tg and pre-melt transitions of PVDF respectively.[16] It can be seen in figure 3.11 there was some contribution from the crystalline region to the transition occurring at –40°C. This may suggest that the Tg, whilst an amorphous transition, affected the

overall relaxation of PVDF to give the impression that the crystalline region was involved in the Tg. The pre-melt transition at +110°C corresponded to the crystalline region only, however with the onset of the melt process at +170°C both regions exhibit a rapid increase in relaxation as the entire polymer motion rapidly increased due to melting.

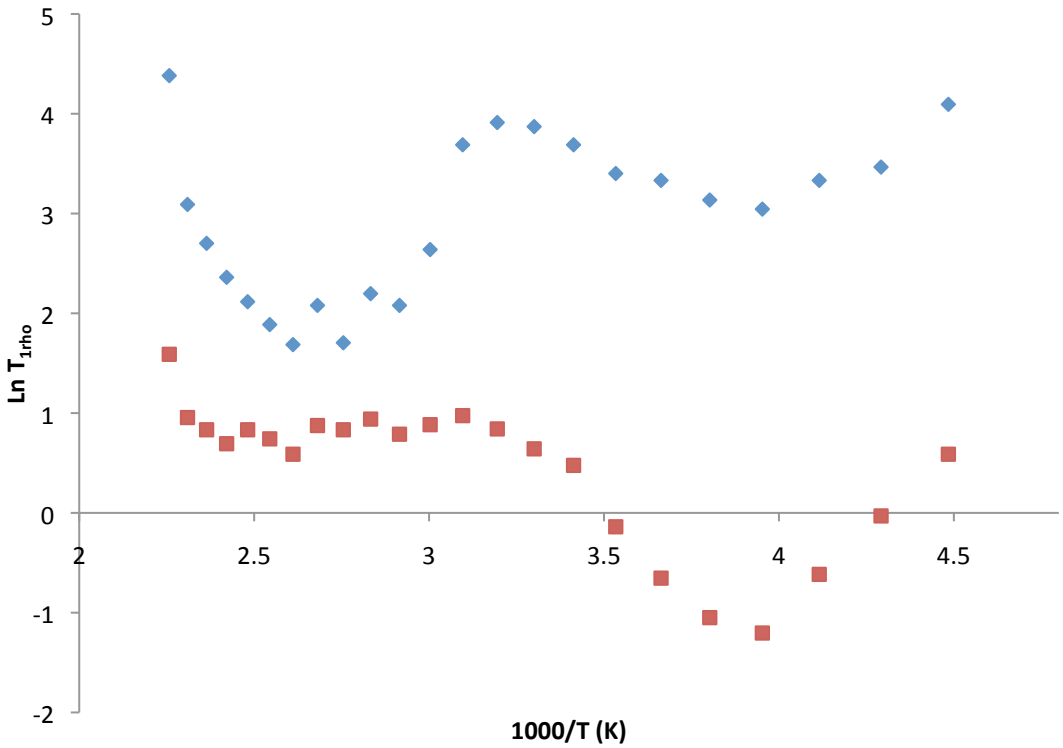

Figure 3.11. The $T_{1\rho}$ relaxation profile of PVDF across –50°C to +180°C, with amorphous (red) and crystalline (blue) regions.

In summary, relaxation studies of PVDF, a well-studied semi-crystalline polymer, indicated the suitability of TD-NMR as a polymer characterisation technique. Furthermore it validated the new apparatus that would form the basis of much analysis in this work. Use of variable temperature to probe relaxation generated relaxation profiles for both T_1 and $T_{1\rho}$ relaxation, delving deeper into the structure of PVDF. The two-component fit of the $T_{1\rho}$ relaxation profile highlighted regional specific transitions, in both crystalline and amorphous regions. Application to low density materials may also yield similar information.

3.12.2 TD-NMR Analysis of Polystyrene GPC Standards

To complete the MQ20 validation process, T_1 and $T_{1\rho}$ relaxation experiments were performed on polystyrene GPC standards (with known molecular weights). Three different molecular weights were chosen as molecular motion, thus relaxation, would behave differently, which would give an insight into relaxation behaviour as a function of molecular weight. The same set-up and experimental parameters used for PVDF were applied to polystyrene, with the exception of a single component for $T_{1\rho}$.

Table 3.15. Details and NMR relaxation times (at 0.47 T) for polystyrene GPC standards.

M_w	M_n	$Đ_M$	T_1 (ms)	$T_{1\rho}$ (ms)
1920	1770	1.08	308.3±5.1	3.25±0.07
96000	92000	1.04	585.3±9.9	2.95±0.10
524000	502000	1.04	768.8±19.3	2.80±0.08

Varied temperature relaxation experiments on the 524000 GPC standard was performed. This material was chosen arbitrarily. Figure 3.12 and 3.13 show the T_1 and $T_{1\rho}$ relaxation profiles respectively. The relaxation profiles were transformed using the natural log, due to the relationship with the equations for relaxation stated in chapter 2. Transforming the data allowed assessment of the molecular motion in the same manner as PVDF. One particularly interesting feature in the T_1 relaxation profile was the point at 373K (2.7 1000/T), which corresponds to the Tg of polystyrene. Unlike PVDF, this transition appears to be observed by T_1 relaxation rather than $T_{1\rho}$ relaxation. Polystyrene is considered a rigid polymer therefore it was expected to exhibit rigid relaxation behavior, however the relaxation profile suggests that the polymer is in a faster motion regime beyond the T_1 minimum (extreme narrowing limit). It was expected that the varied temperature experiments would produce a profile similar to PVDF. Yet this more labile behavior of styrene was welcomed as experiments involving alterative cross-linking percentages would be observable by this technique, as increased rigidity would affect molecular motion.

Many polyHIPEs are based on polystyrene, thus it would be expected that those polyHIPEs would behave in a similar manner to the polystyrene standards here. This suggested that TD-NMR could be useful in characterisation for polymers in general as well as specific applications such as low density porous polymers.

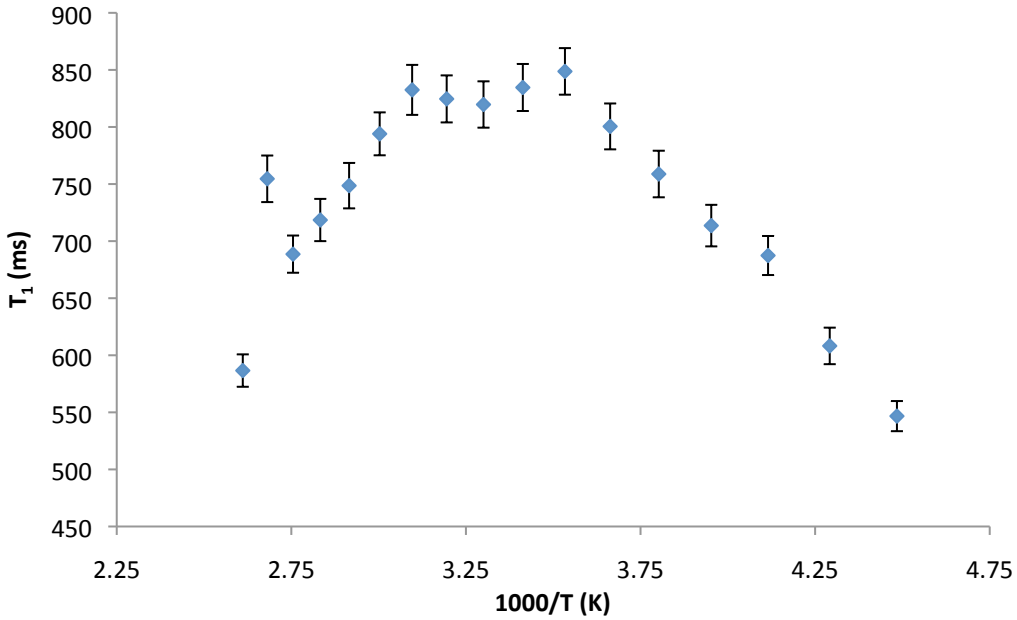

Figure 3.12. The T_1 relaxation profile of polystyrene GPC standard across –50°C to +180°C.

$T_{1\rho}$ relaxation times of polystyrene (figures 3.13) also revealed molecular motion dependency with temperature. This was a result of less efficient polarisation of the spin-lock caused by increased molecular motion as the temperature increased. At lower temperature of this non-crosslinked polymer the structure was considerably easier to spin-lock, possibly due to material density, whereas higher temperatures resulted in increased chain motion increased amorphous-like behavior. Motion was increased significantly with increasing temperatures a dependence on temperature was indicated as a near linear relationship was observed. Figure 3.13 also suggested that polystyrene was in a more rigid motion regime at this frequency of motion compared to T_1 relaxation. Polystyrene in the extreme narrowing limit seemed unlikely given that the Tg of polystyrene is 100°C. However, given the molecular chain length of this sample (524,000), it was assumed that the chains would entangle more than lower molecular chain length polystyrene thus by using NMR the material appeared to be more rigid. Furthermore by combining both sets of relaxation data

another view of polystyrene can be obtained; long, and entangled polymer chains appearing packed somewhat efficiently to allow an efficient spin-lock, yet allowing freedom of aromatic rings to tumble.

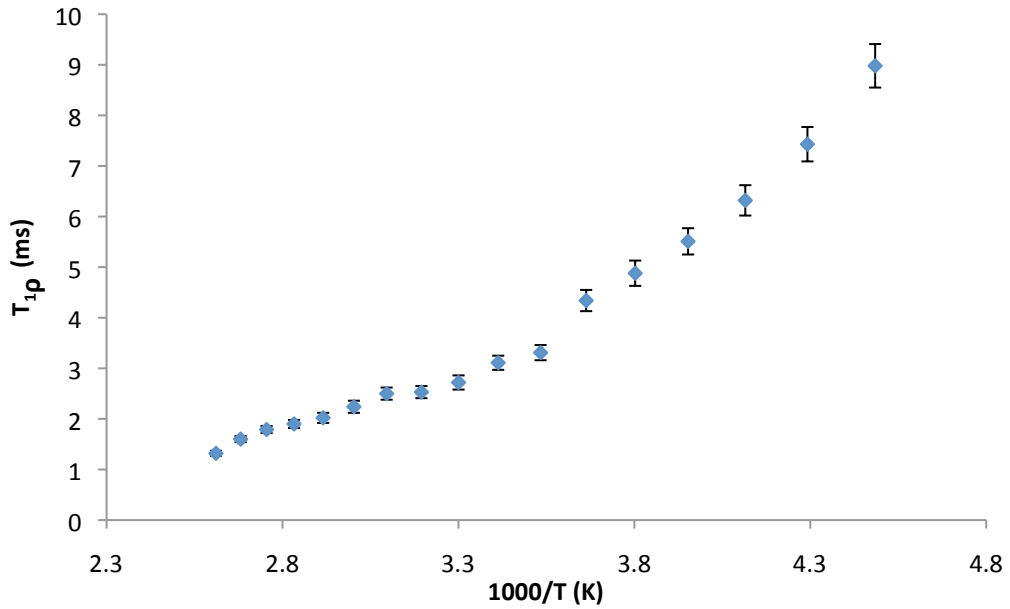

Figure 3.13. The $T_{1\rho}$ relaxation profile of polystyrene across –50°C to +180°C.

TD-NMR relaxation experiments can measure NMR relaxation of polymers at different frequencies of molecular motion. NMR relaxation times of polystyrene GPC standards indicated that faster than expected molecular motion existed despite high molecular weight. The fast motion regime of T_1 was expected to be more sensitive to changes in material cross-linking, which corresponds to motions such as hanging/end group rotations of a polymer. $T_{1\rho}$ relaxation data could be useful in detecting macromolecular chain arrangement of a polymer, which may be reflective of the synthesis conditions to form a structural arrangement that would allow an efficient spin-lock. Spin-lock relaxation observes slow chain rotations of a polymer, thus when combined with T_1 relaxation data, a better understanding of a polymer could be formed. This could allow for specific issues to be highlighted that may otherwise be left unresolved. These preliminary studies indicated that combining data from both relaxation experiments could allow greater understanding of a polymer, in this case PVDF and polystyrene GPC standards. This could greatly aid with characterisation of low density polymeric materials for high energy laser experiments.

3.13 References

1 J. M. Williams, *Water-in-Oil Emulsions and Toroidal microstructures*, Springfield, 1989.

2 P. Wormald, D. C. Apperley, F. Beaume, and R. K. Harris, *Polymer*, 2003, **44**, 643–651.

3 P. Wormald, B. Ameduri, R. K. Harris, and P. Hazendonk, *Solid state nuclear magnetic resonance*, 2006, **30**, 114–23.

4 S. Ando, R. K. Harris, and S. A. Reinsberg, *Magnetic Resonance in Chemistry*, 2002, **40**, 97–106.

5 R. S. Macomber, *A Complete Introduction to Modern NMR Spectroscopy*, John Wliey & Sons, Inc., Canada, 1998.

6 M. J. Duer, *Introduction to Solid-State NMR Spectroscopy*, Blackwell Publishing Ltd, Oxford, 1st edn., 2004.

7 S. Matsuoka, *Relaxation Phenomena in Polymers*, Hanser, New York, 1992.

8 K. P. Menard, *Dynamic Mechanical Analysis*, CRC Press, Boca Raton, 2nd edn., 2008.

9 I. M. Ward, *Machanical Properties of Solid Polymers*, John Wliey & Sons, Inc., 1971.

10 D. W. Van Krevelen, *Properties of Polymers*, Elsevier B.V., Amsterdam, 1st edn., 1997.

11 V. J. McBrierty and K. J. Packer, *Nuclear Magnetic Resonance in Solid Polymers*, Cambridge University Press, Cambridge, 1st edn., 1993.

12 P. J. Hore, *Nuclear Magnetic Resonance*, Oxford University Press, Inc., New York, 1995.

13 P. A. Webb and C. Orr, *Analytical Methods in Fine Particle Technology*, Micromeritic Instrument Corp., 1st edn., 1997.

14 G. H. Michler, R. Godehardt, and V. Seydewitz, *Electron Microscopy of Polymers*, Springer Berlin Heidelberg, Leipzig, 2008.

15 D. Faith, C. J. Horsfield, and W. Nazarov, *Journal of Materials Science*, 2006, **41**, 3973–3977.

16 G. Teyssedre, A. Bernes, and C. Lacabanne, *Journal of Polymer Science Part B: Polymer Physics*, 1993, **31**, 2027–2034.

17 T. Hatakeyama and F. X. Quinn, *Thermal Analysis; Fundamentals and Applications of Polymer Science*, John Wliey & Sons, Ltd., Chichester, 2nd edn., 2000.

18 A. Mousa and J. Karger-Kocsis, *Macromolecular Materials and Engineering*, 2001, **286**, 260–266.

19 M. Tsuji, T. Inoue, and O. Shibata, *Colloids and surfaces. B, Biointerfaces*, 2008, **61**, 61–5.

20 J. V Dawkins and E. Meehan, in *Characterization and Analysis of Polymers*, ed. A. Seidel, John Wliey & Sons, Inc., Hoboken, 2008, pp. 230–252.

21 P. C. Painter and M. M. Coleman, *Fundamentals of Polymer Science*, Technomic Publishing Company, Inc., Lancaster, 1st edn., 1994.

4. PolyHIPEs from Styrene-co-Divinyl Benzene and Derivatives; Preparation, Characterisation, and Investigations using TD-NMR

4.1 Introduction

Styrene-based polyHIPEs have been of interest to applications such plasma physics for many years due to a combination of unique properties such as small pore-size (~1 μm), high modulus and low Z elemental composition. However, in recent years the demand from plasma physics experimentalists for polyHIPEs with empirical formula of $C_1H_{n>1}$, has increased as this generates greater opacity in plasma. This means that less X-ray noise from the foam species contained in the target can interfere with interpretation of the results from the laser experiment. Extensive research has been carried out on HIPEs and polyHIPEs in the last two decades,[1–7] however this research does not address the specific problems and requirements of plasma physics experiments. One aim of this work was to synthesise new polyHIPEs with increased $C_1H_{n>1}$ ratio, whilst retaining pore size of about 1 μm and high modulus at very low density. High modulus at low densities is important in order to be able to machine materials into shapes that can be used in laser experiments. Intrinsically, lower density materials are weaker than their higher density equivalents.[8,9] Researchers have developed an understanding of the synthetic factors that affect polyHIPE physical properties, offering insight into solving this problem.[10,2,11,12] However, there has not been a rigorous investigation of the physical structure as a result of these synthetic factors, particularly by TD-NMR relaxation experiments. TD-NMR measures nuclear spin relaxation times, which can focus on different frequencies of motion of a material, allowing selective observation within a polymer. It was postulated that this technique could reveal more information of a polyHIPE, providing a deeper understanding of the material, which could be relevant to future developments of materials for high energy laser experiments.

This chapter describes the synthesis of styrene-co-divinyl benzene and t-butyl styrene-co-divinyl benzene polyHIPEs. In addition, an analysis of polyHIPE physical structure with an emphasis on TD-NMR is provided to gain an understanding of the

physical and chemical influences on polyHIPE structure and properties. One of the desired properties of polyHIPE to plasma physics experiments is structural modulus. To assess the viability of TD-NMR in determination of this, Young's modulus data and mercury porosimetry were used to compare with TD-NMR.

4.1.1 Microscale Inhomogeneity of PolyHIPEs

Despite the production of acceptable quality polyHIPE in recent years for laser targets, results from plasma physics experiments were not in agreement with predicted theoretical modeling of laser experiments. These models were based on the assumption that polyHIPEs were completely homogeneous. This prompted X-ray radiography analysis of polyHIPEs at AWE, which revealed significant areas of inhomogeneity in the samples (figure 4.1). Appendix 4.7.6 contains additional information. This issue was relevant to this work as application of TD-NMR to investigate structure may provide an insight into polyHIPE inhomogeneity.

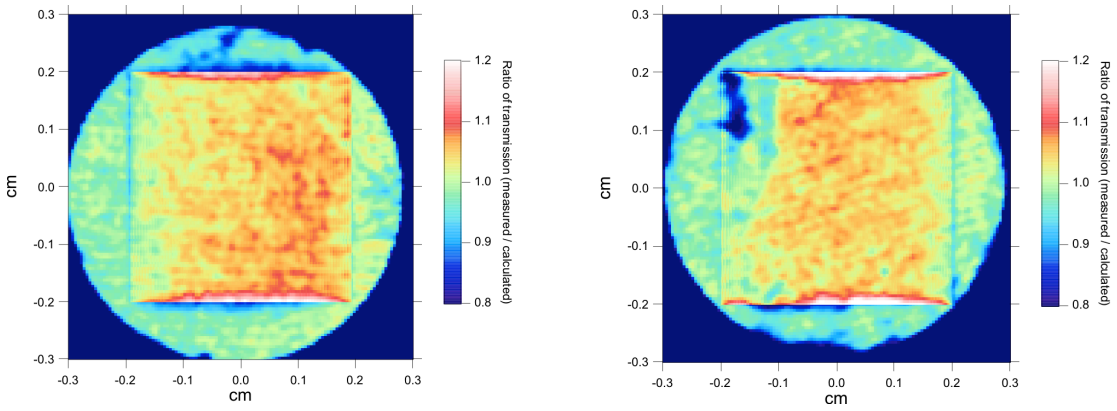

Figure 4.1. Two X-ray contrast images of polyHIPE displaying inconsistent density throughout the monolith. AWE Internal Report, 2013.

The scale of the HIPE monolith and size of laser targets are important factors. HIPE monoliths synthesised in this work were typically 1.5 cm diameter and 6 cm in length. Producing a laser target to micrometer dimensions from this comparatively large volume means that there is a possibility of using a section of the polyHIPE that originates from a region of higher or lower density. Plasma physics experiments require accurate information on material density and composition to ensure

experimental modeling is correct, therefore fabrication of a laser target from an inhomogeneous sample could result in a significant experimental validation problem.

4.2 Materials and Reagents

Reagents used were styrene, deuterated styrene (S-d_8), divinyl benzene 80 (DVB) (technical grade), para-divinyl benzene (85%, 10% meta-divinyl benzene), deionised water, deuterated water (D_2O), sorbitan monooleate (Span® 80), sorbitan monolaurate (Span® 20), azobisisobutyronitrile (AIBN), potassium persulfate, dodecylbenzensulfonic acid (DDBSS) sodium salt, cetyltrimethylammonium bromide (CTAB).

All chemicals were used as received except for the monomers, which had the inhibitor extracted before use.

4.3 Synthesis of PolyHIPEs

All polyHIPEs were prepared using the double syringe method, as described in chapter 3, section 3.1. Details of formulations are also given in chapter 3. The double syringe method was developed at Los Alamos National Laboratory, USA, to reduce the amount of air incorporated into the HIPE, which could have an impact on the quality of the polyHIPE. Pore sizes within polyHIPEs larger than the average pore diameter are unacceptable in plasma physics experiments, and classed as an inhomogeneity. The double syringe method was also used for consistency with AWE polyHIPE production.

HIPEs were prepared in 10 cm^{-3} gas tight glass syringes (Hamilton) then transferred to 10 cm^{-3} plastic syringes, sealed to stop evaporation and polymerised in an oven at 60°C for 72 hours. The aqueous phase contained 5% by weight potassium persulfate initiator. It has been reported that 10% initiator reduces pore size in S/DVB polyHIPEs,[2] however solubility of 10% was an issue and in fact 5% solution seemed to be the solubility limit for potassium persulfate at 20°C. The oil phase

consisted of the monomers and surfactant, which were mixed homogeneously. 28% surfactant concentration was chosen based on previous research, resulting in small pore size without destabilising HIPE.[2] Increased concentrations can reduce interfacial tension of the emulsion, which can produce an unconnected pore structure.

PolyHIPE discs for DMA analysis were prepared by carefully piping HIPE into a cylindrical steel mould, with parallel top and bottom surfaces. Moulds were sealed, and placed into a 60°C oven to polymerise. The polyHIPE discs were removed from the moulds, then washed with water and then methanol and dried in a 30°C oven. 4 discs were synthesised per sample measured to ensure reproducibility of DMA anaylsis.

DVB 80 (DVB) consists of para- and meta-DVB at 80% of the reagent, and para- and meta-ethyl styrene the other 20%. Therefore 10% DVB 80 content is actually 8% DVB. For consistency with literature, DVB was quoted as the amount used from the bottle rather than the amount of DVB present. Synthesis of para-DVB and experiments performed using these polyHIPEs are discussed later in the chapter.

4.4. Instrumentation and Characterisation

Techniques used to characterise polyHIPEs were SEM, mercury porosimetry, elemental analysis, SSNMR, TD-NMR, DSC, GPC, TGA and DMA. Instrument details and specific experiments are given in chapter 3. Additional raw data is contained in the appendix of this chapter.

Densities of polyHIPEs were obtained by mass and volumetric measurements of cylindrical shaped samples. PolyHIPE length and diameters (thus radius and volume) were obtained using a calibrated calipers gauge with an electronic display. The weights of samples were measured using a five figure balance.

4.5 Results and Discussion

4.5.1 Microstructure Investigations of Styrene-co-Divinyl Benzene PolyHIPEs

It was shown that S-co-DVB polyHIPE elastic (Youngs modulus) varied as the percentage of DVB increases, with a peak between 20% and 30%.[2] This gave an insight into the ideal cross-linking percentages for S-co-DVB polyHIPEs to form materials with highest modulus. The reasons for polyHIPE modulus at this level of cross-linking have not been reported. A series of S-co-DVB polyHIPEs discs with increasing DVB content in 10% steps by weight of the monomer were synthesised and characterised. Discs were characterised by SEM, mercury porosimetry, SSNMR, DMA and TD-NMR. Details on synthesis and characterisation are given in the appendix.

SEM images of a S-co-DVB polyHIPE show typical polyHIPE pore architechture, with pore sizes in the region of 1-3 µm, much lower than often reported for polyHIPEs (figure 4.2). This could be due to the syringe method producing higher shear force than other emulsification methods such as conventional overhead stirring. High initiator concentration increased the rate of polymerization, producing smaller pores before emulsion coarsening mechanisms coalesced water droplets significantly. Mercury porosimetry confirmed the pore window size, and were measured below 1 µm on average (table 4.1). The low values obtained from porosimetry were a result of high pressures used for intrusion through the windows to access the entire structure. This allowed access of smaller pores, which were not clearly visible by SEM. Image analysis software could calculate an average pore diameter, however several images combined together would still not be representative of the entire bulk structure thus approximate pore values are used instead. Porosity below 90% of styrene homopolymer indicated shrinkage of the pore structure, however when cross-linked with DVB the porosity increased. This demonstrated the importance of high cross-link density in low density polyHIPEs. Furthermore, the pore size decreased on addition of DVB content, correlating with previously observations of S-co-DVB polyHIPEs.[2,13]

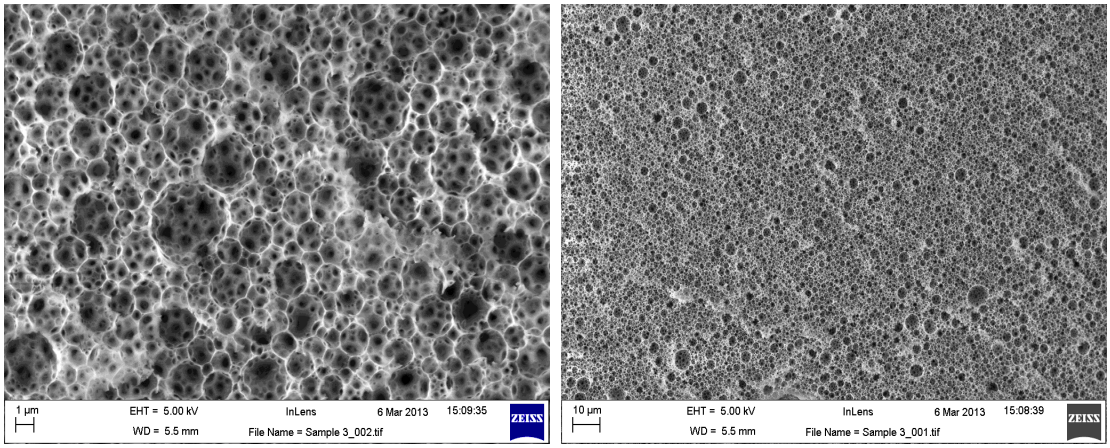

Figure 4.2. SEM images of S-co-DVB (70%:30%) polyHIPE. Scale bars are 1 µm (left) and 10 µm (right).

Table 4.1. Mercury porosimetry data for S-co-DVB polyHIPEs.

PolyHIPE system (S:DVB)	**Average window diameter (µm)**	**Porosity (%)**
S (100)	0.34	86.4
S-co-DVB (70:30)	0.20	90.1
S-co-DVB (30:70)	0.16	89.6
DVB (100)	0.17	91.2

The ^{13}C SSNMR spectra of S-co-DVB polyHIPEs were consistent with literature.[14] A spectrum (figure 4.3) of overlaid ^{1}H-^{13}C CPMAS SSNMR spectra of S-co-DVB benzene polyHIPEs demonstrated the effect DVB had on the structure. The increase in line-width of the vinyl group peak (~40 ppm) suggested that this region was significantly more anisotropic than the aromatic shifts, which remained fairly constant. Cross-linking would produce a rigid structure resulting in many different orientations of these groups, increasing chemical shift anisotropy (CSA), as well as increased dipolar interactions due to polymer chains being closer together. Although MAS reduces or eliminates these interactions, the broadening in the spectra was evident that DVB had a significant effect on polyHIPE structure. It was thought that cross-linking the polymer backbones with DVB would affected the mobility of the aromatic rings

resulting in the whole structure to become more rigid. This would have the effect of increased CSA and dipolar coupling of this region would be observable by SSNMR. To test this postulation, a S-co-DVB polyHIPE was synthesised with deuterated styrene (S-d_8) and deuterium oxide (D_2O) along with DVB, and the ^{1}H-^{13}C CPMAS spectrum obtained (figure 4.4). Using deutrated styrene revealed that aromatic region was particularly broad at the base of the peak suggesting that strong dipolar interactions were created by DVB adding into the polymer. The copolymerisation with DVB would have resulted in a more rigid structure, therefore less molecular motion allowing increased dipolar interaction.

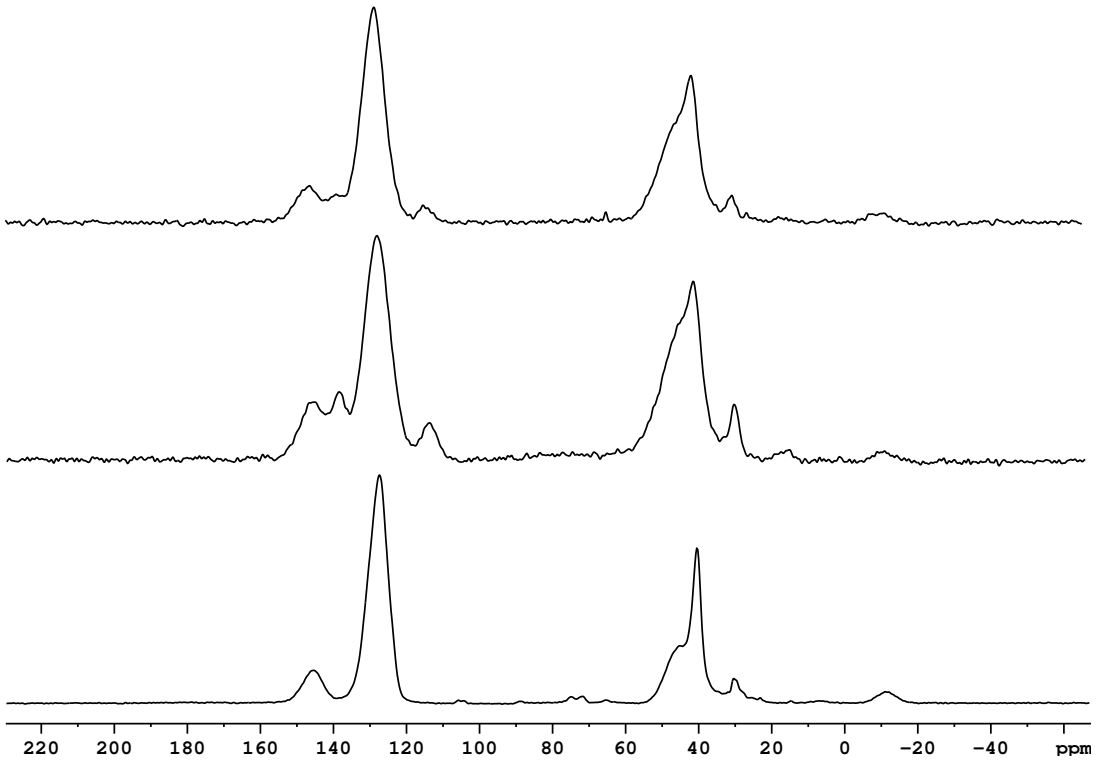

Figure 4.3. ^{1}H-^{13}C CPMAS (14 kHz) SSNMR spectra of S-co-DVB polyHIPEs. 100% DVB (top), 50%:50% S:DVB (middle) and 100% styrene (bottom).

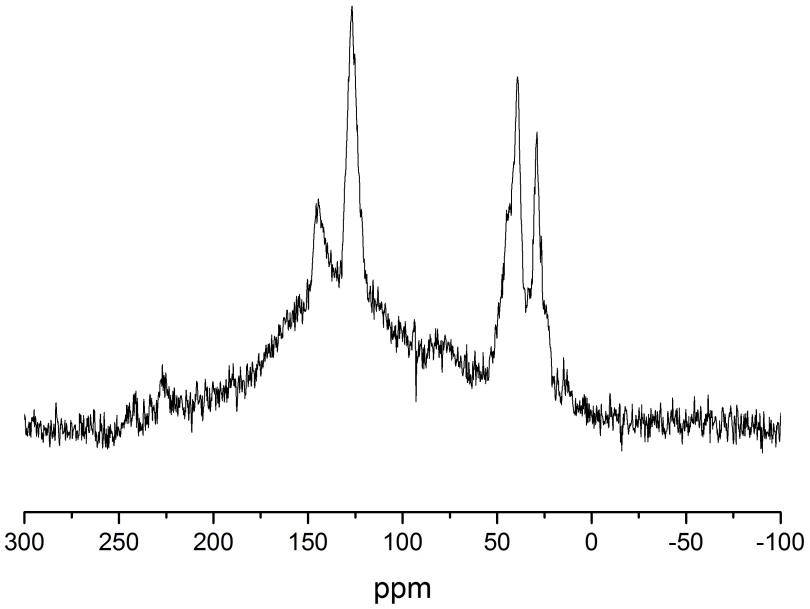

Figure 4.4. ^{1}H-^{13}C CPMAS (15 kHz) SSNMR spectrum of S-d_8-co-DVB polyHIPE.

DMA analysis yielded Young's modulus data of the polyHIPEs (figure 4.5) and these follow a similar trend to literature.[2] The largest modulus was at 10% and 20% DVB content with values of 59.2 and 63.5 MPa respectively. However, variations existed within some samples, indicated by the large error bars. Large density variations of discs within each sample set were ruled out as the reason of this because densities of all discs were taken before DMA analysis were measured to be ~125±7.5 mg/cm $^{-3}$ average disc density for the entire sample set. In addition, literature suggests that larger density variations are required for such a large variation in modulus.[15] Therefore it was more likely that variation originated from the molding process of the discs. Addition of HIPEs into the steel moulds could have incorporated air into the discs, resulting in an inhomogeneous structure, which would have affected the consistency of the Young's modulus measurements. 100% styrene discs were not obtained due to the significant shrinkage that they exhibited on washing and drying with measured densities consistently above 250 mg/cm $^{-3}$. Increased mass would result in higher modulus,[8] therefore discs of styrene were not used. Another feature of the modulus results that correlated with literature[8] was the averaging of the modulus results from 50% to 100% DVB content.

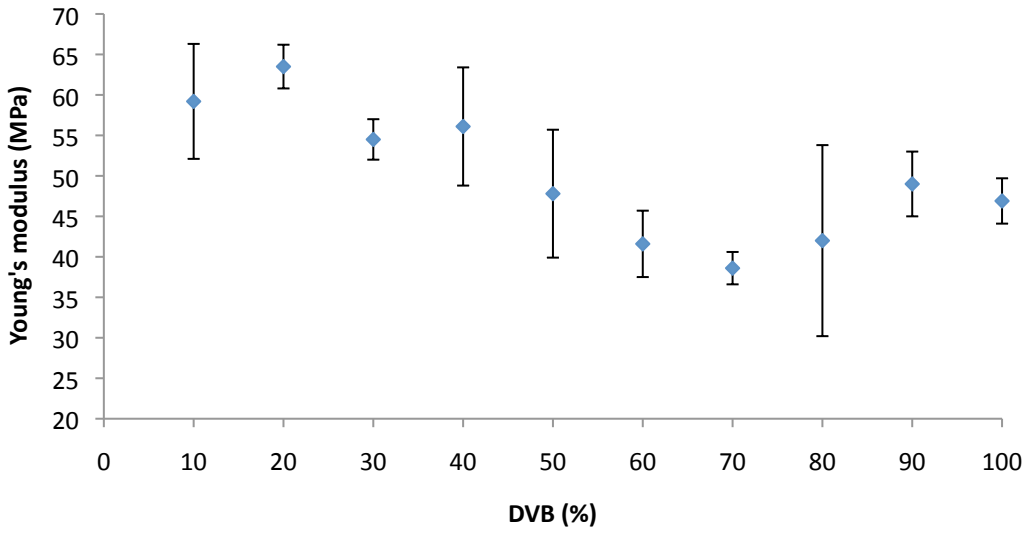

Figure 4.5. Young's modulus data for varied cross-linked S-co-DVB polyHIPEs.

Young's moduli of 59.2 and 63.5 MPa are some of the highest to be reported for S-co-DVB polyHIPEs at these densities (~130 mg/cm^{-3}) and porosities (~90%). Furthermore, polyHIPEs were synthesised using free radical polymerisation rather than a controlled method of polymerization, which has been shown to increase the modulus (45 MPa for S-co-DVB polyHIPE at 130 mg/cm^{-3}, 88% porosity and ~30% DVB content).[16] It was postulated here that smaller pore size meant that the stress that could be sustained by the pore structure was increased.[8] A recent study revealed the dependence of pore size on Young's modulus, but significantly lower than the Young's modulus results here.[15] The pore stress can be described by equation 4.1, where σ_{el}^{*} is the collapse stress, n^2 is a constant which describes the degree of constraint at the end of the wall length, E_s is Young's modulus of the pore wall, I is the second moment of area of the pore wall, and l^4 is the length of the pore walls (3-D pore);

$$\sigma_{el}^{*} = n^2 \pi^2 \frac{E_s I}{l^4} \qquad (4.1)$$

Small pore size and high modulus are desirable properties for laser targets, thus decreasing pore size to increase the modulus was a suitable route to increase polyHIPE modulus. Other applications may require larger pore sizes yet retain a high

modulus thus increasing wall thickness, or wall reinforcement to achieve higher modulus is more appropriate in those cases. High modulus at this density gave confidence that very low density polyHIPEs could be achieved using the methods described here. These polyHIPEs are likely to retain some modulus at low density, which would be an improvement to polyHIPEs currently used for laser targets.

Young's modulus results indicated that 10% to 20% DVB content was ideal to form polyHIPEs with the highest modulus. However, this did not elucidate the structure and a further investigation of the structure was performed using ^{1}H TD-NMR T_1 saturation recovery and $T_{1\rho}$ experiments. It was still unknown why these cross-linking percentages produced high modulus structures. T_1 relaxation measured fast motions (MHz) such as small and hanging and end group rotations, and $T_{1\rho}$ measured slower motions (kHz) such as large polymer chain rotation based upon the structural arrangement of the spins, thus polymer chains and therefore was a measure of order/disorder of structure with respect to NMR despite being an amorphous material. Figure 4.6 contains the T_1 results and figure 4.7 contains the $T_{1\rho}$ results of varied cross-linked S-co-DVB polyHIPEs.

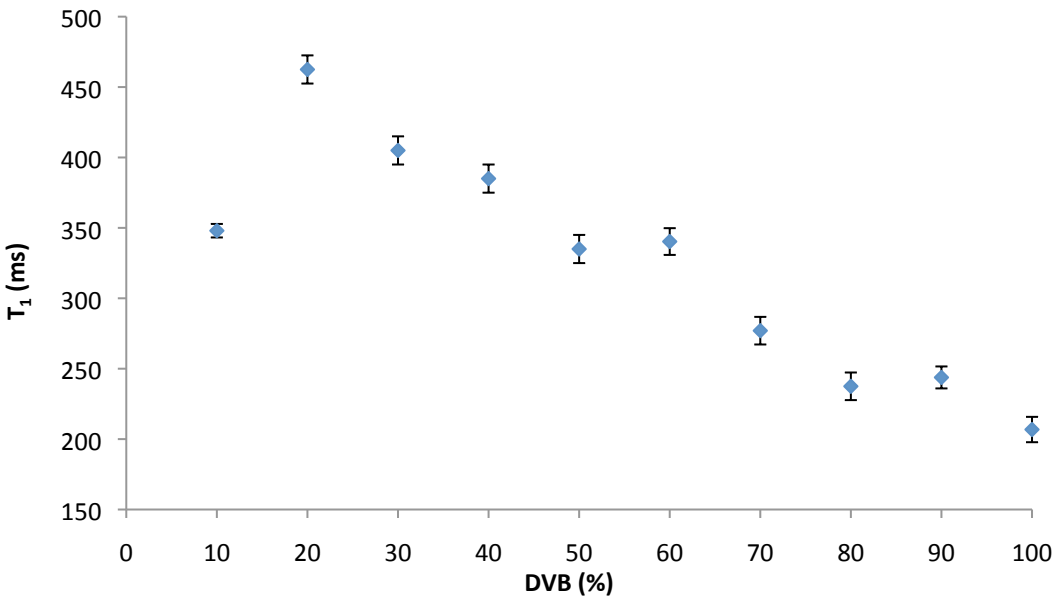

Figure 4.6. T_1 saturation recovery times of varied cross-linked S-co-DVB polyHIPEs. 100% styrene was omitted from the diagram due to the large increase in density.

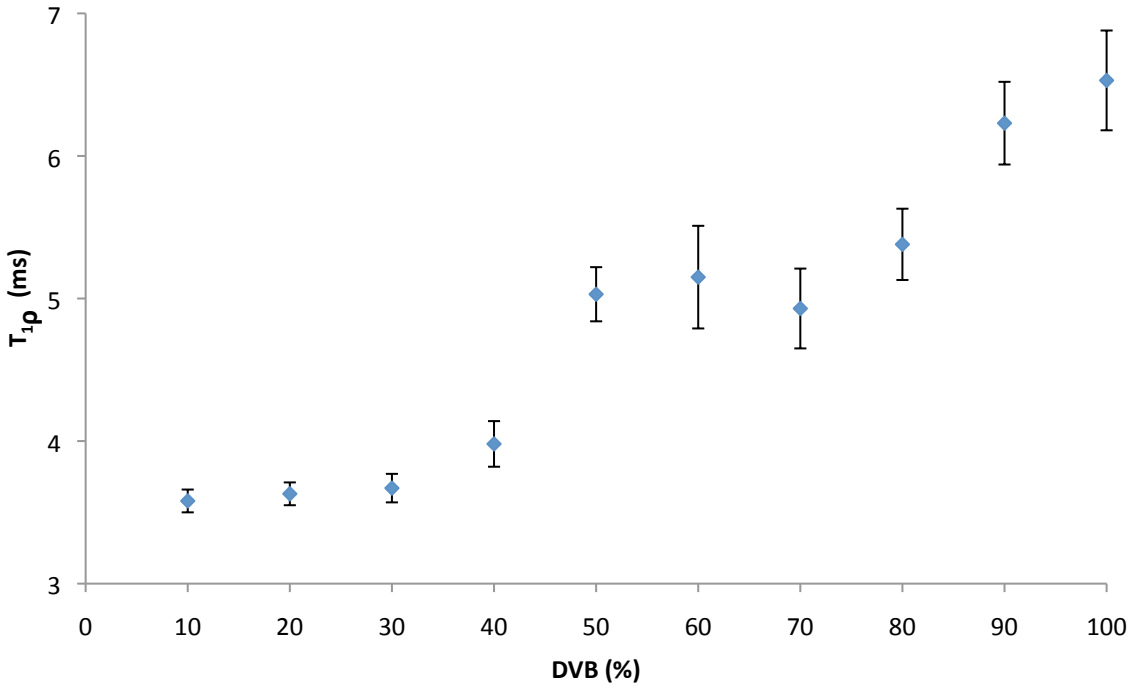

Figure 4.7. $T_{1\rho}$ relaxation times of varied cross-linked S-co-DVB polyHIPEs.

The trend in figure 4.6 shows that 20% DVB content had the longest relaxation time within the set of varied molar ratio S-co-DVB polyHIPEs. Thus, PolyHIPEs with unrestricted rotation of small and hanging group would be expected to relax faster than the polyHIPEs with a more rigid structure due to the dependency of relaxation on molecular motion.[17,18]

Therefore, long T_1 relaxation time at 20% DVB content indicated that this polyHIPE had the most rigid structure by comparison to the rest of the series (figure 4.6), suggesting it could be highly cross-linked. In other words, efficient cross-linking of styrene and DVB restricted motion of the small and hanging groups, preventing efficient relaxation resulting in longer relaxation times. 100% DVB polyHIPE relaxed fastest indicating that the structure was not rigid. This was unexpected as a bifunctional monomer would create a cross-linked network with little motion of the small and hanging groups. This suggested that polyHIPEs made with 100% DVB monomer consisted of many free rotating groups, which could arise for reasons such as significant branching of chains.

However, $T_{1\rho}$ relaxation times were a measure of spin efficiency based on the arrangement of the macromolecular structure of polyHIPEs by probing motions in the frequency order of kHz (large chain rotations), giving more information about the macromolecular structure. Figure 4.7 showed that when DVB content was increased, the structural order within the polyHIPE was increased with constant density. This allowed more efficient polarisation of spins, resulting in longer dephasing times (longer $T_{1\rho}$ time). This behaviour was expected as DVB is a bifunctional monomer, cross-linking large polymer chains, which restricted their motion, creating a rigid polymer chain structure.

Thus for 100% DVB, with consideration of T_1 relaxation data, a model of the structure could be formed that was based on this data correlated with the 'micro-gel' structure that has been suggested previously for free-radical polymerised polyHIPEs.[16] Furthermore, taking SSNMR observations, the freedom of motion suggested that small group motions arose from aromatic ring motions. Cross-linking of polymer back-bones resulted in an increase in dipolar interactions and CSA. It was postulated that rigid cross-linked clusters of DVB polyHIPE were formed on polymerisation, interconnected by long polymer chains (figure 4.8). This arrangement would provide a larger area by which small and end groups to freely rotate at the edges of the clusters, resulting in fast T_1 relaxation times. In addition, presence of rigid cross-linked clusters would explain increasing long $T_{1\rho}$ relaxation times. Clusters of cross-linked DVB would have a rigid polymer back-bone, characterised by long $T_{1\rho}$ times, but many clusters would allow freedom of aromatic rings to relax, characterised by short T_1 times.

Furthermore, this model could explain the low modulus of 100% DVB polyHIPE compared to other materials in the varied cross-linked S-co-DVB polyHIPE series. An inhomogeneous structure consisting of clustered material provided no improvement to modulus compared to polyHIPEs only containing 10% to 20% DVB content, despite decreasing pore size, which would be expected to increase the modulus. Thus it was suggested that polyHIPE structures containing 10% to 20% DVB are significantly

more homogenous, resulting in a higher modulus. A more homogeneous structure, with evenly distributed cross-links are in agreement with TD-NMR observations. Firstly, T_1 relaxation times were longer than 100% DVB indicated that aromatic rings and hanging chains had less motion to relax efficiently, as cross-links were evenly distributed. Secondly, lack of rigid clusters as cross-links were evenly distributed suggesting the structure had sufficient motion to prevent efficient spin polarisation meaning $T_{1\rho}$ times were shorter rather than tight rigid clusters.

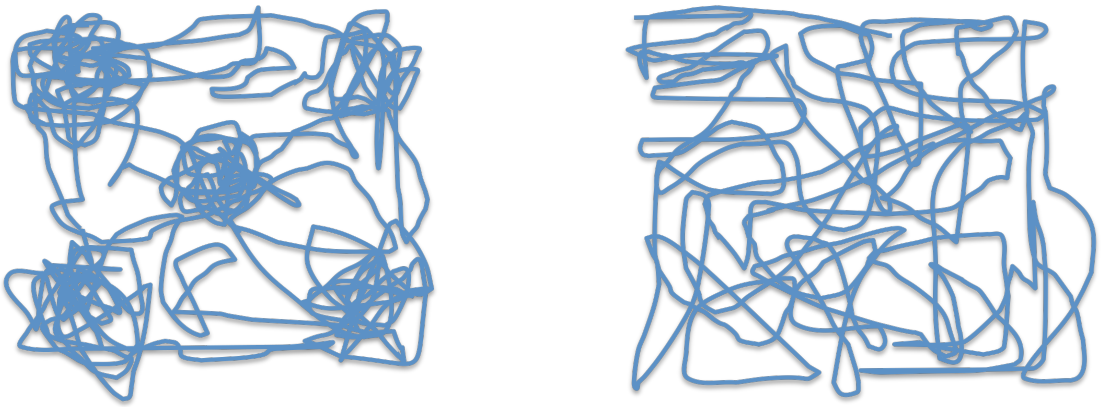

Figure 4.8. Structural models of 'micro-gel' (left) and homogeneous (right) polyHIPE structures within the walls of the polyHIPEs.

It can be seen from figure 4.9 that T_1 relaxation and Young's modulus trends are similar, suggesting that both techniques may be able to indicate structural homogeneity as well as providing further evidence that there is a correlation between the two methods.[19] Specifically, DMA measuring tensile modulus, E'' and TD-NMR measuring T_1 are both dependent on frequency, ω, and temperature. The temperature dependence originates from the parameter called correlation time, τ. In NMR, correlation time is essential to relaxation, and is modulated by molecular motion, whereas DMA correlation time arises in mechanical, creep and dielectric time measurements. Therefore each technique can be an insight into the other, and this relationship may be significant for a field such as laser target material characterisation. More importantly, TD-NMR is a non-destructive technique, which is attractive to laser material target development and characterisation as this technique could be used to compare two similar target material monoliths from the same polymer system, without causing damage, to evaluate modulus. In addition it

could eliminate the need for extra analysis, and the time consuming sample preparation, that DMA requires.

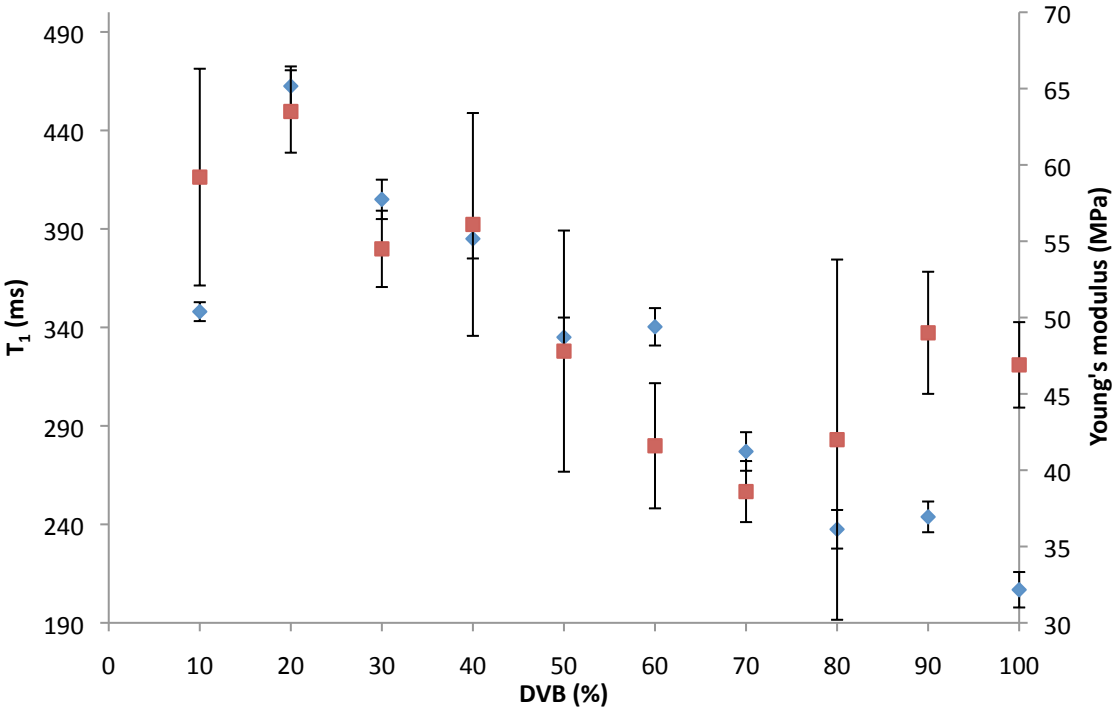

Figure 4.9. Comparison of S-co-DVB DMA data (red) and T_1 relaxation times (blue) as a function of DVB content.

In summary, S-co-DVB polyHIPEs obtained using the two syringe method for emulsification, resulted in small pore size and high modulus polyHIPEs. Modulus results were some of the highest reported for S-co-DVB polyHIPEs at 90% porosity and despite free radical polymerisation. Correlation of Young's modulus data and T_1 relaxation times suggested that TD-NMR could be used to estimate modulus when comparing samples within a polymer system. Furthermore, TD-NMR highlighted structural differences in S-co-DVB polyHIPEs, which developed an understanding into the reason for reduction of modulus as the cross-linking percentage was increased. DVB was shown to form clusters of rigid material, highlighted by T_1 and $T_{1\rho}$ relaxation times respectively, affecting the modulus at higher percent DVB content. This technique will benefit laser target material characterisation as TD-NMR is a non-destructive technique, yet provides potentially valuable structural information that Young's modulus data cannot provide on its own.

4.5.2 Synthesis and Characterisation of t-Butyl Styrene PolyHIPEs

The stringent requirements for laser target materials such as high modulus and low density, combined with the need to increase $C_nH_{>n}$ ratio means that the number of potential new polyHIPEs is small. t-Butyl styrene (t-BS) was considered as a replacement for styrene as the C:H ratio for t-BS is 1:1.33, thus a significant increase in opacity for plasma physics experiments. In addition, as t-butyl styrene is a styrene-derived monomer, it was postulated that the physical properties of t-BS would be similar to styrene. Furthermore, at the time of writing, there were no reports on t-BS polyHIPE synthesis and characterisation.

t-BS-co-DVB polyHIPEs with varied molar ratios were synthesised and characterised using SEM, TD-NMR, SSNMR, elemental analysis, mercury porosimetry, and DMA. T-BS polyHIPEs were smooth and did not exhibit the chalky characteristic that has described styrene polyHIPEs. However, at 70% and higher DVB content, polyHIPEs became 'chalky'. In addition, polyHIPEs made with 100% t-BS 100% were not fragile like 100% styrene polyHIPEs, suggesting that there were differences in the structure that warranted further investigation.

SEM images (figure 4.10) revealed the typical polyHIPE architecture of t-BS. Pore sizes appeared similar to styrene suggesting that the t-butyl group did not increase any emulsion coarsening mechanisms that would have resulted in larger pore size. However mercury porosimetry (table 4.2) results suggested that stability was affected, as indicated by the reduction in porosity compared to styrene. It was thought the t-butyl group would increase the hydrophobicity of the t-BS monomer aiding in emulsification, as the two phases would be less soluble with each other. A material with larger pore size would be expected to weaken the mechanical modulus, lowering the modulus in accordance with equation 4.1. The addition of DVB resulted in a reduction in pore window size, and an increase in porosity, yet, the pore size remained larger than the equivalent molar ratio S-co-DVB polyHIPE indicating that the emulsion stability was affected by the t-butyl group, increasing the rate of emulsion coarsening mechanisms. The increase in pore size is consistent

with previously mentioned S-co-DVB polyHIPE observations. The interesting effect t-BS had on these emulsions and resulting polyHIPEs was worthy of further investigation using TD-NMR.

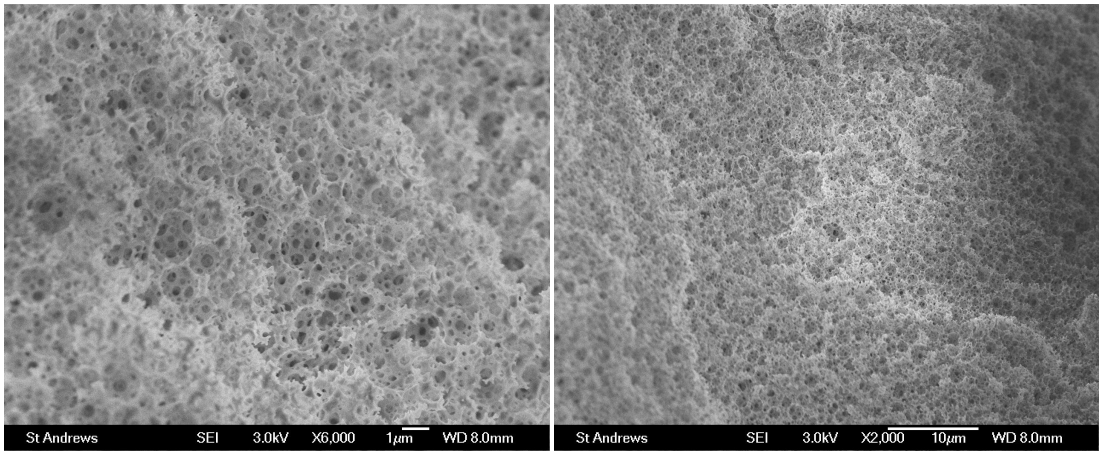

Figure 4.10. SEM images of a t-BS (100%) polyHIPE. Scale bars are 1 μm (left) and 10 μm (right).

Table 4.2. Mercury porosimetry data of t-BS polyHIPE.

PolyHIPE system (t-BS:DVB)	**Average window diameter (μm)**	**Porosity (%)**
t-BS (100)	0.24	83.5
t-BS-co-DVB (70:30)	0.15	95.0
t-BS-co-DVB (30:70)	0.11	98.2

^{1}H-^{13}C CPMAS SSNMR spectrum of t-BS polyHIPE (figure 4.11, left) confirmed the presence of the t-butyl group at ~35 ppm. A large peak was seen due to 9 equivalent protons on the t-butyl group cross-polarising to 3 equivalent carbons, significantly boosting the signal. An interesting feature of the spectrum was that spinning sidebands were present and could not be removed despite high-field strength (9.4 T) and MAS rates (~10 kHz). This indicated that the t-butyl group produced stronger dipolar interactions with neighboring groups compared to styrene. The t-BS-co-DVB spectrum (figure 4.11, right) appeared consistent with other DVB polyHIPE spectra, but with the additional peak from t-BS methyl groups. In addition, the issue of

spinning sidebands was removed which had the effect of reducing the influence of broadening mechanisms such as CSA and the dipolar interaction, likely as a result of DVB increasing distance between t-butyl groups, else, line broadening that occurs with addition of DVB hid the sidebands.

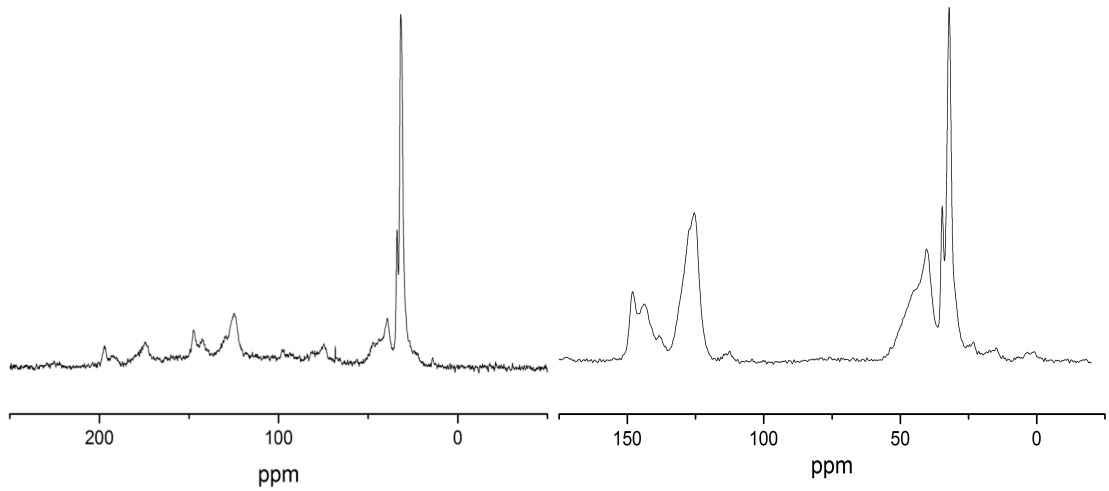

Figure 4.11. ^{1}H-^{13}C CPMAS SSNMR spectrum of t-BS polyHIPE (left, spun at 12 kHz) and t-BS-co-DVB polyHIPE (right, spun at 12.5 kHz). The reduction of broadening mechanisms was particularly evident in the 60-100 ppm region. t-BS-co-DVB (right) is absent of such peaks.

To measure Young's modulus, discs of t-BS-co-DVB polyHIPEs were produced for DMA. The results are summarized in figure 4.12. Compared to S-co-DVB polyHIPEs, it was clear that t-BS-co-DVB polyHIPEs had a lower modulus (table 4.3). The trends were similar, indicating that the required amount of DVB to cross-link was about 10%-30% to form the strongest materials. Lowering of the modulus with increasing DVB content was consistent with the trend identified with S-co-DVB polyHIPEs. However, attributing this low modulus to increased pore size was not straightforward, as higher porosity and lower density of t-BS polyHIPEs would also contribute to lowering of modulus.[8] Thus further structural investigation was carried out using TD-NMR.

Table 4.3. Young's modulus and physical data of t-BS-co-DVB polyHIPEs.

PolyHIPE system	Young's modulus (MPa)	Porosity (%)	Average disc density (mg/cc)
t-BS	12.7±1.3	83.5	130.8±2.3
t-BS-co-DVB 70:30	42.5±7.1	95.0	109.1±3.5
t-BS-co-DVB 30:70	25.1±6.7	98.2	107.5±1.9
DVB	46.9±2.8	91.2	128.8±7.7

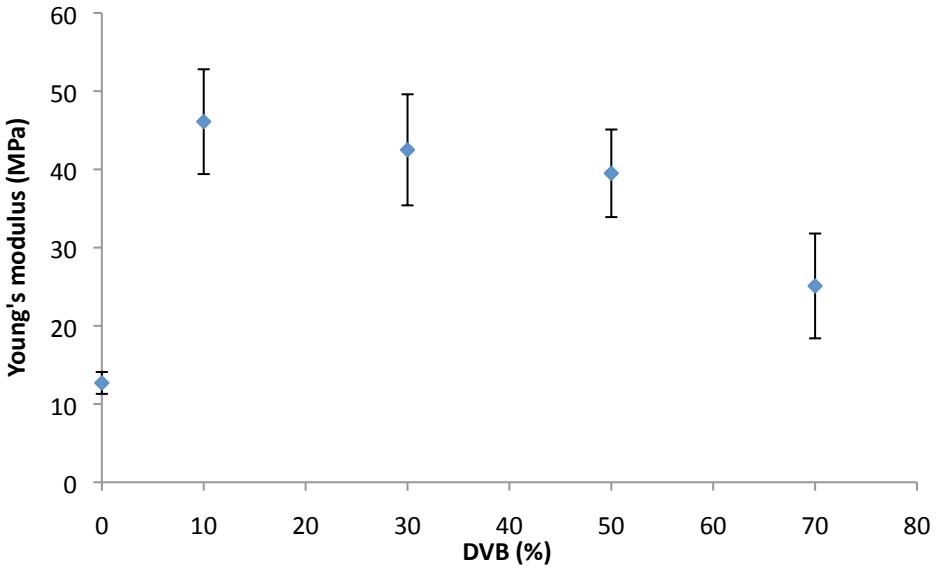

Figure 4.12. Young's modulus data of t-BS-co-DVB polyHIPEs.

T_1 and $T_{1\rho}$ relaxation times for t-BS-co-DVB polyHIPEs are presented in figures 4.13 and 4.14 respectively. The trend of T_1 relaxation was similar to S-co-DVB polyHIPEs with longest relaxation times in the region of 10% to 30% DVB content, indicating that the structure was at its most rigid. In addition, T_1 and modulus results followed a similar trend to S-co-DVB data, suggesting that T_1 relaxation times could be used as an indicator of modulus within a polymer data set. Generally, the relaxation times were shorter than for S-co-DVB, which can be attributed to the effect the t-butyl

group had on relaxation. Freely rotating t-butyl group allowed efficient relaxation as molecular motion was unrestricted likely as a result of an increase in polymer free volume created by the t-butyl group by comparison to styrene.

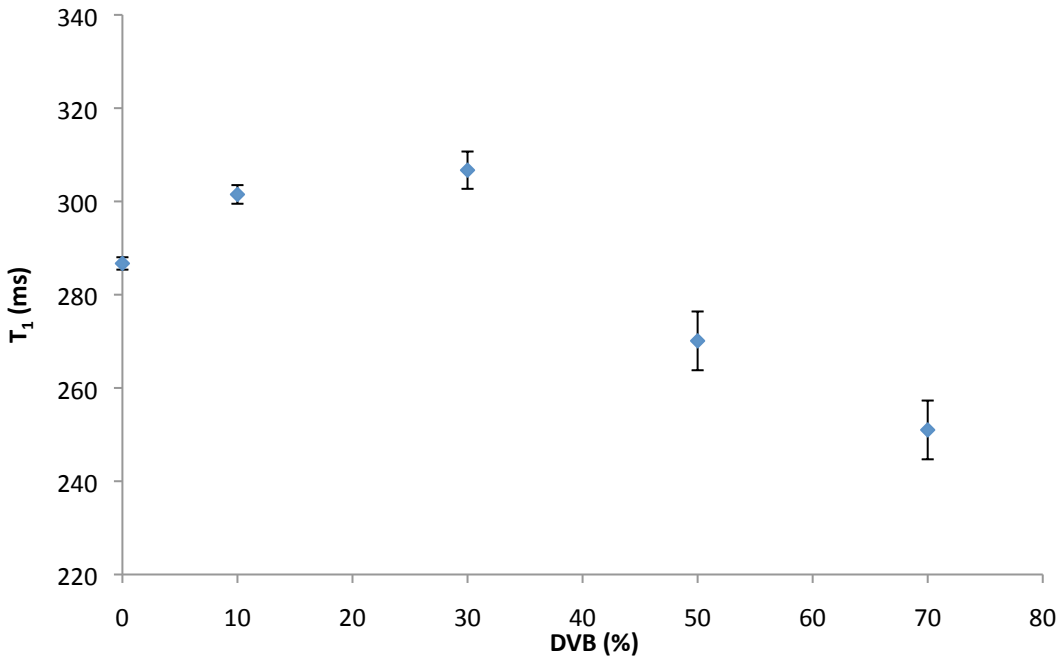

Figure 4.13. T_1 relaxation times for t-BS-co-DVB polyHIPEs with varied DVB content.

$T_{1\rho}$ relaxation times were near constant across the t-BS-co-DVB polyHIPE series. One reason could be that the increased free volume created by the t-butyl group between polymer chains meant that macromolecular chain motion was unaffected by increasing DVB content. Cross-linking DVB could not pull chains closer together, which had the effect of increasing polarisability of spins in the macromolecular structure in S-co-DVB polyHIPEs. As a result, the increased free volume and clustering of DVB were reasons for lowering of the modulus. Furthermore, if an increase in free volume occurred, this could prevent clustering from affecting $T_{1\rho}$ relaxation times.

Compared to styrene, t-BS $T_{1\rho}$ relaxation times were longer suggesting that t-BS had more polarisable spins than styrene, suggesting a more favourable arrangement of macromolecular chains. It was possible that t-BS contributed to emulsion

stabilisation, after a period of coalescence that increased pore size. Thus on polymerisation, the macromolecular chains were in a better structural arrangement by NMR than styrene to polarise spins resulting in longer $T_{1\rho}$ relaxation times as the emulsion did not coarsen significantly. It was also possible that the t-butyl group restricted polymer chain motion, suggesting that the polymer was more rigid by comparison to styrene.

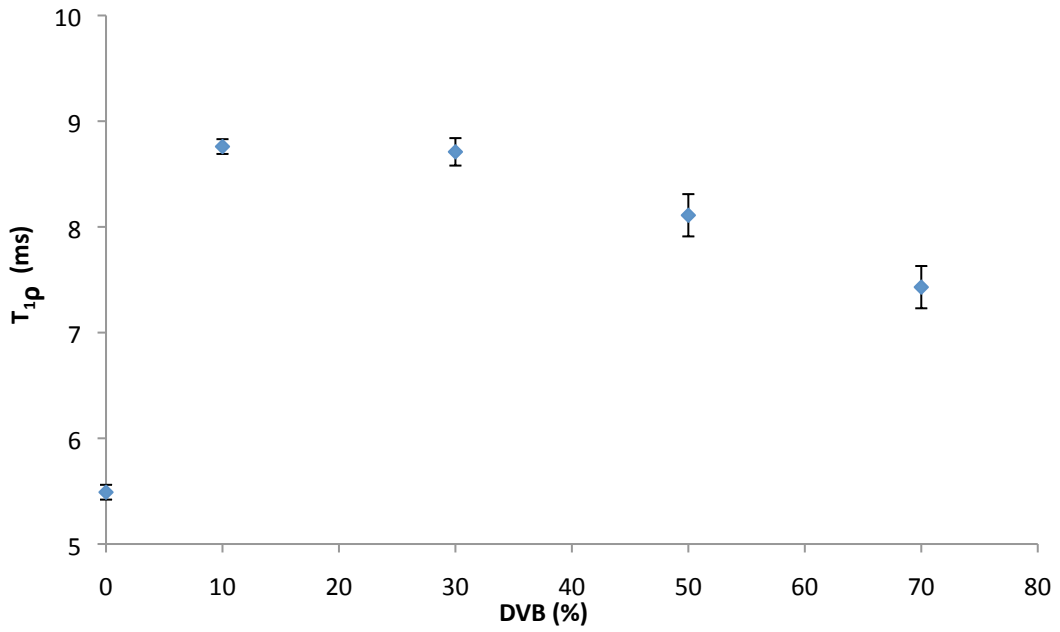

Figure 4.14. $T_{1\rho}$ relaxation times of t-BS-co-DVB polyHIPEs with varied DVB content.

TD-NMR experiments did not provide reasonable explanation for having a lower modulus of t-BS polyHIPEs than 100% styrene polyHIPEs, partly due to clustering of DVB being unobservable. Subsequently styrene, t-BS and DVB modulus and porosity data were compiled (table 4.4) with the aim of resolving this question. With the exception of t-BS homopolymer, t-BS-co-DVB polyHIPEs had a higher porosity and lower density (including low shrinkage) than all other polyHIPEs measured in this work suggesting that the emulsion was more stable than originally thought despite the increased pore size. All polyHIPEs were synthesised with consistent formulation and conditions, however different results suggested that the emulsion chemistry was influential to these outcomes. It was postulated that the t-butyl group could be interacting with the very hydrophobic surfactant chains, in effect acting as a co-

surfactant to Span® 80 at the interface between the oil and water phases, which had the effect of reduced coarsening mechanisms after some coarsening whilst t-BS migrates to the phase boundary (figure 4.15). However, this indicated that increased porosity and reduced density were the cause of decreased modulus in addition to likely clustering of DVB and polyHIPE density inhomogeneity.

Table 4.4. Young's modulus and porosity data of S-co-DVB and t-BS-co-DVB polyHIPEs.

PolyHIPE system	Young's modulus (MPa)	Porosity (%)	Average disc density (mg/cc)
Styrene	N/A	86.4	N/A
t-BS	12.7±1.3	83.5	130.8±2.3
S-co-DVB 70:30	54.5±2.6	90.1	128.0±8.4
t-BS-co-DVB 70:30	42.5±7.1	95.0	109.1±3.5
S-co-DVB 30:70	38.6±2.0	89.6	121.1±7.0
t-BS-co-DVB 30:70	25.1±6.7	98.2	107.5±1.9
DVB	46.9±2.8	91.2	128.8±7.7

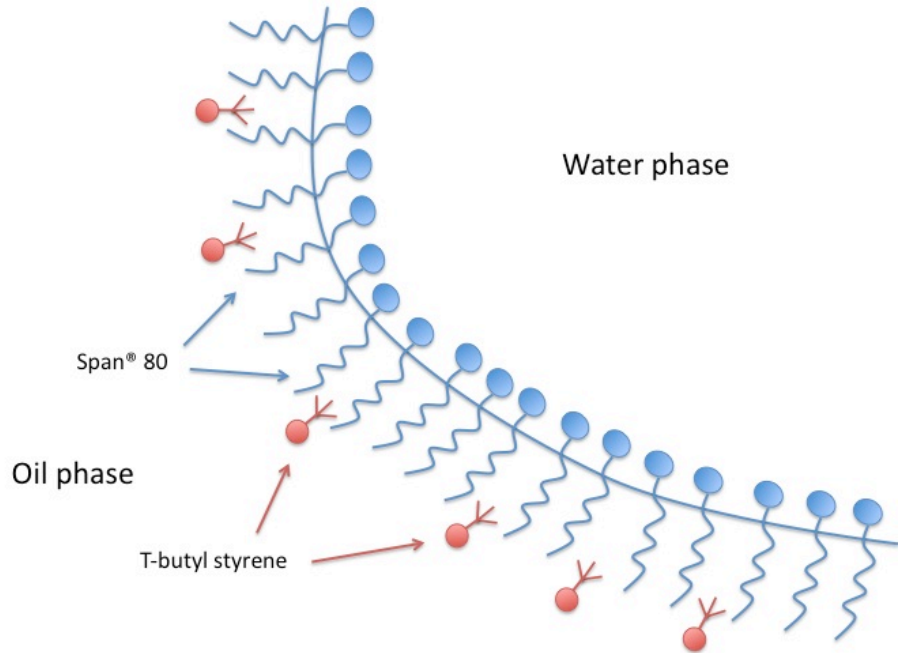

Figure 4.14. Model of HIPE droplet with t-BS interacting with the surfactant aliphatic chains.

To summarise, t-BS polyHIPEs were synthesised and characterised for the first time. The t-BS monomer increased the C:H ratio favorably to 1:1.33 (reduced to 1.3 when cross-linked by 30% DVB), whilst retaining ~80% of the modulus compared to S-co-DVB polyHIPEs. Structural differences to styrene included larger pore size, but an increased porosity and reduced shrinkage. It was postulated that t-butyl group helped to stabilise the emulsion after a period of coarsening, resulting in more efficient polarisation of spins as a result of the structure, which was characterised by increased $T_{1\rho}$ relaxation time. T_1 relaxation times followed the trend of modulus values in the same manner as S-co-DVB polyHIPEs, providing further evidence that T_1 relaxation times could be used as an indicator of material modulus. $T_{1\rho}$ relaxation times highlighted the t-butyl group effect on the structure; an increase in free volume meant that on cross-linking with DVB, there was no tightening of the structure or reorganisation due to clustering, as the $T_{1\rho}$ time remained constant.

4.5.3 Comparative analysis of styrene-type monomers

Comparison of S-co-DVB and t-BS polyHIPEs highlighted that complex interactions exist between chemical and physical properties of polyHIPEs. There was a lack of experimental evidence to suggest that the t-butyl group acted as a co-surfactant to increase emulsion stability without performing experiments such as ^{1}H NMR diffusion, which has been used for testing HIPE stability before,[12] other approaches were required. Furthermore, using DVB as a cross-linker, a mixture of isomers and other reagents, was questioned as TD-NMR suggested that increasing concentrations of DVB formed clusters of cross-linked material. This resulted in reduced modulus values despite a decrease in pore size suggesting the polyHIPE was increasingly inhomogeneous. Improving physical properties was one of the aims for this work, and understanding components of HIPEs such as cross-linker and surfactant were essential. Investigating individual polymerisable styrene-type monomers (styrene, t-BS, DVB 80 and para-DVB) could allow identification of potential issues in relation to physical modulus, and application of possible solutions.

Para-DVB was investigated as a separate component to DVB 80 as the contribution para-DVB had to cross-linking and structural influences in polyHIPEs had not been investigated before. It was postulated that para-DVB could improve mechanical properties as removal of the ethyl styrene isomers may result in a more homogeneous material. Reactivity ratios (r_1 and r_2) of meta-DVB and para-DVB indicate how each isomer may react with styrene (as M_1, and the isomer M_2).[20] Styrene copolymerised with meta-DVB has r_1 and r_2 values of 0.58, which indicates formation of copolymers, whereas for styrene-co-para-DVB r_1 is 0.26 and r_2 is 1.18 indicates that homopolymers of para-DVB will form and growing styrene chains will copolymerise with para-DVB. The difference in these reactions was motivation to investigate para-DVB, and possibly provide clarity to the discussions about S-co-DVB polyHIPE structure. It was possible that these reactions could have an impact in polymerisation of these monomers in HIPEs, influencing the resulting polymer structure, which was an important factor high energy laser target materials.

In addition to para-DVB studies, it was indicated by t-BS that emulsion stablilty was an issue. Thus, another experiment performed applied different surfactant systems in order to investigate emulsion stability and the effect on structure. A 3-surfactant system consisting of Span® 80, CTAB and DDBSS, which has been shown to increase emulsion stability,[12] and a mixture of two nonionic surfactants Span® 80 and Span® 20 were used as an nonionic surfactant mixture in contrast to the 3-surfactant system. PolyHIPEs were synthesised in the same manner as previously described, then characterised using TD-NMR, SEM, mercury porosimetry and DMA.

The 3-surfactant system is reported to increase HIPE stability,[12] however polyHIPEs produced here using the 3-surfactant system were fragile often crumbling when dried, which meant that they did not fit the requirements of materials for laser experiments. PolyHIPEs using Span® 80/20 did not have this problem. It was possible that the 3-surfactant system reduced the surface tension and electrochemical barrier, due to the cationic and anionic charged surfactants too much that there

were no more repelling forces between the two phases (figure 4.15, top left and right). This resulted in a HIPE in which the components were no longer in the correct proportions for an open cellular polyHIPE in accordance with foam microstructure diagrams. Mixed Span® homopolymer polyHIPEs appeared to improve stability as SEM images revealed homogeneous structures (figure 4.15, middle and bottom). However it was clear with t-BS polyHIPEs that perhaps the entire structure was still inhomogeneous, which provided further evidence that the t-butyl group may increase emulsion coarsening. Despite homogeneous SEM images, para-DVB HIPEs were not particularly stable, often resulting partial breaking before polymerisation occured. Para-DVB polyHIPEs that did not split were fragile and chalky, which was similar to previous descriptions of DVB polyHIPEs,[2, 11, 12] suggesting that the chalky behaviour of these polyHIPEs could be due to para-DVB component rather than the other species in DVB 80. More images of all polyHIPEs with different surfactant systems are contained within appendix 4.7.1.

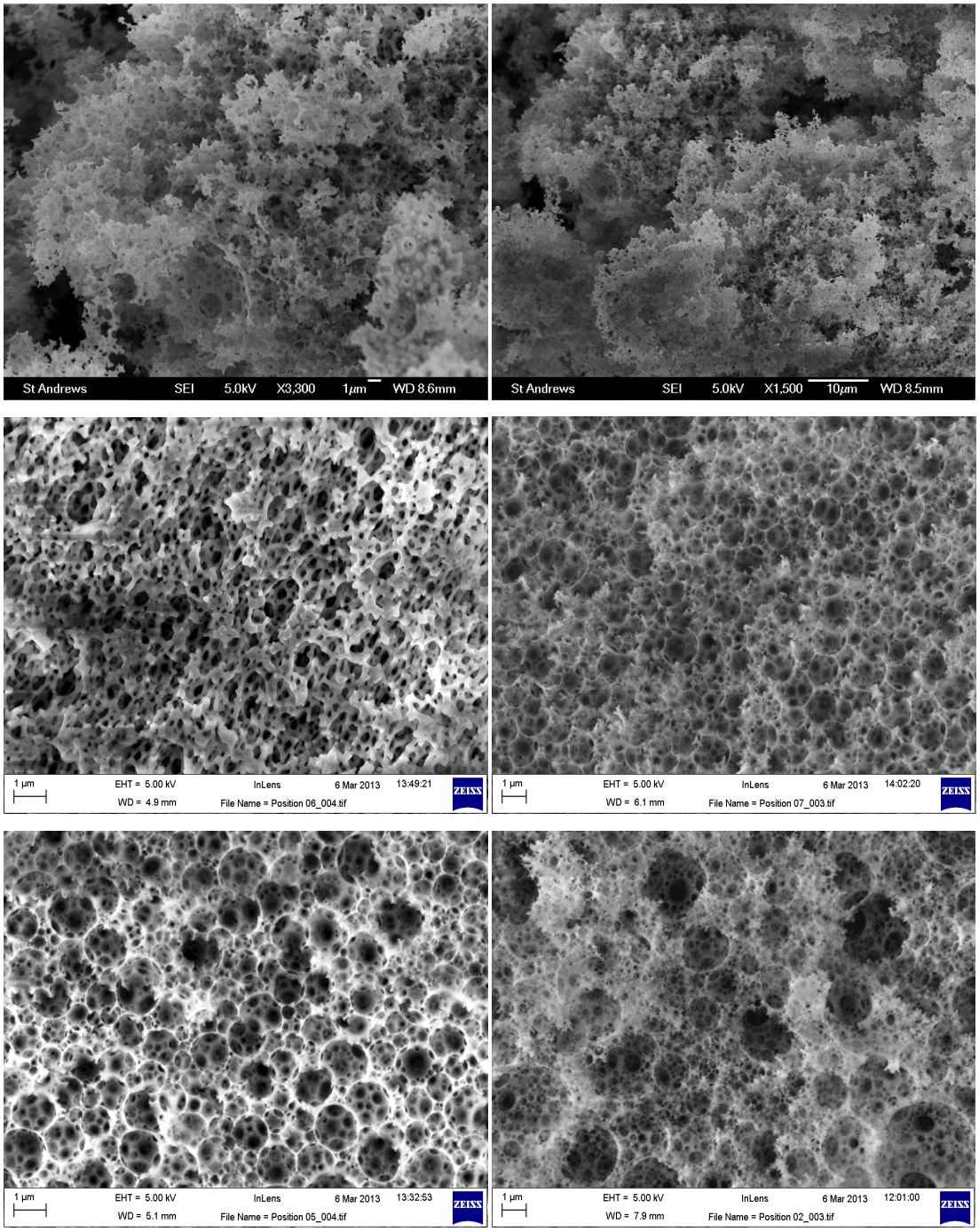

Figure 4.15. SEM images of 3-surfactant system DVB polyHIPE (top left and right) and Span® 80/20 polyHIPEs of styrene (middle left), DVB 80 (middle right), para-DVB (bottom left) and t-BS (bottom right).

To compliment SEM, mercury porosimetry was performed, and results compared to Span® 80 homopolymer porosimetry data that was previously obtained in this work (table 4.5).

Table 4.5. Mercury porosimetry data for S, t-BS, DVB 80 and para-DVB polyHIPEs.

PolyHIPE system	Surfactant system	Average window diameter (μm)	Porosity (%)
Styrene	Span® 80	0.34	86.4
	Span® 80/20	0.11	64.9
t-BS	Span® 80	0.24	83.5
	Span® 80/20	0.22	92.5
DVB 80	Span® 80	0.17	91.2
	Span® 80/20	0.15	89.4
Para-DVB	Span® 80	0.28	91.6
	Span® 80/20	0.12	92.5

An interesting trend was the reduction of pore window diameter, the small gaps contained within a pore. It has been shown that window formation was a result of volume contraction of the monomer on polymerisation to a solid.[4] Another explanation suggests that windows are formed through mechanical action of droplets bursting.[21] A plausible explanation for this trend was that the emulsions were stabilised longer before polymerisation occurred, thus droplets were smaller, therefore volume contraction around the droplets was not as large resulting in smaller window diameter. If so this indicated that the mixed Span® surfactant film was stronger, thus able to withstand the pressure exerted by coarsening mechanisms attempting to burst the surfactant film, allowing polymerisation to occur whilst the emulsion was more homogeneous.

HIPEs are complicated systems, where simultaneous growth of droplets through coarsening mechanisms and conversion from liquid to solid is occurring at the same time. Pore droplet size is dependent, amongst other factors, on the surfactant film to resist coarsening; therefore a growing droplet would increase the pressure exerted on the surfactant film around the droplet. When the pressure is too great, the surfactant film can burst. However, if the polymerisation of the monomer is

occurring when this event happened, unexpected structures of the polymer are likely to arise with the burst droplet essentially locked in that structure.

For t-BS and para-DVB the effect of mixed Span® surfactants resulted in a reduction in pore size and increase in porosity. It was expected that a decrease in pore size would result in an increase in porosity, as the HIPE was more stable creating a more homogeneous structure resulting in less shrinkage. Styrene, which was not cross-linked, could have shrunk significantly during washing and drying stages, which would reduce porosity. However, a decrease in porosity has been shown to occur alongside a decrease polyHIPE pore sizes.[22] The effect on styrene polyHIPEs was varied; pore sizes decreased, but the porosity decreased. DVB results were largely constant, suggesting that a balance between destabilised ethyl styrene, and more stabilised para-DVB, effectively cancelling their contribution to the structure.

For the interest of laser target materials, mercury porosimetry indicated that para-DVB in a polyHIPE system using only Span® 80 as the surfactant increased the pore size of polyHIPEs. Identification of this could help resolve issues that are experienced in the synthesis of these materials. Such issues are the inhomogeneous formation of regions of high and low density, and large void formation, both of which would result in a material failing to meet the required specifications for laser target materials (see section 4.2). Increased porosity and reduced pore size suggested that application of the mixed Span® surfactant system to polyHIPEs presents a possible solution to polyHIPE inhomogeneity. In addition, the surfactant system produced polyHIPEs that are very close to the laser target material specification.

Further to SEM and mercury porosimetry observations, ^{1}H TD-NMR relaxation experiments were performed to examine the macromolecular structure in more detail. It was hypothesised that structural differences using the mixed Span® surfactant system would have an effect on molecular motion, and thus on relaxation. Characterising these differences may prove beneficial to laser target material characterisation, helping to solve current synthetic issues such as regions of higher and lower density material through greater understanding of the structure.

Furthermore, it was an assessment of limitations that TD-NMR could achieve with polyHIPEs and the viability of the technique to be applied to laser target material characterisation. The structural differences were small according to porosimetry, and thus provided an appropriate level of difficulty for the technique. Table 4.6 summarises the relaxation times of the homopolymers using both Span® 80 and mixed Span® surfactant system.

Table 4.6. ^{1}H TD-NMR relaxation times for homopolymer polyHIPEs with different surfactant systems.

PolyHIPE system	**Surfactant system**	T_1 **(ms)**	$T_{1\rho}$ **(ms)**
Styrene	Span® 80	538.8±8.3	2.80±0.80
	Span® 80/20	544.1±8.5	3.15±0.06
t-BS	Span® 80	287.7±1.3	5.49±0.07
	Span® 80/20	352.3±3.7	8.39±0.13
DVB	Span® 80	206.8±9.0	6.53±0.35
	Span® 80/20	210.2±6.4	6.16±0.29
Para-DVB	Span® 80	164.0±6.5	3.37±0.11
	Span® 80/20	189.8±6.5	5.33±0.26

TD-NMR relaxation times and porosimetry results produced consistent trends within each polymer system. Styrene and DVB polyHIPEs T_1 relaxation times indicated little differences between using either surfactant system, which correlated with porosimetry results. The similar pore size of styrene and DVB meant there was no effect on molecular motion and therefore the T_1 relaxation time remained constant. In addition, there was no indication of the effect of reduction of window size on relaxation, suggesting that that window size did not affect the molecular motion in the same manner as pore size. Styrene and DVB $T_{1\rho}$ relaxation times were also similar (within each system) despite choice of surfactant system, following the trend of porosimetry results, indicating that the macromolecular structures were similar. Being able to discriminate between pore size due to the effect on molecular motion demonstrates the detailed available using TD-NMR.

The mixed Span® surfactant system of t-BS polyHIPEs exhibited an increase in T_1 relaxation time compared to the single Span® equivalent. This was consistent with the reduction of pore size observed by porosimetry as this would increase the modulus, which has been shown earlier in the chapter to affect molecular motion resulting in increased T_1 relaxation times. $T_{1\rho}$ relaxation times also increased for the mixed Span® system polyHIPEs, signifying that the macromolecular chain structure allowed more efficient spin polarisation, possibly due to improved emulsion stability effect on the structure. Greater structural organisation allows more efficient polarisation of spins, which consequently took longer to dephase. Overall improvement in pore size and macromolecular structure highlighted the effectiveness of the mixed Span® surfactant system on t-BS polyHIPE. This was in contrast to increased relaxation times as a result of clustering, which was observed in copolymers containing DVB.

The trends in para-DVB relaxation times were similar to those for porosimetry. Similar T_1 relaxation times indicated a similar structural motion despite a large reduction in pore size, which would affect molecular motion. However, increased $T_{1\rho}$ relaxation times suggested an improved macromolecular chain structure on application of the mixed Span® system. It was postulated that improved emulsion stability allowed this improvement to the arrangement of the polymer backbones as polymerisation occurred before emulsion breaking or significant coarsening could occur. Furthermore, it was likely that para-DVB was composed of clustered regions of polymer, akin to the DVB polyHIPEs described in section 4.5.1. Therefore para-DVB likely formed a similar structure, which coupled with greater emulsion stability to increase the organisation of these clusters, resulted in longer $T_{1\rho}$ relaxation time. However, due to the clustering of polymer there were many hanging/end groups that could freely rotate and therefore little difference in T_1 relaxation was observed, indicating little improvement in the mechanical properties. In addition, shorter T_1 relaxation times of para-DVB than DVB suggested that the modulus was lower in this system than DVB. However, NMR relaxation times alone could not be used to make conclusions and so polyHIPEs of S-co-para-DVB were synthesised and characterised

using DMA and TD-NMR. Investigating para-DVB as a cross-linker was essential in gaining a better understanding of DVB as a cross-linker, and the impact this has on laser target materials.

It was assumed that a cross-linker composed of fewer isomers would enhance physical properties as excess chemicals and isomers were eliminated. This would attempt to resolve the significant issue of the formation of regions of higher and lower density in S-co-DVB polyHIPEs, which is unacceptable on a micrometer scale for laser targets (appendix 4.7.5). Span® 80 was chosen as the surfactant as it has been used for S-co-DVB polyHIPEs for laser targets previously, and is the surfactant system in which this problem arises. Dried para-DVB polyHIPEs were noticeably less robust than S-co-DVB polyHIPEs at corresponding cross-linking percentages; materials were more fragile and 'chalky' than DVB equivalents, indicating that para-DVB was responsible for this 'chalky' characteristic. NMR relaxation times of para-DVB suggested that inconsistent physical properties existed in this system, specifically poor macromolecular structure and low modulus. S-co-para-DVB polyHIPE discs were analysed by DMA, and compared to S-co-DVB polyHIPEs (figure 4.16). A spread of cross-linked percentages was chosen to analyse the high rigidity regions at 20% and 30% DVB content, and the lower rigidity regions 70% and 100% DVB content.

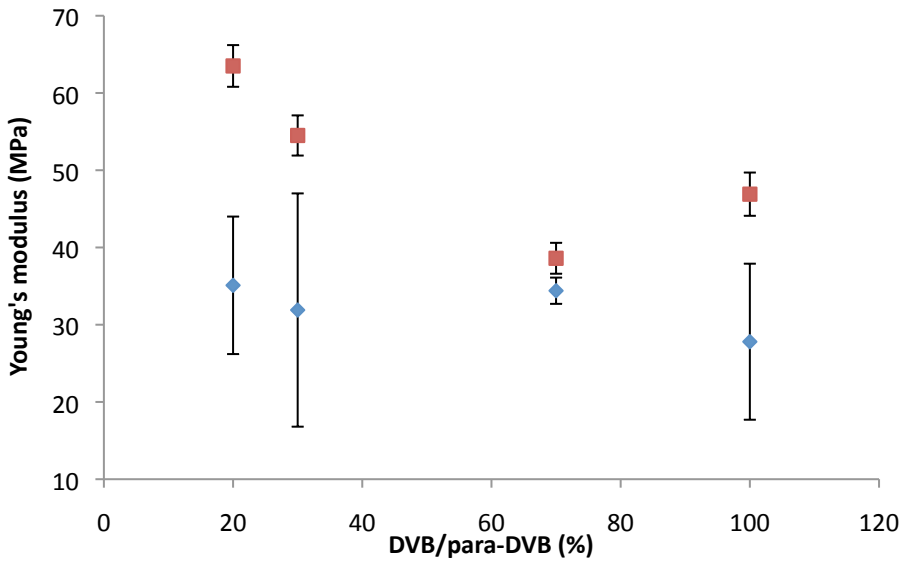

Figure 4.16. Young's modulus data of S-co-DVB (red) and S-co-para-DVB polyHIPEs (blue).

As expected, S-co-para-DVB polyHIPEs produced a lower modulus than S-co-DVB polyHIPEs. These large errors for S-co-para-DVB polyHIPEs are a cause for concern to laser target materials based upon styrene and DVB, which contain para-DVB. This could also explain large errors in previous mentioned S-co-DVB polyHIPEs DMA data. The exception to this was 30:70% S:DVB/para-DVB content which had similar modulus and small error, suggesting that para-DVB was stable in that particular system. Porosimetry and TD-NMR data of para-DVB indicated that structural inhomogeneity, large pore size and clustering were the reasons for the detrimental effect on physical properties. Poor stability of para-DVB in the HIPE, indicated by large pore size from mercury porosimetry, resulted in greater emulsion coarsening, with droplets growing to a large size and having a detrimental effect on the modulus by comparison to DVB. The poor arrangement of the macromolecular structure of para-DVB was characterised by shorter $T_{1\rho}$ relaxation time, and the lower modulus was characterised by shorter T_1 time than DVB.

It was demonstrated that polyHIPEs containing DVB 80 compared to para-DVB had significantly improved structures. This was due to the effect of the other isomers contained in DVB 80, such as polymerisation of ethyl styrene plasticising the polyHIPEs to some degree. Also, the lack of para-DVB in DVB 80 meant that there was reduced polymer clustering. Nevertheless, issues with physical properties were likely a result of poorly stabilised para-DVB within the system. The mixed Span® surfactant system was shown to slightly improve the physical properties of para-DVB, lowering pore size and increasing structural order. In addition, the mixed Span® surfactant system indicated potential for improving para-DVB physical properties. However, application of the mixed Span® surfactant system to styrene or DVB polyHIPEs did not result in such improvement. Highlighting such problems associated with para-DVB may help to resolve the synthetic issues of laser target materials based on S-co-DVB polyHIPEs in the future. TD-NMR was a valuable characterisation technique for identifying this issue, and was sensitive enough to detect structural changes between surfactant systems indicating potential for future polyHIPEs

characterisation by affecting pore size, which in turn affected molecular motion. The ability to probe different molecular motion regimes allowed a clearer understanding of the polyHIPE structures, which meant the issues with para-DVB could be more easily understood.

4.6 Conclusions

The results presented here demonstrated a correlation between T_1 relaxation and Young's modulus. This represented a new application for TD-NMR, which will facilitate routine analysis and characterisation of polyHIPEs, and other porous materials in the future. The Young's modulus data was some of the highest reported for S-co-DVB polyHIPEs at 90% porosity, which demonstrated that the physical structure, such as small pore size, was just as important in achieving a high modulus rather than additional structural reinforcement with carbon nanotubes[23] or controlled polymerisation techniques.[16,24,25] TD-NMR relaxation time data revealed structural differences at distinctive orders of frequency (molecular motion), which assessed the contribution of DVB cross-linking with styrene. Clustering of DVB formed an inhomogeneous structure, reducing the modulus, and was identified by both T_1 and $T_{1\rho}$ relaxation time. Additionally, correlations between T_1 relaxation time and modulus suggested that TD-NMR could be used to estimate polyHIPEs modulus within a polymer system.

t-BS polyHIPEs were synthesised for the first time, and cross-linked with DVB. SEM, SSNMR, elemental analysis, DMA and TD-NMR were used for characterisation. t-BS is a derivative of styrene, and as expected when cross-linked with DVB, produced structural similarities to S-co-DVB polyHIPEs were evident. Once such similarity was with T_1 relaxation times and modulus data. This was further evidence of ideal cross-linking percentages in these systems and that T_1 relaxation measured by TD-NMR could be used to evaluate polyHIPE modulus. SEM, TD-NMR, SSNMR and porosimetry were used to examine the effect of the t-butyl group on the structure; affecting factors such as emulsion stability and free-volume. The increase in free-

volume was identified by $T_{1\rho}$ relaxation. T-BS polyHIPEs had a 1:1.33 carbon to hydrogen ratio, which is of interest to opacity experiments using high energy lasers.

Investigations into styrene, DVB, t-BS and para-DVB homopolymer polyHIPEs revealed information on the stability of each polymer system. This was to identify and resolve synthetic issues that affect inhomogeneity; forming regions of higher and lower density polymer within the same polyHIPE monolith. Mercury porosimetry data indicated increased emulsion stability that could be attributed to the mixed Span® surfactant system. T_1 relaxation times were correlated to differences in pore size, due to the effect on molecular motion, highlighting another possible use for this technique in characterisation of laser target materials. Para-DVB was shown to be unstable during polymerisation, and the most probable source of inhomogeneity in S-co-DVB polyHIPEs.

In summary, small alterations to HIPE chemistry had significant effects on the physical properties and structure of the resulting polyHIPE, which are both significant parameters for laser target materials. T_1 and $T_{1\rho}$ TD-NMR experiments were used to characterise polyHIPEs, probing different molecular motion regimes to form accurate structural information that correlated to established polymer characterisation techniques. T_1 relaxation times correlated with Young's modulus data and porosimetry data suggesting that it could be used in combination with other techniques to powerful effect. Finally, TD-NMR is a non-destructive technique that is relatively easy to use, increasing the throughput of characterisation compared to DMA, which requires laborious preparation of samples particularly for low density materials such as polyHIPEs.

4.7 Appendix

4.7.1 SEM images of S-co-DVB polyHIPEs

SEM images of all varied molar ratio S-co-DVB polyHIPEs were obtained, and revealed typical polyHIPE structure. PolyHIPEs were imaged uncoated, with some exhibiting charging, which arises when the material cannot distribute the charge from the electron beam across the structure.

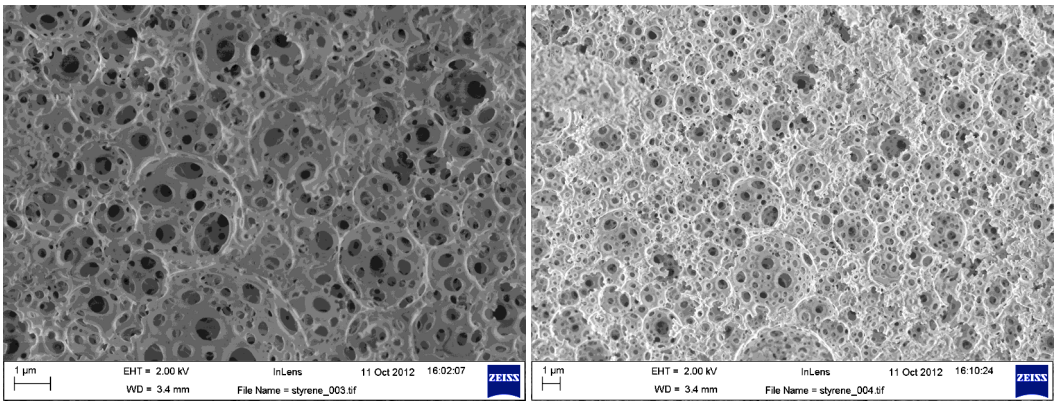

Figure 4.17. SEM images of S-co-DVB (100:0%) polyHIPE. Scale bars are both 1 µm.

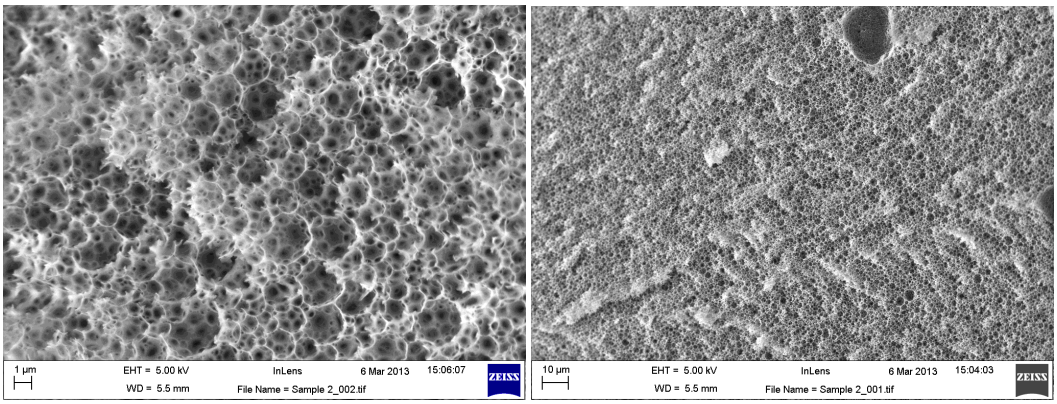

Figure 4.18. SEM images of S-co-DVB (90:10%) polyHIPE. Scale bars are 1 µm and 10 µm respectively.

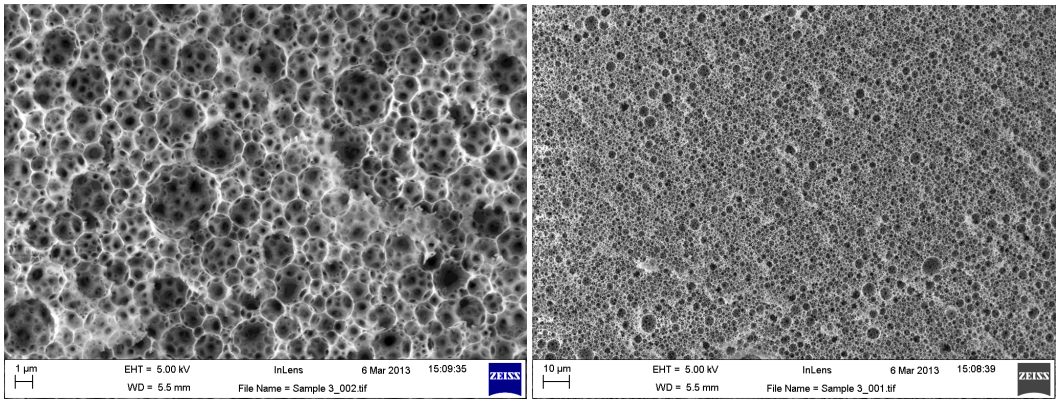

Figure 4.19. SEM images of S-co-DVB (80:20%) polyHIPE. Scale bars are 1 µm and 10 µm respectively.

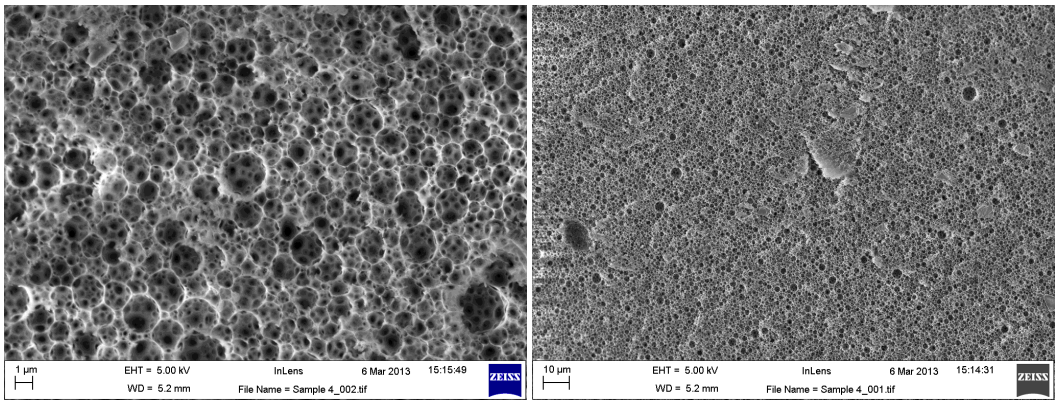

Figure 4.20. SEM images of S-co-DVB (70:30%) polyHIPE. Scale bars are 1 µm and 10 µm respectively.

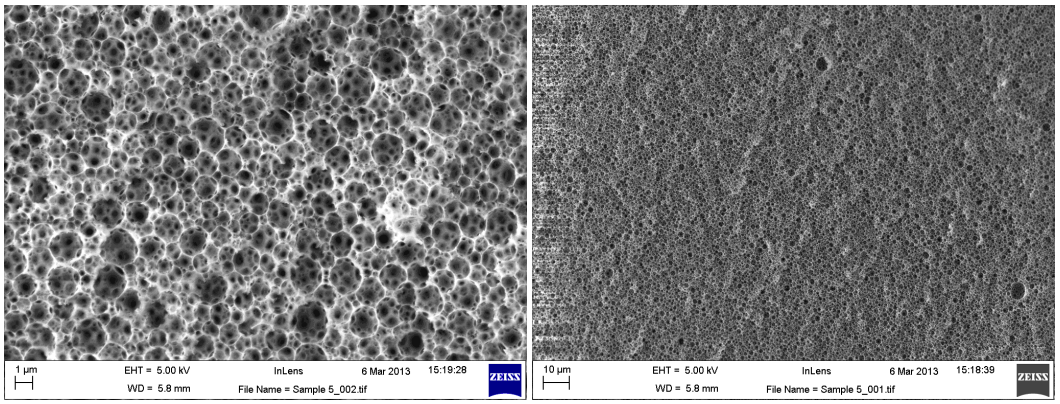

Figure 4.21. SEM images of S-co-DVB (60:40%) polyHIPE. Scale bars are 1 µm and 10 µm respectively.

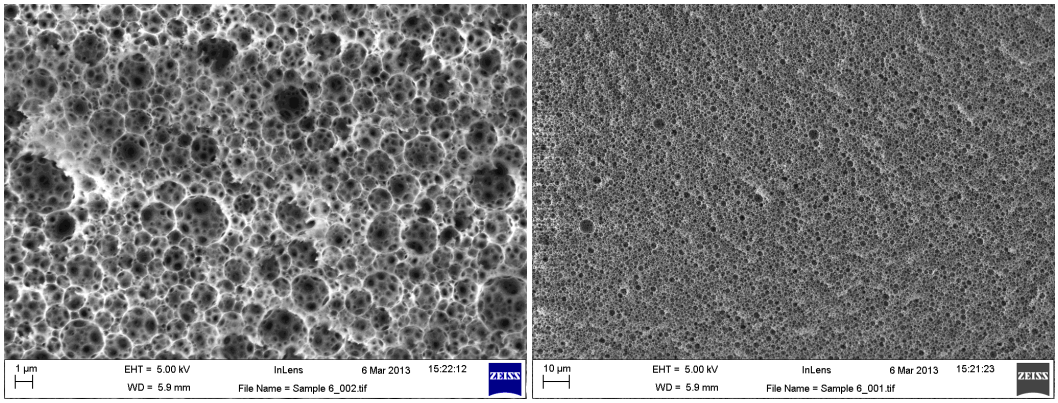

Figure 4.22. SEM images of S-co-DVB (50:50%) polyHIPE. Scale bars are 1 µm and 10 µm respectively.

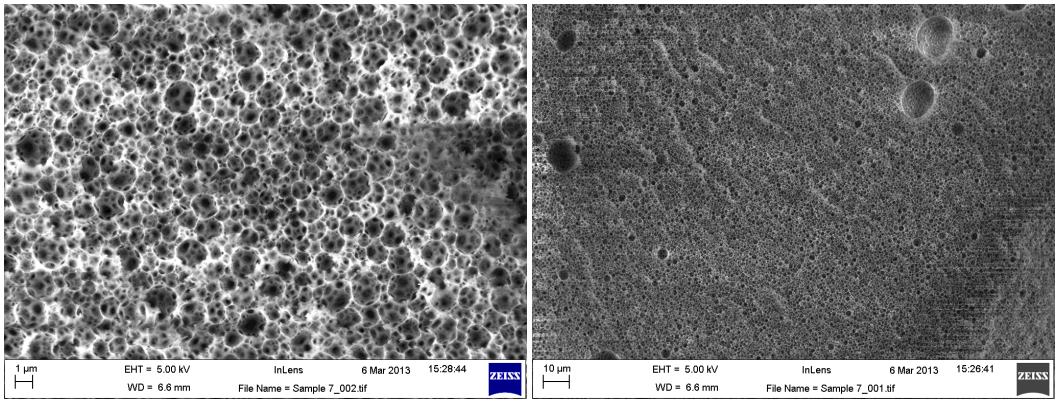

Figure 4.23. SEM images of S-co-DVB (40:60%) polyHIPE. Scale bars are 1 µm and 10 µm respectively.

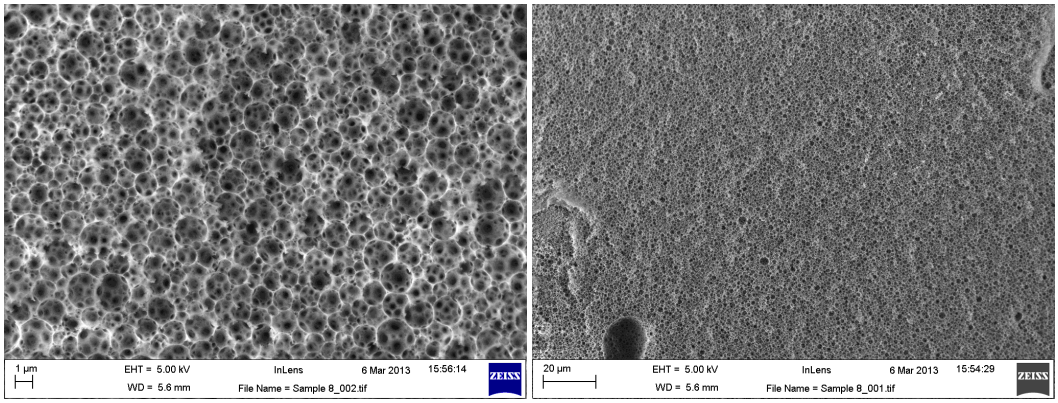

Figure 4.24. SEM images of S-co-DVB (30:70%) polyHIPE. Scale bars are 1 µm and 10 µm respectively.

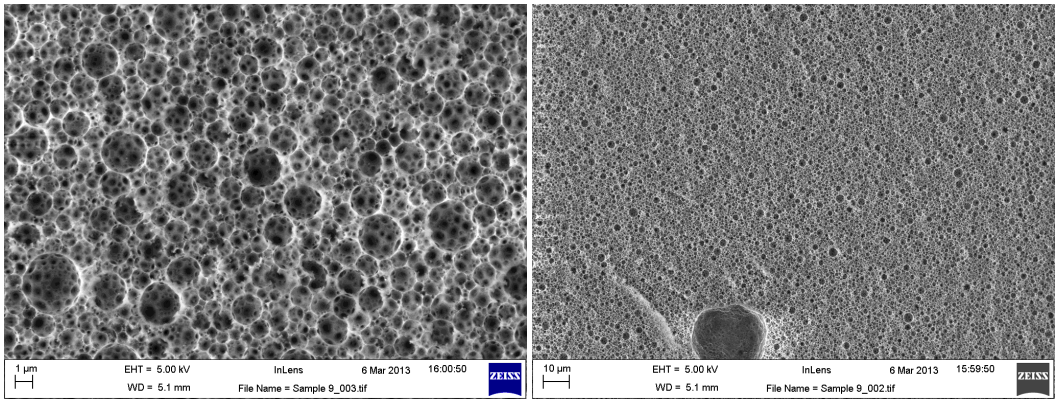

Figure 4.25. SEM images of S-co-DVB (20:80%) polyHIPE. Scale bars are 1 µm and 10 µm respectively.

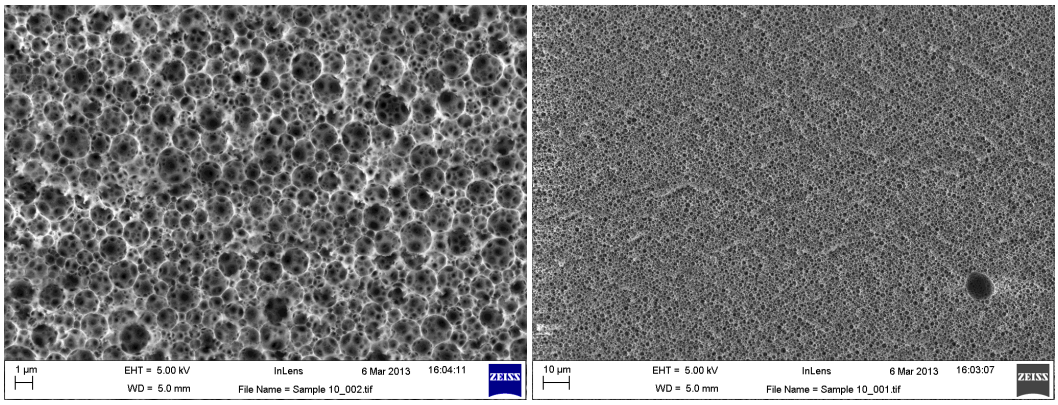

Figure 4.26. SEM images of S-co-DVB (10:90%) polyHIPE. Scale bars are 1 µm and 10 µm respectively.

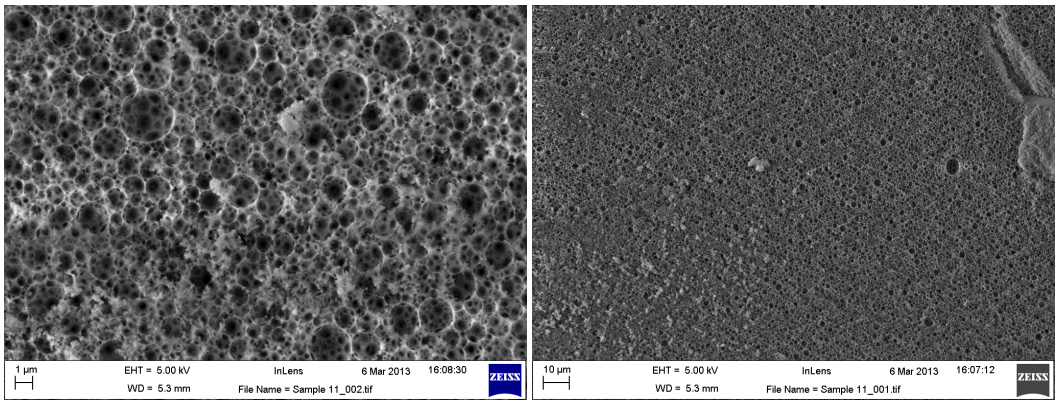

Figure 4.27. SEM images of S-co-DVB (0:100%) polyHIPE. Scale bars are 1 µm and 10 µm respectively.

4.7.2 DSC and TGA data of S-co-DVB polyHIPEs

DSC traces of varied molar ratio S-co-DVB polyHIPEs revealed the effect cross-linking had on the behaviour of polyHIPEs under thermal conditions. Particularly from 20% DVB content onwards, the distribution of thermal transitions was bimodal suggesting a two-phase system had developed, however this was at decomposition temperatures. The trace of styrene 100% polyHIPE contained a small transition at the Tg for styrene. Only one example of the other varied molar ratio polyHIPEs was included for reference. There was no transition at 100°C in these polyHIPEs.

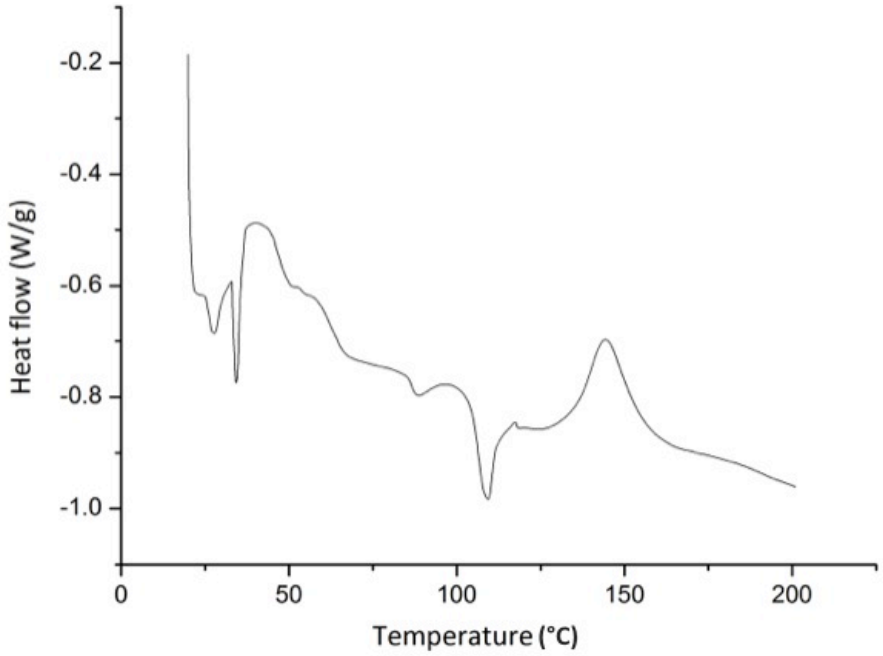

Figure 4.28. DSC trace of S-co-DVB polyHIPE (100:0%).

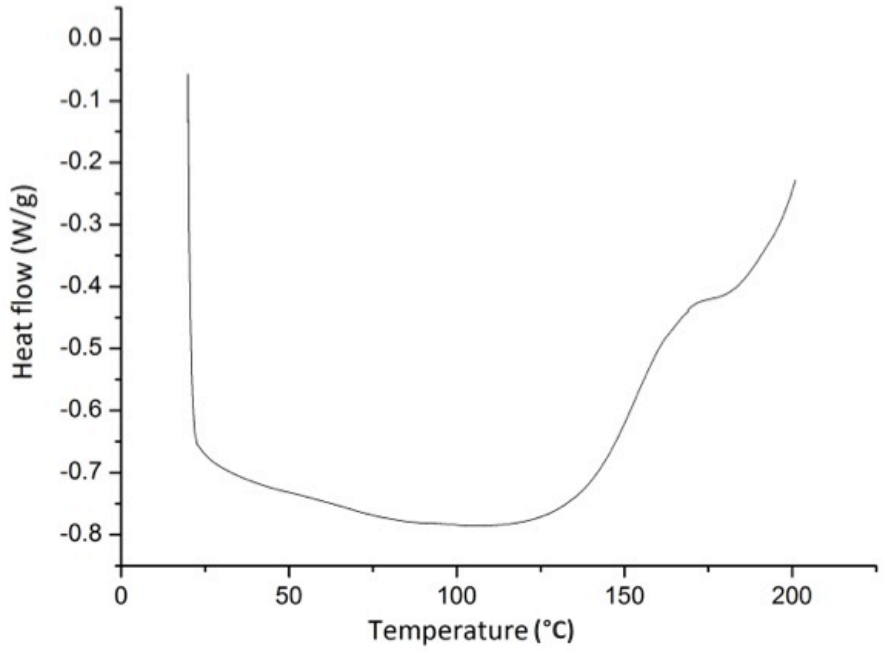

Figure 4.29. DSC trace of S-co-DVB polyHIPE (50:50%).

TGA traces of S-co-DVB polyHIPEs were obtained to investigate decomposition behaviour, particularly as a function of cross-linking. SSNMR and TD-NMR data suggested that these regions could be cross-linking clusters and the other, uncross-linked long chains.

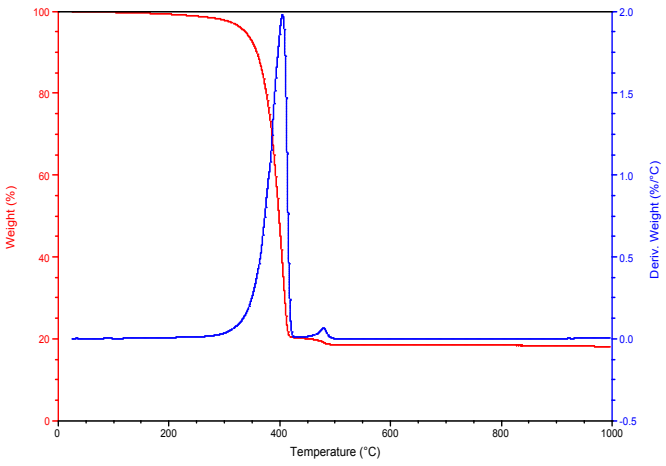

Figure 4.31. TGA trace of S-co-DVB polyHIPE (100:0%). The red line indicated percentage mass loss, and the blue line indicated percentage differential.

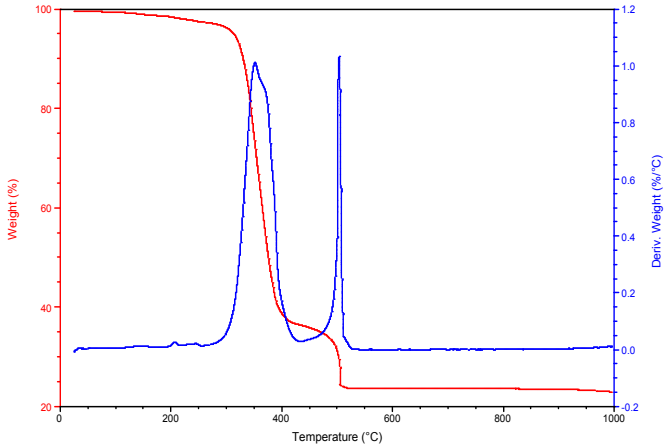

Figure 4.32. TGA trace of S-co-DVB polyHIPE (90:10%).

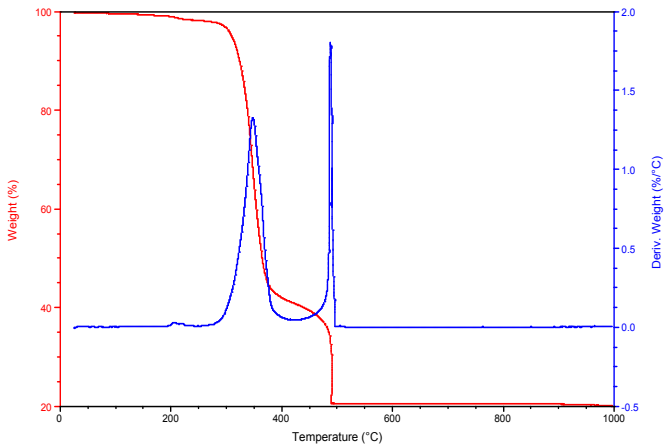

Figure 4.33. TGA trace of S-co-DVB polyHIPE (80:20%).

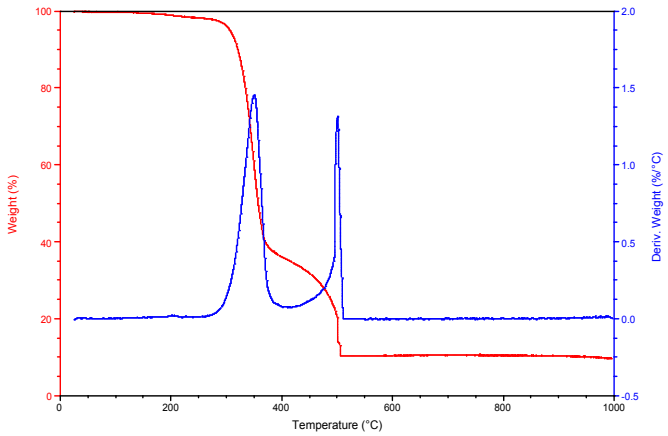

Figure 4.34. TGA trace of S-co-DVB polyHIPE (70:30%).

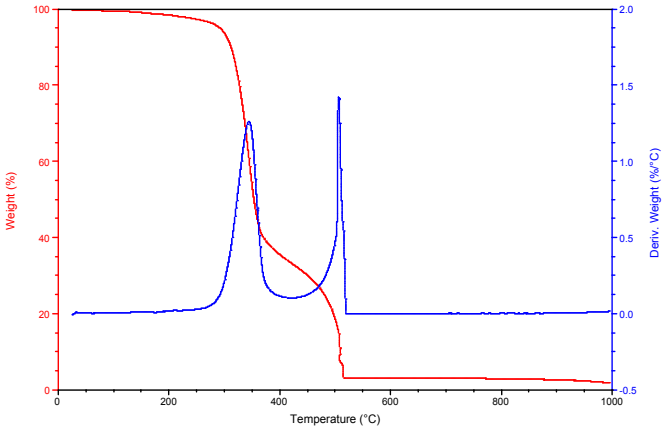

Figure 4.35. TGA trace of S-co-DVB polyHIPE (60:40%).

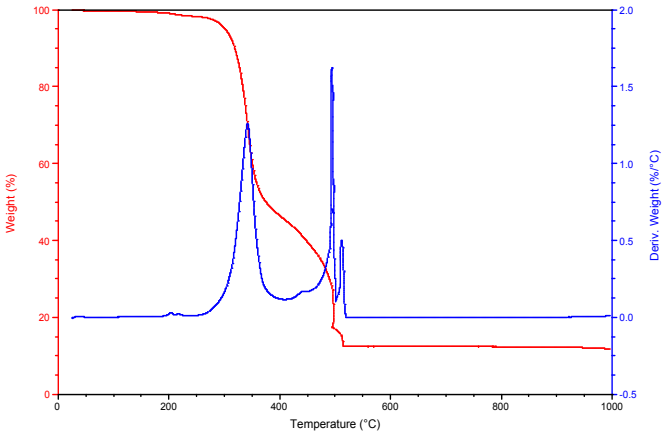

Figure 4.36. TGA trace of S-co-DVB polyHIPE (50:50%).

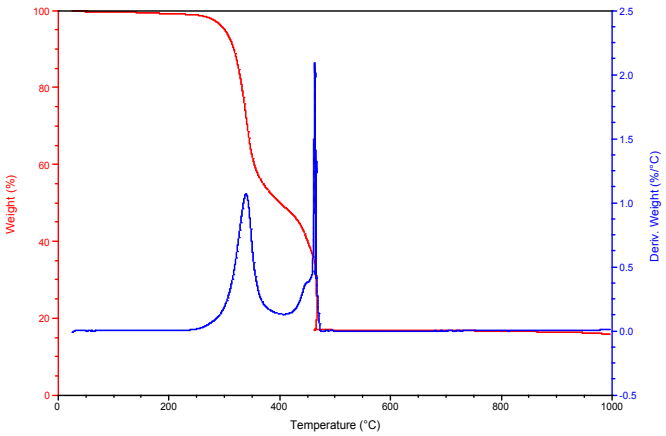

Figure 4.37. TGA trace of S-co-DVB polyHIPE (40:60%).

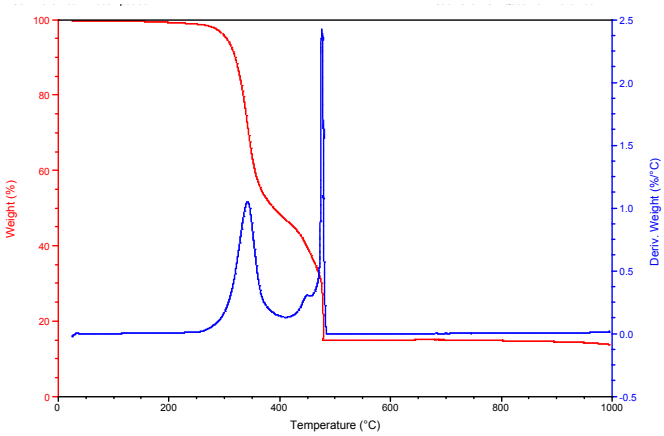

Figure 4.38. TGA trace of S-co-DVB polyHIPE (30:70%).

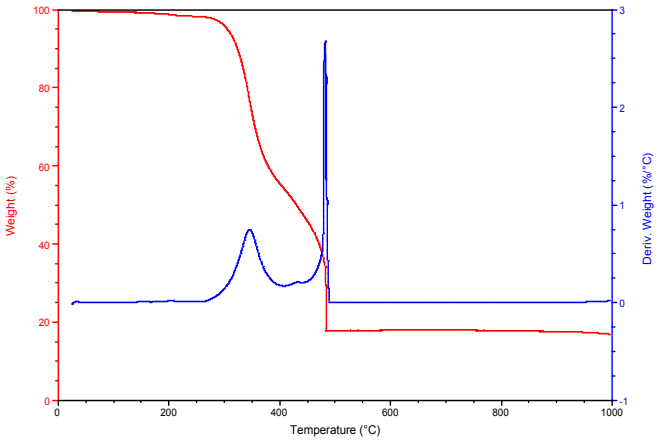

Figure 4.39. TGA trace of S-co-DVB polyHIPE 20:80%).

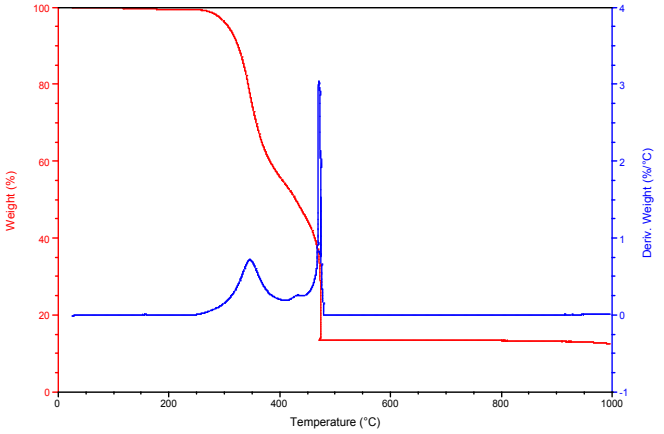

Figure 4.40. TGA trace of S-co-DVB polyHIPE (10:90%).

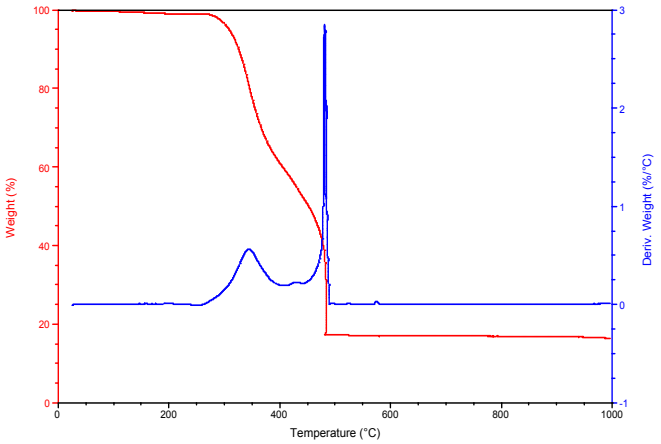

Figure 4.41. TGA trace of S-co-DVB polyHIPE (0:100%).

4.7.3 SEM images of t-BS-co-DVB polyHIPEs

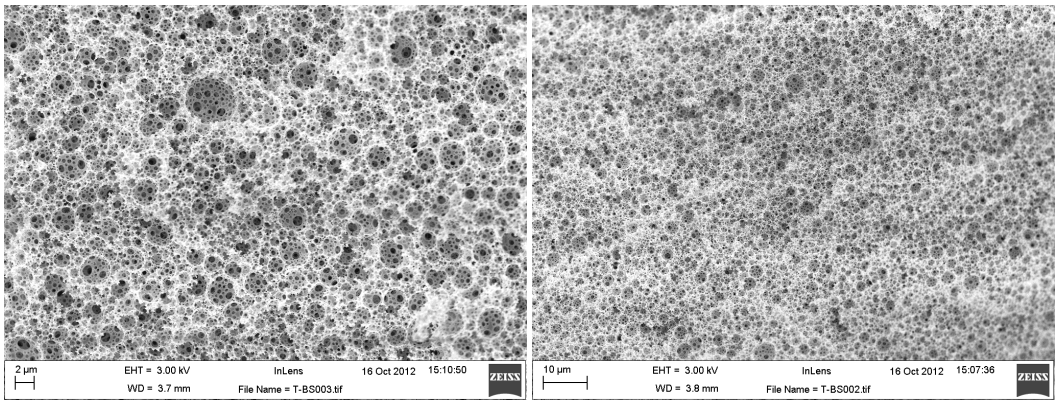

Figure 4.42. SEM images of t-BS-co-DVB (100%) polyHIPE. Scale bars are 2 µm and 10 µm respectively.

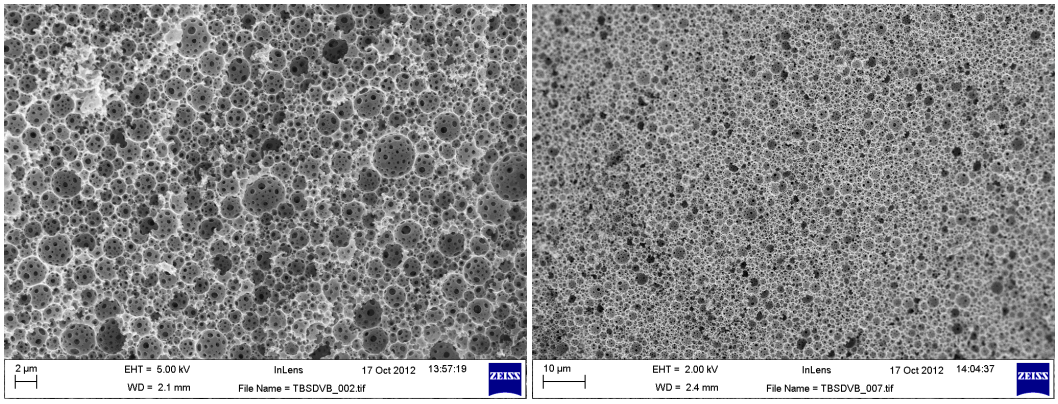

Figure 4.43. SEM images of t-BS-co-DVB (70:30%) polyHIPE. Scale bars are 2 µm and 10 µm respectively.

4.7.4 SEM images of S-co-para-DVB polyHIPEs

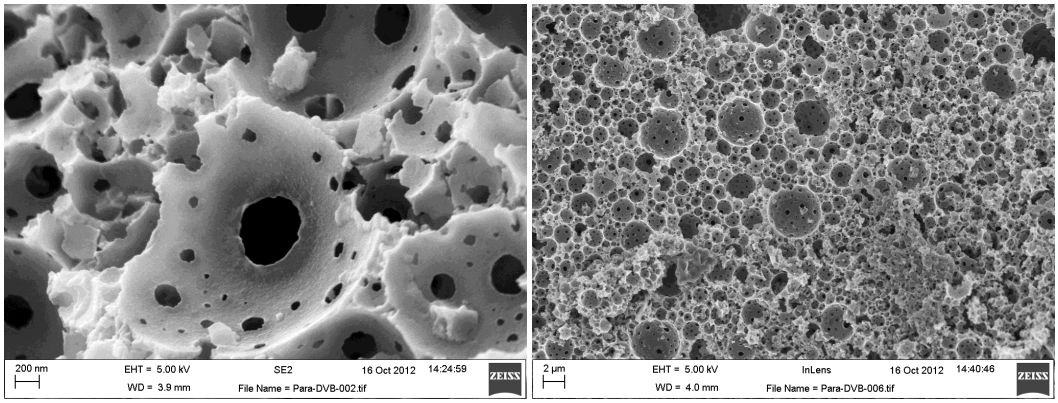

Figure 4.44. SEM images of S-co-para-DVB (100:0%) polyHIPE. Scale bars are 200 nm and 2 µm respectively.

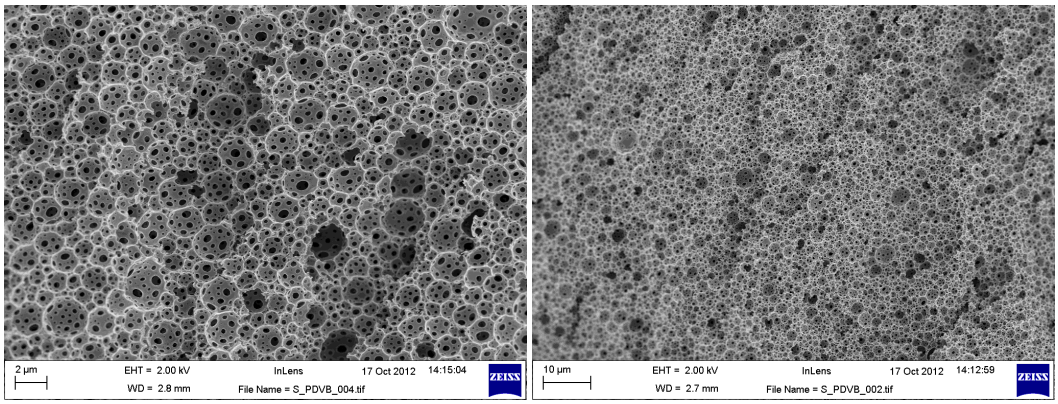

Figure 4.45. SEM images of S-co-para-DVB (70:30%) polyHIPE. Scale bars are 2 µm and 10 µm respectively.

4.7.5 SEM Images of Mixed Surfactant System PolyHIPEs

SEM images from mixed surfactant system polyHIPEs were obtained (figures 4.46-4.49). PolyHIPEs were fragile in most cases and so all materials were not coated with metal to inhance image contrast. Inhomogeneous 3-surfactant system structures exhibited charging, acquiring damage from the electron beam on imaging.

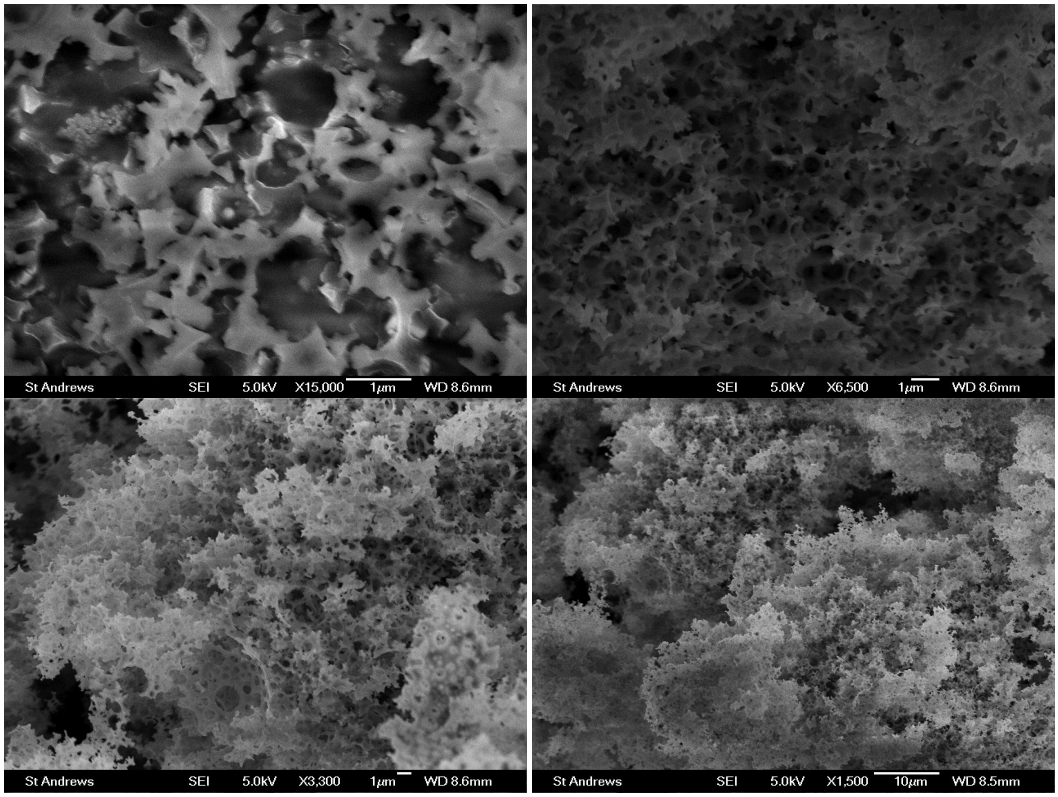

Figure 4.46. SEM images of a DVB polyHIPE using CTAB, DDBSS and Span® 80 surfactant system. Scale bars are 1 μm (top left, top right, bottom left) and 10 μm (bottom right).

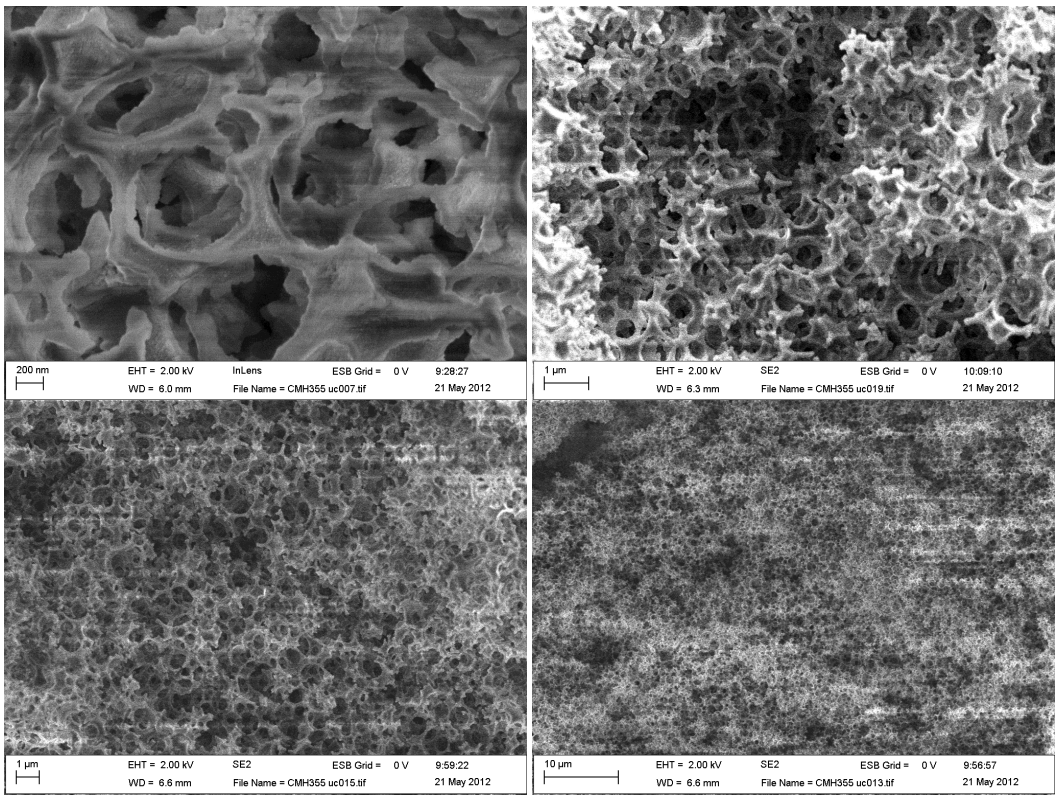

Figure 4.47. SEM images of a DVB polyHIPE using CTAB, DDBSS and Span® 20 surfactant system. Scale bars are 200 nm (top left), 1 μm (top right, bottom left) and 10 μm (bottom right).

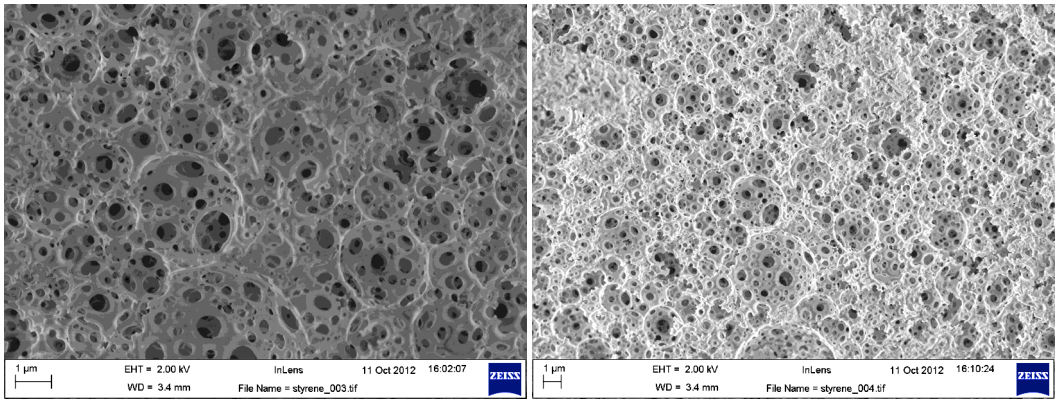

Figure 4.48. SEM images of a styrene polyHIPE using Span® 80 surfactant system. Scale bars are 1 µm (left and right).

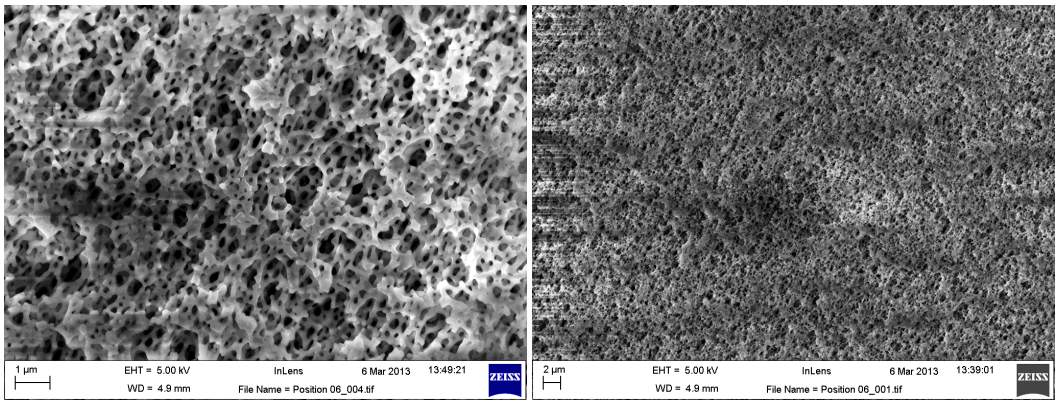

Figure 4.49. SEM images of a styrene polyHIPE using Span® 80/20 surfactant system. Scale bars are 1 µm (left and right).

T-BS polyHIPE SEM images are given in figures 4.50 and 4.51.

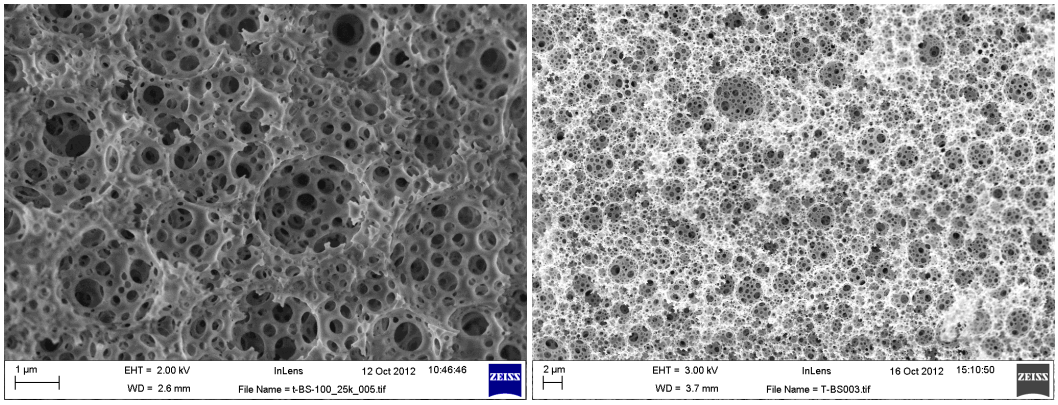

Figure 4.50. SEM images of a t-BS polyHIPE using Span® 80 surfactant system. Scale bars are 1 µm (left) and 2 µm (right).

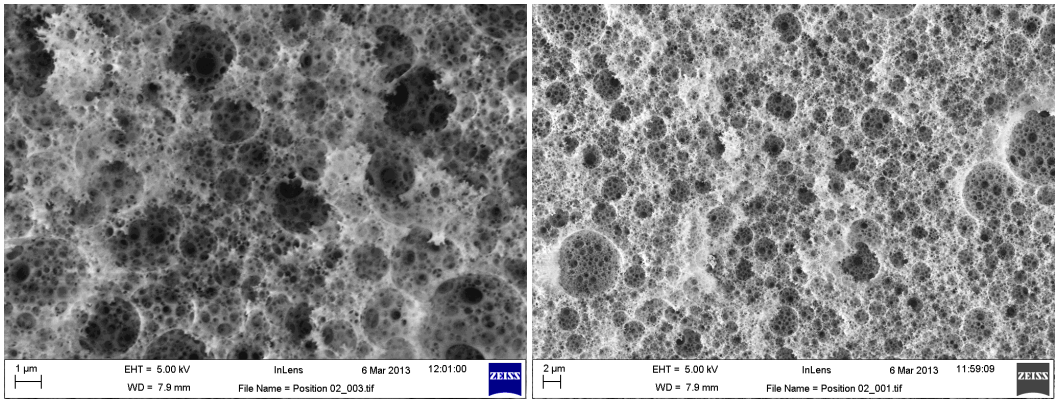

Figure 4.51. SEM images of a t-BS polyHIPE using Span® 80/20 surfactant system. Scale bars are 1 μm (left) and 2 μm (right).

DVB polyHIPE SEM images are given in figures 4.52 and 4.53.

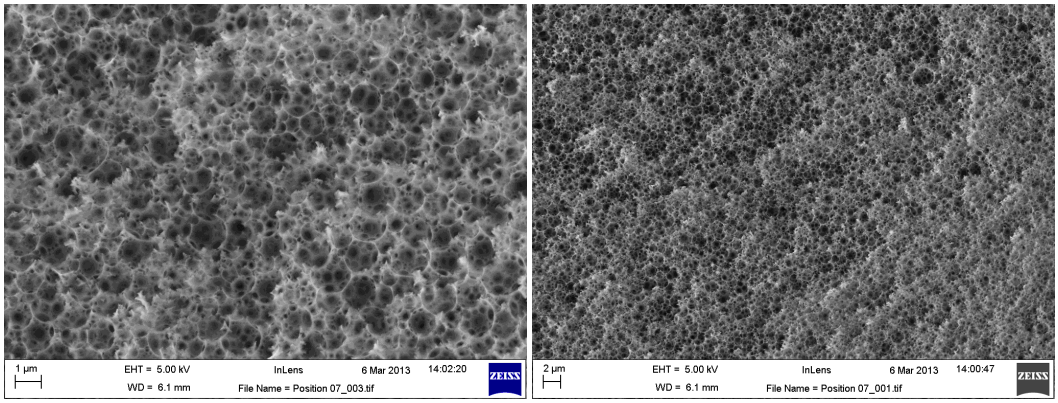

Figure 4.52. SEM images of a DVB polyHIPE using Span® 80/20 surfactant system. Scale bars are 1 μm (left) and 2 μm (right).

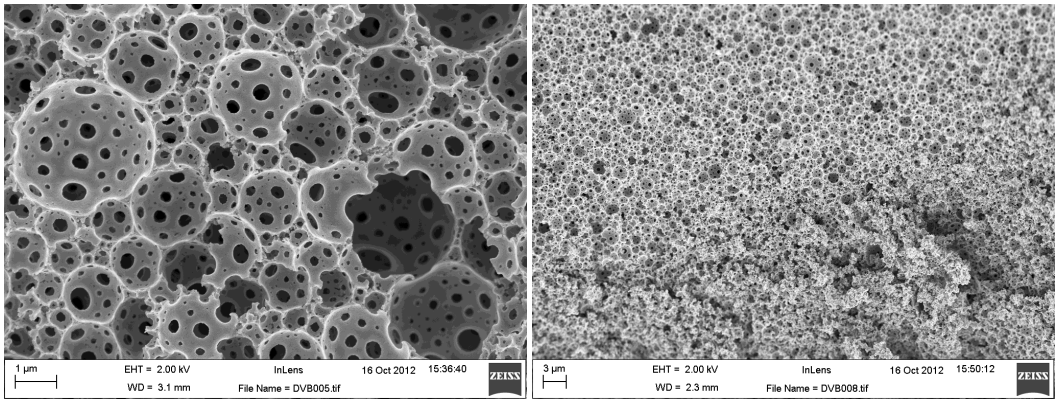

Figure 4.53. SEM images of a DVB polyHIPE using Span® 80 surfactant system. Scale bars are 1 μm (left) and 3 μm (right).

Para-DVB images are given in figures 4.54 and 4.55.

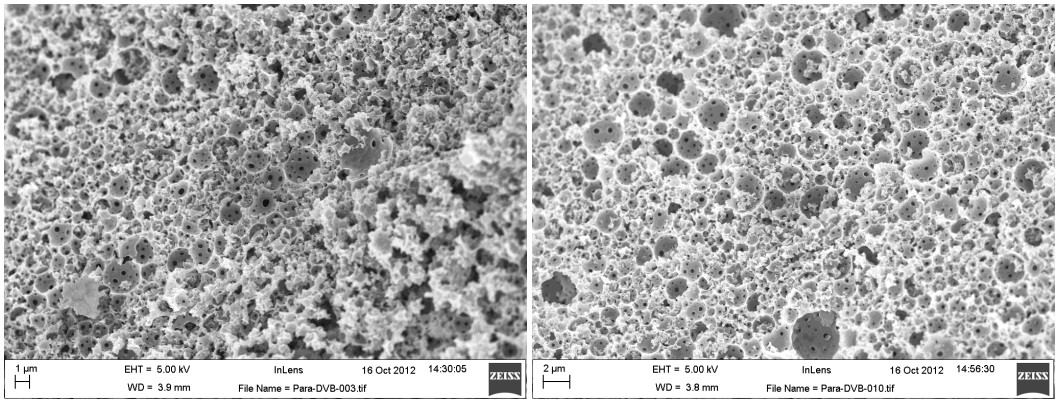

Figure 4.54. SEM images of a para-DVB polyHIPE using Span® 80 surfactant system. Scale bars are 1 µm (left) and 2 µm (right).

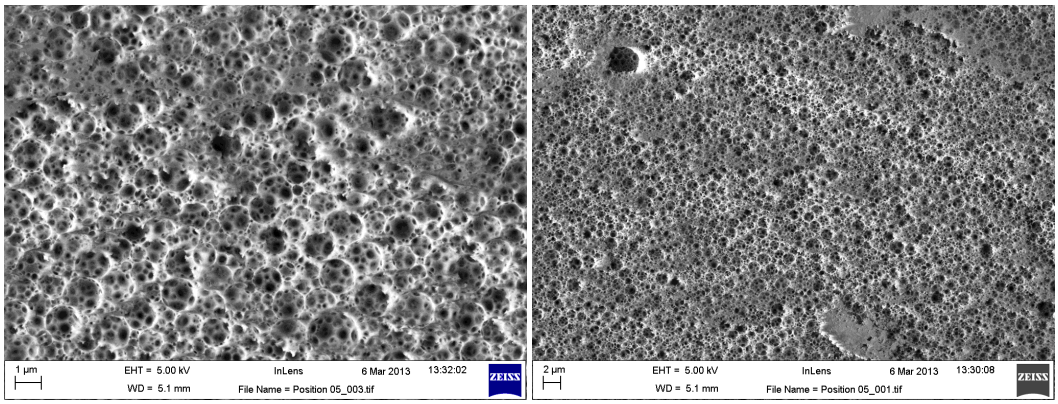

Figure 4.55. SEM images of a para-DVB polyHIPE using Span® 80/20 surfactant system.

4.7.6 Mercury Porosimetry Distributions of PolyHIPEs

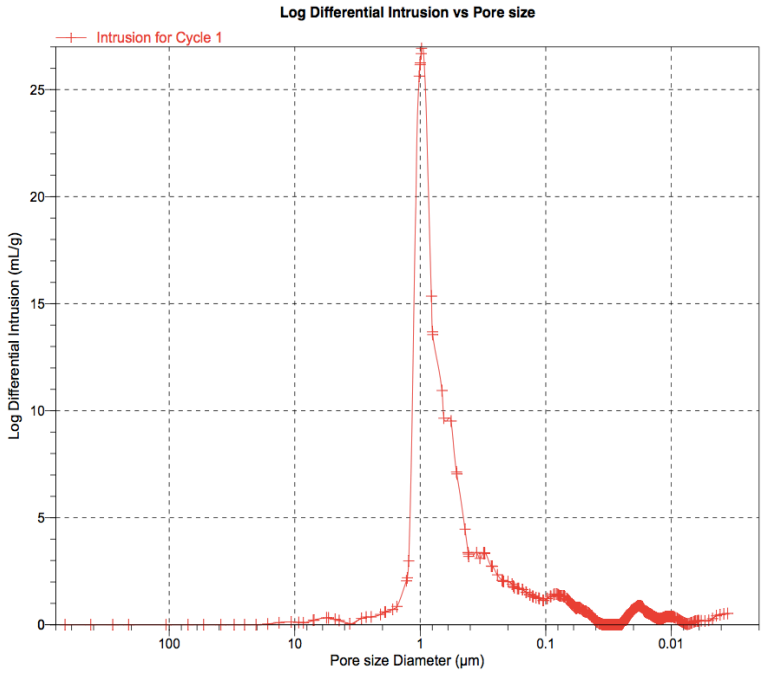

Figure 4.56. Pore intrusion distribution for S-co-DVB (80:20%) polyHIPE.

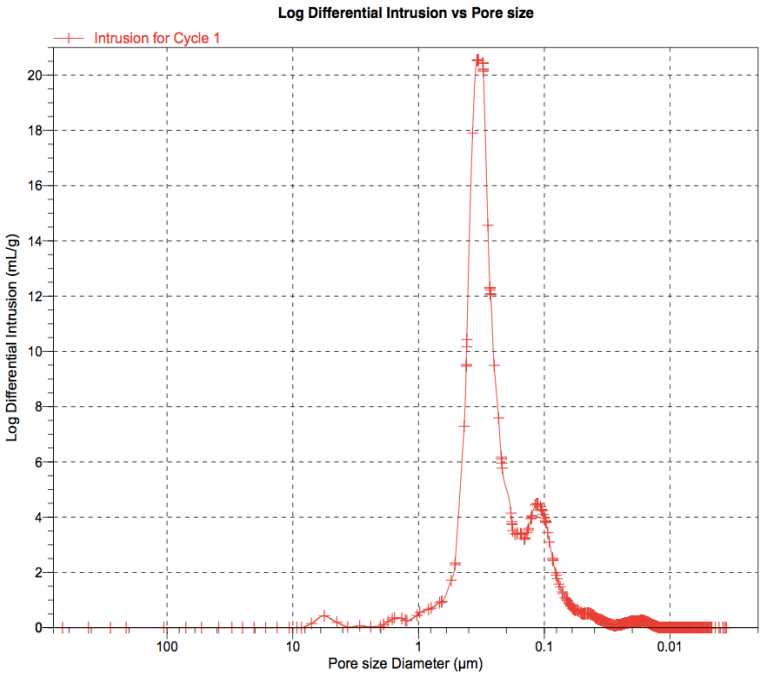

Figure 4.57. Pore intrusion distribution for S-co-DVB (70:30%) polyHIPE.

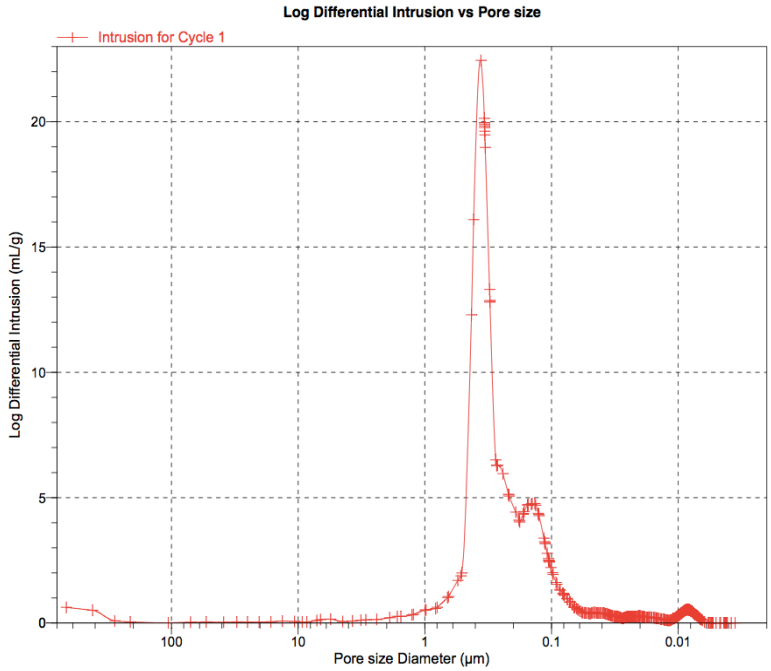

Figure 4.58. Pore intrusion distribution for S-co-DVB (30:70%) polyHIPE.

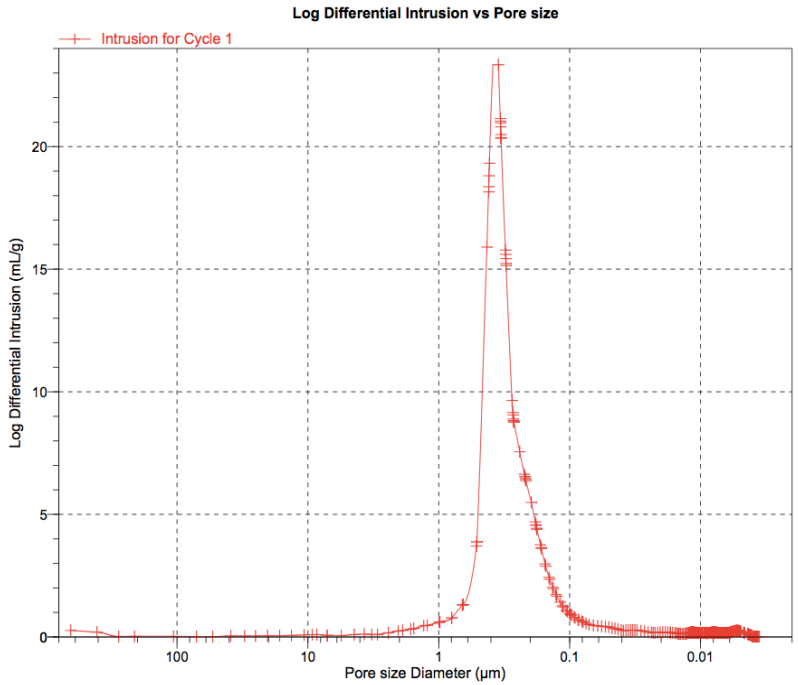

Figure 4.59. Pore intrusion distribution for 100% DVB polyHIPE.

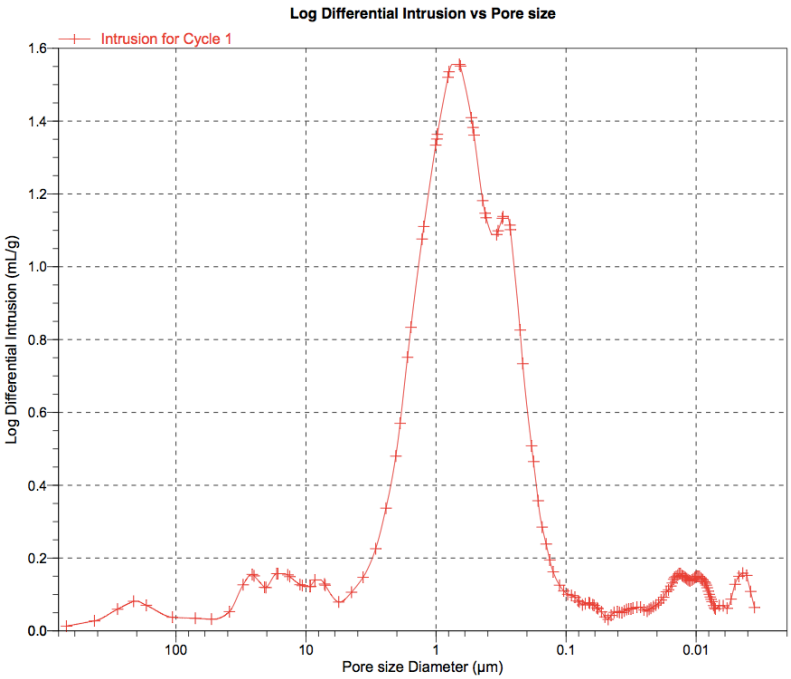

Figure 4.60. Pore intrusion distribution for 100% styrene polyHIPE with Span® 80/20 surfactant system.

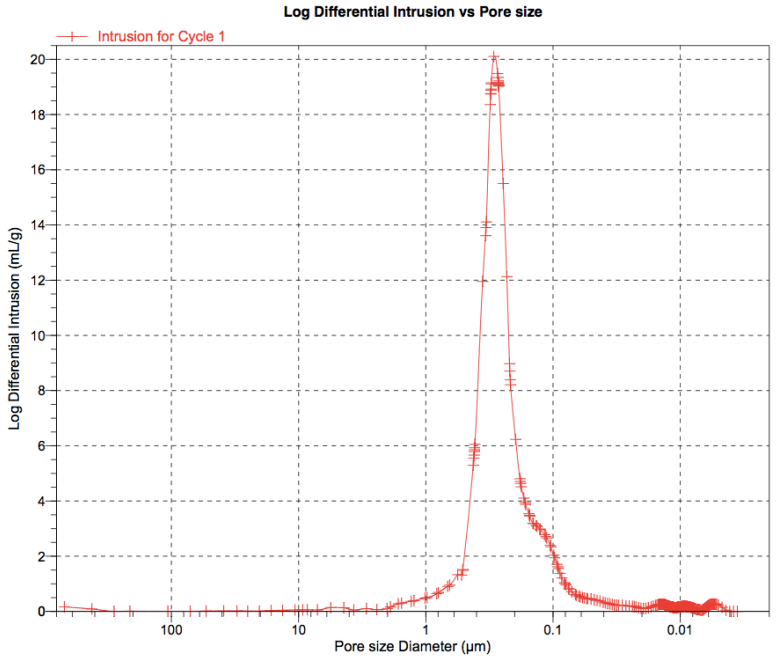

Figure 4.61. Pore intrusion distribution for DVB polyHIPE with Span® 80/20 surfactant system.

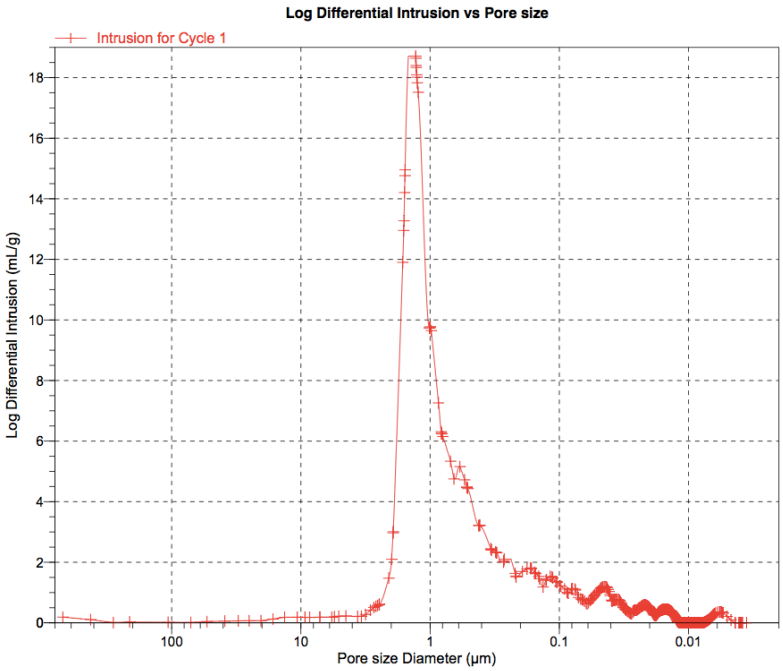

Figure 4.62. Pore intrusion distribution for t-butyl styrene polyHIPE with Span® 80/20 surfactant system.

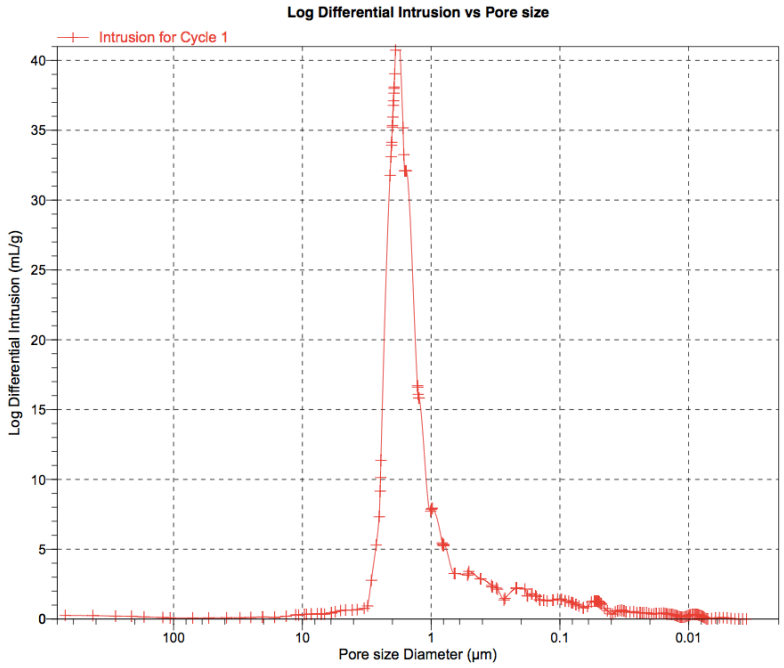

Figure 4.63. Pore intrusion distribution for para-DVB polyHIPE with Span® 80/20 surfactant system.

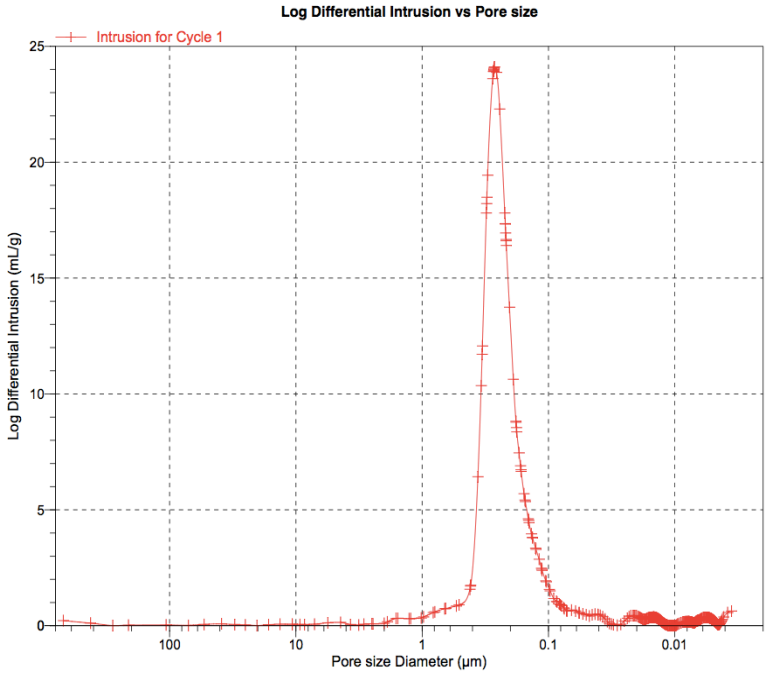

Figure 4.64. Pore intrusion distribution for 100% t-BS polyHIPE.

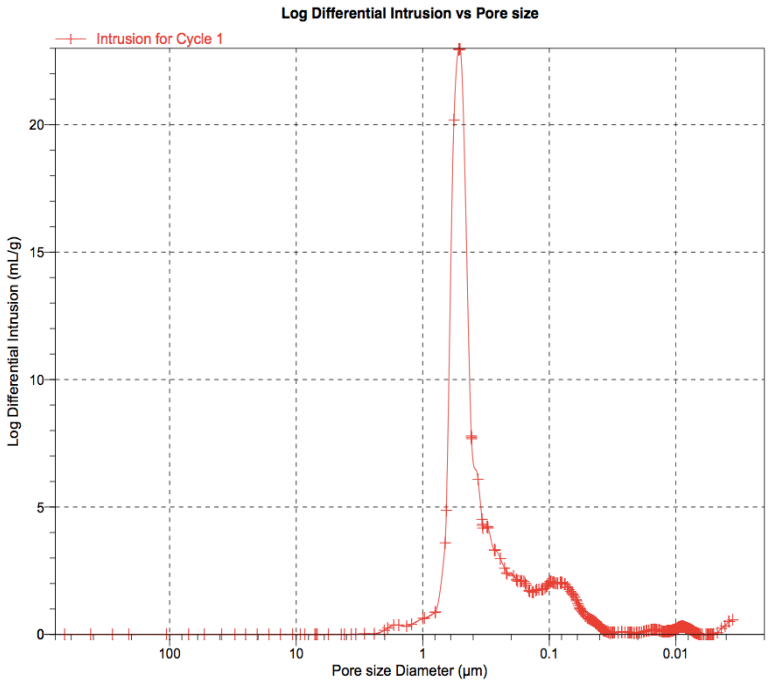

Figure 4.65. Pore intrusion distribution for t-BS-co-DVB (70:30%) polyHIPE.

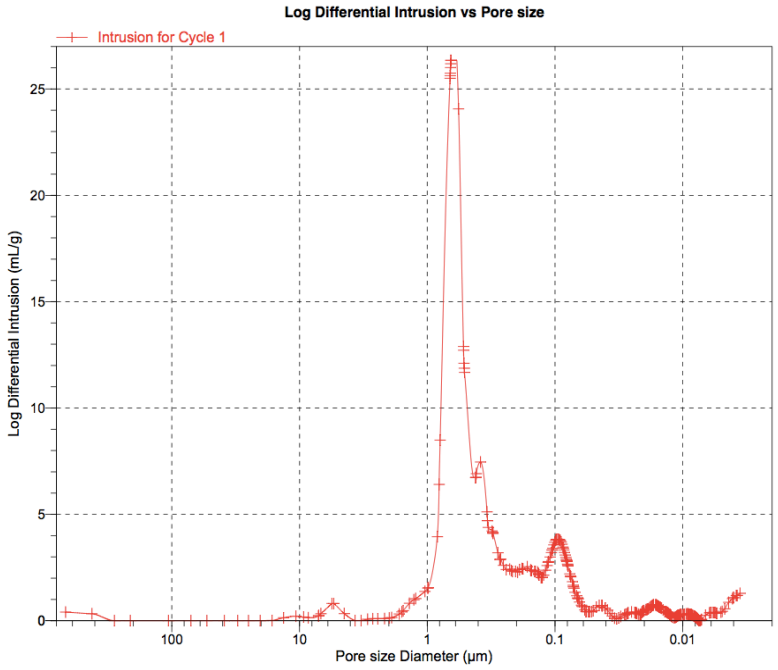

Figure 4.66. Pore intrusion distribution for t-BS-co-DVB (30:70%) polyHIPE.

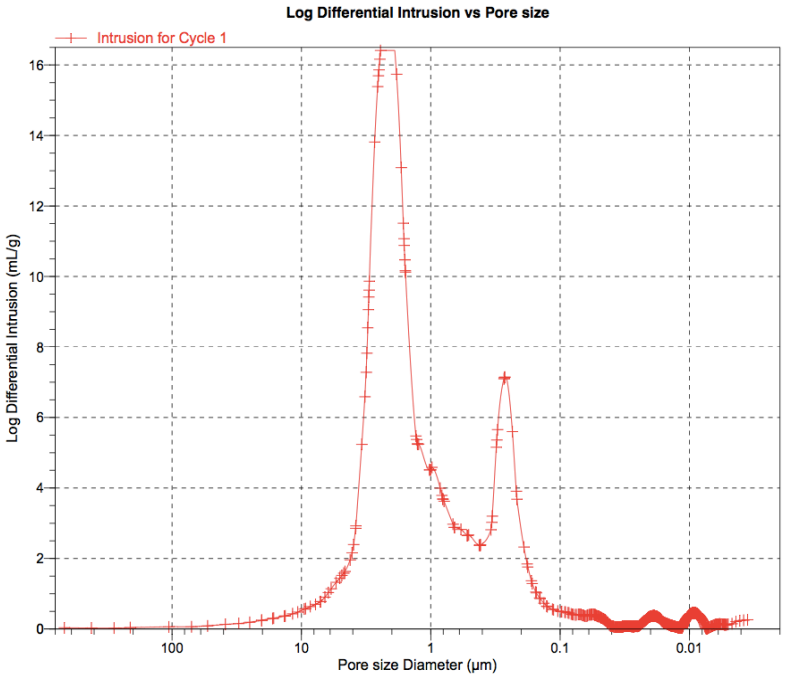

Figure 4.67. Pore intrusion distribution for 100% para-DVB polyHIPE.

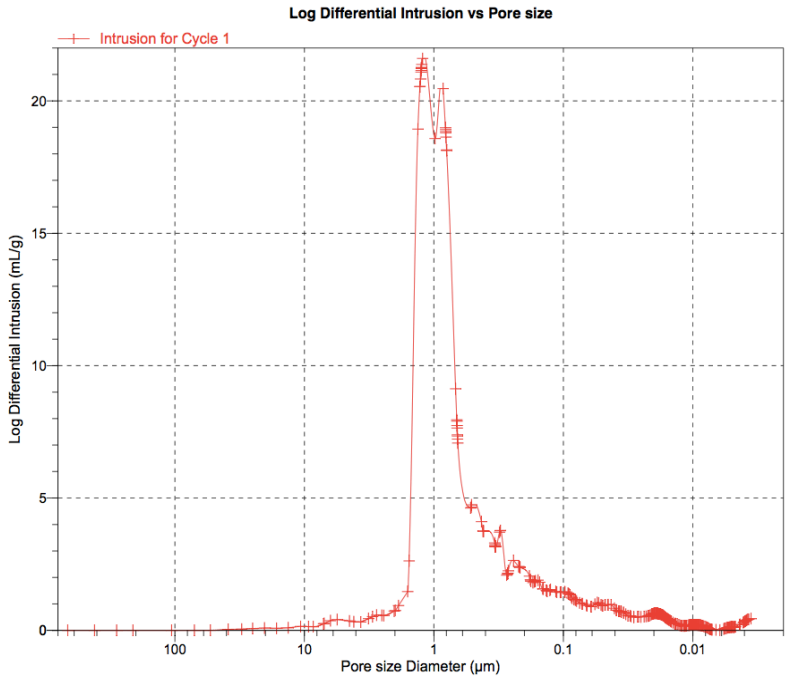

Figure 4.68. Pore intrusion distribution for S-co-para-DVB (70:30%) polyHIPE.

4.7.7 Microscale Inhomogeneity of PolyHIPEs from X-ray Radiography

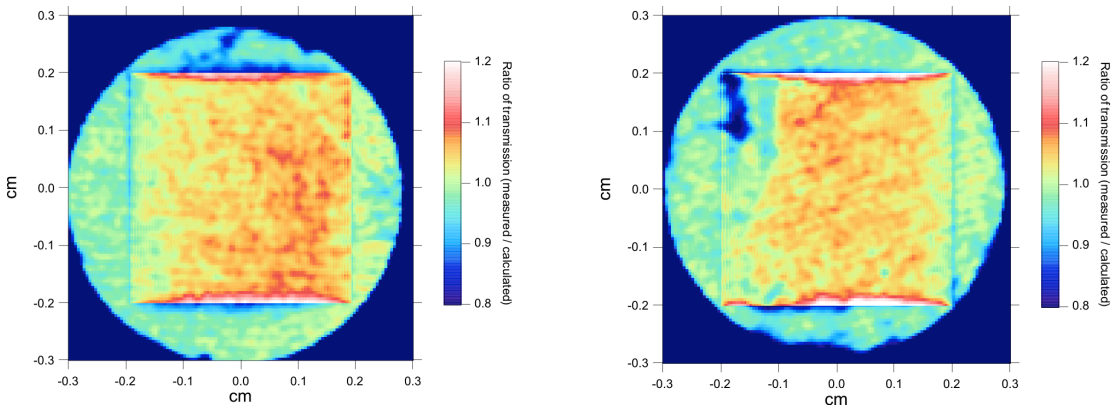

Figure 4.69. X-radiographs of two different S-co-DVB polyHIPEs. The red areas indicate regions of higher density. AWE Internal Report, 2013.

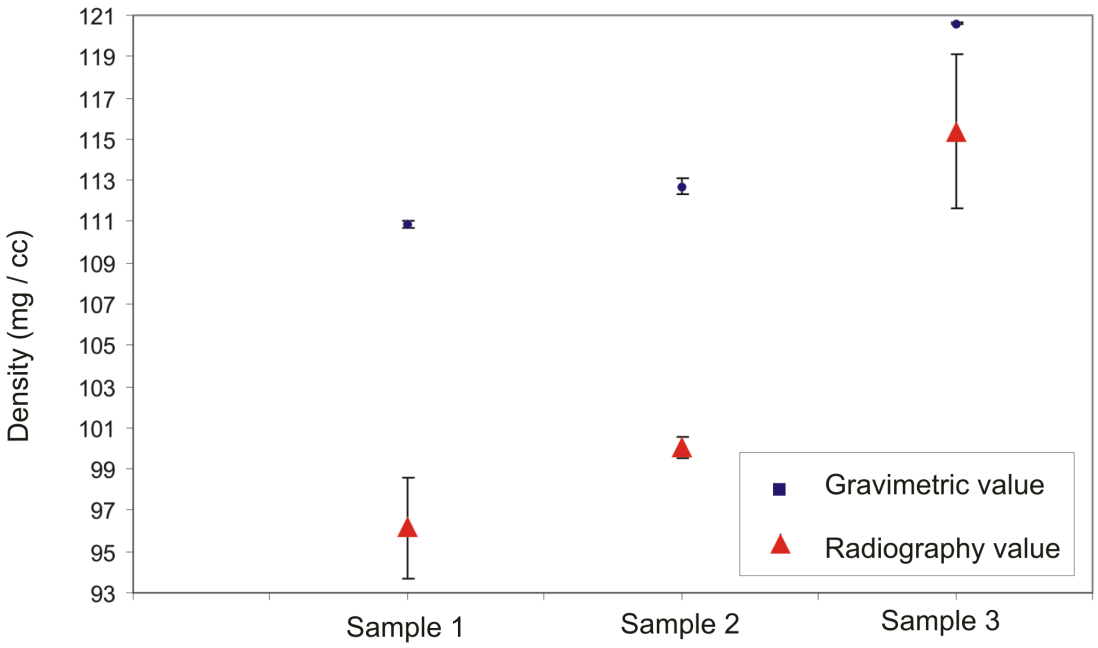

Figure 4.70. S-co-DVB polyHIPE density measurements from radiography and gravimetric techniques.

4.8 References

1 J. M. Williams and D. A. Wrobleski, *Langmuir*, 1988, **4**, 656–662.

2 J. M. Williams, A. J. Gray, and M. H. Wilkerson, *Langmuir*, 1990, **6**, 437–444.

3 P. Hainey, I. M. Huxham, B. Rowatt, D. C. Sherrington, and L. Tetley, *Macromolecules*, 1991, **24**, 117–121.

4 N. R. Cameron and D. C. Sherrington, *Colloid and Polymer Science*, 1996, **274**, 592–595.

5 A. Barbetta, M. Dentini, E. M. Zannoni, and M. E. De Stefano, *Langmuir*, 2005, **21**, 12333–41.

6 D. Barby and Z. Haq, Eur. Pat. Appl. 60138, 1982.

7 M. S. Silverstein, *Progress in Polymer Science*, 2014, **39**, 199–234.

8 M. F. Ashby, *Metallurgical Transactions A*, 1983, **14A**, 1756–1768.

9 J. M. Williams, J. J. Bartos III, and M. H. Wilkerson, *Journal of Materials Science*, 1990, **25**, 5134–5141.

10 J. M. Williams, *Water-in-Oil Emulsions and Toroidal microstructures*, Springfield, 1989.

11 N. R. Cameron and A. Barbetta, *Journal of Materials Chemistry*, 2000, **10**, 2466–2471.

12 A. Barbetta and N. R. Cameron, *Macromolecules*, 2004, **37**, 3202–3213.

13 N. R. Cameron, *Polymer*, 2005, **46**, 1439–1449.

14 A. Mercier, S. Kuroki, I. Ando, H. Deleuze, and O. Mondain-Monval, *Journal of Polymer Science Part B: Polymer Physics*, 2001, **39**, 956–963.

15 G. Ceglia, L. Mahéo, P. Viot, D. Bernard, A. Chirazi, I. Ly, O. Mondain-Monval, and V. Schmitt, *The European physical journal. E, Soft matter*, 2012, **35**, 9708.

16 Y. Luo, A.-N. Wang, and X. Gao, *Soft Matter*, 2012, **8**, 1824–1830.

17 P. J. Hore, *Nuclear Magnetic Resonance*, Oxford University Press, Inc., New York, 1995.

18 R. K. Harris, *Nuclear Magnetic Resonance; A Physiochemical View*, Longman Scientific & Technical, Harlow, 2nd edn., 1987.

19 V. Hronský, J. Murín, and J. Uhrin, *Czechoslovak Journal of Physics*, 2006, **56**, 289–302.

20 J. Brandrup and E. H. Immergut, *Polymer Handbook*, Wiley-Interscience, 3rd edn., 1989.

21 A. Menner and A. Bismarck, *Macromolecular Symposia*, 2006, **242**, 19–24.

22 Y. Luo, A.-N. Wang, and X. Gao, *Soft Matter*, 2012, **8**, 7547.

23 A. Menner, R. Verdejo, M. Shaffer, and A. Bismarck, *Langmuir : the ACS journal of surfaces and colloids*, 2007, **23**, 2398–403.

24 H. Deleuze, R. Faivre, and V. Herroguez, *Chemical communications*, 2002, 2822–3.

25 K. Benmachou, H. Deleuze, and V. Heroguez, *Reactive & Functional Polymers*, 2003, **55**, 211–217.

5. TD-NMR Thermal Analysis Studies Investigating Molecular Motion of Styrene-co-Divinyl Benzene PolyHIPEs and Derivatives

5.1 Introduction

PolyHIPEs for laser targets require extensive characterisation, sometimes at the micro-scale depending on the specific application. PolyHIPEs are complicated emulsion systems with a dependency on many chemical and physical factors that can affect the resulting structure. The high internal phase volume of HIPEs puts an increased strain on the stabilising surfactant film, and as a result polyHIPEs synthesised from the same starting materials can have different properties depending on the conditions of polymerisation. TD-NMR which measures nuclear spin relaxation times was identified as a new technique to characterise polyHIPEs in chapter 4. Thus, variations in polyHIPE synthesis will affect the structure (and molecular motion) and hence will affect NMR relaxation times. In addition, different orders of frequency can be probed by this technique, which allows for an examination of different frequencies of motion. Investigations using styrene and t-butyl styrene demonstrated the effect of a large group on relaxation. Synthesis and investigation of a vinyl naphthalene polyHIPE provided some information on the effect of a large planar group on relaxation. Studying NMR relaxation as a function of molecular motion at different temperatures aimed to answer questions that were not clear in chapter 4 on polyHIPE emulsion instability.

This chapter describes the NMR relaxation properties of polyHIPEs at different temperatures. The effects of different groups attached to the styrene aromatic ring such as t-butyl and vinyl naphthalene were investigated. Deuterated styrene was copolymerised with DVB to investigate clustering of DVB in more detail by measuring NMR relaxation times at varied temperatures.

5.2 Materials and reagents

Reagents used were styrene, divinyl benzene (80), para-divinyl benzene, methyl methacrylate, methanol, 2-vinyl naphthalene, deionised water, deuterated water (D_2O), Span® 80 (sorbitan monooleate), azobisisobutyronitrile (AIBN), potassium persulfate.

All chemicals were used as bought except for the monomers where the inhibitors were extracted using a silica column before use.

5.3 Synthesis of polyHIPEs

All polyHIPEs were prepared using the double syringe method, as described in chapter 3, section 3.1. Details of formulations and experiments are also described in chapter 3, section 3.1.

The HIPEs were prepared in 10 cm^{-3} glass syringes (Hamilton) and then transferred to 10 cm^{-3} plastic syringes to polymerise in an oven (60°C, 72 hours). The aqueous phase contained 5% potassium persulfate initiator by weight. It has been reported that 10% initiator reduces pore size in S-co-DVB polyHIPEs,[1,2] however solubility of 10% was an issue so 5% was used instead, and the solubility limit of potassium persulfate at 20°C is 4.5 g per 100 mL. The oil phase contained the monomers and surfactant, which were mixed thoroughly. The surfactant concentration (28%) was chosen for similar reasons to the initiator.

Variable temperature T_1 and $T_{1\rho}$ relexation experiments were generally performed between –50°C and +150°C in 10°C steps (detailed in chapter 3) using the TD-NMR apparatus. Furthermore, this is beyond the +100°C Tg of styrene meaning any changes in relaxation with phase transition could be observed. Table 5.1 lists the materials used for analysis. All data for the relaxation profiles was transformed into the natural log to be consistent with literature.[3,4]

Table 5.1. PolyHIPE systems that underwent varied temperature TD-NMR relaxation experiments.

PolyHIPE system
S 100%
S-co-DVB (80:20)
S-d8-co-DVB (80:20)
S-co-para-DVB (70:30)
t-BS-co-DVB (70:30)

The formulations of S-co-DVB containing 10% to 30% DVB corresponded to the highest modulus S-co-DVB polyHIPE in this work and literature.[5] PolyHIPEs in this region were chosen for varied temperature relaxation experiments. TD-NMR identified this formulation to be most rigid (chapter 4). Furthermore, variable temperature relaxation measurements of the non-deuterated equivalent were obtained to compare the structural relaxation. It was postulated that a better understanding of why these polyHIPEs had high modulus could be gained by investigating these particular formulations using variable temperature relaxation experiments.

5.4 Instrumentation and characterisation

Techniques used to characterise polyHIPEs were SEM, mercury porosimetry, elemental analysis, SSNMR, TD-NMR, DSC, GPC, TGA and DMA. Instrument and experiment details are given in chapter 3.

5.5 Results and discussion

5.5.1 Variable temperature NMR relaxation of polyHIPEs

Variable temperature NMR relaxation experiments were performed to provide more information on the molecular motion of polyHIPEs. Polystyrene GPC standards revealed molecular motion behaviour beyond the T_1 minimum. However, it was unknown how the molecular motion of polyHIPEs compared to GPC standards, and the effect on specific regions that can arise from cross-linking. Also, these experiments complemented the work carried out on these materials in chapter 4, providing a deeper understanding of these materials.

Initially, experiments were performed on a polyHIPE composed of 100% styrene in order to gain an understanding how factors such as density and polyHIPE structure affect molecular motion, and thus relaxation. The styrene polyHIPE relaxation was similar to the polystyrene GPC standard but more downshifted by comparison (figure 5.1). Downshift is in reference to what part of the curve is visible compared to what was seen by the GPC standard in chapter 3, and literature.[4] GPC data measured the Mw of styrene polyHIPE to be 55,000 whereas the polystyrene GPC standard was 524,000 therefore it was thought that the polyHIPE structure could be the reason for increased rigidity than the higher molecular weight species. Free radical polymerisation of the monomer in the gaps between water droplets created a rigid network of polystyrene. This meant that the small group rotations of styrene polyHIPE were constrained by comparison to the GPC standard. Furthermore, it was though that the polyHIPE structure was the reason for shorter relaxation times in styrene polyHIPE (figure 5.2). Additional oxygen present in air would allow for more efficient relaxation (appendix 5.7.1).

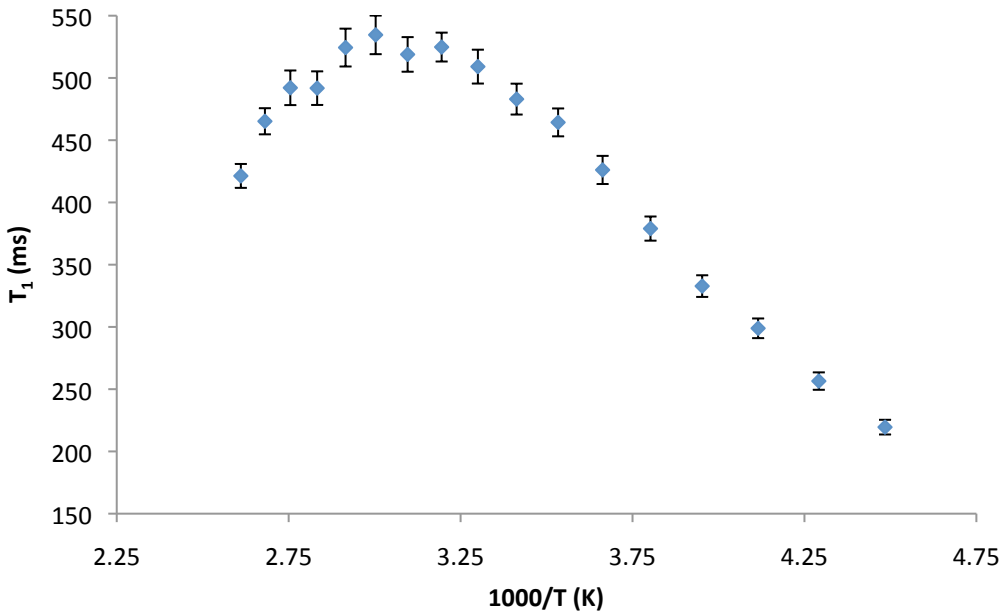

Figure 5.1. T_1 relaxation profile of styrene 100% polyHIPE between –50°C and +110°C.

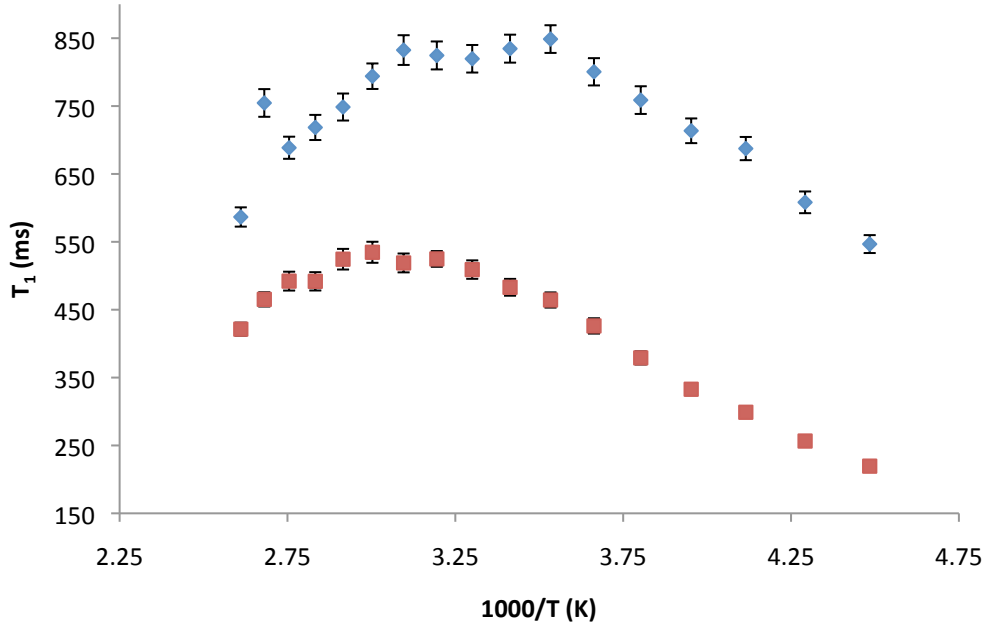

Figure 5.2. T_1 relaxation profiles of styrene 100% polyHIPE (red) and styrene GPC standard (blue) between –50°C and +110°C.

The variable temperature $T_{1\rho}$ relaxation profile of S polyHIPE revealed a different behaviour to T_1 (figure 5.3). This can be explained by the different dependency the frequency of motions that T_1 and $T_{1\rho}$ are dependent on; $T_{1\rho}$ is more dependent on the strength of the magnetic field rather than the resonance frequency, whereas T_1

is the opposite.[4] Further explanation was given in chapter 3 for the polystyrene GPC standard. Decreasing relaxation times with temperature suggested that at this order of frequency, the material was in a rigid motion regime before the $T_{1\rho}$ minimum. Substantial extension of the temperature range would be required to include all the motion regimes, which would be difficult to achieve without causing damage to the polyHIPEs. In addition, there was one curved section in the profile between 10°C and 100°C, which could be attributed to a pre glass transition motion as seen in PVDF, or rotation of polymer chains as a function of density or proximity to each other as the temperature increased. DSC indicated a transition at 110°C, which could fit with the pre glass transition motion. This was not clear so further experiments with t-butyl styrene polyHIPEs were performed (section 5.5.2).

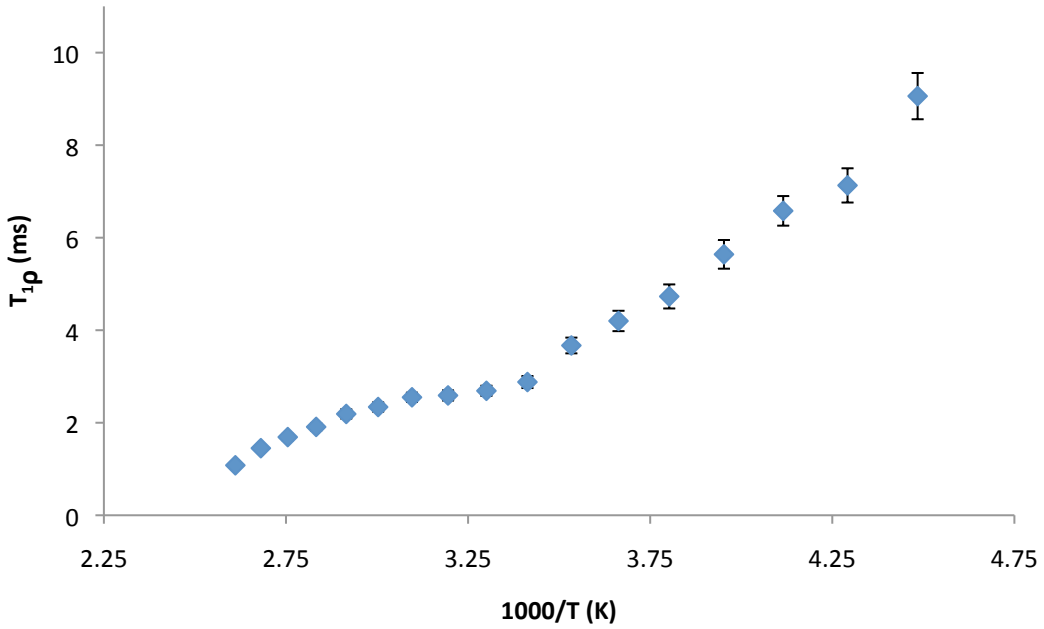

Figure 5.3. $T_{1\rho}$ relaxation profile of styrene 100% polyHIPE between –50°C and +110°C.

Comparison of polystyrene GPC standard and styrene polyHIPE $T_{1\rho}$ relaxation revealed almost identical behaviour despite the large difference in molecular weights (figure 5.4). This seemed to contradict the preliminary study (chapter 3) on different molecular weight GPC standards, but NMR relaxation is dependent on more than just molecular weight (though molecular motion). The two samples differed in molecular weight, but also microstructure; polystyrene GPC standard

consisting of entangled chains of polymer whereas styrene polyHIPE is a pore-templated low density polymer. Perhaps the unique arrangement of polyHIPE structure resulted in an efficient configuration of the polymer chains according to NMR, which resulted in near identical relaxation to the GPC standard.

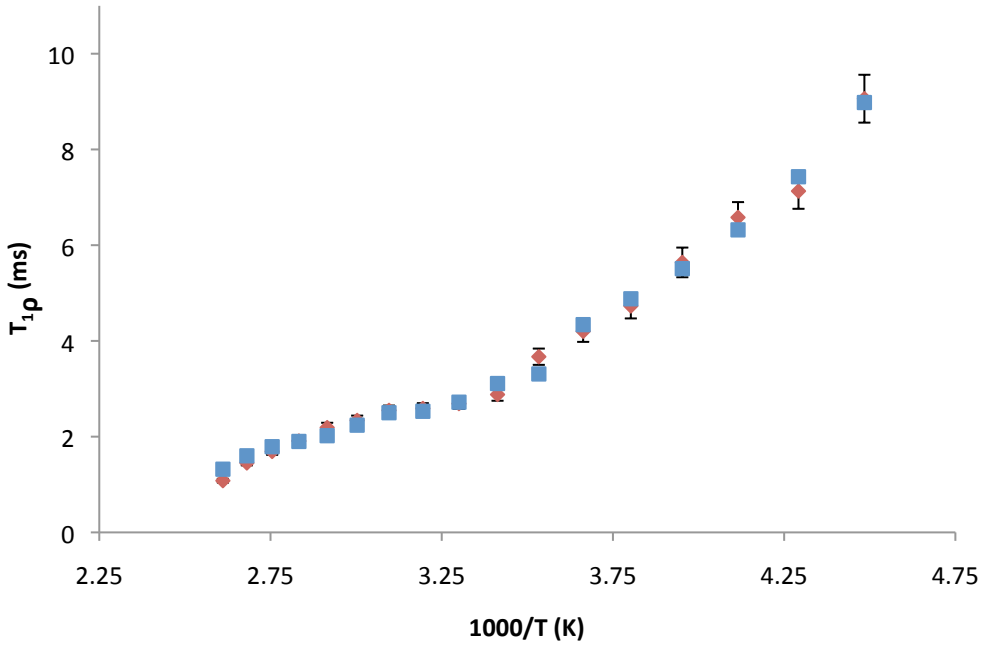

Figure 5.4. $T_{1\rho}$ relaxation profiles of styrene 100% polyHIPE (red) and styrene GPC standard (blue) between –50°C and +110°C.

Relaxation behaviour of cross-linked regions and DVB in S-co-DVB polyHIPEs was unclear after studies of styrene polyHIPEs from chapter 4. ^{13}C CPMAS SSNMR data revealed that the backbone region became more rigid with cross-linking, this was highlighted in the variable temperature $T_{1\rho}$ relaxation measurements of 100% styrene polyHIPE. In addition, ^{13}C CPMAS SSNMR of S-d_8-co-DVB suggested that the aromatic region was a particularly disordered in S-co-DVB polyHIPEs. To investigate cross-linking regions in more detail, styrene protons were masked from TD-NMR by synthesis of a polyHIPE with 99.9% styrene-d_8 and D_2O internal phase, resulting in DVB as the only portion of the material that was observed by ^{1}H NMR. SEM images of S-d_8-co-DVB polyHIPE revealed typical polyHIPE architectue (figure 5.5).

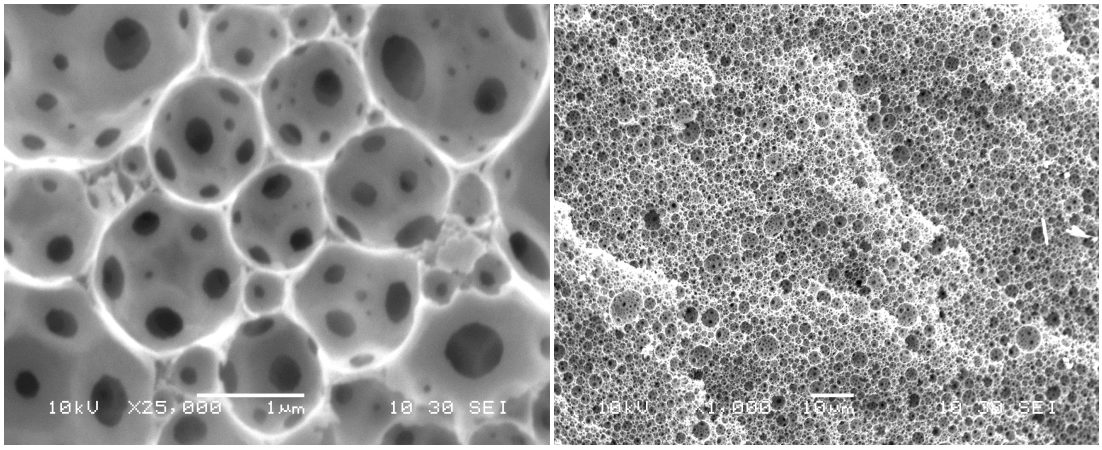

Figure 5.5. SEM images of S-d_8-co-DVB polyHIPE with D_2O internal phase. Scale bars are 1 μm (left) and 10 μm (right).

Variable temperature T_1 and $T_{1\rho}$ relaxation experiments for S-d_8-co-DVB and S-co-DVB polyHIPEs revealed quite different behaviour of motion (figure 5.6). The relaxation profile of S-co-DVB agreed with that for styrene polyHIPE whereas the deuterated S-d_8-co-DVB polyHIPE indicated increased rigidity as a result of cross-linking DVB as the profile was downshifted by comparison. Furthermore, the relaxation times for S-d_8-co-DVB polyHIPE were shorter than S-co-DVB polyHIPE suggesting that the observed region relaxed efficiently, which appeared to contradict what may be expected for cross-linking regions in a polyHIPE. A plausible explanation was that DVB was clustering and TD-NMR can detect these regions. The effect was to speed up relaxation due to efficient motion of hanging/end groups of DVB. This was unexpected as the 80:20 molar ratio chosen was the 'ideal' cross-linking according to previous T_1 and Young's modulus data reported in chapter 4. This highlighted that stability issues with surfactants in polyHIPEs were more prevalent than originally assumed.

The prohibitive cost of purchase and technical difficulties in synthesising 100% deuterated DVB meant that performing relaxation experiments with the cross-linking regions masked was not practical. It would be expected that the relaxation profile of 100% deuterated DVB (in S-co-DVB) would resemble the profile of the polystyrene GPC standard; higher shifted by comparison to S-co-DVB. Whilst it is known that many different relaxations exist in materials,[6–8] thus it has not been

shown in polyHIPEs using TD-NMR before. For laser target materials detailing multiple relaxations was significant because understanding of polyHIPE structure can help to characterise polyHIPEs for future high energy laser experiments that heavily rely on homogeneity of structure.

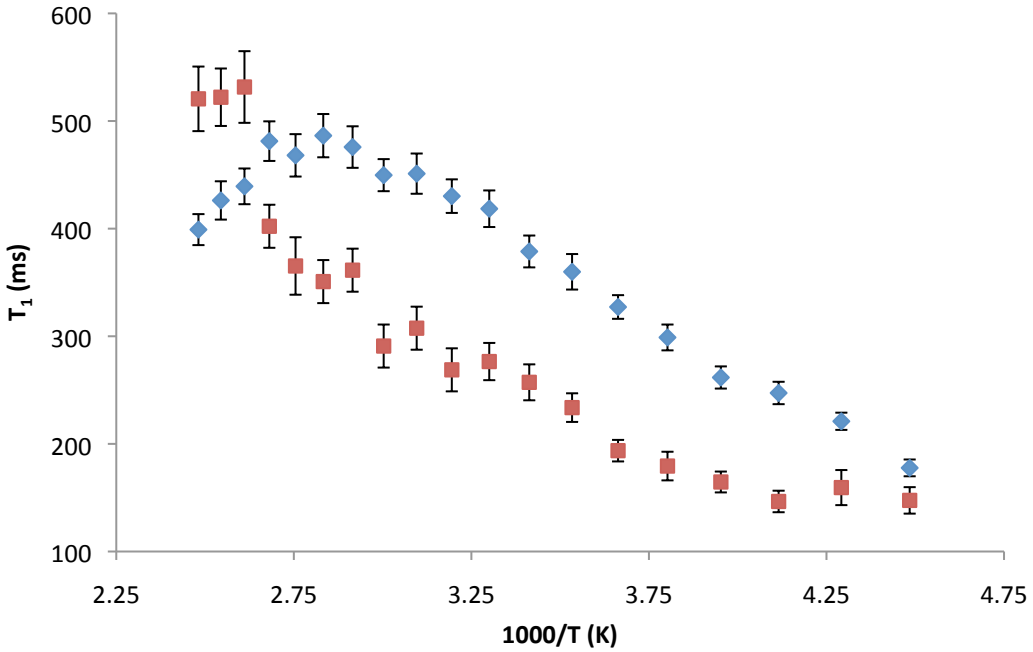

Figure 5.6. T_1 relaxation profiles of S-co-DVB (blue) and S-d_8-co-DVB (red) polyHIPEs between –50°C to +130°C.

$T_{1\rho}$ data for S-d_8-co-DVB revealed interesting behaviour, particularly in comparison to S-co-DVB (figure 5.7). Considering S-d_8-co-DVB first, the relaxation across the temperature range has a sinusoidal behaviour that was decreasing in relaxation time as the temperature was increased. The decrease in relaxation time as a function of temperature was consistent with the other materials examined in this manner throughout this work. However, the wave type behaviour of the relaxation profile is more difficult to explain. One postulate considered that there were many clusters of DVB of different sizes and shapes and the increasing temperature was effectively releasing these clusters depending on their size/structure. The releasing of these structures could allow for more structural motion of the polymer chains, decreasing the molecular order that $T_{1\rho}$ is dependent on. Another possibility was experimental

error as the quantity of protonated species was very low, because both trends were consistent.

Moreover, the increased relaxation times of S-d_8-co-DVB indicated that the polymer chains were a significantly different structural arrangement than the bulk polyHIPE. This behaviour was attributed to the fact that the floppy styrene chains were not observed. In addition, the longer relaxation times reflected the effect of cross-linking and clustering of the polymer chains creating a structure that allowed more efficient spin polarization. It would be expected that with improved synthetic procedures greater homogeneity of the polyHIPE would be realised, and these improvements can be observed using this technique. The ability to selectively observe these regions by incorporation of deuterated styrene in the polyHIPE could result in wider application of this method to other applications using other deuterated monomers.

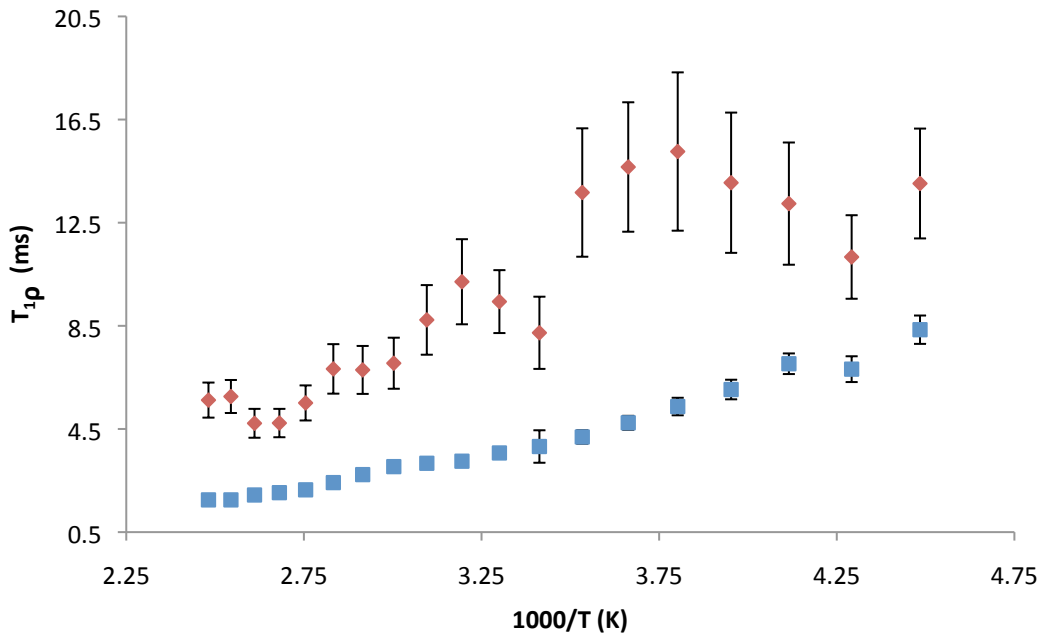

Figure 5.7. $T_{1\rho}$ relaxation profiles of S-co-DVB (blue) and S-d8-co-DVB (red) polyHIPEs between –50°C to +130°C.

In addition, studies of polyHIPEs in chapter 4, including S-co-para-DVB, highlighted that para-DVB was detrimental to polyHIPE modulus as a result of poor emulsion stability and clustering of DVB. Variable temperature relaxation measurements for S-co-para-DVB were additional methods by which to understand the effect on

polyHIPE structure (figure 5.8). As expected, the relaxation profile indicated that S-co-para-DVB and S-co-DVB were similar with a small peak at 313 K that could correspond to the peak in styrene GPC standard at 283 K, which implies that para-DVB does not cross-link extensively. In addition, comparison with S-co-DVB and S-d_8-co-DVB gave a further insight into the structural effects of para-DVB on polyHIPE structure (figure 5.9). It was evident that the relaxation of S-co-DVB and S-co-para-DVB became very similar, which could be explained by the increase in molecular motion at higher temperature. The S-d_8-co-DVB relaxation profile had faster relaxation times than both S-co-DVB and S-co-para-DVB polyHIPEs, indicating that clustering of DVB was significant. This provided further evidence that clustering was likely occurring resulting in smaller modulus values of S-co-para-DVB polyHIPEs. As such, a visual model of the S-d_8-co-DVB polyHIPE structure can be thought of a cross-linked network, with small branches of tightly packed DVB (figure 5.10).

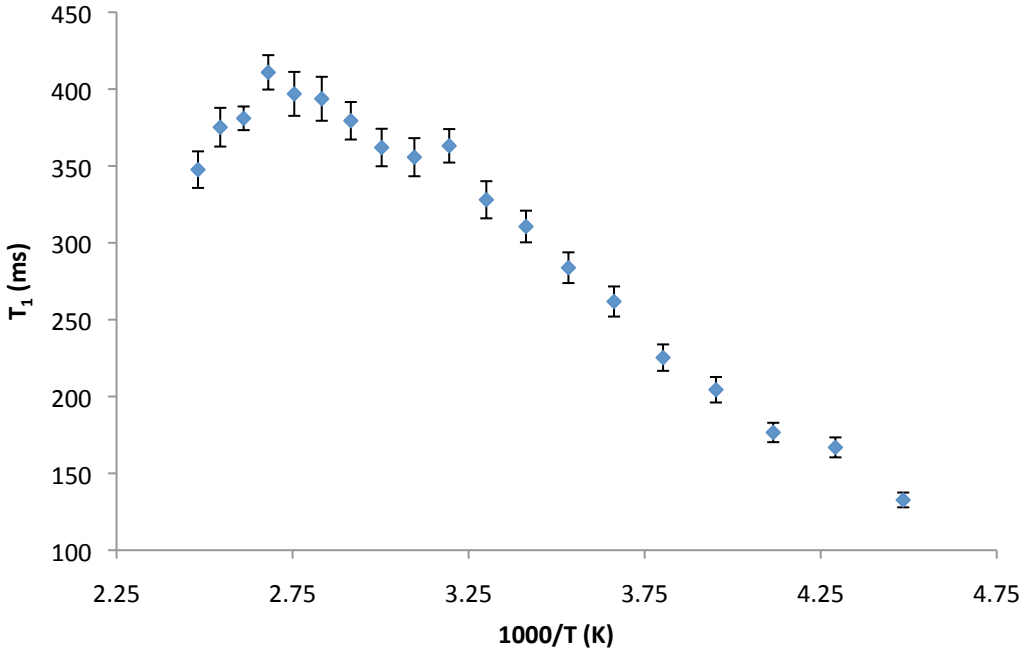

Figure 5.8. T_1 relaxation profile of S-co-para-DVB polyHIPE between –50°C and +130°C.

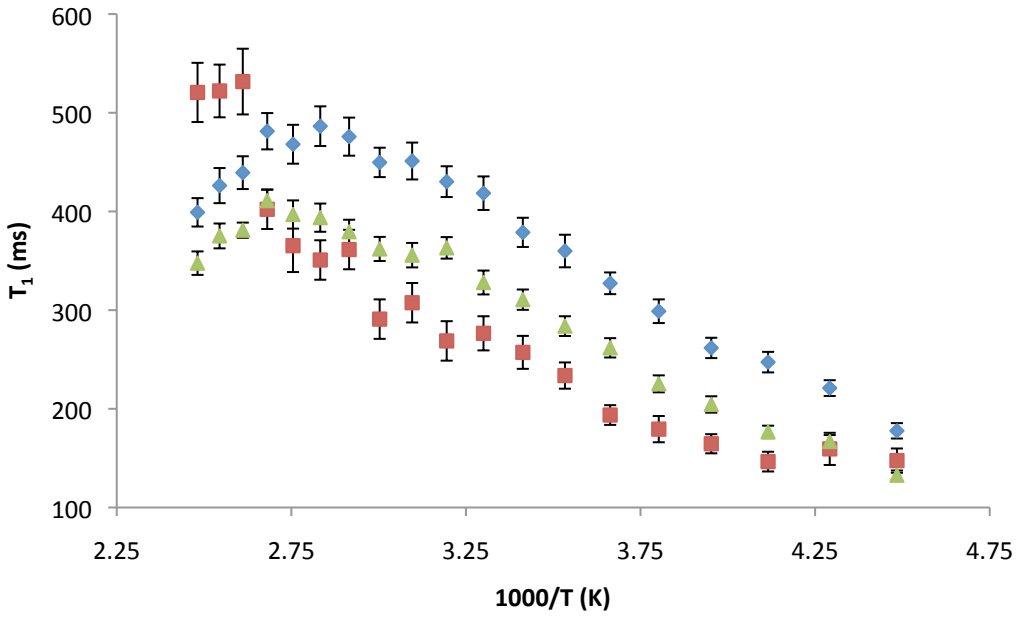

Figure 5.9. T_1 relaxation profiles of S-co-DVB (blue), S-d8-co-DVB (red) and S-co-para-DVB (green) polyHIPEs between –50°C and +130°C.

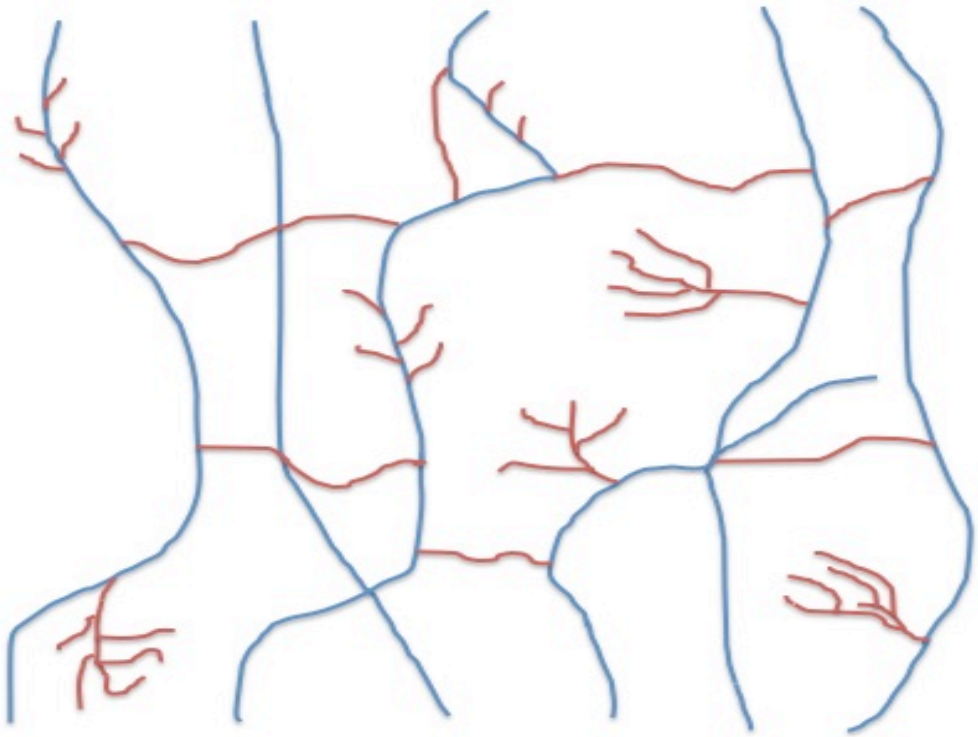

Figure 5.10. Schematic of a deuterated polyHIPE structure (blue) and ^{1}H observed cross-linking regions and clusters (red).

An interesting feature of figure 5.11 was that para-DVB and S-co-DVB $T_{1\rho}$ relaxation times were very similar suggesting that clustering was maybe not as prominent in para-DVB. It was postulated that that increased para-DVB content would increase

clustering which would have been reflected by longer relaxation times as the clustering would have been more prominent affecting the bulk of the polyHIPE. As described in chapter 4, para-DVB was detrimental to emulsion stability, thus to polyHIPE structure and its physical properties. Therefore, the most probable explanation was that the data indicated further evidence that DVB clusters were more exclusively composed of para-DVB rather than other DVB isomers. Despite affecting emulsion stability any cross-linking would create a structure of very large molecular weight using either DVB 80 or para-DVB, it can be assumed that the NMR data here was dependent on the effects on the bulk structure.

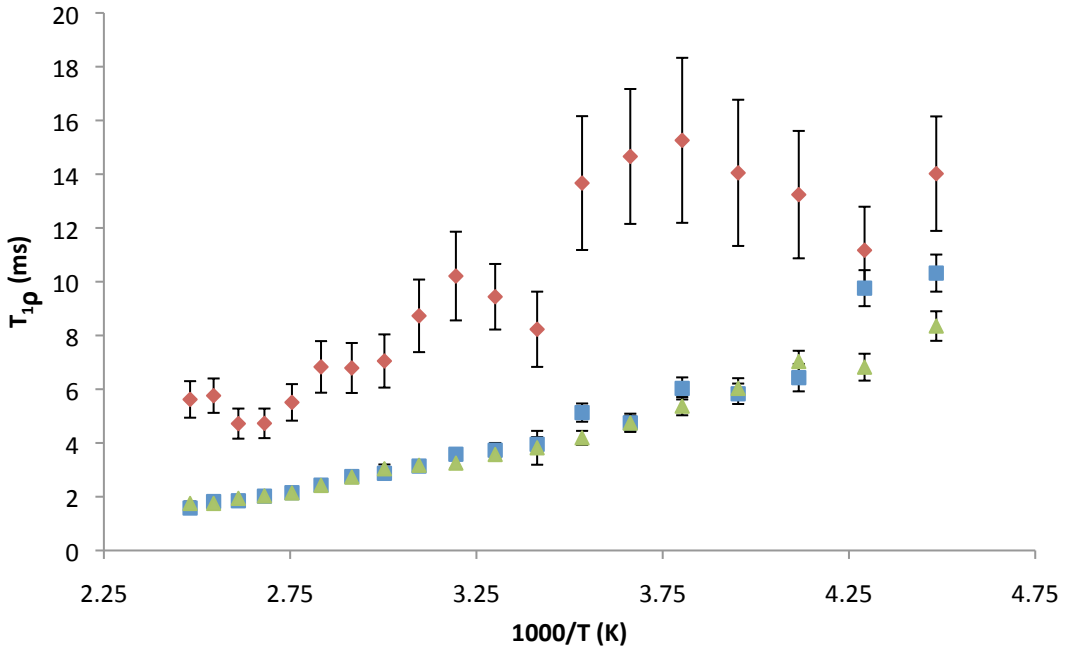

Figure 5.11. $T_{1\rho}$ relaxation profiles of S-co-DVB (blue), S-d_8-co-DVB (red) and S-co-para-DVB (green) polyHIPEs between –50°C to +130°C.

In summary, variable temperature TD-NMR relaxation experiments of styrenic polyHIPEs revealed previously unknown aspects of polyHIPE structure. T_1 relaxation profile of 100% styrene polyHIPE indicated similar behaviour to GPC standard polystyrene but shorter times reflected the addition of air into the porous polyHIPE compared to the GPC standard. All other polyHIPEs exhibited this behaviour, with the exception of S-co-para-DVB. T_1 relaxation indicated that molecular motion was closer to the GPC standard polystyrene, suggesting that para-DVB was not cross-

linking effectively with styrene to affect relaxation. The T_1 relaxation profile of S-d_8-co-DVB compared to S-co-DVB revealed that clustering of DVB was more prevalent than previously assumed in chapter 4. In addition, comparison of S-co-DVB and S-co-para-DVB $T_{1\rho}$ data provided more evidence that para-DVB was the source of clustering. Identification of these issues is critically important to laser target materials based on polyHIPEs because inhomogeneities such as these are not acceptable. By incorporating TD-NMR characterisation in future projects, significant developments can be made into resolving these issues.

5.5.2 t-Butyl Styrene PolyHIPE Variable Temperature NMR Relaxation Measurements

Variable temperature NMR relaxation measurements were applied to t-BS-co-DVB polyHIPEs in the same manner as S-co-DVB polyHIPE. New information was obtained on polyHIPE structure using this technique and application to t-BS could reveal new information on the effect of the large t-butyl group on polyHIPE structure that was not observed in chapter 4.

The T_1 relaxation profile for t-BS-co-DVB polyHIPE was consistent with previous polyHIPEs indicating that t-BS-co-DVB was in a fast motion regime (figure 5.12). However, absence of a peak in the profile suggested t-BS-co-DVB behaved similarly to S-d8-co-DVB, exhibiting more rigid behaviour rather than 100% styrene or S-co-para-DVB polyHIPEs. A notable characteristic was that t-BS-co-DVB had longer and shorter relaxation times at higher and lower temperatures, respectively, compared to S-co-DVB. This can be attributed to sensitivity to the motion of the t-butyl group at the extremes of the temperature range. One explanation was that at lower temperatures the t-butyl group still had sufficient motion to relax efficiently, whereas at higher temperatures the motion of t-butyl group increased the energy required for small chain rotations to activate.[4] Steric interactions of t-butyl could repel nearby small chains, which could justify this postulate resulting in the increased temperatures required to promote this motion.

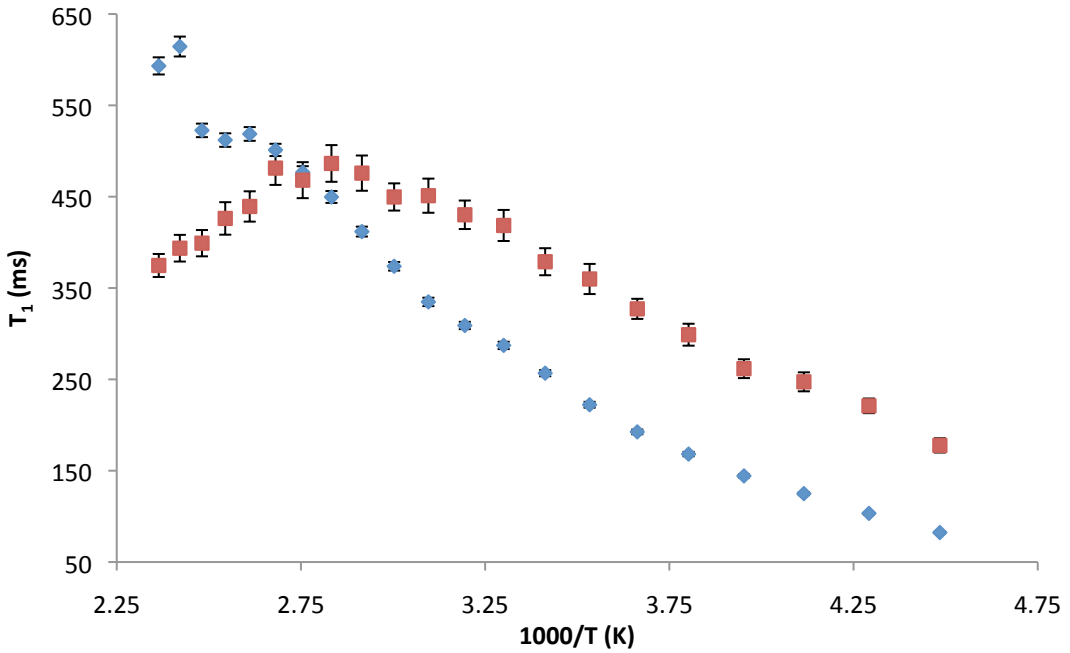

Figure 5.12. T_1 relaxation profile of t-BS-co-DVB polyHIPE (blue) and S-co-DVB polyHIPE (red) between –50°C and +150°C.

The $T_{1\rho}$ relaxation profile of t-BS-co-DVB was consistent with previous styrene polyHIPEs (figure 5.13). The non-linear behaviour at low temperatures suggested that there could be more than one component present, but at 7.5 ms relaxation time on average spin diffusion was efficient on that timescale (4 ms) questioning that hypothesis. Spin diffusion would mean that there would be no way to distinguish multiple components using this technique. This was highlighted at higher temperatures as relaxation times were shorter and linear behaviour was observed. Another possibility could be that increased free volume from the t-butyl group caused a lowering of the temperature of the transition seen in styrene 100% (figure 5.13). The t-BS $T_{1\rho}$ relaxation profile suggested that this transition was in fact a large chain motion likely related to chain proximity rather than a pre glass transition motion (at ~130°C), which was larger than the equivalent styrene transition. Thus the increase in free volume caused large chain motion to be activated at lower temperature than styrene. In addition, the narrow range of the $T_{1\rho}$ data support the increase in free volume postulated in chapter 4. The increased free volume affected the polarisability of t-BS meaning that t-BS was less sensitive to structural changes at this frequency of motion. The increase in free volume may also explain why Young's

modulus results for t-BS were lower than equivalent styrene materials. Loose packing of polymer chains arose from repelling of the t-butyl group on neighbouring chains, which may reduce the intermolecular forces (Van der Waals) that provide strength by comparison to styrene.

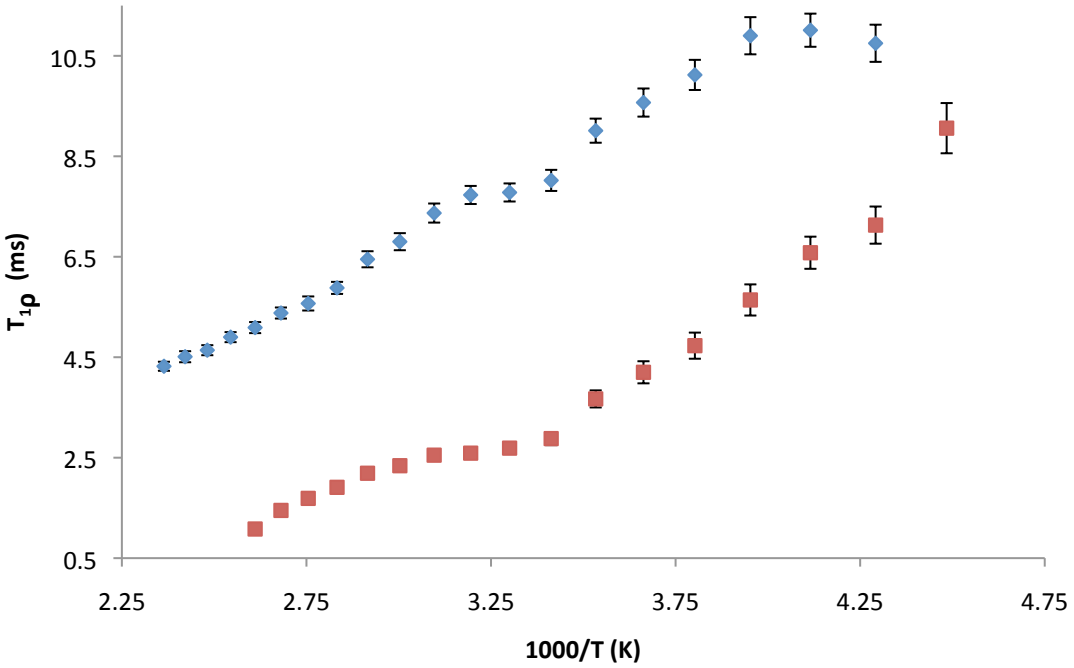

Figure 5.13. $T_{1\rho}$ relaxation profile of t-BS-co-DVB polyHIPE (blue) and S-co-DVB polyHIPE (red) between –50°C and +150°C.

In conclusion, TD-NMR provided further evidence of the effect of the t-butyl group on polyHIPE molecular motion across a temperature range. T_1 relaxation experiments at different temperatures demonstrated that t-BS-co-DVB had an unexpectedly rigid molecular motion at higher temperatures. A suggestion was that the t-butyl group restricted small chain motions by comparison to styrene, thus required higher temperatures to active chain motion. Varied $T_{1\rho}$ relaxation experiments indicated that there was an increase in polymer free volume from the t-butyl group. TD-NMR was able to observe activation of large polymer chain motion at lower temperature by comparison to styrene 100% polyHIPE. It was postulated that the reduction of Young's modulus for t-BS-co-DVB polyHIPEs was due to an increase in free volume causing less efficient chain packing. TD-NMR was shown to be powerful in deeper structural analysis of t-BS-co-DVB polyHIPEs, which

complemented initial characterisation results from chapter 4. Furthermore, application of this technique to characterisation of these type of low density polymers was a novel approach. Using t-butyl styrene, TD-NMR was shown to be valuable, suggesting that other modified styrene monomers could be easier examined using this technique.

5.5.3 Vinyl Naphthalene PolyHIPEs

2-Vinyl naphthalene polyHIPEs were synthesised in order to investigate the effect of the large and aromatic planar group structure of the monomer, which was of interest to NMR relaxation behaviour. This would form a contrast between styrene and t-butyl styrene polyHIPE relaxation based on different types of groups attached to the styrene aromatic ring. In addition 2VN polyHIPEs were new polyHIPEs that have not been reported before, which could be of interest to fields that modify the surface of polyHIPEs post polymerisation. SEM images revealed structures that were not typical for polyHIPEs indicating that synthesis was not optimised (figure 5.14). Despite synthesis of 2VN-co-DVB polyHIPE, which was a robust monolith, typical polyHIPE pore structure was not achieved (figure 5.15). This indicated that in both polyHIPEs the surfactant system was not ideal, and no improvement was gained when varied amounts of Span® 80 was used to form HIPEs. Altering the concentration of the surfactant was performed because polyHIPE structure is influenced by surfactant concentration.[5] Surfactants with correct HLB for HIPE is required for stable emulsions to be formed and it was clear that Span® 80 HLB of 4.3 was not ideal. However, on addition of DVB there was evidence of a pore structure, which indicated that the monomers were stabilised more efficiently by Span® 80 (figure 5.15). Addition of DVB would change the HLB compared to just vinyl naphthalene. Testing with higher and lower HLB valued surfactants could resolve this issue and an improved pore structure could be achieved.[9] Refinement was not pursued, as the priority was to produce a polyHIPE suitable for urgent TD-NMR investigation.

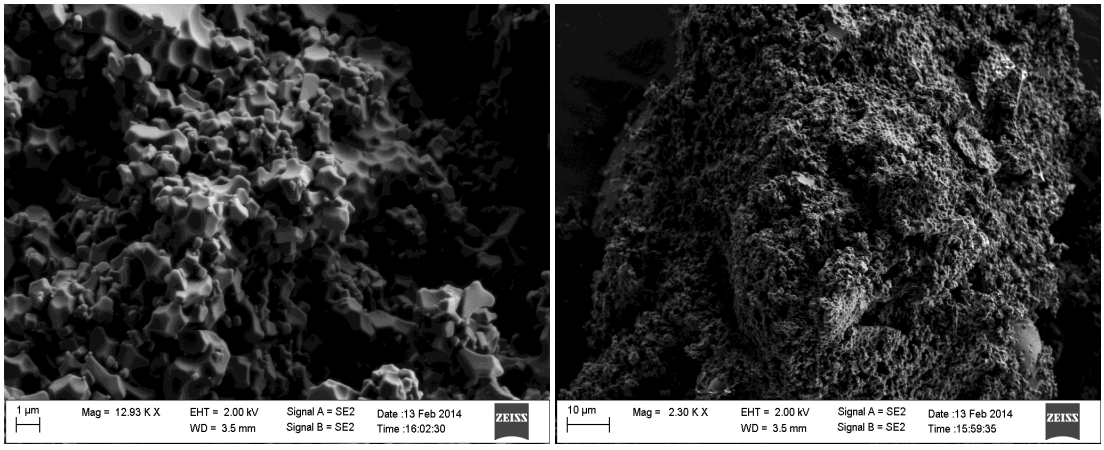

Figure 5.14. SEM images of a 2-vinyl naphthalene (2VN) polyHIPE. Scale bars are 1 μm (left) and 10 μm (right).

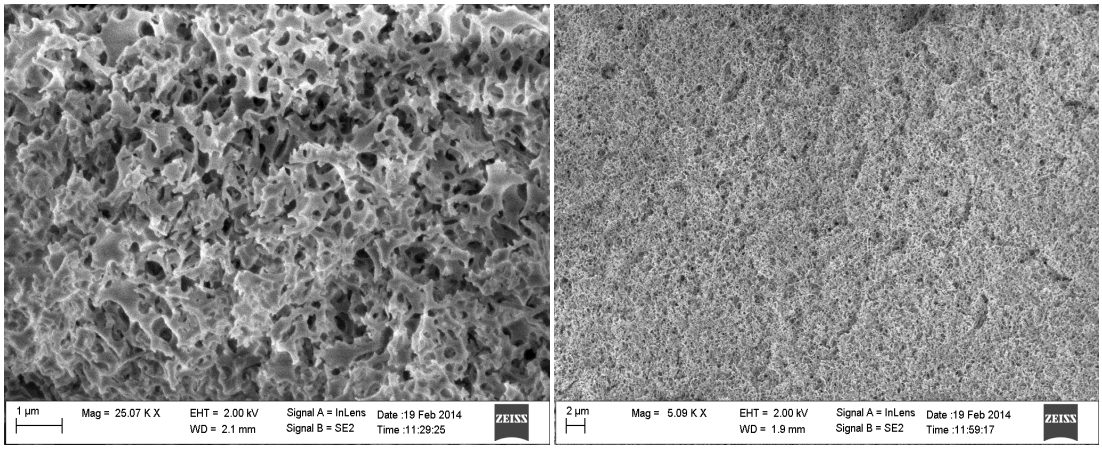

Figure 5.15. SEM images of a 2VN-co-DVB polyHIPE. Scale bars are 1 μm (left) and 2 μm (right).

^{13}C SSNMR spectra of 2VN polyHIPE (figure 5.16) showed a similar spectrum to styrene polyHIPEs, which was expected due to the related molecular structures of naphthalene and styrene. There was no apparent increase in backbone disorder on cross-linking with DVB that was seen with S-co-DVB polyHIPEs, which could be as a result of the low percentage of cross-linker (figure 5.17). This low percentage of DVB did not influence of spectral broadening mechanisms significantly, which would increase in line-widths.

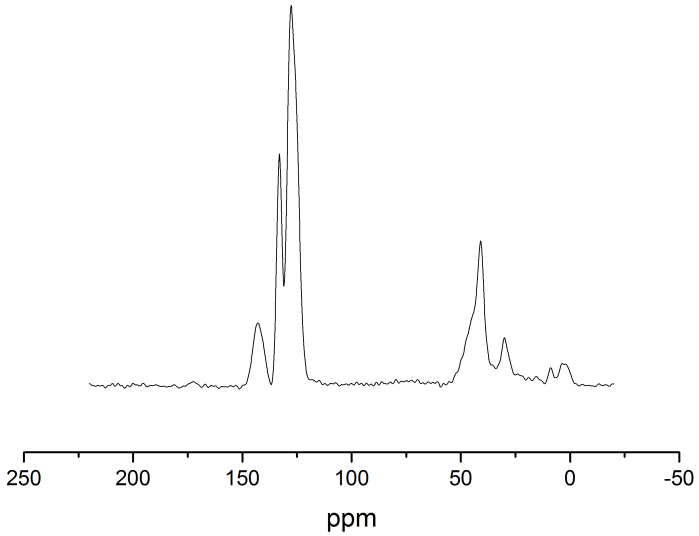

Figure 5.16. ^{13}C SSNMR spectra of 2VN polyHIPE obtained at 400 MHz spinning at 12 kHz CPMAS.

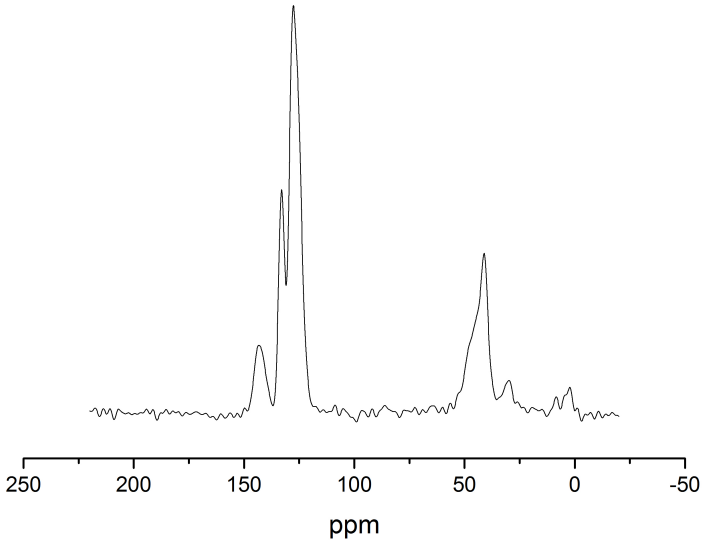

Figure 5.17. ^{13}C SSNMR spectra of 2VN-co-DVB polyHIPE obtained at 400 MHz spinning at 12 kHz CPMAS.

The main purpose of 2VN polyHIPEs in this work was to investigate the NMR relaxation properties. T_1 relaxation times of 2VN polyHIPEs were similar to styrene polyHIPE (table 5.2). This suggested that there was very little freedom of motion from the additional aromatic ring of vinyl naphthalene, which contrasts the additional freedom that t-butyl styrene protons have. It is possible that the naphthalene ring system may have been more flexible increasing molecular motion compared to styrene, thus relax more efficiently. SEM images revealed that the 2VN polyHIPE structure was not typical of polyHIPEs, which could mean that there was increased mobility of the polymer resulting in shorter than expected relaxation

times. If 2VN had a typical polyHIPE structure, perhaps the relaxation time would be much longer. This could be explained by the size of the naphthalene ring system resulting in more efficient pi stacking creating a rigid system preventing freedom of motion. In addition, this would have the effect of organising the larger chains, which would account for both T_1 and $T_{1\rho}$ data of 2VN. Very long $T_{1\rho}$ relaxation times suggested that the larger chain motion of 2VN were organised, allowing efficient polarisation of spins. Yet, SEM indicated collapsed HIPE structures indicated by longer relaxation times could not reflect this behaviour unless longer $T_{1\rho}$ relaxation times correlated to DVB clustering, such as seen in S-co-DVB polyHIPEs. Alternatively a broken emulsion created high density, and ordered regions by which allowed efficient spin polarisation for long $T_{1\rho}$ relaxation measurements to be obtained. Higher density regions could also account for increased T_1 relaxation times compared to 100% styrene polyHIPE. Obtaining a 2VN polyHIPE, with typical polyHIPE architecture, and performing NMR relaxation experiments would resolve this.

Table 5.2. ^{1}H TD-NMR relaxation data of 2VN, styrene and t-BS polyHIPEs.

PolyHIPE system	T_1 **(ms)**	$T_{1\rho}$ **(ms)**
2VN	536.7±8.7	14.65±1.15
2VN-co-DVB (95:5)	571.2±17.0	18.83±1.82
Styrene	524.8±11.6	2.59±0.11
t-BS	287.7±1.3	5.49±0.07

Experiments with 2VN polyHIPE were necessary in order to compare to styrene polyHIPEs. This helped to provide more information on the molecular motion of styrene polyHIPEs, particularly the effect of large groups attached to the aromatic ring and the resulting effect on structural order. Despite SEM revealing a non-typical polyHIPE structure, the increased T_1 relaxation time compared to styrene was attributed to efficient pi stacking creating a more ordered structure, or higher density. This was in contrast to the t-butyl group, which decreased T_1 relaxation times due to freely rotating methyl groups. Long 2VN $T_{1\rho}$ relaxation times could be

an indicator to emulsion homogeneity due to the correlation to S-co-DVB studies in chapter 4. Although 2VN polyHIPE synthesis and characterisation was in its infancy, relaxation data potentially provides significant evidence that TD-NMR relaxation times can give an indication to emulsion homogeneity and physical properties. This effect on polyHIPE structural order and molecular motion has not been reported in the literature before and could be interesting future research.

5.6 Conclusions

PolyHIPE varied temperature NMR relaxation experiments using TD-NMR allowed more thorough structural investigations. Revealing molecular motion of both non cross-linked and cross-linked polyHIPEs as a function of temperature was valuable in accessing structural differences. This was particularly evident with deuterated styrene copolymerised with DVB to reveal shorter than expected T_1 relaxation times, which indicated that clustering of DVB could be more extensive than first thought. Thus, this work contributed significantly at identifying the scale of application related inhomogeniety issue, as well as demonstrating TD-NMR as a technique by which such an issue can be observed.

$T_{1\rho}$ relaxation indicated that the t-butyl group increased polymer free-volume by comparison to styrene. Increased molecular motion was possible if the t-butyl group increased space between polymer chains, allowing greater motion over the applied temperature range. In addition, this could help explain why t-butyl styrene has a lower modulus than styrene. Large polymer chains of t-butyl styrene had more flexibility and motion compared to styrene resulting in less rigid structure, which has the effect of lowering modulus. For plasma physics experiments this is a significant factor and t-butyl styrene is an acceptable low density porous material for new laser target materials.

2VN polyHIPEs were of interest due to the large planar ring system effect on polyHIPE structure. There was an increase in T_1 relaxation time, suggesting the

structure was more ordered than styrene, possibly due to be a result of efficient pi stacking of the aromatic rings or increased density. This effect in polyHIPEs was not investigated before, and could be used as a tool in the development of new polyHIPEs that relies on structural order. Finally, 2VN $T_{1\rho}$ relaxation times correlated to the S-co-DVB inhomogeneity issue, suggesting that TD-NMR could be used to assess the homogeneity of polyHIPE structures. However, a point of reference would be required based on a homogeneous structure, which can only be obtained through improved synthesis methods. Studies using alternative groups on the styrene aromatic ring reveal microstructure features of polyHIPEs that can greatly aid characterisation of materials for high energy laser experiments.

5.7 Appendix

5.7.1 Relaxation under Different Atmospheres

Oxygen has a paramagnetic isotope, which is known to reduce T_1 relaxation times.[4] Experiments comparing T_1 relaxation times of S-co-DVB polyHIPEs and GPC standards were performed to demonstrate possible differences in relaxation times between a low density, porous polymer against a full density equivalent (table 5.3).

Table 5.3. Effect of atmosphere on T_1 relaxation in the MQ20 used in this work.

Polymer system	T_1 **in air (ms)**	T_1 **in N_2 (ms)**
Styrene GPC standard	483.7±3.0	713.3±5.0
100% styrene polyHIPE	538.8±8.3	940.0±33.3
100% t-BS polyHIPE	306.7±4.0	545.3±9.7

5.8 References

1 J. M. Williams, A. J. Gray, and M. H. Wilkerson, *Langmuir*, 1990, **6**, 437–444.

2 N. R. Cameron, *Polymer*, 2005, **46**, 1439–1449.

3 P. J. Hore, *Nuclear Magnetic Resonance*, Oxford University Press, Inc., New York, 1995.

4 R. K. Harris, *Nuclear Magnetic Resonance; A Physiochemical View*, Longman Scientific & Technical, Harlow, 2nd edn., 1987.

5 J. M. Williams and D. A. Wrobleski, *Langmuir*, 1988, **4**, 656–662.

6 H. W. Spiess, *Colloid*, 1983, **261**, 193–209.

7 D. Hentschel, H. Sillescu, and H. W. Spiess, *Macromolecules*, 1981, **14**, 1607–1608.

8 A. Mercier, S. Kuroki, I. Ando, H. Deleuze, and O. Mondain-Monval, *Journal of Polymer Science Part B: Polymer Physics*, 2001, **39**, 956–963.

9 J. M. Williams, *Langmuir*, 1991, **7**, 1370–1377.

6. Aerogel Synthesis; New Carbon-Hydrogen Aerogels and Aerogels with a Density Gradient

6.1 Introduction

Aerogels are established materials and used in plasma physics experiments including inertial confinement fusion (ICF) research for many years.[1–4] Experiments utilising low density aerogels in laser experiments is an important factor in developing ICF as an energy source.[5,6] One aspect of this work was concerned with new low density carbon-hydrogen aerogels, with the aim of reaching a C:H ratio of 1:2, and densities below 50 mg/cc. Increased hydrogen content increases the opacity of plasma at this ratio as there is less carbon, which is of higher Z than hydrogen. Very low density aerogels are required because with less mass, there is less absorption and scattering of X-rays in the plasma, which can interfere with experiments. New aerogels facilitate the design of new experiments, which can help further understanding of the behaviour of plasma at high temperature and pressure conditions created by high energy lasers.

A long standing interest to experimentalists are materials with a density gradient, but these have been limited to date.[7,8] The change in material density causes an acceleration or deceleration of the shock front depending on orientation to the laser.[7] Study of plasma shock fronts requires homogeneous materials and in certain studies with a density gradient, but currently materials are often fabricated from components of different densities, fabricated separately then joined together. Thus, when constructed into the final target, this often contains small air gaps and high density regions at the ends of each component.[9,10] Other methods of mixing gels of different density that diffuse into each other to achieve a homogenous material have also been tried.[11–13]

In this chapter, different polymerisable hydrocarbons were studied to determine their suitability for the development towards a material that could be utilised as targets for high energy physics experiments. This chapter also describes the

synthesis of new carbon-hydrogen aerogels, carbonised aerogels and the synthesis of a novel one-step density gradient DVB aerogel, and characterisation of these materials.

6.2 Materials and reagents

Divinyl benzene 80 (DVB), methanol, benzene, toluene, 1,2-dichloroethane (DCE), azobisisobutyronitrile (AIBN), tin (IV) chloride, dicylcopentadiene (DCPD) (mixture of exo- and endo- isomers), norbornene (mixture of isomers), 5-vinyl-2-norbornene (5V2N) (mixture of isomers), 1,4-dichloro p-xylene (DCPX), chlorobenzene, bromobenzene, benzylidene-bis (tricyclohexylphosphine)-dichlororuthenium (Grubbs 1), bis(tricyclohexylphosphine)-3-phenyl-1H-inden-1-ylideneruthenium dichloride (LG Grubbs), (1,3-Bis(2,4,6-trimethylphenyl)-2-imidazolidinylidene) dichloro(phenylmethylene) (tricyclohexylphosphine) ruthenium (Grubbs 2).

All chemicals were used as received except for monomers which had the inhibitor extracted before use using a silica column.

6.3 Aerogel synthesis and characterisation

The details on aerogel synthesis and characterisation is given in chapter 3. General aerogel formation was to combined the monomer, the solvent and the initiator into a suitable vessel, usually a glass vial. Once polymerised, gels were removed from the glass vial and exchanged with a suitable solvent to then be dried by a CPD.

Techniques used to characterise aerogels were SEM, elemental analysis, SSNMR, TD-NMR and X-ray tomography. The instrument and experiment details are given in chapter 3.

6.4 Results and discussion

6.4.1 Low Density DVB Aerogels

DVB was chosen for aerogel synthesis as it was a bifunctional monomer. AIBN initiated DVB produced aerogels as low as 31 mg/cm^{-3} density (table 6.1). SEM images revealed the aerogel structure (figure 6.1), with pore sizes in the region of 100 nm. In addition, the structure appears to be comprised of many polymer clusters aggregated together, which is typical of aerogels.

Table 6.1. Densities of DVB aerogels prepared from AIBN initiation.

Density (mg/cm^{-3})	Shrinkage (%)
132.3±1.0	32.3
61.4±1.1	22.8
31.0±0.6	24.0

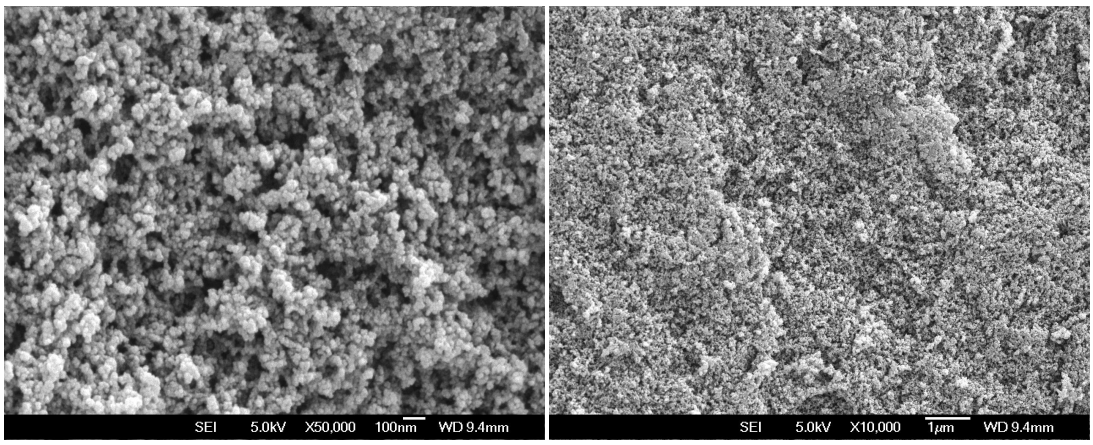

Figure 6.1. SEM images of a DVB aerogel (20% AIBN). Scale bars are 100 nm (left) and 1μm (right).

Despite low density formation, aerogels fractured on machining by a lathe, and the stringent requirements on dimensions of plasma physics materials meant that they were unsuitable to pursue further as the likelihood of error was high when working on a micrometer scale. The lowest material density achieved was 31.1 mg/cm^{-3}, accounting for 30% shrinkage on average. This was also the lowest density aerogel synthesised from the entirety of aerogel investigations.

Aerogel fracturing at low densities suggested that the polymer network was not sufficiently strong enough. This is an issue for high energy laser target production as materials that break easily mean it is more difficult to machine these to the correct dimension. This could most likely be as a result of the characteristics of DVB, which is a rigid but brittle polymer. Thus, it was evident here that at very low densities this characteristic is highlighted. Explaining this behaviour could likely be explained by that synthetic conditions were not ideal despite very low densities formed using a typically hard to control free radical polymerisation. High initiator concentrations meant that many different polymer chains were forming simultaneously, and bifunctional DVB meant that it could cross-link chains effectively, forming a gel, but these high concentrations would cause shorter polymer chains to form. The most likely reason was due to the strength of the structure being insufficient despite being composed of small pores. The strength was such that the aerogel had enough strength once the gel network had formed, but not as a dried species.[14] Comparatively, the same material consisting of smaller pore diameters would sustain greater stress than the larger pore diameter equivalent, unless the pore structure is inhomogeneous, akin to structural issues discussed in chapter 4 (S-co-DVB polyHIPEs). Equation 6.1 represents the stress a 3-D pore can undergo.

$$\sigma_{el} = n^2\pi^2 \frac{E_s I}{l^4} \qquad (6.1)$$

σ_{el} is the stress, n is a constant, E_s is Young's modulus, I is the second moment of area and l is the length of a column (or pore).

Due to the nature of DVB in polymerisation at low densities, fracturing was more likely in these aerogels. TD-NMR investigations from chapters 4 and 5 showed that DVB formed localised clusters of cross-linked polymer rather than even distribution, therefore could explain why the aerogels fractured at lower densities despite a small pore size. The uncontrollable free-radical polymerisation, and sol-gel chemistry

meant that extended structural organisation did not exist, thus the aerogel overall was weak.

6.4.2 Aerogels Synthesised from Grubbs type Catalysts

Problems with DVB aerogels instigated using another monomer that could produce stronger aerogels, namely DCPD. This monomer was chosen as it was known for strong mechanical properties,[15] and has been used to produce low density aerogels including below 40 mg/cc.16,17,2 Gels were prepared from three Grubbs type catalysts (chapter 3, figure 3.2) using a ROMP reaction, however aerogels were only produced from 1st generation type catalysts. Gels from the 2nd generation catalyst shrunk considerably on dying despite using super critical fluid extraction. One possible reason for high shrinkage was due to differences in the catalytic action to produce gels; 1st generation catalysts have higher rates of initiation than 2nd generation catalysts, and 2nd generation have higher rates of propagation over 1st generation.[18] Thus, more chains growing simultaneously established gel networks more efficiently using 1st generation catalysts than 2nd generation. 2nd generation catalysts likely produced gels consisting of long chains but did not produce a strong three-dimensional network. Furthermore, gels using either catalyst generation did not form at 0.1% catalyst loading, suggesting that too many polymer chains were initiated thus were unable to form the required three dimensional structure for gel formation.

Table 6.2. Densities of DCPD aerogels formed from different Grubbs type catalysts.

Catalyst	**Catalyst generation**	**Density (mg/cm $^{-3}$)**	**Shrinkage (%)**
Grubbs 1	1st	100.0±2.3	2.3
1st gen derivative	1st	98.7±0.4	0.4
Grubbs 2	2nd	N/A	N/A

Density measurements revealed that aerogels produced by Grubbs catalysts had significantly less shrinkage that AIBN initiated aerogels, 1% compared to 25-30% on average (table 6.2). This suggested that Grubbs type catalyst were more efficient at forming networks than free radical polymerisation. Examination of DCPD SEM images (figure 6.2) at high magnification reveals a highly interconnected structure that could explain the low shrinkage observed, as the network is rigid due to the catalyst cross-linking the polymer despite an irregular pore structure. DCPD appears as many fibrous-type chains linked together whereas DVB consists of many small clusters aggregated to form the gel structure.

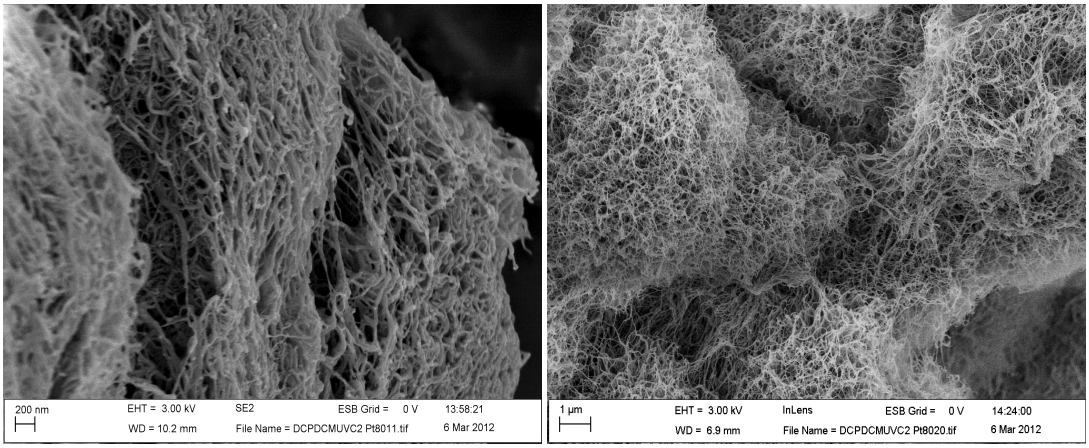

Figure 6.2. SEM images of a DCPD aerogel. Scale bars are 200 nm (left) and 1μm (right).

Despite little shrinkage, forming aerogels below 40 mg/cm $^{-3}$ was difficult to achieve, ~50 mg/cm $^{-3}$ was the lowest value obtained, but aerogels were very fragile - more so than DVB at equivalent densities and crumbled easily. This was unexpected considering reported strong mechanical properties of DCPD. Inspection of SEM images of DVB and DCPD aerogels at lower magnification (figure 6.3, left) revealed that both aerogels have structural similarities; both are comprised of polymer clusters that aggregated together to form the gel network, which is typical of aerogels.[19] It is important to note the scale of both images and how much smaller DVB pore structure is compared to DCPD, which according to equation 6.1 can impact on strength. Both structures were somewhat irregular with areas of high cluster aggregation, which could also affect the mechanical strength.[14] Thicker walls and/or shorter distances between pores and clusters increase strength, but DCPD

has thin walls (figure 6.3), large distances between clusters, which are combined irregularly, whereas DVB has much smaller distances between pores. Therefore at lower densities this became an issue for DCPD as there was less material present to form a strong gel network. One suggestion to overcome this issue was to alter the gel formulation as DVB formulations resulted in porous materials of very low densities.

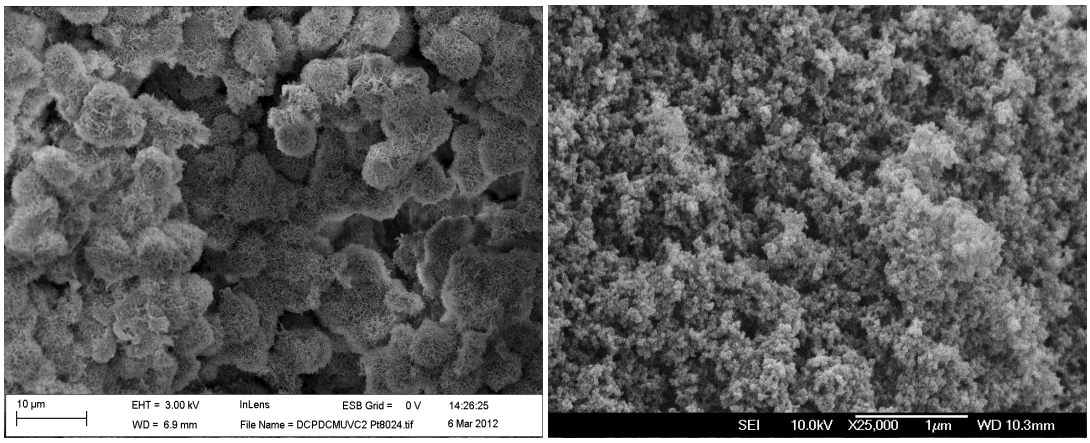

Figure 6.3. SEM images of a DCPD (left) and DVB (right) aerogels. Scale bars are 10 μm (left) and 1μm (right).

Moreover, for high energy lasers experiments, problems with the DCPD structure would become a significant issue for machining to target dimensions in a similar manner to polyHIPE inhomogeneity (chapter 4). The low strength of DCPD aerogels due to these issues prevented lower density gels being obtained, which can not be offset by the favourable increase in carbon-hydrogen ratio ($C_1H_{1.2}$ vs C_1H_1 of DVB). Compared to DVB, which achieved very low densities, which could be utilised in high energy laser experiments. A more thorough investigation was necessary in order to synthesise DCPD aerogels with requisite specifications, which was beyond the scope of this project. Consequently, DCPD aerogels synthesis was not pursued as a matter of priority.

6.4.3 Norbornene and Derivatives; Grubbs Catalyst and Tin (IV) Chloride Initiated Aerogels

Norbornene and 5V2N were studied because of structural similarities with DCPD; both contain a strained ring, and in fact DCPD is a derivative of norbornene. In the case of 5V2N there is an extra vinyl group, and both norbornene and 5V2N are known polymers.[20–23] Therefore the same conditions used for DCPD gels were utilised for gel formation using norbornene and 5V2N. However, Grubbs type catalysts did not polymerise norbornene, and no gels were formed with 5V2N. Norbornene formed gel but minutes after formation, gels returned to a liquid state (figure 6.4). It was thought that either the unsaturated norbornene polymer underwent depolymerisation by the catalysts used for gel formation, which are capable of depolymerisation.[24] Similarly, it may also be that the gel collapsed rather than breaking of the polymer chains. Polymer aggregates could only be interacting weakly with nearby aggregates, and the lack of cross-linking due to only having one reactive centre meant that over time that the system was essentially phase separating. In any case, DCPD was able to cross-link as it contained two groups capable of ROMP whereas both norbornene and 5V2N only had one ROMP ring meaning they were unable cross-link on their own. This meant that DCPD was more resistant to depolymerisation, which could highlight this action of the catalyst in these mono functional monomers.

In order to prevent depolymerisation it was thought that adding DCPD would help as it may take part in cross-linking with norbornene monomers. However no gel was formed when DCPD was added to either monomer system. One explanation for this could be that norbornene and DCPD do not react together with these particular catalysts as this falls into a different class of reactions; ring opening cross metathesis (ROCM). Alternatively, DCPD was polymerised over 5V2N and norbornene creating ‘micro-gels’ of DCPD that did not result in copolymerisation in a similar manner to para-DVB in S-co-DVB polyHIPEs.

Figure 6.4. Images of depolymerised norbornene gels using different catalyst loadings.

5V2N did not form gels with Grubbs type catalysts. The reason why gels did not form was unclear. It was postulated that the polymer formed was soluble in the solvent, rather than forming a gel network through any cross-linking from the vinyl group. It must be remembered that ROMP reactions are designed for efficient chain growth rather than gel network formation, which required polymer aggregation, therefore the long chain formed could be soluble. To explore hanging vinyl group polymerisation, two additional initiators were chosen, AIBN and tin (IV) chloride, to attempt gel formation. The initiation and propagation mechanisms of all initiators, AIBN, tin (IV) chloride and ROMP are different to each other. The mechanisms of AIBN and tin (IV) chloride do not open the strained ring system efficiently like Grubb's catalysts, thus assumed to react with only on the vinyl group.

Gels of 5V2N were formed using tin (IV) chloride but not with AIBN, and were dried using a CPD. Aerogels exhibited ~60% shrinkage. This suggested poor polymer mechanical properties possibly due to the formation of short polymer chains

resulting in a weak gel network that shrunk on drying. SEM images (figure 6.5) revealed a typical aerogel structure consisting of an aggregated polymer network. DCE was the solvent for gelling and chlorine containing solvents are known to have higher chain transfer constants than solvents such as toluene, resulting in earlier termination of propagating chains.[25] In addition, the polymer may be less soluble in DCE than toluene causing the polymer to precipitate, which encouraged gel formation despite likely formation of short chains.

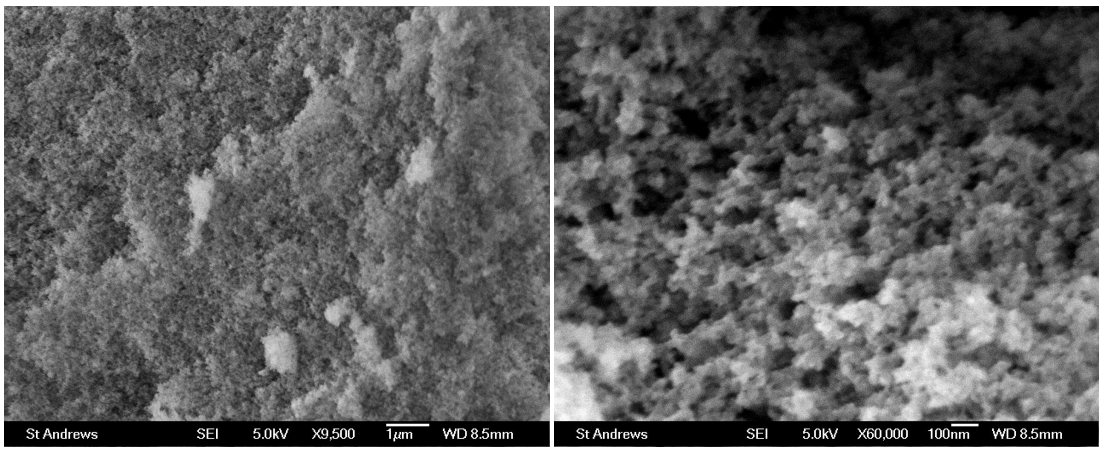

Figure 6.5. SEM images of a 5V2N aerogel. Scale bars are 1 μm (left) and 100 nm (right).

To improve the mechanical properties of 5V2N gels, post cross-linking by ROMP using Grubbs catalysts was performed as the vinyl group in the strained ring remained after tin (IV) chloride polymerisation. Capitalising on the specificity of Grubbs to target this ring could improve the network strength, preventing the high level of shrinkage on drying. Initial experiments were performed by treating the gel with Grubbs, then analysing the structure before addition of another monomer. 1.5 x 10^{-3} g of Grubbs 1 was added to 0.05g (10% by volume) of either DCPD or norbornene in toluene before addition to 5V2N gels. The system was left to react for 24 hours at RT before methanol exchange and drying in a CPD.

Resulting aerogels shrunk significantly (figure 6.6) and densities were measured to be ~315 mg/cm $^{-3}$. Table 6.4 compares densities before and after post cross-linking. Before treatment with Grubbs, the polymer would have a larger free volume than the corresponding opened structure due to the norbornene ring size. Opening of the

ring would allow packing of the structure, reducing free volume and increasing density. This should not be observed if cross-linking monomers were incorporated into the chain, which would occupy the space that the ring opening created. Thus it was indicated that the incorporation of cross-linker was minimal and had little effect on the structure.

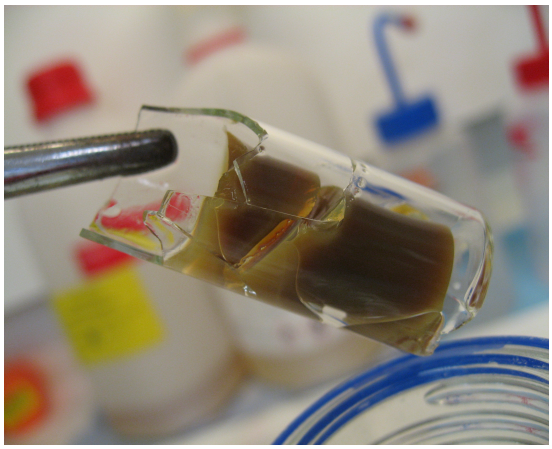

Figure 6.6. An image of a 5V2N gel after post cross-linking with a Grubbs type catalyst.

Table 6.4. Comparison of 5V2N aerogel densities before and after treatment by Grubbs catalyst.

5V2N aerogel	**Density (mg/cm $^{-3}$)**
Non Grubbs treated	165.8±10.2
Grubbs treated	315.2±13.0

Comparison of ^{1}H-^{13}C CP SSNMR (figure 6.7) spectra for a 5V2N aerogel treated with and without Grubbs type catalyst showed that the post cross-linking did not affect the local chemical structure significantly. Opening of one vinyl group by Grubbs type catalysts produce two more vinyl groups in a polymer chain. Therefore if post cross-linking was extensive, local chemical environments would have changed, as the peak at 140 ppm would have grown. Contributions to other chemical shifts would have been observed but the relative intensity remained the same.

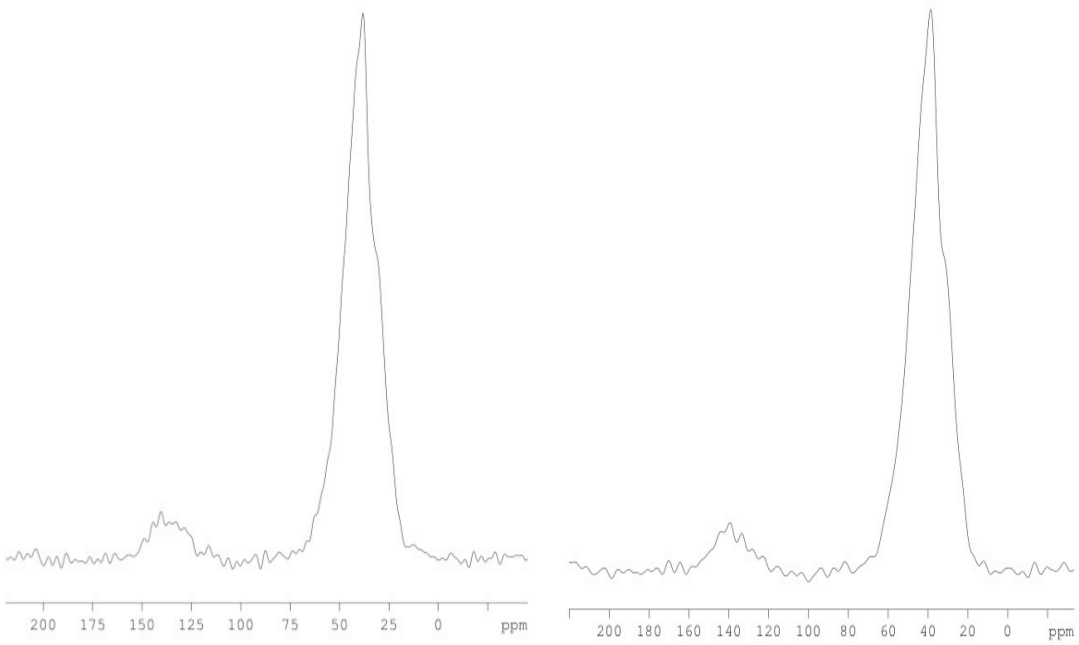

Figure 6.7. ^{1}H-^{13}C CPMAS SSNMR spectra for 5V2N aerogel non-Grubbs treated (left) and Grubbs treated (right) spinning at 12.5 kHz.

To investigate structural differences, TD-NMR T_1 saturation recovery and $T_{1\rho}$ experiments were performed on 5V2N aerogels. The collated data is contained in table 6.5. $T_{1\rho}$ relaxation times, which measure rotation of polymer chains, indicated no significant chain modification through treatment with Grubbs type catalysts occurred despite the shrinking of the aerogel that was visible to the eye. Similar $T_{1\rho}$ relaxation times suggested that Grubbs type catalysts were not causing any significant depolymerisation of the backbone or incorporating additional monomers as both of these effects would alter chain motion, which relaxation is dependent on. New polymer chains propagating would have affected the backbone motion whereas depolymerisation would deconstruct polymer chains causing them to become more mobile, also affecting relaxation.

T_1 saturation recovery times of the non-Grubbs treated and Grubbs treated aerogel were significantly different (table 6.6). T_1 measures small group and end group rotations, which are modulated by molecular motion.[26,27] T_1 relaxation measurements were performed at –50°C and +100°C and determined that the aerogels were in an increased molecular motion regime (appendix 6.5.1), akin to

styrene type molecular relaxation behaviour. Therefore, shorter relaxation time of Grubbs' treated aerogel could indicate a more mobile structure. However, the relaxation times could also reflect the large increase in density of the aerogel by changing molecular motion significantly. In this case, Grubbs catalysts opened the norbornene ring, without any significant increase in structural order or cross-linking according to $T_{1\rho}$ measurements. It could be that some chain rigidity was lost due to ring opening, increasing molecular motion. This meant that spin-lattice relaxation efficiency was quicker despite the large density increase. The increased end group motion resulted in faster T_1 relaxation times compared to the rigid norbornene ring in the non-Grubbs treated aerogel. The structure of the aerogel could be represented by figure 6.8.

Table 6.5. ^{1}H TD-NMR data for 5V2N aerogel non-Grubbs treated and Grubbs treated.

Material	T_1 **(ms)**	$T_{1\rho}$ **(ms)**
Non-Grubbs treated	395.8±7.0	13.35±1.61
Grubbs treated	172.8+4.0	11.90±1.13

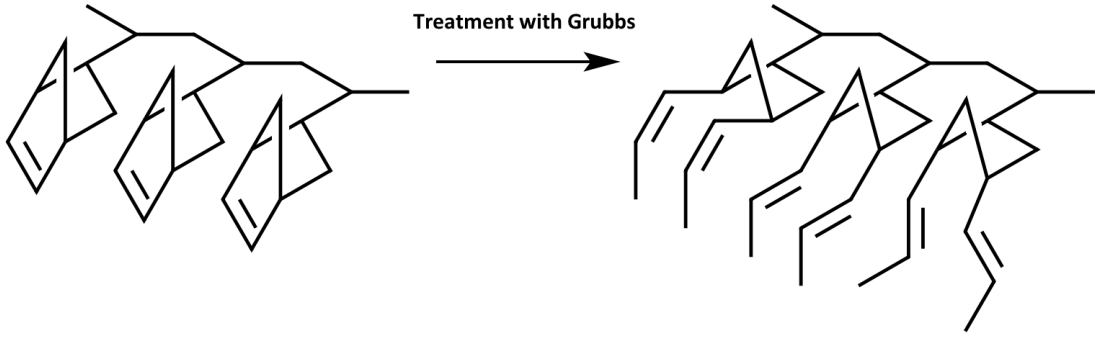

Figure 6.8. A scheme of the structural difference in a 5V2N aerogel chain before (left) and after (right) treatment with Grubbs type catalyst.

5V2N aerogels below 50 mg/cm^{-3} were difficult to form, however, gels that did eventually form contained large cracks, and gels that dried were brittle. Evidence of increased shrinkage in post cross-linking experiments using Grubbs type catalysts meant that experiments on 50 mg/cm^{-3} gels were not considered a valuable use of time. In addition, there was a lack of evidence to suggest that post cross-linking experiments were successful. The inability to cross-link and increasing the density

was a significant issue. Shrinkages are often irreproducible and therefore unreliable for experiments that run in large number using different batches of materials. However, TD-NMR was a valuable characterisation technique in assessing the results of synthetic experiments, and showed where structural modifications took place in the material.

6.4.4 Tin (IV) Chloride polymerisation to DVB and DCPX aerogels

Successful vinyl polymerisation using tin (IV) chloride suggested that that other carbon-hydrogen vinyl monomers could produce gels under similar conditions. DVB and DCPX were used for further investigation. DVB contains two vinyl groups, and formed gels from free-radical polymerisation (section 6.2.1), achieving low densities. DCPX is a monomer used in gel formation, usually as a cross-linker.[28] Despite no vinyl groups being present it was thought that it would share similar chemistry to a well-known monomer for aerogels, rescorcinol,[29,19] to form homopolymer gels via cationic polymerisation. Resorcinol gels can achieve very low densities due to a highly cross-linked network but contain oxygen which is sometimes not desirable for some experiments.[30,31] Thus DCPX and DVB were considered to be a suitable alternative.

100 mg/cm $^{-3}$ density gels were prepared with DCE as the solvent for DVB monomer, and toluene for DCPX monomer. Conditions used for formation of aerogels are given in table 6.6. SEM revealed pore sizes in the region of 100 nm (figure 6.9), and a typical aerogel structure of aggregated clusters akin to previous aerogels synthesised. Large volumes of initiator were used in DCPX gel formation as these volumes produced gels whereas as lower volumes (1-50 μL) did not produce gels.

Table 6.6. Conditions used for formation of DVB and DCPX aerogels.

Monomer	Volume of $SnCl_4$ (μL)	Gelling time (mins)	Temperature (°C)
DVB	25, 50, 100	~1	5
			RT
DCPX	125, 250	~1440	85

Density measurements of DCPX aerogels indicated that gels shrunk by 27% on drying. Aerogels were measured at 126.7±6.3 mg/cm $^{-3}$. Elemental analysis indicated that not all functional groups reacted during the polymerisation showing that aerogels contained approximately 15% chlorine by weight compared to 40.5% of the monomer.

DVB initiated by tin (IV) chloride gelled quickly at room temperature, taking seconds to form a firm gel but which was heterogeneous in appearance. Corresponding aerogels shrunk significantly on critical point drying by up to 160%. Lewis acid catalysis is more efficient at low temperatures.[25] It was postulated that gel networks would be stronger as a result, thus may shrink less on drying. Gels were synthesised at 5°C, and as expected, took longer to polymerise. However, low temperature gels shrunk significantly more than gels formed at room temperature. As a result, further polymerisations at low temperature were not pursued. The gel network provided little strength regardless of an apparent increase in the efficiency of polymerisation, which highlighted that low density gel formation requires sufficient aggregation of polymer clusters into a gel.

TD-NMR comparison of DVB aerogels from tin (IV) chloride and DVB aerogels from AIBN initiation was not pursued as a matter of priority. TD-NMR studies of S-co-DVB polyHIPEs revealed that pore size contribution of about 300 nm did not affected relaxation significantly, which is the same pore size range as these aerogels. Therefore other strategies in order to investigate microstructures more effectively would need to be considered in a future project.

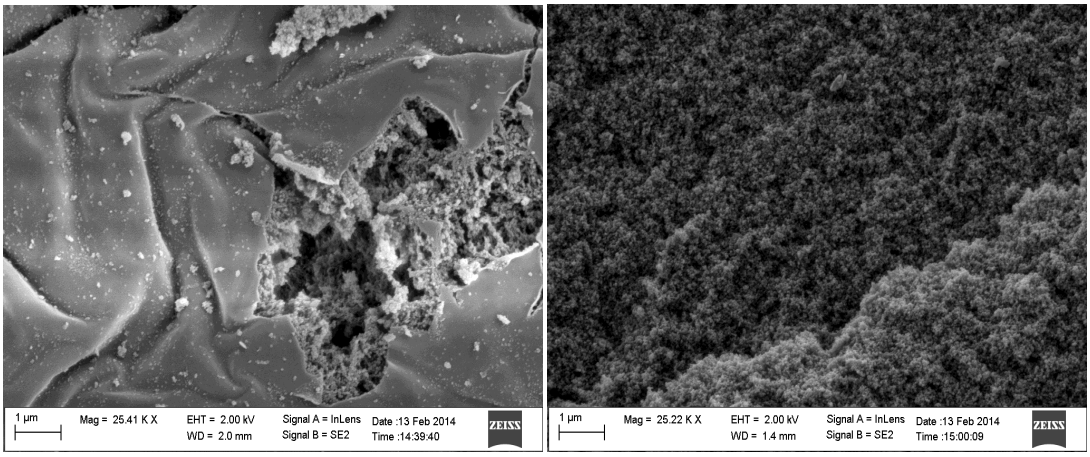

Figure 6.9. SEM images of DCPX aerogel non-carbonised (left) and carbonized (right). A higher density skin is present in the non-carbonised material as a result of contact with the walls of the polymerisation vessel.

6.4.5 Carbonisation of DCPX Aerogels

To produce aerogels consisting of carbon and hydrogen, resorcinol-formaldehyde (RF) aerogels undergo carbonisation by heating in a high temperature furnace to remove oxygen and other elements that are undesirable to plasma physics experiments. As a result the structure is rearranged, and the carbonisation process puts the material under great stress. To ensure all chlorine was removed from DCPX, it was carbonised in a furnace with a ramp rate of 2 degrees per minute up to 400 °C for 6 hours, and kept at 400°C for one hour.

Carbonisation of DCPX was successful and without significant shrinkage by comparison to RF aerogels, which shrink by 50-75%. SEM images revealed a pore structure (figure 6.10) and elemental analysis indicated that the chlorine content was reduced to 5% from about 15%, which could be from the initiator. These properties, akin to RF aerogels, showed that DCPX has potential as a new laser material target. Furthermore, preparation of DCPX requires 1 week compared to 4 weeks for RF aerogels. This is particularly important to machining as this process is perhaps the most time consuming aspect of target fabrication. In addition, RF aerogels shrink after CPD and carbonisation by 50-75%, making very difficult to synthesise very low density carbonised aerogels. For example, if the intended density of the carbonised RF aerogel was 50 mg/cc, then RF aerogels with densities

of 20-25 mg/cm $^{-3}$ are needed prior to carbonisation to account for density increase due to shrinkage.

The lowest density DCPX aerogel achieved was 72.4±2.5 mg/cm $^{-3}$. Attempts to lower the density were performed by making alterations to the gel formulation. This included decreasing the initiator concentration, but resulted without success – no gels were formed. Although lower densities would be of interest, it was decided not to pursue this exhaustively as discovering DCPX as a new aerogel system with potential for use in high energy laser experiments was considered acceptable at this stage. Both carbonised and uncarbonised DCPX aerogels produced very little shrinkage and strong enough for machining, which was a significant improvement on equivalent RF aerogels.

A summary of all aerogels obtained in this work with the lowest density achieved and C:H ratio of each (Table 6.7).

Table 6.7. Summary of aerogel synthesised throughout this work. The errors are given elsewhere in this chapter.

Aerogel	**Nominal C:H ratio**	**Lowest density achieved (mg/cc)**
DVB	1:1	31.1
DCPD	1:1.2	51.1
DCPX (uncarbonised)	1:1	72.4
5V2N	1:1.4	165.8

6.4.6 DVB Density Gradient Aerogels Synthesis from Lewis Acid Catalysis

Fast formation of DVB gels by tin (IV) chloride inspired the idea of one-step synthesis of density gradient aerogels. Usually synthesis of gels involved mixing solvent and monomer before adding the initiator. Instead, the solvent and initiator were combined before controlled addition of DVB, thus polymerisation began on contact with the solvent mix. DCE was chosen as the solvent as it is denser than DVB (1.28 and 0.914 g cm^{-3} respectively). The difference in density meant that there were two opposing forces that created the density gradient. After monomer addition, DVB moved towards the bottom of the vessel, through the denser DCE/initiator mix slowing this downward motion, as well as simultaneous polymerisation. After some initial trials, a 50:50% mix of DCE and benzene was used to examine the effect of solvent density on gel formation (figure 6.10). This was performed to explore the possibility of controlling the density gradient. Density measurements of the DCE and 50:50 DCE:benzene aerogels showed some control over density gradients using different solvent systems (table 6.8). The aerogels were accurately cut into cylindrical geometry under a microscope in order to obtain accurate measurements (dimensions and weight) and then volume was calculated. From volume and weight, densities were calculated.

Figure 6.10. Images of original observed density gradient DVB aerogels using DCE (left) and 50:50 DCE:benzene mix (right).

Table 6.8. Density measurements of the top and bottom of aerogels synthesised in DCE and a 50:50 mix of DCE and benzene. The error is ± 13.9 mg/cc.

Solvent mix	**Density top (mg/cm^{-3})**	**Density bottom (mg/cm^{-3})**	**Gradient (mg/cm^{-3})**
DCE	308.4	213.1	95.3
DCE + Benzene (50:50)	313.2	300.0	13.2

Despite evidence of a density gradient, the gels formed were inconsistent; some gels mixed completely and had no gradient, others occupied half of the vial used for polymerisation with remaining solvent and catalyst solution underneath. Yet the majority of gels produced appeared to be solid plastic at the top of the vial and a gel at the bottom, giving a visual impression of a density gradient.

To improve reproducibility, melting point tubes were quickly inserted into to the polymerisation mixture after addition of DVB. It was postulated that capillary action of the gel mixture caused by the narrow tube would result in density gradient gels more consistently, and resulting gels would be closer to laser material target dimensions. This technique significantly improved the density gradient because the melting point tube created a smaller area for the reaction to continue regardless of remaining solvent surrounding the tube yet the issue of measuring the density gradient remained. Gels were subsequently dried using a CPD. The dried aerogels were on average 1 mm in diameter and 7 mm in length.

SEM images (figure 6.11) revealed a density gradient, the structure varied from the dense end of the gel with no apparent pore structure confirming it was high density, whereas images from the low density end had a porous, typical aerogel, structure with pore sizes in the region of 20-50 nm. The structure of the middle displayed characteristics of both ends; small pores appearing to decrease in size as the mass increased up the length of the aerogel.

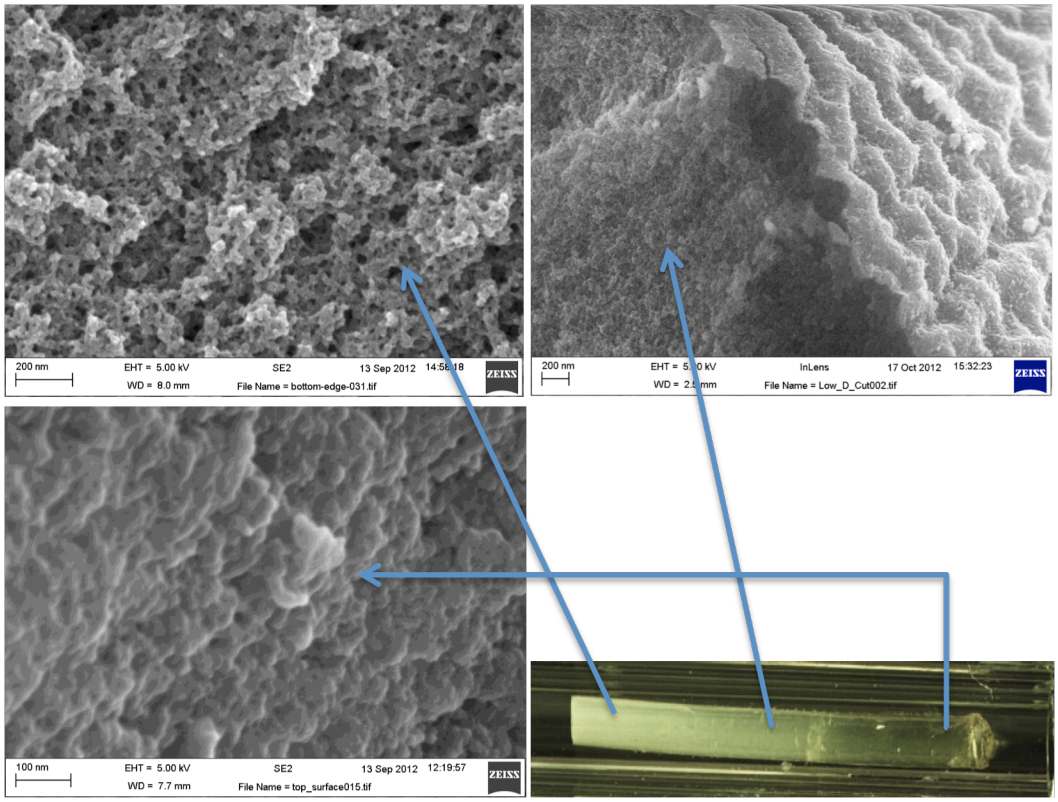

Figure 6.11. SEM images of a density gradient aerogel from low density (top left), medium density (top right) and the high density regions (bottom left). The arrows indicated the region of the material they were taken from (bottom right).

Use of melting point tubes resulted in gels that were physically more consistent, and reproducible but this did not give evidence of the nature of the density gradient. One technique that could measure this was X-ray tomography, with thanks to collaborators at the Lebedev Physical Institute, Moscow.[32] X-rays scanned entire aerogels and using a calibration sample of known density generated a density profile. The absorption of X-rays by the aerogels is related to the mass of the sample; higher density regions absorb more than lower density regions therefore tomography could detect if a density gradient was present. Tomography of aerogels measured densities that ranged from 50-600 mg/cm^{-3} and 400-1000 mg/cm^{-3} at the largest and 750-900 mg/cm^{-3} at the smallest (figure 6.12).[32] This revealed that the aerogel was a homogeneous material with a continuous change in density, but highlighted that the melting point tube method produced inconsistent density gradients.

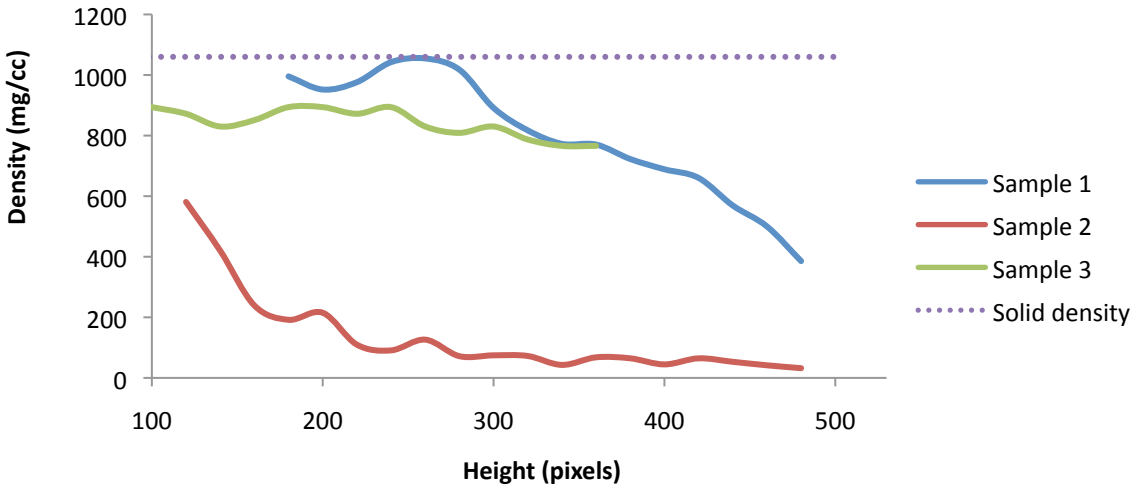

Figure 6.12. Vertical x-ray density profile of 3 density gradient DVB aerogels. The dotted line shows solid density.

Variable density was caused by an inconsistent monomer addition, altering the flow of fluids whilst polymerising, as random addition of the monomer would interact with the solvent/catalyst mix differently each time. Fast monomer addition would cause a more complete mixing of the monomer and solvent/catalyst, which produced gels more homogenous in colour, whereas slower addition meant that less mixing occurred and a variation in colour was seen. The rate of addition and accurate delivery of monomer could improve reproducibility of density gradient over a prescribed length significantly.

Homogenous density gradient gels prepared by a one step Lewis acid method for the first time was published in the duration of this work.[32] Despite this progress, the technique needs further development to refine the synthetic process to ensure that aerogels can be produced with designed density gradients consistently. Addition of monomer by hand created inconsistency, which was confirmed by X-ray tomography. Once these issues have been resolved, reducing the aerogel size to target dimensions would be desirable.

6.5 Conclusions

New low density carbon-hydrogen aerogels were synthesised. Synthesis of promising new materials with further development offers a potential increase in the capabilities of plasma physics applications. DVB aerogels with density gradients were also synthesised by developing a new technique. Controlling density gradients and formation of aerogels in one-step are difficult to achieve, and this technique partly overcomes these issues. With refinement to improve control of density gradients, these aerogels would satisfy an area of high interest to plasma physics applications.

With the exception of DVB, strong carbon-hydrogen aerogels below 50 mg/cm^{-3} proved difficult to synthesise. Some gels were formed but did not have suitable mechanical properties to prevent large shrinkage on drying. The discovery of new aerogels with increased hydrogen content took precedence over synthetic refinement. DCPD was not a new aerogel whereas 5V2N, DCPX, and DVB with density gradient aerogels have not been reported before. SEM imaging of all aerogels revealed typical aerogel structure that appeared as aggregated clusters. DVB aerogels from AIBN initiation reached as low as 31.0 mg/cm^{-3} density was attributed to near ideal synthetic conditions, producing small pore sizes, which were strong enough to retain its structure after drying.

1st generation Grubbs type catalysts were successful in producing DCPD aerogels. The enhanced mechanical properties and higher C:H ratio than DVB was favourable, however at 50 mg/cm^{-3} and below aerogels lost mechanical strength. SEM images revealed a clustered structure comprised of fibrous chains. Despite the small pore size between the fibrous chains, there is a lack of regular structure between these pores and large distance between polymer clusters that may have reduced strength at these lower densities. For example, refining the synthetic process by, for example, using monomer that effectively cross-link may resolve this.

Aerogels of 5V2N were synthesised for the first time using tin (IV) chloride. Post-cross-linking using Grubbs type catalyst to enhance mechanical properties was not

successful as materials shrunk significantly. On treatment of Grubbs, TD-NMR experiments showed that T_1 relaxation became more efficient indicating structural changes, which was justified by opening of secondary rings, or more likely a density increase. However, similar $T_{1\rho}$ relaxation times and SSNMR indicated that the macrostructures remained unchanged suggesting that post cross-linking was ineffective.

Although gels below 50 mg/cm^{-3} were not achieved with the monomer reported here, the very small pore size of DCPX helped to provide enough strength to survive carbonisation. Successful carbonised DCPX with no significant shrinkage other than carbonised RF aerogels is now available. Carbonised RF aerogels shrink more than 50-70% at lower densities. DCPX has been accepted for incorporation into new experiments in the future.

Use of tin (IV) chlorine, DVB and DCE allowed formation of density gradient aerogels. Using a solvent of higher density than the monomer, pre loaded with initiator allowed density gradient formation. These aerogels were the first to be synthesised using this technique. X-ray tomography indicated a uniform increase in density gradient and SEM confirmed the structure types along the length of the material. Further research to develop this technique could result in consistent and controlled density gradients, and be developed into density gradient across a specified length.

6.6 Appendix

6.6.1 Variable Temperature NMR Relaxation Experiments of 5V2N Aerogels

Variable temperature T_1 relaxation experiments were performed in order to determine the molecular motion behaviour of the material. Liquid nitrogen contained in a Dewar was evaporated with a cryogen probe, which monitored temperature and evaporation rate, was inserted and connected to the TD-NMR probe to cool to –50°C (223 K). Flow rates of 400 L/h were used. To achieve +100°C (343 K), a nitrogen gas cylinder was connected to the TD-NMR probe, which has a gas heating function, with a flow rate of 400 L/h. A period of 20/30 minutes was used to ensure the material had fully cooled/warmed before measurements were obtained.

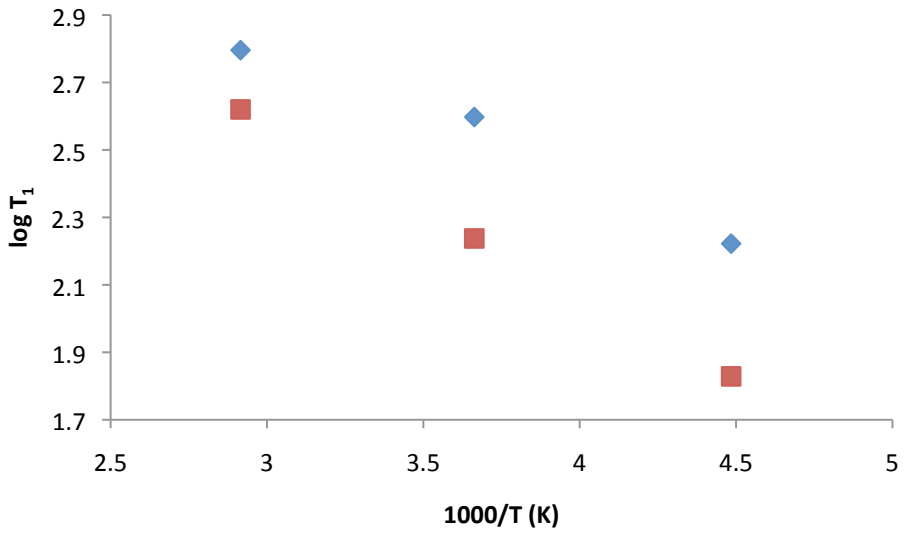

Figure 6.13. Log of T_1 relaxation times of 5V2N aerogel (blue) and 5V2N post cross-linked aerogel (red).

Figure 6.13 suggested that the aerogels were in a fast motional process, unexpected for a rigid polymer, both cross-linked and non cross-linked. Specifically, this is a motion above the T_1 minimum, between fast group rotations and slower chain rotations.[26] However, there is a rigidity difference between materials, which was

detailed in the main body of the text, due to treatment with Grubbs catalyst after gellation of 5V2N and/or increased density of the post cross-linked aerogel.

6.6.2 Elemental Anaylsis of DCPX Aerogels

TEST REPORT

WAS: 25873 **Sample ID**: DCPX 100 **Sample Type**: Solid

Technique	Element	Units	Result		Date
SOP 31	Carbon	%wt/wt	80.09	81.76	17-Mar-14
	Hydrogen		5.23	5.44	
	Nitrogen		0	0	

Insufficient sample for further analysis

Figure 6.14. Elemental anaylsis data of DCPX aerogel before carbonisation.

TEST REPORT

WAS: 25872 **Sample ID**: DCPX 100C **Sample Type**: Solid

Technique	Element	Units	Result		Date
SOP 31	Carbon	%wt/wt	93.26	93.14	17-Mar-14
	Hydrogen		1.78	1.73	
	Nitrogen		0	0.04	

Figure 6.15. Elemental anaylsis data of DCPX aerogel post carbonisation.

6.6.3 Solvent Effect on Density Gradient

To demonstrate the effect the solvent had on the density gradient of DVB during formation, a series of different solvent mixtures were prepared using DCE and toluene. After the solvent mixtures had been prepared, a pipette was used to add DVB as evenly as possible between all mixtures. Figure 6.9 was obtained after additional of DVB into every mixture. Table 6.17 contains the calculate density of the solvent mixtures. The varying density values explain why DVB was sinking down into the solvent mixture in samples 9 and 10 and not in the samples 4-7, which contained

more DCE. Samples 1-3 were near identical to sample 4, thus were not included in the original image.

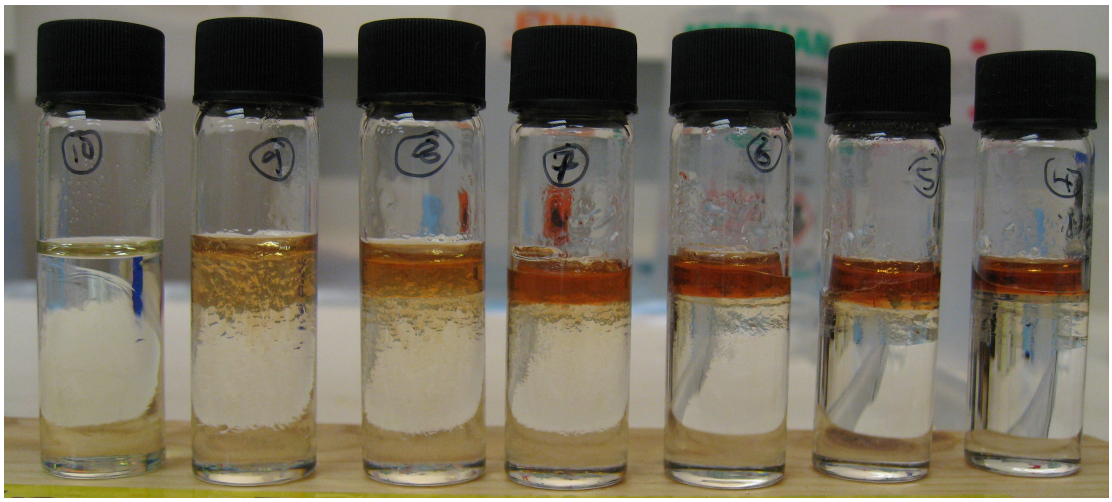

Figure 6.16. Image of DVB aerogel formation in DCE:toluene solvent mixtures. Samples 1-3 were observed to be similar to sample 4 and were left out of the original photograph.

Table 6.9. Density of DCE:toluene solvent mixtures. Samples 1 was 100% DCE.

Nominal density of DCE:Toluene (g/mL)	DCE:Toluene ratio (% by volume)	Sample number
1.214	90:10	2
1.756	80:20	3
1.137	70:30	4
1.099	60:40	5
1.060	50:50	6
0.983	40:60	7
0.944	30:70	8
0.906	20:80	9
0.867	10:90	10

6.7 References

1 J. Biener, S. O. Kucheyev, M. Y. Wang, C. Dawedeit, M. A. Worsley, S. H. Kim, C. Walton, G. Gilmer, L. Zepeda-Ruiz, A. Chernov, J. I. Lee, T. M. Willey, M. M. Biener, T. van Buuren, K. J. Wu, J. H. Satcher, and A. Hamza, *Final report SI 08-SI-004 : Fusion application targets*, 2010.

2 J. Biener, C. Dawedeit, S. H. Kim, T. Braun, M. a. Worsley, a. a. Chernov, C. C. Walton, T. M. Willey, S. O. Kucheyev, S. J. Shin, Y. M. Wang, M. M. Biener, J. R. I. Lee, B. J. Kozioziemski, T. van Buuren, K. J. J. Wu, J. H. Satcher, and a. V. Hamza, *Nuclear Fusion*, 2012, **52**, 062001.

3 B. Loupias, C. D. Gregory, E. Falize, J. Waugh, D. Seiichi, S. Pikuz, Y. Kuramitsu, A. Ravasio, S. Bouquet, C. Michaut, P. Barroso, M. Rabec le Gloahec, W. Nazarov, H. Takabe, Y. Sakawa, N. Woolsey, and M. Koenig, *Astrophysics and Space Science*, 2009, **322**, 25–29.

4 C. D. Gregory, B. Loupias, J. Waugh, P. Barroso, S. Bouquet, E. Brambrink, S. Dono, E. Falize, J. Howe, Y. Kuramitsu, R. Kodama, M. Koenig, C. Michaut, S. Myers, W. Nazarov, M. M. Notley, A. Oya, S. Pikuz, M. Rabec le Gloahec, Y. Sakawa, C. Spindloe, M. Streeter, L. a Wilson, and N. C. Woolsey, *Plasma Physics and Controlled Fusion*, 2008, **50**, 124039.

5 Z. Lin, T. Yongjian, Z. Chifeng, L. Xuan, and Z. Houqiong, *Nuclear Instruments and Methods in Physics Research Section A*, 2002, **480**, 242–245.

6 N. G. Borisenko, A. E. Bugrov, I. N. Burdonskiy, I. K. Fasakhov, V. V Gavrilov, A. Y. Goltsov, A. I. Gromov, A. M. Khalenkov, N. G. Kovalskii, Y. A. Merkuliev, V. M. Petryakov, M. V Putilin, G. M. Yankovskii, and E. V Zhuzhukalo, *Laser and Particle Beams*, 2008, **26**, 537.

7 M. Koenig, A. Benuzzi-Mounaix, F. Philippe, B. Faral, D. Batani, T. A. Hall, N. Grandjouan, W. Nazarov, J. P. Chieze, and R. Teyssier, *Applied Physics Letters*, 1999, **75**, 3026.

8 R. Teyssier, D. Ryutov, and B. Remington, *The Astrophysical Journal Supplement Series*, 2000, **127**, 503–508.

9 Y. Zhong, B. Zhou, J. Gui, A. Du, Z. Zhang, and J. Shen, *Fusion Engineering and Design*, 2011, **86**, 238–243.

10 L. P. Martin, J. R. Patterson, D. Orlikowski, and J. H. Nguyen, *Journal of Applied Physics*, 2007, **102**, 023507–023507–10.

11 S. M. Jones, *Journal of Sol-Gel Science and Technology*, 2007, **44**, 255–258.

12 J.-Y. Gui, B. Zhou, Y.-H. Zhong, A. Du, and J. Shen, *Journal of Sol-Gel Science and Technology*, 2011, **58**, 470–475.

13 A. Du, B. Zhou, J.-Y. Gui, G.-W. Liu, Y.-N. Li, G.-M. Wu, J. Shen, and Z.-H. Zhang, *Acta Phys. Chim. Sin*, 2012, **28**, 1189–1196.

14 M. F. Ashby, *Metallurgical Transactions A*, 1983, **14A**, 1756–1768.

15 M. R. Kessler and S. R. White, *Journal of Polymer Science Part A: Polymer Chemistry*, 2002, **40**, 2373–2383.

16 J. K. Lee and G. L. Gould, US 0229374 A1, 2006.

17 J. K. Lee and G. L. Gould, *Journal of Sol-Gel Science and Technology*, 2007, **44**, 29–40.

18 M. S. Sanford and J. A. Love, in *Handbook of Metathesis volume 1*, ed. R. H. Grubbs, Wiley-Vch, 1st edn., 2003, pp. 112–131.

19 R. W. Pekala and C. T. Alviso, in *Materials Research Society Symposium*, Livermore, CA, 1992, vol. 270, pp. 3–14.

20 R. H. Grubbs, *Tetrahedron*, 2004, **60**, 7117–7140.

21 C. Slugovc, *Macromolecular Rapid Communications*, 2004, **25**, 1283–1297.

22 H. Lasarov and T. T. Pakkanen, *Macromolecular Chemistry and Physics*, 2000, **201**, 1780–1786.

23 C. Zhao, M. Ribeiro Rosário, and M. F. Portela, *Journal of Molecular Catalysis A: Chemical*, 2002, **185**, 81–85.

24 R. H. Grubbs and S. T. Nguyen, US 5728917, 1998.

25 J. M. G. Cowie, *Polymers: Chemistry and Physics of Modern Materials*, Blackie and Sons, Limited, London, 2nd edn., 1991.

26 R. K. Harris, *Nuclear Magnetic Resonance; A Physiochemical View*, Longman Scientific & Technical, Harlow, 2nd edn., 1987.

27 P. J. Hore, *Nuclear Magnetic Resonance*, Oxford University Press, Inc., New York, 1995.

28 E. Ruckenstein and X. Chen, *Macromolecules*, 2000, **33**, 8992–9001.

29 R. W. Pekala, C. T. Alviso, F. M. Kong, and S. S. Hulsey, in *Third International Symposium on Aerogels*, 1991, pp. 2–8.

30 R. W. Pekala, US 4873218, 1989.

31 S. Mulik, C. Sotiriou-Leventis, and N. Leventis, *Polymer Preprints*, 2006, **47**, 364–365.

32 N. G. Borisenko, W. Nazarov, C. S. A. Musgrave, Y. A. Merkuliev, A. S. Orekhov, and L. A. Borisenko, *Journal of Radioanalytical and Nuclear Chemistry*, 2014, **299**, 961–964.

7. Conclusions and Future Work

The stringent requirements of laser target materials for plasma physics experiments have set new challenges for synthesis and characterisation techniques for low density porous polymers. Novel and imperative high energy laser physics experiments can be designed by developing new materials and characterisation techniques, some based on the improvements of existing methods, are an essential part of this success. One of the most important plasma physics experiments relevant here is generating plasmas with increased opacity.[1–3] In order to achieve this increased opacity, materials with an empirical formula of C_1H_2 are needed, as currently C_1H_1 materials used for other experiments cannot generate the required opacity. The increased hydrogen content reduces the level of absorbed/scattered higher energy X-rays that can cause interference in diagnostics.

Studies of plasma shock fronts, another important aspect of plasma physics also requires low density porous polymers with sub micrometer pore sizes and a density gradient.[4] Typically these porous polymers are required to have low density at one end and gradually increasing to full density at the other end with prescribed density increase per unit length. Some density gradient aerogels have been reported in literature.[5–8] However, these density gradient aerogels are based on silica or contain oxygen in their composition, and produced in multiple steps, which can produce inhomogeneity at the edges between two regions of different density. The density gradient aerogels reported here are DVB aerogels (carbon-hydrogen composition) made in one step, which reduces the risk of inhomogeneity. Furthermore, DVB aerogels do not have heavy elements such as silicon, which could be a problem for some experiments depending on the diagnostic equipment used. In addition, the aerogels synthesised were required to possess high mechanical strength at low density, which is not always easy to achieve.

Part of the work reported here was concerned with addressing these important issues. A significant improvement to mechanical properties of established S-co-DVB polyHIPEs was achieved. This was compared to previous research to understand how

the improvement was influenced by polyHIPE structure. In addition, homogeneous density gradient aerogels were synthesised from a one-step process and characterised for the first time.[9]

In addition to development of new synthetic porous materials, TD-NMR was used throughout this work as a new characterisation technique, and was presented as one of the first instances of characterisation of low density porous polymers. Developing TD-NMR as a novel tool for characterisation of low density polymers was of interest. Nuclear spin relaxation times are dependent on molecular motion, therefore by observation of relaxation times it was possible to analyse differences in polyHIPE and aerogel structure. Also, different frequencies of observation could probe different frequencies of molecular motion. Relaxation studies have been carried out on a number of solid materials including polymers,[10–12] however, very little research concerned with low density polymers.[13] A preliminary study was therefore undertaken using established polymer systems (polystyrene and PVDF) to evaluate the capabilities of the apparatus. T_1 and $T_{1\rho}$ experiments probed different orders of frequency thus molecular motion of these polymers, which characterised each polymer in more detail. PVDF relaxation data correlated to existing studies that used high magnetic fields strengths.[14,15] Varied temperature $T_{1\rho}$ relaxation measurements demonstrated the molecular motion of PVDF, revealing that specific phase transitions (glass transition and melt) were region specific. This was also the first time PVDF had been investigated using TD-NMR. Polystyrene relaxation data was not as revealing as PVDF due to the different properties of polystyrene. However, in this work low density polymers were largely based on styrene, and these preliminary experiments were applied to these materials. Overall, this initial study gave some confidence when studying polyHIPEs and aerogels, and provided a framework for investigation.

PolyHIPEs and aerogels synthesised in this work were investigated by TD-NMR. For S-co-DVB polyHIPEs it was known that varying cross-linking percentage altered the mechanical properties.[16,17] In addition, the factors affecting mechanical properties of

materials including low density have been discussed in detail. Yet the discussion had not considered the influence of pore size and the discussions have been based on wall thickness and controlled synthetic routes only. Furthermore, explanations why physical strength varied as a function of cross-linking percentage were not addressed. In the field of laser target material development strategies to improve physical properties, had not been extensively investigated until this study.

It has been shown that enhanced mechanical properties in polyHIPEs has a dependency on pore size dependency,[18] which this work benefited from, and can further contribute to that discussion. The double syringe technique to form HIPEs was considered to generate increased shear force by comparison to overhead stirring mixing. This produced smaller emulsion droplets resulting in a small pore sized polyHIPE. Emulsion formulation was also important, using formulations based on previous studies that aid in formation of small pore size and high mechanical strength polyHIPEs.[16] Investigating different cross-linked polyHIPEs with TD-NMR could provide explanations as to why this occurred.

Mechanical analysis of varied cross-linked S-co-DVB polyHIPEs correlated with previous studies,[19] however polyHIPE mechanical strength here was higher than other reports that used ~130 mg/cc density polyHIPEs.[20] SEM and mercury porosimetry revealed pore sizes of about 1 μm and 0.4 μm respectively, which would contribute to increased mechanical strength of polyHIPEs compared to larger pore sized equivalent (with constant wall thickness). Using TD-NMR, T_1 relaxation experiments of varied cross-linked S-co-DVB polyHIPEs correlated to Young's modulus data, with longer relaxation times indicating a larger Young's modulus. Long relaxation times reflected a rigid structure of small group rotations, indicating cross-linking was effective at 10-30% percentage of DVB. Whereas shorter relaxation times meant that these groups had freer motion, thus less effective copolymerisation and lower Young's modulus values. $T_{1\rho}$ relaxation data, which measured slower motions such as large chain rotation, suggested that polyHIPEs became more rigid with increasing DVB content but later identified to be clustering of DVB polymer.

Combining data from both relaxation experiments provided deeper analysis of the structure, which helped to identify clustering of DVB in polyHIPEs. Clustering was characterised as regions of cross-linked DVB polymer with numerous hanging/end groups. This arrangement was justified by fast T_1 times of hanging/end groups and longer $T_{1\rho}$ relaxation times of larger chain motion. Poor emulsion stability was given as the primary reason for clustering to occur, but needed further investigation.

This work also complemented X-ray radiography of polyHIPEs. Radiography revealed inhomogeneous regions of higher and lower density within polyHIPEs, which could be related to DVB clusters. Identification of the location and nature of clustering DVB was important as this could help address crucial issue of homogeneity of polyHIPEs necessary for laser targets. Experimental modeling requires density measurements accurate to within 1 mg/cc or less of target density. Therefore inhomogeneity presents a number of issues if laser targets are machined from a region of higher or lower density. For example, a target shaped (machined) from such high or low density region will give vastly different density to bulk density. Thorough investigations using TD-NMR were performed in order to understand the extent of clustering and apply focused strategies to resolve this problem.

Varible temperature TD-NMR experiments using S-d_8-co-DVB revealed that clustering was present to a significant extent. With styrene masked from observation, T_1 relaxation times of areas would observe rigid regions including cross-linked areas only, however, fast relaxation times indicated the presence of many freely rotating groups. This was only possible if clustering of DVB was extensive to create many free rotating groups resulting in the observed fast relaxation times. These experiments were performed in the ideal cross-linking percentage region, which was unexpected. It was suggested that emulsion stability was the route of this issue, affecting physical properties. However, the prohibitive cost of obtaining deuterated DVB meant that masking of these rigid regions was not possible, which would have been valuable in understanding the molecular motion of clusters allowing a better understanding of the problem. Alternative strategies to resolve the

problem were attempted using a cross-linker with higher purity, and different surfactant systems.

DVB 80 is a stock bought mixture of monomers and non-reacting species could create inhomogeneous polyHIPE microstructures due to differences in stability of each species in the emulsion. In order to establish this, experiments were carried out using para-DVB (85%) as a crosslinker instead of DVB 80 in S-co-DVB polyHIPE. It was postulated that this would improve mechanical properties. However, emulsion stability and mechanical strength deteriorated with para-DVB compared to DVB 80 containing polyHIPEs. Visible degradation was clear, and TD-NMR, SEM and mercury porosimetry characterisation provided more evidence for this deterioration. DVB 80 contains para-DVB, thus para-DVB could be contributing to poor emulsion stability and causing clustering in polyHIPEs cross-linked by DVB 80, which could prevent even higher modulus being achieved. X-ray radiography had demonstrated the effect of poor emulsion stability leading to regions of high density clusters, which produced unacceptable polyHIPEs for laser targets. However, small improvements to pore size were achieved by use of a mixed Span® 80/20 surfactant system in polyHIPEs containing either DVB 80 or para-DVB provided a future avenue of research to pursue. A 3-surfactant system, which has been shown to improve emulsion stability,[21] was attempted but resulting polyHIPEs were fragile and crumbled. Structural details observed by SEM revealed a non-HIPE structure suggesting that the interfacial tension between the immiscible liquids may have been reduced too far and to such an extent that the phases became miscible. Studies into the mixed Span® surfactant system were not exhaustive to fully resolve this issue. The mixed Span® surfactant system decreased pore size, which could improve polyHIPE strength. Given that pore size and homogeneity contribute to physical strength, and the mixed Span® surfactant system made significant contributions opening up an interesting area to investigate further.

Studies of polyHIPE physical properties using TD-NMR have not been reported in literature. The correlation of T_1 relaxation to mechanical strength in polyHIPEs was an innovative contribution to the non-destructive characterisation of materials for

high energy laser experiments. This work not only demonstrated TD-NMR as a characterisation technique for laser target material, but also could be applied to other fields that are interested in polyHIPE physical properties. The capabilities of TD-NMR could allow this technique to be used to screen material strength within a system of interest and give an idea of material inhomogeneity. Whilst it cannot replace techniques such as DMA because TD-NMR cannot place quantitative values on strength, assessment of strength using a non-destructive technique can offer faster characterisation of structures without the need for laborious preparation of polyHIPE discs. With the expansion of potential bio-medical applications of polyHIPEs,[22–27] TD-NMR could be valuable tool to assess these materials during development. Analysis of structure in regional detail based on specific frequencies of molecular motion is something conventional polymer characterisation techniques cannot achieve. In addition, this could be used to help understanding of structural differences between two materials based on the same polymer system that have different effectiveness for the application, much in the same manner as this work comparing different level of cross-linked S-co-DVB polyHIPEs.

Despite faster data acquisition than DMA, one small issue with TD-NMR was that the processing of data was slower. The MQ20 NMR machine was not designed for research applications such as this, but for commercial qualitative applications. This meant that the fitting software was approximate rather than precise resulting in external processing to be performed, which took additional time for the volume of experiments performed. Processing data in this manner was often laborious and, on occasion, led to confusion. NMR relaxation can be difficult to understand, especially when trying to evaluate data from multiple experiment types. DVB clusters postulate originated from what appeared to be a contradiction between T_1 and $T_{1\rho}$ relaxation data, which could only be explained by clusters of cross-linked material, however this took time to ascertain and eventually resolve.

Another primary objective in this work was synthesis of new materials with increased hydrogen to carbon ratio, ideally to C_1H_2. C_1H_2 foams are used for opacity experiments in laser physics as the high hydrogen content makes the resulting

plasma more opaque. The most widely used porous material for these experiments is polymethylpentene, commercially known as TPX®. TPX® is extremely difficult to synthesise from the monomer because of the conditions used in the synthesis, this could only be done in an industrial set up. However, it is feasible to synthesise porous TPX® from solutions of TPX® dissolved in different solvents by chemical, thermal and solvent induced phase separation techniques. TPX® foams have been produced by these methods for opacity experiments for many years.[28,29] Despite this, there are substantial issues with the production of TPX® foams using phase separation techniques. The two most persistent problems are large shrinkage when TPX® is dried, and achieving small pore size. Pore diameters below one micrometer are very difficult to achieve, thus other alternatives have been looked at. This work provided a number of new low density foams to be considered as an alternative.

Although the ideal material for opacity experiments is C_1H_2, hydrogen to carbon ratios larger than one will be acceptable for the majority of opacity experiments. TPX® is unique and there is no reported material in the literature with the same empirical formula, therefore any material with empirical formula $C_1H_{n>1}$ will be of great importance to high energy laser experiments.

Some novel and interesting aerogels were also developed, using a number of established synthetic methods including ROMP and cationic polymerisation. Although 5-vinyl norbornene and dichloroparaxylene (DCPX) had acceptable pore structure and uniformity, the hydrogen to carbon ratios of $C_1H_{1.33}$ based on the monomer were also the highest achieved in this work were sufficiently high to be considered for opacity experiments. However, DCPX contained chlorine from the monomer and the cationic initiator tin (IV) chloride, which could interfere with X-rays. Both aerogels had issues in achieving very low densities that would need to be resolved through future investigations as it is a requirement for opacity materials.

There have been no reports in literature for the synthesis and characterisation of t-butyl styrene polyHIPE and the significance of its hydrogen to carbon ratio to opacity experiments. T-butyl styrene polyHIPEs have a reasonably high CH ratio for $C_1H_{1.33}$.

High strength and a large increase in hydrogen content suggested it could be machined and used a target in opacity experiments. At the time of writing, t-butyl styrene polyHIPE has already been accepted as a possible material for opacity experiments. TD-NMR demonstrated the effect of the large t-butyl group, increasing polymer free-volume of the structure, which was seen by TD-NMR. It was postulated that the increased free volume lowered the Young's modulus by comparison to styrene by preventing close packing of the polymer chains. T-butyl polyHIPE has highlighted that changes to the HIPE chemistry can significantly affect the physical properties of the material, which would need to be taken into account when developing new laser target materials with even higher hydrogen to carbon ratio.

There are always demands for nanoporous and carbonised nanoporous materials for a wide variety of experiments in high energy physics that do not require specific empirical formulae. It was suggested here that DCPX aerogel could be an alternative to established resorcinol-formaldehyde (RF) and carbonised RF aerogels. RF aerogels are laborious to prepare taking at least one month, whereas DCPX gels, including carbonisation, require half the time. DPCX aerogels had acceptable homogeneous pores and the only aerogel in this work that survived the carbonisation process without loss of other mechanical properties. More importantly, DCPX did not shrink during carbonisation, which is a common occurrence with aerogels including RF, suggesting it has a strong structure. There appears to be no reports on DCPX or carbonised DCPX aerogels in the literature, and this new aerogel could be a significant new aerogel for designing new high energy laser experiments. DCPX aerogels are in the first phase of development, but more research is needed to resolve some minor synthetic issues to achieve very low densities.

A one-step synthesis of DVB aerogels with a homogenous density gradient was the most substantial aerogel advancement. Homogeneous density gradient materials are difficult to achieve for aerogels with carbon-hydrogen composition. This could be due to a lack of interest in carbon-hydrogen aerogels, as silica aerogels have been employed for large-scale projects.[30,8] Yet, for plasma physics experiments, low density carbon-hydrogen materials with a homogeneous density gradient would

increase understanding of some aspects of high temperature and pressure physics experiments using high energy lasers, for example plasma shock fronts.[4] Currently, the production of this type of material reported in the literature is by fabrication of different components or formed through complicated synthetic procedures, which is not ideal as this creates abrupt changes in density from one component to the other and irreproducible inhomogeneity.[5,31] The one step production method reported here demonstrated a new technique to form homogeneous density gradient carbon-hydrogen aerogels. By using liquid monomer and a solvent/catalyst mix that have different densities from each other, a density gradient is developed as polymerisation progresses.[9] The difference in density of the two liquids and the rate of addition of the monomer into the mix produce the density gradient as polymerisation begins on monomer/solvent contact. These aerogels had dimensions of 1mm x 6mm on average and whilst too large for laser targets the potential to develop these materials remains feasible. Perhaps a challenging aspect of this production method reported here, and remains to be resolved, was the high variance in density gradient of the aerogels. The gradient was as high as 500 mg/cc and low as 100 mg/cc.[9] The inability to control the density gradient is very limiting due to the requirement for accurate density measurements to ensure correct modeling and interpretation of results.

Overall this work demonstrated increased polyHIPE mechanical strength, a new technique for characterisation using TD-NMR, and synthesis of a variety of new low density materials with the potential for development into a laser target material. For laser target materials, both of these aims were significant steps towards achieving materials that would allow greater capabilities for plasma physics experiments. Perhaps S-co-DVB was regarded as a well-studied polymer system, but at micro-scale level polyHIPE structure revealed interesting structural behaviours and molecular motions that were not reported before because of the scale of this application compared to others. HIPEs are complicated emulsions and resulting polyHIPEs are dependent on the emulsion chemistry and synthetic conditions. The complexity of HIPEs can often be understated in literature; this work demonstrated that polyHIPE structures are not particularly well understood at the micro-scale. In relation to the

applications of polyHIPE in this work, the areas of inhomogeneity observed and investigated will have an impact on future synthetic strategies for laser targets. Whilst established techniques remain valuable to polyHIPE characterisation, they were not addressing the problems that are specific to materials synthesised for laser targets. TD-NMR addressed some of these issues, however, TD-NMR is not a stand-alone technique that can be used in place of a suite of techniques due to factors such as slow data processing. Nevertheless, TD-NMR proved to be faster than DMA, and use in conjunction with other techniques showed promise as additional tool in elucidating micro-scale structures.

A new one-step synthesis of density gradient aerogel was developed, which once refined further will facilitate series of novel high energy laser physics experiments. DCPX aerogels were prepared and carbonised with minimum shrinkage in half the time of equivalent RF aerogels. This offers a possible alternative material for plasma physics experiments and may even replace RF aerogels once very low density DCPX aerogels are produced.

7.1 Future Work

During this project a number of problems were addressed and resolved, however, due to the lack of time a few issues that could not be looked into deserves further attention. These were categorised as short-term objectives, which would take approximately 6 months to complete and would compliment the work presented here. Predictably, some interesting projects were identified during the course of this work, which would require long-term research. These projects would take the duration of a year or more to complete effectively.

7.1.1 Short-term Objectives

TD-NMR showed promise as a new characterisation technique for low density porous polymers, however time did not allow for varied temperature relaxation experiments of many systems including t-BS and para-DVB homopolymer polyHIPEs. This will provide more structural information, based on molecular motion, allowing better characterisation of these polyHIPEs. It was thought that the homopolymers would exhibit more molecular motion than the cross-linked equivalents that were analysed in this work. This would confirm the effect on molecular motion that cross-linking has on the structure, particularly the effect of the t-butyl group. The freely rotating t-butyl group of t-BS may exaggerate molecular motion as a function of temperature due to increased free volume, revealing more features of the relaxation profile.

A thorough investigation of the mixed Span® surfactant system on S-co-DVB polyHIPEs could be performed to identify the required surfactant concentrations to improve physical properties. Varying concentrations of Span® 80 to Span® 20 in S-co-DVB polyHIPEs would affect the pore structure of the resulting polyHIPE, and using SEM and porosimetry would characterise these differences effectively to distinguish the ideal mixture of surfactants to use. Reduction of the emulsion coarsening mechanisms would likely result in smaller pore sizes and a more homogeneous structure. Furthermore, this would contribute towards a larger goal of resolving the inhomogeneity issue in S-co-DVB polyHIPEs. TD-NMR could be used to characterise the effect on molecular motion, with the aim of finding the relationship between polyHIPEs made using different surfactant systems and its impact on pore size and strength.

7.1.2 Long-term Objectives

Longer term projects would encompass resolving of PolyHIPE and density gradient aerogel synthetic issues, as well as further evidence is required to substantiate the claims of TD-NMR. One strategy for addressing PolyHIPE synthetic issues is to apply different surfactant systems, including the previously mentioned mixed Span® system and 3-surfactant system, to achieve improved pore homogeneity. Applying various surfactant systems could target better stabilisation of the emulsion, reducing coarsening mechanisms whilst the monomers cure into a polyHIPE. The resulting polyHIPE may have more homogeneous pore structure, which could be probed by SEM, mercury porosimetry and TD-NMR in the same manner as this work to determine the effect of these different surfactant systems. TD-NMR could also investigate the extent of clustering of DVB in each system by using deuterated styrene and varied temperature relaxation experiments. However, clustering could be an inherent issue with DVB and styrene as a polymer system that specifically relates to high density clusters found in S-co-DVB polyHIPE. Higher reactivity of DVB than styrene could result in formation of DVB polymer regions over suitable copolymerisation, thus investigation of cross-linkers other than DVB is required. Another likely possibility is that clustering and poor emulsion stability cannot be eliminated in HIPE as the high internal phase volumes put too much pressure on the surfactant films to prevent microscale inhomogeneities forming. These two issues are related thus requires an extensive study to distinguish these issues from each other.

Surfactant systems such as the 3-surfactant system could be investigated in more detail, which has demonstrated its effectiveness in HIPE stability.[21] Investigations using a 3-surfactant system in this work were limited, with characterisation results indicating that it perhaps not effective on the pore size scale of polyHIPEs made in this work. It is possible that the smaller pore size of polyHIPEs produced by the two-syringe method requires different concentrations of surfactants than larger pore sized equivalents. Smaller pore sized emulsions are more stable than larger ones, thus reducing the concentration of the 3-surfactant system could result in improve

stability by comparison to Span® 80 alone. If improvements to the homogeneity of polyHIPEs are gained, this would not only benefit laser target material development but possibly other applications reliant on homogeneity of microstructure in polyHIPEs.

In addition to the aforementioned studies, application of TD-NMR to a different polymer system is necessary to ensure validation of its capabilities and to find out its limits, particularly to low density materials. S-co-DVB is a rigid polymer, but was shown to be mobile by magnetic relaxation experiments. PVDF was investigated to validate this work using preliminary studies. Since PVDF is a full density polymer and laser target materials are low density polymer systems, another low density polymer should be investigated. One such system that would be relevant is resorcinol-formaldehyde aerogels especially as no aromatic rings are present. RF polymerisation undergos many steps before completion to a laser target; initial gel formation, post cross-linking and carbonisation. TD-NMR could be applied at each of these stages to investigate the structure, and see the structural differences at each stage compared to the previous step. It would be expected that after initial gel formation and the first cross-linking process the structure would become significantly more rigid, particularly by T_1 relaxation times. $T_{1\rho}$ could be more complicated to predict, as increased cross-linking will increase the rigidity of the structure. However, $T_{1\rho}$ relaxation measures the polarisability of the magnetisation based on order. Thus, increased cross-linking may result in an increased disorder of the structure resulting in faster relaxation times as the structure is locked into random, but rigid, order. The sample temperature inside TD-NMR apparatus can be set and controlled accurately, which can give an advantage of studying polymerisation from the onset of gelation of the system, allowing study of polymerisation in real time. SSNMR would be able to confirm this due to the dependency of line-widths on structure. Carbonisation removes by-products from the synthetic process, which also has the effect of rearranging the structure. The effect on structure would be dramatic as removal of any hanging chains and groups

will increase T_1 relaxation times, with $T_{1\rho}$ possibly increasing too as structural rearrangement creates a more ordered structure.

Finally, developing DVB density gradient aerogels, one of the interesting challenges of the future, would require significant effort in the synthetic process. For this density gradient aerogel to be a viable material for laser applications, two important goals need to be accomplished. The first is the ability to control the density gradients to a prescribed maximum and minimum per unit length of the aerogel, and to be able to reproduced this. The second is to be able to produce these prescribed density gradient aerogels closer to laser target dimensions. A technique to standardise the controlled addition of the monomer to the solvent/catalyst mix is first required. Commercially available micropipettes used in pharmaceutical preparation could be used to deliver precise and repeatable quantities of monomer as low as nanoliters. These machines can dispense precise and repeatable quantities of monomer with each payload, and with adjustable frequencies. This would give the consistency to the synthetic process that lacked in this work. X-ray tomography was the most efficient characterisation technique and could be used to monitor consistency in density gradient aerogels. Assuming the effectiveness of the liquid dispenser and X-ray tomography characterisation, varying the volume or frequency of insertion could be tested as a method to control the gradient produced. The synthetic process of density gradient aerogels is challenging and could be time-consuming to resolve, especially reducing the aerogel scale closer to a laser target size. Reducing the scale reduces the mass and therefore strength of the material, which could result in damage to the aerogel from the drying process. In addition, reduced mass will result in reduced X-ray absorption, affecting the material contrast for imaging. These challenging problems could take a long time to resolve, nevertheless would be a significant contribution to the laser experiment community, and is a worthwhile investment in time and effort.

7.2 References

1 M. Ragheb, *Inertial Confinement Fusion*, 2008.

2 Y. Dong, J. Yang, L. Zhang, W. Shang, and T. Song, *Physics Letters A*, 2014, **378**, 813–816.

3 A. I. Gromov, N. G. Borisenko, S. Y. Gusikov, Y. A. Merkuliev, and A. V. Mitrofanov, *Laser and Particle Beams*, 1999, **17**, 661–670.

4 R. Teyssier, D. Ryutov, and B. Remington, *The Astrophysical Journal Supplement Series*, 2000, **127**, 503–508.

5 S. M. Jones, *Journal of Sol-Gel Science and Technology*, 2007, **44**, 255–258.

6 C. Torres-Sánchez and J. R. Corney, *Journal of Materials Science*, 2010, **46**, 490–499.

7 Y. Zhong, B. Zhou, J. Gui, A. Du, Z. Zhang, and J. Shen, *Fusion Engineering and Design*, 2011, **86**, 238–243.

8 A. Du, B. Zhou, J.-Y. Gui, G.-W. Liu, Y.-N. Li, G.-M. Wu, J. Shen, and Z.-H. Zhang, *Acta Phys. Chim. Sin*, 2012, **28**, 1189–1196.

9 N. G. Borisenko, W. Nazarov, C. S. A. Musgrave, Y. A. Merkuliev, A. S. Orekhov, and L. A. Borisenko, *Journal of Radioanalytical and Nuclear Chemistry*, 2014, **299**, 961–964.

10 K. Saalwächter, *Journal of the American Chemical Society*, 2003, **125**, 14684–5.

11 A. Papon, K. Saalwächter, K. Schäler, L. Guy, F. Lequeux, and H. Montes, *Macromolecules*, 2011, **44**, 913–922.

12 G. C. Borgia, P. Fantazzini, A. Ferrando, and G. Maddinelli, *Magnetic Resonance Imaging*, 2001, **19**, 405–9.

13 E. W. Hansen, G. Fonnum, and E. Weng, *Journal of Physical Chemistry B*, 2005, **109**, 24295–24303.

14 P. Wormald, B. Ameduri, R. K. Harris, and P. Hazendonk, *Solid State Nuclear Magnetic Resonance*, 2006, **30**, 114–23.

15 T. Montina, P. Wormald, and P. Hazendonk, *Macromolecules*, 2012, **45**, 6002–6007.

16 J. M. Williams, A. J. Gray, and M. H. Wilkerson, *Langmuir*, 1990, **6**, 437–444.

17 J. M. Williams, J. J. Bartos III, and M. H. Wilkerson, *Journal of Materials Science*, 1990, **25**, 5134–5141.

18 G. Ceglia, L. Mahéo, P. Viot, D. Bernard, A. Chirazi, I. Ly, O. Mondain-Monval, and V. Schmitt, *The European Physical Journal. E*, 2012, **35**, 9708.

19 J. M. Williams and D. A. Wrobleski, *Langmuir*, 1988, **4**, 656–662.

20 Y. Luo, A.-N. Wang, and X. Gao, *Soft Matter*, 2012, **8**, 1824–1830.

21 A. Barbetta and N. R. Cameron, *Macromolecules*, 2004, **37**, 3202–3213.

22 H. Zhang and A. I. Cooper, *Soft Matter*, 2005, **1**, 107–113.

23 R. S. Moglia, J. L. Holm, N. A. Sears, C. J. Wilson, D. M. Harrison, and E. Cosgriff-Hernandez, *Biomacromolecules*, 2011, **12**, 3621–3628.

24 F. Audouin, R. Larragy, M. Fox, B. O'Connor, and A. Heise, *Biomacromolecules*, 2012, **13**, 3787–94.

25 E. M. Christenson, W. Soofi, J. L. Holm, N. R. Cameron, and A. G. Mikos, *Biomacromolecules*, 2007, **8**, 3806–14.

26 P. Krajnc, N. Leber, D. Stefanec, S. Kontrec, and A. Podgornik, *Journal of Chromatography A*, 2005, **1065**, 69–73.

27 W. Busby, N. R. Cameron, and C. A. Jahoda, *Biomacromolecules*, 2001, **2**, 154–64.

28 N. Elliott, *Nuclear Instruments and Methods in Physics Research Section A: Accelerators, Spectrometers, Detectors and Associated Equipment*, 1995, **362**, 112–113.

29 W. L. Perry, R. C. Dye, P. G. Apen, L. Foreman, and E. Peterson, *Applied Physics Letters*, 1995, **66**, 314.

30 S. M. Jones, *Journal of Sol-Gel Science and Technology*, 2006, **40**, 351–357.

31 J.-Y. Gui, B. Zhou, Y.-H. Zhong, A. Du, and J. Shen, *Journal of Sol-Gel Science and Technology*, 2011, **58**, 470–475.